PONTIFICIA UNIVERSIDAD CATÓLICA DEL PERÚ

Escuela de Posgrado

The role of organic carbon and arsenic in the formation of sediment-hosted gold deposits: A case study of the Shahuindo and Algamarca epithermal deposits, Peru

Tesis para optar el grado académico de Doctor en Ingeniería que presenta:

Renzo Andres Galdos Postigo

Asesores:

Asesor PUCP: *Jean Vallance*

Asesor UPS: *Gleb S. Pokrovski*

Co-Asesor UPS: *Patrice Baby*

Lima, 2024

Informe de Similitud

Yo, Jean Francois Victor VALLANCE, **docente de la Escuela de Posgrado de la Pontificia Universidad Católica del Perú, asesor de la tesis "El** rol del carbono orgánico y del arsénico en la formación de los depósitos de oro hospedados en sedimentados: caso de estudio de los depósitos epitermales de Shahuindo y **Algamarca, Perú"**, **del autor** Renzo Andrés Galdos Postigo,dejo constancia de lo siguiente:

- El mencionado documento tiene un índice de puntuación de similitud de 51%. Así lo consigna el reporte de similitud emitido por el software *Turnitin* el 09/04/2004. El alto nivel de similitud encontrado en la tesis se debe al hecho de que el manuscrito incluye en su estructura 2 artículos publicados en la revista *Economic Geology* (enero 2024, https://doi.org/10.5382/econgeo.5040) y en la revista *Ore Geology Review* (marzo 2024, https://doi.org/10.1016/j.oregeorev.2023.105857), correspondiendo a la modalidad de "tesis por compendio de publicaciones" actualmente de uso común en numerosas universidades del mundo, incluido en la PUCP.
- He revisado con detalle dicho reporte y la Tesis o Trabajo de Suficiencia Profesional, y no se advierte indicios de plagio.
- Las citas a otros autores y sus respectivas referencias cumplen con las pautas académicas.

Lugar y fecha: Toul, Francia, el 09 de abril de 2024

Apellidos y nombres del asesor: Vallance, Jean Francois Victor	
CE: 000687831	Firma
ORCID: 0000-0002-3242-8242	

Acknowledgements

ABSTRACT

The goal of this study is to determine the source of gold and the role played by organic carbon and arsenic in the formation of sediment-hosted gold deposits. The effect of and link between these two ubiquitous ingredients yet remains unresolved, even though most mineable gold in the Earth's crust is hosted by this type of deposits. In this work, we tackled these fundamental questions in a case study of the Shahuindo and Algamarca deposits in the Marañon Fold and Thrust Belt of the Peruvian Andes. These deposits are representative of sediment-hosted deposits in which gold mineralization is closely associated with both carbonaceous material and arsenian pyrite. We combined a range of complementary approaches including regional-scale basin analysis, mineralogical, geochemical, and fluid-inclusion studies, coupled with modeling of fluid-rock interactions.

Our results show that both Shahuindo and Algamarca deposits are located in an imbricated system of four thrust-related anticlines. The mineralization, which is predominantly present in the form of invisible gold in arsenian pyrite, is hosted by sandstone reservoirs of the Cretaceous Chimú, Carhuaz and Farrat formations of an overmature petroleum system. The intersection of thrust structures with transverse strike-slip faults controlled the location of the gold mineralization. Analyses of quartz-hosted fluid inclusions for homogenization temperature, salinity and element concentration patterns collectively point to a magmatic origin of the mineralizing fluid(s). In addition, our fluid-inclusion data reveal intensive interactions between the fluid and organic carbon within the sedimentary basin, leading to large concentrations of CO_2 CH_4 and H_2S in the fluid. These reactions result in an enhancement of Au solubility in the form of Au^I hydrosulfide complexes, due to the increase in H_2S and pH in the fluid. These key chemical changes in the fluid upon its reaction with organic matter promoted the transport of gold through the fold and thrust belt, followed by the gold-bearing fluid accumulation in structural traps such as anticlines, and subsequent gold intake by arsenian pyrite.

The ensemble of the results obtained in this work allowed us to propose a novel genetic model of formation for Shahuindo and Algamarca deposits. The model integrates the positive combined effect role of organic carbon and arsenic in the transport and concentration of gold, coupled with a favorable structural architecture of the fold and thrust belt. Furthermore, our data point to a concealed porphyry-style mineralization that may be present beneath the basin hosting the Shahuindo and Algamarca epithermal deposits. The results of this work contribute to the improvement of exploration strategies for sediment-hosted gold deposits in Northern Peru and worldwide.

Key words: Andes, Peru, sedimentary basin, Marañon Fold and Trust Belt, epithermal deposit, sediment-hosted gold deposit, arsenian pyrite, invisible gold, organic carbon, hydrothermal fluid, fluid inclusion, LA-ICPMS, Raman spectroscopy, microanalysis, thermodynamic modeling of fluid-rock interactions.

RÉSUMÉ

L'objectif de cette étude est de déterminer la source de l'or, le rôle du carbone organique et de l'arsenic dans la formation des gisements d'or hébergés dans des sédiments. L'effet et le lien entre ces deux ingrédients omniprésents dans de tels systèmes n'ont pas encore été élucidés, même si la majeure partie de l'or exploitable dans la croûte terrestre se trouve dans ce type de gisements. Dans ce travail, nous avons abordé ces questions fondamentales par une étude de cas en choisissant les gisements de Shahuindo et d'Algamarca situés dans la ceinture de plis et chevauchements du Marañon dans les Andes péruviennes. Algamarca et Shahuindo sont représentatifs des gisements hébergés dans des sédiments dans lesquels la minéralisation aurifère est étroitement associée à la fois au carbone organique et à la pyrite arséniée. Dans cette étude, nous avons combiné une série d'approches complémentaires, comme l'analyse structurale et de bassin à l'échelle régionale, des études minéralogiques, géochimiques et d'inclusions fluides, associées à la modélisation thermodynamique des interactions fluides-roches.

Nos résultats montrent que les gisements de Shahuindo et d'Algamarca sont situés dans un système imbriqué de quatre chevauchements et anticlinaux associés. La minéralisation, sous forme d'or « invisible » dans la pyrite arséniée, se trouve dans les réservoirs gréseux des formations crétacées Chimú, Carhuaz et Farrat appartenant à un système pétrolier surmature. Les intersections d'anticlinaux ou de failles de chevauchement avec des failles transverses de décrochement ont contrôlé l'emplacement de la minéralisation aurifère. Nos analyses des inclusions fluides piégées dans le quartz démontrent, par leurs températures d'homogénéisation, salinités et signatures d'éléments trace, une origine magmatique des fluides minéralisateurs. En outre, elles révèlent des interactions intenses entre le fluide et le carbone organique au sein du bassin sédimentaire, conduisant à de fortes teneurs en CO_2, CH_4 et H_2S dans le fluide. Ces réactions ont entraîné une augmentation de la solubilité de l'or sous forme de complexes hydrosulfurés, en raison de l'augmentation du pH et de la concentration en H_2S dans le fluide. Ces changements de composition du fluide ont favorisé le transport de l'or à travers le bassin sédimentaire plissé et faillé. Puis les fluides aurifères se sont accumulés dans des pièges structuraux comme les anticlinaux, et l'or a été finalement incorporé dans la pyrite arséniée.

L'ensemble des résultats obtenus dans ce travail nous permettent de proposer un nouveau modèle génétique de formation pour les gisements de Shahuindo et d'Algamarca. Ce modèle intègre l'effet combiné du carbone organique et de l'arsenic dans le transport et la concentration de l'or, couplé à un environnement structural très favorable, dans un bassin sédimentaire plissé et faillé. En outre, nos données indiquent qu'une minéralisation cachée de type porphyrique pourrait exister en profondeur, sous les sédiments encaissants les gisements épithermaux de Shahuindo et d'Algamarca. Les résultats de ce travail contribueront à l'amélioration des stratégies d'exploration des gisements d'or dans les sédiments du nord du Pérou et dans le reste du monde.

Mots clés : Andes, Pérou, bassin sédimentaire, Marañon Fold and Trust Belt, gisement épithermal, gisement d'or hébergés dans des sédiments, pyrite arséniée, or invisible, carbone organique, fluide hydrothermal, inclusion fluide, LA-ICPMS, spectroscopie Raman, microanalyse, modélisation thermodynamique des interactions fluide-roche.

RESUMEN

El objetivo de este trabajo es determinar el origen de los fluidos mineralizantes y el rol del carbón orgánico y el arsénico en la génesis de los depósitos de oro hospedados en sedimentos. El rol y el vínculo entre estos dos ingredientes omnipresentes aún sigue sin resolverse a pesar de que la mayor parte del oro explotable en la corteza terrestre se concentra en este tipo de depósitos. En el presente trabajo vamos a abordar estas dos interrogantes primordiales mediante el caso de estudio de los depósitos de Shahuindo y Algamarca en la faja corrida y plegada del Marañon de los Andes peruanos. Depósitos representativos de depósitos de oro hospedados en sedimentos, en los cuales la mineralización de oro se encuentra estrechamente asociada con la materia orgánica y la pirita arsenical. En este trabajo combinamos una serie de metodologias complementarias que incluyen el análisis estructural y de cuenca a escala regional, estudios mineralógicos, geoquímicos y de inclusiones fluidas, combinado con modelamiento termodinámico de las interacciones fluido-roca.

Los resultados muestran que los depósitos de Shahuindo y Algamarca se encuentran localizados en un sistema imbricado de cuatro sobreescurrimientos y anticlinales asociados. La mineralización, la cual se encuentra predominantemente en forma de oro invisible en pirita arsenical, esta hospedada en reservorios de areniscas cretácicas de las formaciones Chimú, Carhuaz y Farrat de un sistema petrolero sobremadurado. La intersección entre los anticlinales o fallas de sobreescurrimiento con las fallas de rumbo transversales controlaron la localización de la mineralización de oro. Los datos obtenidos de las inclusiones fluidas en cuarzo (temperatura de homogenización, salinidad y patrones de concentración de elementos) indican un origen magmático. Adicionalmente los datos de inclusiones fluidas revelan intensas interacciones entre el fluido y el carbón orgánico presente en la cuenca sedimentaria, produciendo altas concentraciones de CO_2 CH_4 y H_2S en el fluido. Estas reacciones resultan en un incremento en la solubilidad del oro en forma de complejos de hidrosulfuro, debido al incremento del H_2S y el pH en el fluido. Esto promueve el transporte del oro atreves de la cuenca sedimentaria plegada y fallada, posteriormente los fluidos auríferos son acumulados en trampas estructurales tales como anticlinales, y por último el oro es extraido del fluido por la pirita arsenical.

El conjunto de datos obtenidos en este trabajo permite proponer un novedoso modelo genético de formación para los depósitos de Shahuindo y Algamarca. Este modelo integra el efecto positivo combinado del carbón orgánico y el arsénico en el transporte y concentración del oro, junto a un ambiente estructural favorable, en la faja corrida y plegada. Además, nuestros datos indican la posible presencia de una mineralización oculta del tipo pórfido por debajo de los sedimentos que albergan a los depósitos epitermales de Shahuindo y Algamarca. Estos resultados contribuyen a mejorar las estrategias de exploración para depósitos de oro hospedados en sedimentos en la faja corrida y plegada del Marañon y en otros contextos similares alrededor del mundo.

Palabras clave: Andes, Perú, cuenca sedimentaria, faja corrida y plegada del Marañon, deposito epitermal, depósito de oro hospedado en sedimentos, pirita arsenical, oro invisible, carbón orgánico, fluido hidrotermal, inclusión fluida, LA-ICPMS, espectroscopia Raman, modelamiento termodinámico de las interacciones fluido-roca.

CONTENTS

Chapter I. INTRODUCTION

Gold has captivated humanity for millenia. Ancient civilizations around the world used gold to create jewelry and different decorative and religious objects. Due to its nice color and luster, prominent weight, very low chemical reactivity and the absence of oxidation, and ease of working, it was one of the first metals to be mined and used. Due to these unique properties, combined with its scarcity in nature, gold has historically been used to hold wealth and as currency. The oldest known coins date back to the 7th century BC in the Kingdom of Lydia (part of modern Turkey). Today, gold continues to play an important financial role. Due to its null or very low devaluation, it is a financial refuge in times of crisis and political and economic instability. Most of gold produced has been hoarded, with only a minor portion being used for industrial purposes, such as chemical catalysis, drugs and electronics.

Among all metals, gold is the king of ore deposit research, and its deposits have been mined for about 5000 years. However, many fundamental questions yet remain either unanswered at all or strongly debated about the sources, formation processes, association with other chemical elements, and distribution and location of gold deposits in the crust. One such fundamental debate, the role of organic matter and arsenic in the genesis of sediment-hosted gold deposits, is addressed in this thesis. Before dealing with these issues in detail, in this introduction I will briefly overview the main aspects of gold as a commodity, its properties, main geochemical features and major types of deposits. I then present the state of the art on sediment-hosted gold deposits and discuss the enigmatic gold associations with organic matter and arsenic. These topics will be addressed in depth in this thesis work using a case study of representative sediment-hosted epithermal gold deposits in northern Peru, the Shahuindo and Algamarca deposits.

I.1. Chemistry, economic significance mineralogy and abundance of gold

I.1.1. Geochemical and economic considerations

Gold, a chemical element of atomic number 79, belongs to the group of transition metals. Like other elements of this group, gold is a good conductor of heat and electricity, it is ductile, malleable and has a nice metallic (golden) luster. Gold has a density of 19.32 g/cm^3, making it one of the densest elements in the Periodic Table (along with some platinoids and actinides). But the unique feature of gold compared to most metals of the Periodic Table is its exceptional resistance to oxidation and any other type of chemical

alteration, making it a truly "noble" metal. Today, gold remains one of the most valuable precious metals. Gold reached a historically high price value in 2012, with US$1670 per troy ounce (one troy ounce contains 31.1 grams), followed by only a moderate decrease (Fig. 1). In 2020, gold reached a new price height of US$1770 per troy ounce. Since then, of its price gold has shown an upward trend. For example, in March 2024, the price of gold reached a value of US$2115 per troy ounce (= US$68 $ per gram).

Gold price per year
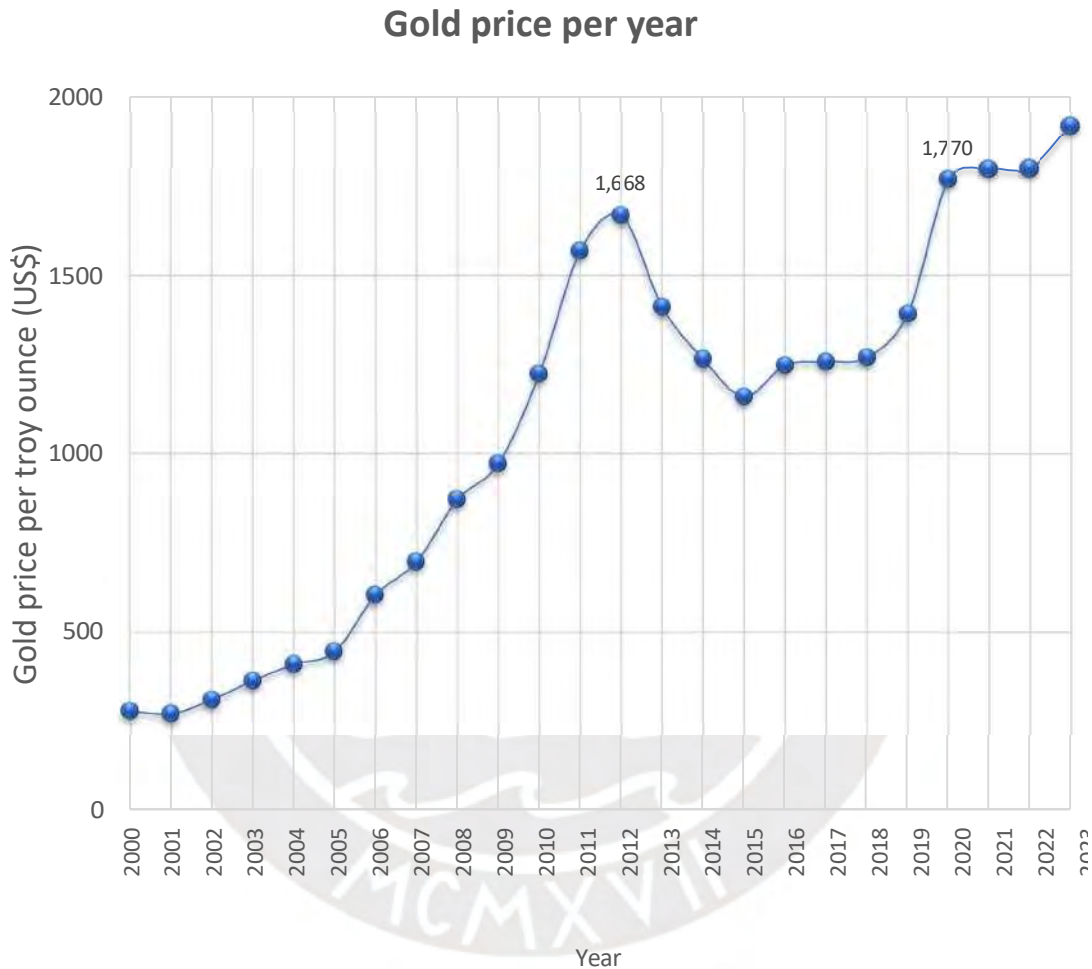
Fig. 1. The evolution of the annual gold price, in the 21th century (in US$/troy ounce). Data source: Banco Central de Reserva del Perú (2023).

The price of raw materials is sensitive to economic and geopolitical crisis. At the beginning of the COVID-19 pandemic, the prices of crude oil and base and most other precious and high-technology metals collapsed. Paradoxically, economic uncertainties caused by pandemics (e.g., COVID-2019) and geopolitical crisis (e.g., Russia-Ukraine

conflict) produce a "positive" effect on the gold price, in contrast to many other commodities (Akcil et al., 2020; Shahzad et al., 2023). Gold usage in 2022 was distributed as follows: jewelry 47%, hoarding 37%, coins and medals 9%, electronic and industrial applications 6%, and other 1%. China was the world's largest gold producer in 2022, with 330 tons of gold per year while Peru was the ninth largest gold producer, with 100 tons per year (excluding illegal mining production). Peru has reserves (i.e. economically exploitable) of 2900 tons of Au, making it the fifth country with the largest gold reserves in the world (USGS, 2023).

I.1.2 Gold mineralogy

Being a noble metal, native (i.e., metallic) gold is the most thermodynamically stable and widely occurring Au state across a wide range of natural conditions. Nevertheless, in nature, gold can also occasionally form different chemical compounds with several elements such as: intermetallic compounds, tellurides, sulfides, sulfosalts, antimonides, selenides, bismuthides, and multi-element chalcogenides (e.g., Palyanova, 2020; Table 1). For instance, gold can form a complete solid solution with silver; the variety of native gold containing >20 wt% silver is known as electrum (Jones and Fleischer, 1969). Other gold alloys are also well known in industry and widely used in laboratory such those with nickel, platinum or palladium, but they have not yet been unambiguously recognized in nature. Gold counts 36 so far registered minerals occurring in nature (Palyanova, 2020; Table 1). Another, yet not fully understood, state of gold in nature is its ubiquitous association with hydrothermal sulfarsenide minerals, such as arsenian pyrite, arsenopyrite, and löllingite (e.g., Reich et al., 2005; Deditius et al., 2014; Pokrovski et al., 2021). These minerals are capable of hosting 100s to 1,000s ppm of Au in a chemically bound state within their crystal lattice. None of other major element sulfide minerals is known to have such a capacity. Although this bound gold falls into the so-called "invisible" gold (i.e., not detectable by conventional microscopic methods), it should not be confused with the nanoparticles of native gold and its own other minerals listed in Table 1. As such, this chemically bound gold likely represents the second major state of the metal in ore deposits after the native one. More discussion about invisible gold and its association with arsenic will be presented below in this thesis manuscript.

Table 1. Known gold minerals (modified from Palyanova, 2020).

Mineral name	Formula
Native metals	
Native gold	$Au_{1.00-0.35}Ag_{0.00-0.65}$
Native silver	$Ag_{0.65-1.00}Au_{0.35-0.00}$
Intermetallic compounds	
Weishanite	(Au, Ag, Hg)
Aurihydrargyrumite	Au_6Hg_5
Tetra-auricupride	AuCu
Cuproauride	Cu_3Au
Auricupride	Cu_3Au
Anyuiite	$AuPb_2$
Hunchunite	Au_2Pb
Novodneprite	$AuPb_3$
Yuanjiangite	AuSn
Rumoiite	$AuSn_2$
Sulfides	
Uytenbogaardtite	Ag_3AuS_2
Petrovskaite	AuAgS
Sulfosalts	
Jonassonite	$AuBi_5S_4$
Montbrayite	$(Au,Ag,Sb,Bi,Pb)_{23}(Te,Sb,Bi,Pb)_{38}$
Selenide	
Fischesserite	Ag_3AuSe_2
Tellurides	
Calaverite	$AuTe_2$
Petzite	Ag_3AuTe_2
Mutmannite	$AuAgTe_2$
Sylvanite	$(Au, Ag)_2Te_4$
Krennerite	Au_3AgTe_8
Kostovite	$CuAuTe_4$
Bezsmertnovite	$(Au, Ag)_4Cu (Te, Pb)$
Bilibinskite	$PbCu_2Au_3Te_2$
Bogdanovite	$(Au, Te, Pb)_3(Cu, Fe)$
Honeaite	Au_3TlTe_2
Antimonide	
Aurostibite	$AuSb_2$
Bismuthide	
Maldonite	Au_2Bi
Complex chalcogenides	
Pampaloite	AuSbTe
Maletoyvayamite	$Au_3Se_4Te_6$
Criddleite	$TlAg_2Au_3Sb_{10}S_{10}$
Buckhornite	$AuPb_2BiTe_2S_3$
Museumite	$[Pb_2(Pb, Sb)_2S_8][(Te, Au)_2]$
Nagyágite	$[Pb_3(Pb, Sb)_3S_6](Au, Te)_3$
Penzhinite	$(Ag, Cu)_4Au (S, Se)_4$

I.1.3 Abundance of gold in nature

A number of compilations and more specific studies have been conducted to determine average gold concentrations in crustal and mantle rocks (e.g., Crocket, 1991; Pitcairn, 2013; Rudnick and Gao, 2014; Saunders et al., 2018, to name a few). These concentrations refer to rocks that have not been affected by mineralizing processes. Analyses were performed on individual minerals or whole rocks. These data clearly demonstrate that gold is a scarce metal both in the upper crust and lithospheric mantle. The Au average Clarke value in the continental crust is between 1 and 2 ppb, according to different estimates (Rudnick and Gao, 2014). The mantle, as represented so far by rocks from peridotite massifs and mantle xenoliths, shows a mean value of 1.2 ppb Au, with a relatively homogeneous distribution among different geographical localities and geological ages (Saunders et al., 2018). Based on the chondritic meteorite compositions that are representative of the Solar system's element abundance, the bulk Earth gold abundance was estimated to be 160 ppb (McDonough, 2003). Thus, combined with the sizes of the major Earth's envelopes, more than 98% of the Earth's gold is concentrated in the core, amounting at least several hundreds of ppb. Thus, if Earth had no metallic core, gold economic value and ore deposit research would have been very different.

The different types of crustal rocks (igneous, metamorphic, and sedimentary) display variable gold concentrations. For example, igneous mafic rocks exhibit generally higher values than felsic rocks (Fig. 2). The gold concentrations in igneous rocks are also influenced by the presence of sulfur. Thus, sulfide-saturated silicate rocks are depleted in gold because it is strongly scavenged by accessory sulfide and sulfarsenide minerals (e.g., Pitcairn, 2013). Other accessory (e.g., oxide) minerals in igneous rocks, such as magnetite, can also contain up to 10 times more gold than the major silicate minerals, such as quartz, mica or feldspar (Crocket, 1991). Metamorphic rocks have generally lower gold values than sedimentary rocks (Pitcairn, 2013). Metamorphic rocks with a higher degree of metamorphism generally have the lowest gold concentration values within the metamorphic rocks because these rocks must have lost gold to the fluid phase during metamorphic events (Crocket, 1991; Pitcairn, 2013; Hofmann et al., 2017).
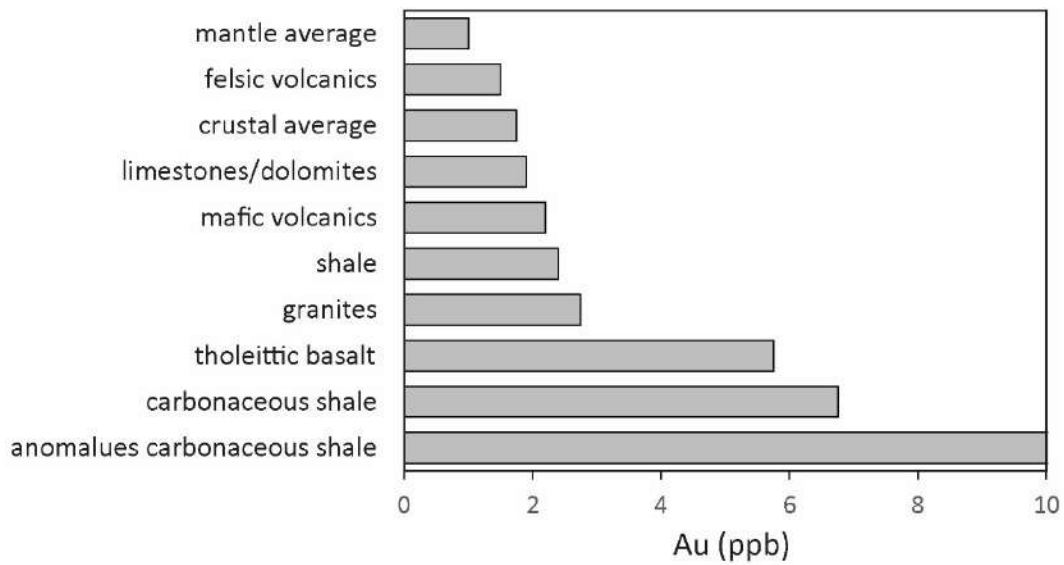
Fig. 2. Gold concentrations in different types of rocks (adapted from Large et al., 2011).

Carbonaceous sedimentary rocks such as black shales may exhibit sometimes quite anomalous gold values, up to 6 ppb (Fig. 2). Indeed, during certain periods of Earth's history, carbonaceous shales enriched in organic carbon and metals were deposited; they are termed "highly metalliferous black shales" by Johnson et al. (2017). Periods of the Earth's evolution with optimal conditions for the development of life allowed the accumulation of abundant phytoplankton in the sediments that served as the source of organic matter to shales. Due to efficient scavenging of trace redox-sensitive elements from the seawater black shales are enriched in those elements (Johnson et al., 2017; references therein). The high gold content relative to other rocks in the crust and mantle (Fig. 2) allowed these rocks to be considered as the source of gold for sediment-hosted gold deposits, as suggested by some models (e.g., Large et al., 2011).

I.2. Gold ore deposits

Gold ore deposits correspond to anomalous concentrations of this element in the Earth's crust. In such localities, gold is enriched by several orders of magnitude compared to the average concentration in common crustal and mantle rocks (~ 1 ppb, see above), making it economically extractable. On a global geochemical scale, however, such settings hold a tiny fraction of the total gold in the crust (about 1:10[7]; Frimmel, 2008). Gold is present as the main metal of economic interest or as an important by-product in at least 11 different types of defined ore deposits that include paleoplacer, orogenic, porphyry, epithermal, Carlin, placer, reduced intrusion-related, volcanogenic massive sulfide, skarn, carbonate replacement, and iron oxide-copper-gold deposits (Sillitoe, 2020). They can contain up to 6,200 tons of gold in a single gold deposit (e.g., Muruntau; Yakubchuk, 2023) and up to 96,000 tons of gold in a gold province (such as Witwatersrand; Sillitoe, 2020). In the following sections we will present a brief description of the genetic models of gold deposits that can be hosted by sedimentary rocks, called sediment-hosted gold deposits, which is the main topic of this thesis. These are orogenic, Carlin, and epithermal sediment-hosted gold deposits that formed in different geological settings and at different depths (Fig. 3). These deposits are spatially associated with carbonaceous material, and a significant portion of the gold occurs as invisible gold in arsenian pyrite.
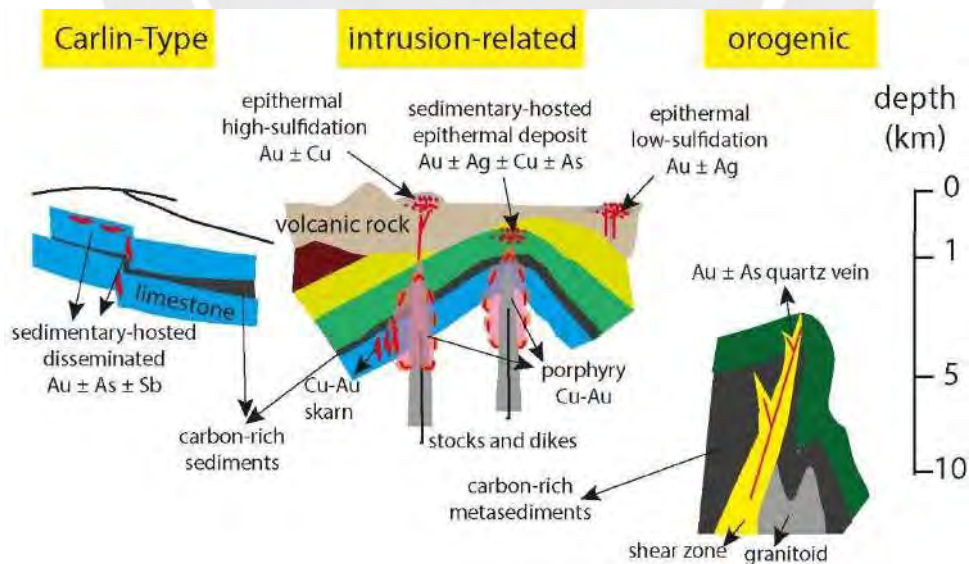
Fig. 3. Schematic representation of the geologic settings and depths of formation for major types of gold deposits (adapted from Simmons et al., 2020).

I.2.1. Carlin type gold deposits

Carlin type gold deposits were formed at depths ranging from 0.3 km to 7 km, with most deposits formed at depths 1-3 km (Cline et al., 2005). This type of gold deposits occurs in the western USA (mainly Nevada) and southern China. These deposits are hosted by carbonaceous siltstones and carbonate rocks. The gold mineralization is disseminated within the rock, with the main Au-bearing ore mineral being arsenian pyrite. In addition, lesser part of gold is present in arsenopyrite and marcasite. Native, visible, gold is rather scarce and is mainly confined to a supergene altered portion of the deposit. Associated major gangue minerals are quartz, followed by dickite, kaolinite, illite, smectite, calcite, dolomite, ankerite, siderite, barite, and adularia (Saunders et al., 2014; Li et al., 2020). Common sulfides, other than sulfarsenides, include stibnite, cinnabar, lorandite, galkhaite and sphalerite (Saunders et al., 2014). Fluid inclusions from Carlin type gold deposits show homogenization temperatures from 100 to 300 °C and salinities of <7 wt% NaCl eq. (Bodnar et al., 2014). The fluid inclusions contain relatively low but ubiquitous amounts of CO_2 (usually 1-4 mol %; Bodnar et al., 2014; Saunders et al., 2014).

The mecanisms of gold deposition in Carlin type deposits have been extensively studied, but the source of the gold is still a matter of debate. Two different sources have been proposed. The first model, so called sedimentary, suggests that the gold, initially found in the sedimentary basin, is re-mobilized and re-concentrated by meteoric or metamorphic fluids (e.g., Emsbo et al., 2003; Large et al., 2011). The second proposal, so called magmatic, advances that the gold is introduced into the basin by fluids of magmatic origin (e.g., Sillitoe and Bonham, 1990; Kesler et al., 2005; Barker et al., 2009; Large et al., 2016; Holley et al., 2022). The sedimentary model obviously requires sediments that are pre-enriched with gold. Black shales have been proposed as a possible source (Large et al., 2011), since these rocks generally contain a high gold content relative to other rocks present in the crust (Fig. 2). Gold pre-enrichment in sedimentary rocks may occur during deposition by mechanisms similar to those that produce SEDEX-type deposits (Emsbo et al., 2003). This elevated gold content in sediments is further re-concentrated by fluids of meteoric origin. Their evidence stems mostly from $\delta^{18}O$ and δD values measured in ore-stage clays and quartz, which are consistent with a meteoric origin (Emsbo et al., 2003). Given that much of the gold and arsenic in the sediments is hosted in the sedimentary pyrite, metamorphism is critical for the release and mobilization of gold from the pyrite. Indeed, during high metamorphism, pyrite is converted to pyrrhotite, a process in which gold, arsenic and sulfur are released from the pyrite into the metamorphic fluid; this reaction is favored by the presence of

organic carbon, which is abundant in sediments related to sediment-hosted gold deposits (Tomkins, 2010; Large et al., 2011). On the other hand, the presence of magmatic activity contemporaneous with Carlin type deposits suggests a possible magmatic source (e.g., Sillitoe and Bonham, 1990). Interestingly, the suite of elements in which Carlin deposits are enriched is similar to that of high-sulfidation epithermal deposits, which have been widely regarded to be of a magmatic origin (e.g., Kesler et al., 2005; Barker et al., 2009). This similarity has been used as evidence for a magmatic origin of the gold and associated elements. Furthermore, in Carlin type deposits, the composition of the fluid inclusions and their metal ratios were recently shown to be consistent with fluids of magmatic origin (Large et al., 2016).

Additional constraints about the fluid sources stem from traditional stable isotopes of H, C, O and S. These studies have been key to the developement of genetic models for different types of mineral deposits including porphyry, epithermal, orogenic, and Carlin type. Stable isotope geochemistry tools greatly help define the origin of the fluids and track different geochemical and geological processes (Huston et al., 2023). One of the limitations in the use of these tools for tracing hydrothermal fluid sources is an inevitable overlap of isotope signatures, for example in the δD and $\delta^{18}O$ values of many magmatic and metamorphic fluids (Fig. 4). The isotope composition of ore fluids (δD, $\delta^{18}O$, $\delta^{13}C$ and $\delta^{34}S$) can be deduced from the isotope composition of minerals that precipitated from or coexisted with the ore fluid. The estimation of the isotope composition of water requires knowledge of the temperature of mineral deposition, extracted from mineral geothermometers or thermometry of fluid inclusions, and the isotope fractionation factors between the mineral and water, which are relatively well known to date or may be predicted for most traditional isotopes mentioned above (e.g., Clayton, 1961; O'Neil and Taylor, 1967; Matsuhisa et al.,1979; Vho et al., 2019). Furthermore, the hydrogen and oxygen isotope composition of ore fluids can be determined by direct measurement of water extracted from fluid inclusions contained in gangue and ore minerals (e.g., Deen et al., 1994; Cline and Hofstra, 2000). In most Carlin type gold deposits, the δD values are relatively low (<-110 ‰; gray area in Fig. 4) compared to magmatic waters, which would be consistent with mid-Tertiary meteoric water as the plausible source. The higher values of $\delta^{18}O$ compared to meteoric water (as shown by blue rectangles for the Meikle and Betze-Post deposits in Fig. 4) are interpreted as result of water-rock exchange during the circulation of meteoric water in sedimentary sequences (e.g., Hofstra and Cline, 2000; Emsbo et al., 2003). In contrast, the isotopic composition of fluid from the Getchell deposit has higher δD values than Meikle and Betze-Post deposits (yellow and red rectangular symbols, most of which
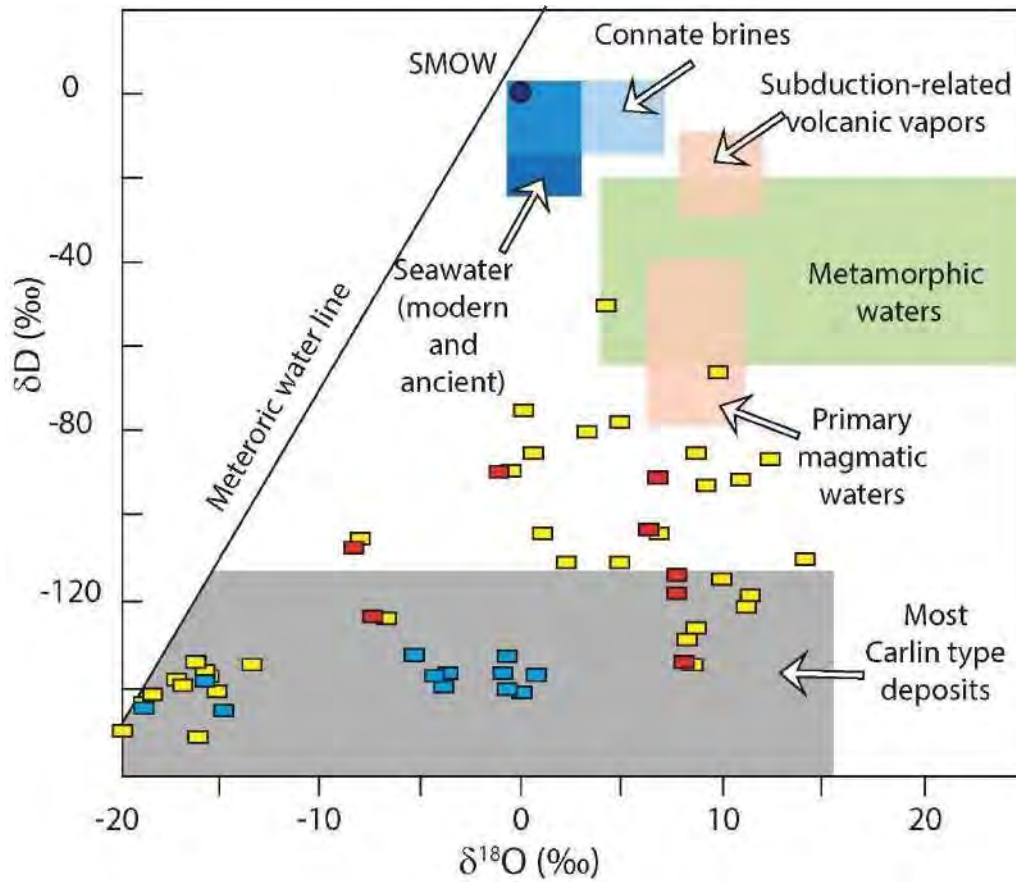
Fig. 4. Hydrogen and oxygen isotope composition of ore-forming fluids for Carlin type gold deposits, Meikle and Betze-Post deposits (calculated based on data from ore-stage clay minerals such as kaolinite, smectite, and illite, or measured in fluid inclusions in late ore-stage orpiment; blue rectangles; Emsbo et al.,2003), Getchell and Twin Creeks deposits ($\delta^{18}O$ values calculated based on data from calcite, and δD measured in fluid inclusion in calcite; red rectangles; Groff, 2018), and compilation of data from Carlin-type gold deposits (calculated based on data from kaolinite and quartz, and measured in fluid inclusion; yellow rectangles; Hofstra and Cline, 2000). Fields for magmatic and metamorphic fluids, seawater and connate brines are from Huston et al. (2023). Data for most Carlin type deposits (gray field; Hofstra and Cline, 2000). The arrows are pointing to the corresponding indicated isotope reservoir. SMOW = standard mean oceanic water.

plotting above the grey area Fig. 4). Such isotope compositions of water inferred in the Getchell deposit are consistent with a mixing between meteoric and magmatic fluids. The O and H isotope composition of pre-ore and ore-fluids at Getchell displays a magmatic component, while post-ore fluids are more consistent with a meteoric origin (Cline and Hofstra, 2000; Groff, 2018). Pyrite from Carlyn type deposits shows a marked difference in the $\delta^{34}S$ values between the gold-rich and poor-gold pyrite bands, differences that have been evidenced by the high-spatial resolution SIMS analyses (Kesler et al., 2005; Barker et al., 2009; Holley et al., 2022). Sulfur isotope data from ore pyrite from the Deep Star, Beast, Turquoise Ridge, and Getchell deposits point to a magmatic origin at least

for the sulfur associated with gold deposition, with $\delta^{34}S$ values of gold-rich pyrite being similar to those of the regional magmatic fluids in the Battle Mountain district, whereas gold-poor pyrites having seemingly more meteoric/sedimentary-like signatures or larger $\delta^{34}S$ data scatter (e.g., Holley et al., 2022). Arsenic sulfides (realgar), corresponding to a post-ore stage at Getchell, have higher $\delta^{34}S$ values than previous stages and overlap with $\delta^{34}S$ values of diagenetic pyrite (Groff, 2018). In summary, sulfur isotope data indicate that both meteoric and magmatic fluids were part of a hydrothermal system, but the latter brought the gold to the deposit (Holley et al., 2022).

I.2.2. Orogenic deposits

Orogenic gold deposits were usually formed at depths between 3 and 20 km (Saunders et al., 2014; references therein). Depending on emplacement depth, orogenic deposits are classified as epizonal (<6 km), mesozonal (6-12 km), and hypozonal (>12 km). They occur in metamorphic belts, hosted by greenstones (Precambrian orogenic gold) and metaturbidites (Phanerozoic orogenic gold). The metamorphic rocks show generally greenschist facies and, locally, amphibolite facies. The mineralization consists mainly of quartz veins (so called lodes), with minor amounts of mineralization occurring as disseminations and veinlets. Gold occurs as electrum, tellurides, antimonides, bismuthides, and some, poorly quantified, part of gold is in invisible form in arsenopyrite and pyrite (Saunders et al., 2014). Associated gangue minerals are quartz, sericite, Fe-Mg bearing carbonates, calcite, biotite, amphibole, anorthite, K-feldspar, tourmaline (Saunders et al., 2014; Li et al., 2022). Common sulfides are pyrrhotite, arsenopyrite, and pyrite, followed by less abundant löllingite, realgar, orpiment, and cinnabar. Other sulfides in trace amounts such as chalcopyrite, galena, sphalerite, and tetrahedrite also occur (Saunders et al., 2014). Fluid inclusions from orogenic gold deposits have homogenization temperatures of 150 to 400 °C and relatively low salinities, of <10 wt% NaCl eq. The carbonic fluid inclusions may contain 4-25 mol% amounts of CO_2, however higher concentrations occur in some deposits. The presence of methane is also common in many deposits (Groves et al., 1988; Bodnar et al., 2014; Hu et al., 2017), its occurrence is attributed to the presence of carbonaceous matter in surrounding rocks (e.g., Vallance et al., 2003).

The nature of the fluid and the source of the gold in orogenic deposits are still questioned, similarly to Carlin type deposits. A number of proposals has been put forward in the literature to try to answer these questions. Magmatic, meteoric and metamorphic origins have been suggested (Bodnar et al., 2014; Saunders et al., 2014). However, the

resolution of this question of origin is complex because the orogenic deposits are old, being mostly of Archean age, with the youngest significant orogenic gold deposits of at least 50 million years old (Goldfarb et al., 2001). In addition, orogenic gold deposits are regarded as long-lived systems, because they are controlled by intrinsically slow metamorphic processes. In addition, due to the advanced age and large periods of evolution, orogenic deposits are often affected by tectonic or hydrothermal events after they have been formed. Such events further complicate the resolution of the deposit genesis. The weakness of the igneous origin proposal is that in many cases it is not possible to associate the igneous activity in space and time with the formation of the orogenic deposits. For the metamorphic-derived fluid model, the problem is that some orogenic deposits were formed several million years after the regional metamorphic events. A more recent model proposes that the fluid and gold are derived from devolatilization of the subducted oceanic plate and sediments or from the hydrated mantle wedge; these fluids ascend through deep cortical faults to the site of gold deposition (Goldfarb and Groves, 2015; Groves et al., 2020). However, many unknowns yet remain, such as the abundance of gold (which is rather low in mantle wedge, see above) and the nature and transporting capacity of such fluids.

The O and H isotope composition of water calculated based on O and H isotope data from quartz, albite, ankerite, biotite, calcite, chlorite, dolomite, muscovite, scheelite, sericite, and tourmaline, from orogenic deposits plots mostly in the field of metamorphic and magmatic fluids (Fig.5). The evidence for a meteoric component is usually unseen or detectable only in late stages not associated with the gold deposition or those corresponding to later remobilization events. The hydrothermal fluids from orogenic deposits are interpreted as mixing between a deep-seated hot fluid with low δD and high $\delta^{18}O$ values compared to the standard mean oceanic water, of metamorphic origin, and a cold shallow fluid of surficial origin present in the porosity of the rocks with high δD and low $\delta^{18}O$ values compared to the deep-seated hot fluids (Fig. 5; Quesnel et al., 2023). The sulfides (pyrite, arsenopyrite, and galena) from the orogenic deposit have a large range of $\delta^{34}S$ values between −30‰ and 10‰. This variation in the $\delta^{34}S$ values is interpreted as the result of mixing between multiple reservoirs, or changes in the key parameters of the hydrothermal fluid, like changes in the oxygen fugacity due to redox reactions with the host rock. Generally, the isotope composition (H, O, S) of fluids in orogenic deposits is consistent through the time, (from Archean to Cenozoic, indicating that the source of fluids and metals remained constant through the time, with only a

secular variation in $\delta^{34}S$ for orogenic deposits hosted in sediments reflecting the evolution of the sulfur cycle at the Earth surface (Quesnel et al., 2023).
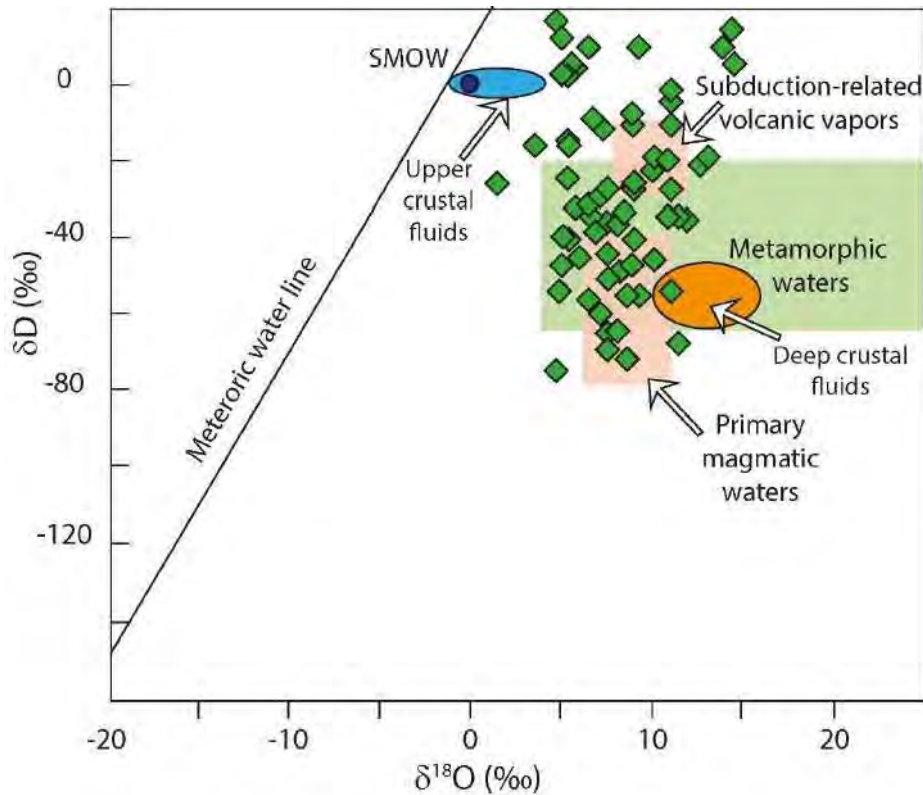
Fig. 5. Hydrogen and oxygen isotope composition of ore-forming fluids of orogenic deposits calculated from quartz and OH-bearing minerals (from Quesnel et al, 2023). Fields for magmatic and metamorphic fluids, seawater, and connate brines are from Huston et al. (2023). The arrows are pointing to the corresponding indicated isotope reservoir. SMOW = standard mean oceanic water.

I.2.3. Epithermal gold deposits

Epithermal gold deposits are deposits formed near the paleo-surface (typically <1.5 km). This type of deposits mainly occurs in the Pacific Rim and other convergent tectonic settings of subduction. All of them have been regarded as related to magmatic activity (e.g, Camprubí et al., 2003; Sillitoe, 2010; Simmons et al., 2020). Based on the sulfide mineral assemblage, epithermal gold deposits can be classified into high sulfidation, intermediate sulfidation and low sulfidation (Hedenquist et al., 2000). Fig. 6 shows the basics of this classification in terms of sulfur fugacity, based on the main mineral sulfide assemblages, and shows the sulfidation state of different deposit types, including porphyry, orogenic and epithermal types.

The distribution of the different types of epithermal deposits in some belts seems to be controlled by the volcano tectonic settings, and, consequently, by the nature of the

magma in each scenario.Sillitoe and Hedenquist (2003) proposed in this sense that high sulfidation and intermediate sulfidation epithermal deposits are generally associated in magmatic arc terranes (i.e. plate convergence settings), while epithermal low sulfidation deposits are more frequently found in divergent settings (i.e. such as rifts). However, this issue is more complex. For example, low and intermediate sulfidation epithermal deposits do coexist in arc terranes in the Sierra Madre Occidental and Sierra Madre southern Mexico (Camprubí and Albinson, 2007). Therefore, controls other than or additional to the tectonic setting control should also operate in the distribution of the different types of epithermal deposits, such as the depth of emplacement of the parental stock and the nature of the host rock (Camprubí and Albinson, 2007; Rottier et al., 2016).
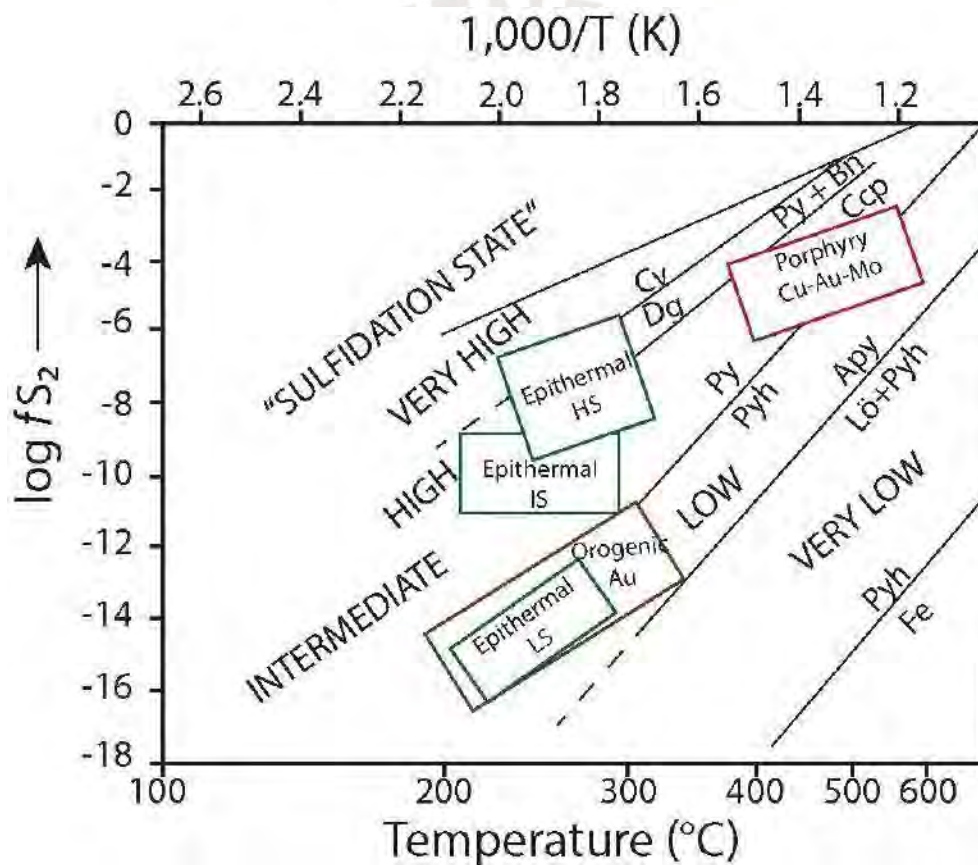
Fig. 6. Log fS_2 versus temperature diagram, illustrating various sulfidation states of the hydrothermal fluids, based on stable sulfide mineral assemblages (from Einaudi et al., 2003). Log fS_2 versus temperature estimated for various hydrothermal ore deposits are also plotted (from Fontboté et al., 2017). Colors are visualization aids only. Mineral abbreviations follow Warr (2021).

Epithermal gold deposits are generally hosted by igneous rocks, but can also be hosted by sedimentary and metamorphic rocks (e.g., Bissig et al., 2015). The major and most typical Au-bearing minerals in epithermal deposits are known to be native gold,

electrum, and sometimes Au tellurides (White and Hedenquist, 1995; Simmons et al., 2005), but arsenian pyrite has also been recognized as an important gold carrier in some cases (e.g., Reich et al., 2005; Deditius et al., 2014; Morishita et al., 2018; Sykora et al., 2018; references therein). Associated ore and gangue minerals are mostly function of the hydrothermal fluid nature and composition. Thus, in low sulfidation epithermal deposits, the diagnostic minerals are pyrrhotite, arsenopyrite, pyrite, and iron-rich sphalerite (as ore minerals), and quartz-calcite-adularia-illite (as gangue mineral assemblage). In high sulfidation epithermal deposits, the diagnostic minerals are enargite, luzonite, covellite, pyrite and chalcopyrite (as ore minerals), and quartz-alunite-pyrophyllite-dickite-kaolinite (as gangue mineral assemblage; White and Hedenquist, 1995; Simmons et al., 2005; Hedenquist and Arribas, 2022). In epithermal deposits, fluid inclusions have homogenization temperatures ranging from 100 to 450 °C, with most values being between 120 and 310 °C. Salinities are typically <10-20 wt% NaCl eq. (Bodnar et al., 2014).

High and intermediate sulfidation epithermal deposits are spatially associated with porphyry-type deposits (Hedenquist et al., 1998; Sillitoe et al., 2010). In the porphyry system model, both types of mineralization are genetically and spatially integrated and often overlapped (Sillitoe, 2010). However, in contrast to deeper porphyry deposits that usually do not show meteoric fluid contribution (Kouzmanov and Pokrovski, 2012; references therein), alteration minerals and fluid inclusions in epithermal deposits have isotopic compositions ($\delta^{18}O$ and δD) that reveal a significant component of meteoric water (e.g., Deen et al., 1994; Albinson et al., 2001; Camprubí et al., 2006). This is because the epithermal deposits are formed near the surface, and meteoric water infiltrates and mixes with the magmatic fluid. The convection cell, created by the heat of the magmatic intrusion, causes meteoric water to circulate and can mix or superimpose its signature on that of the magmatic fluid. The superposition mostly occurs at the end of magmatic activity, when meteoric fluids are dominant in the hydrothermal system. Despite a large contribution of meteoric water in hydrothermal systems forming low, intermediate and high sulfidation epithermal deposits, the predominant source of metals and ligands is likely to be magmatic (e.g., Camprubí et al., 2006). For example, in the modern hydrothermal system of White Island associated with a volcano in New Zealand, it has been calculated that degassing of magma in the hydrothermal system releases 100 tons of Cu and 350 kg of gold in one year (Hedenquist and Lowenstern, 1994). This is a sufficient amount of metals to form a mineral deposit, considering that the lifespan of such deposits is typically thousands up to more than one millions years (Chiaradia, 2023). LA-ICPMS analyses of fluid inclusions from the Fresnillo district (Mexico) show

that sufficiently high metal contents in mineralizing fluids (e.g., up to 30 ppm Ag) can form an epithermal silver deposit in a short period of time, of 50 to 500 years, with a modest upflow rate of 100 kg sec^{-1} and a total volume of 1.8 km^3 of magmatic brine underneath such a deposit (e.g., Wilkinson et al., 2013).

The O and H isotope compositions of water in ancient hydrothermal systems associated with the formation of low sulfidation epithermal deposits were commonly studied in gangue minerals (e.g., quartz, chalcedony, carbonate minerals) and fluid inclusions they host. However, gangue and ore minerals, which may apparently look cogenetic as inferred from petrographic observations, do not always precipitate from the same fluid (e.g., Kouzmanov et al., 2010). The O and H isotope composition of water determined from gangue mineral shows a predominantly meteoric signature with a variation in the $\delta^{18}O$ values due to interactions with rocks, as, for example, for fluids from the Axi and Mule Canyon deposits (Fig. 7). In some epithermal low sulfidation deposits like Comstock Lode, it has been noted that barren events have a meteoric isotope signature (open star in Fig. 7), whereas mineralizing events show distinctly higher δD and $\delta^{18}O$ values, thereby suggesting a magmatic component (close star in Fig. 7; Hedenquist and Lowenstern, 1994). A similar observation in low sulfidation deposits in Mexico was presented by Albinson et al. (2001). Ratios of N_2/Ar measured in fluid inclusions from ore minerals indicate a magmatic origin. In contrast, the N_2/Ar ratios from fluid inclusions in gangue minerals are more consistent with meteoric fluids. While the meteoric water component is important in a hydrothermal system associated with an epithermal mineralization, the bulk of the metals is likely provided by magmatic fluids (Deen et al., 1994; Albinson et al., 2001; Camprubí et al., 2006; Wilkinson et al., 2013; Rottier et al; 2018). In contrast to low sulfidation deposits, the fluids from high sulfidation deposits exhibit a clearly magmatic isotope signature as shown in Fig. 7 by the isotope composition of fluids from Cerro Quema and Lagunas Norte. In the high sulfidation epithermal deposit of Julcani, Peru, the isotopic composition of fluid inclusions in minerals associated with the mineralizing event indicates a magmatic origin, while inclusions in the barren late stage have an isotopic composition indicative of meteoric fluids (Fig. 7; Deen et al., 1994).

The cooling of a magmatic-hydrothermal fluid result in the disproportionation reaction of SO_2 to sulfide and sulfate:

$$4SO_2 + 4H_2O = H_2S + 3H_2SO_4 \qquad (1)$$
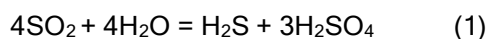
These reaction produces a distinctive isotope fractionation, $\Box^{34}S_{sulfate-sulfide}$ ~5-20‰ (Huston et al., 2023). On the base of this fractionation, the formation temperatures

for high sulfidation deposits could be estimated from sulfide-sulfate mineral pairs. These pairs yield temperature values ranging between 200 and 400 °C, which are consistent with temperatures estimated by fluid inclusion microthermometry (e.g., Arribas, 1995). The δ^{34}S values for total sulfur in the hydrothermal fluid (δ^{34}S $_{\Sigma S}$) for high sulfidation epithermal deposits are generally similar to the S isotope composition of the igneous rocks genetically associated with the mineralization (e.g., Corral et al.,2017).
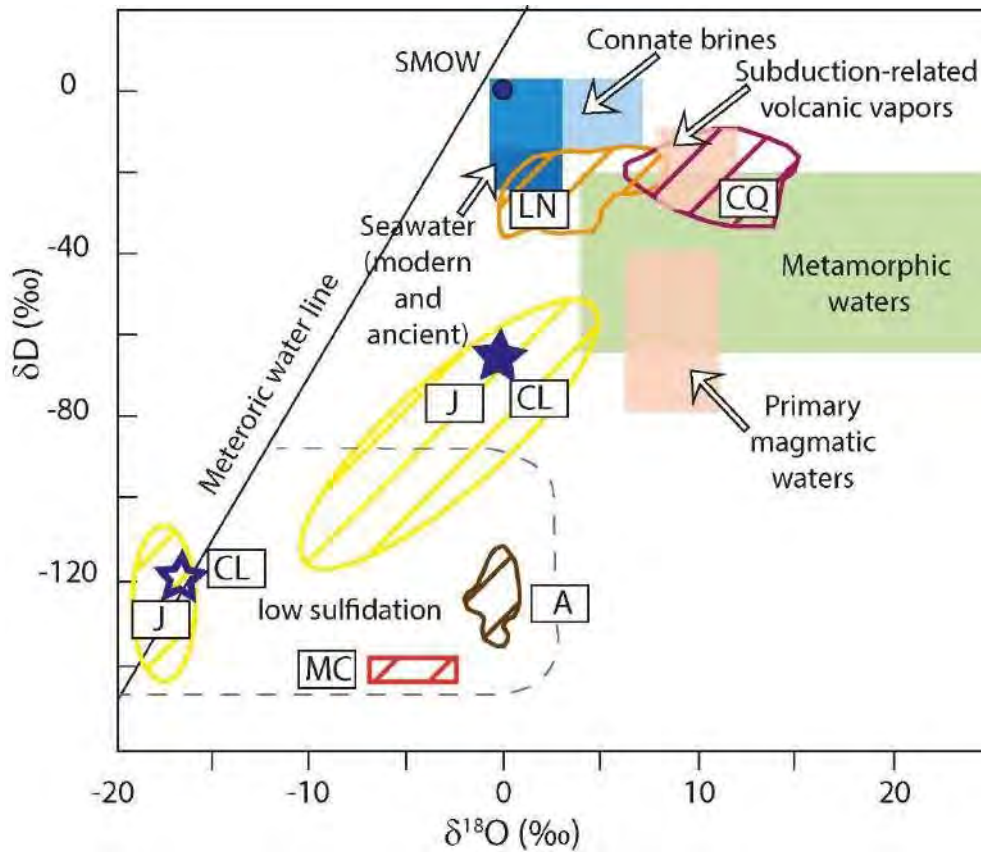
Fig. 7. Hydrogen and oxygen isotope composition of ore-forming fluids for the different epithermal gold deposits, Julcani (measured in fluid inclusion; Deen et al., 1994), Lagunas Norte (calculated based on data from alunite; Cerpa et al., 2019), Cerro Quema (calculated based on data from kaolinite and dickite; Corral et al., 2017), Mule Canyon (δ^{18}O values calculated based on data from quartz, chalcedony and opal, and δD measured in fluid inclusion in silica phases; John et al., 2003), Axi (δ^{18}O values calculated based on data from quartz and chalcedony, and δD measured in fluid inclusion in quartz; Zhai et al., 2009), and Comstock Lode (δ^{18}O values calculated based on data from quartz, and δD measured in fluid inclusion in quartz; Hedenquist and Lowenstern, 1994). Fields for magmatic and metamorphic fluids, seawater, and connate brines are from Huston et al. (2023). Field for water that precipitate barren quartz in low sulfidation deposits (area delimited by dotted lines; Hedenquist and Lowenstern, 1994). The arrows are pointing to the corresponding indicated isotope reservoir. Abbreviations: SMOW (Standard mean oceanic water), J (Julcani deposit, Peru), LN (Lagunas Norte deposit, Peru), CQ (Cerro Quema deposit, Panama), MC (Mule Canyon deposit, United States), A (Axi deposit, China), CL (Comstock Lode, United States).

I.2.4. Transport and deposition of Au by hydrothermal fluids

Fluid inclusions provide the only straightforward way to assess the fluid composition in paleo hydrothermal settings hosting most gold deposits. In particular, the last 20 years developments of LA-ICPMS techniques for analyzing individual fluid inclusions (e.g., Günther et al.,1998; Schirra et al., 2022) opened a new door to our understanding of gold hydrothermal transport. These data show quite elevated gold concentrations up to 30 ppm in porphyry systems and related skarn and epithermal deposit (e.g., Kouzmanov and Pokrovski, 2012), which is thousands of times more than Au concentrations measured in modern geothermal deep-sea and in-land sources (e.g, Hannington et al., 2016; Simmons et al., 2016). In orogenic gold deposits, analyzed Au concentrations are often in the range between 100s ppb and a few ppm (e.g., Garofalo et al., 2014; Rauchenstein-Martinek et al., 2016). Interpretation of Au concentrations in high T-P ore-forming fluids, almost inaccessible to direct observation, requires knowledge of Au aqueous complexes and physical-chemical factors leading to gold mobilization and precipitation.

Indeed, despite the noble nature of gold, this strongly chalcophile element may be highly soluble in sulfur-rich fluids under hydrothermal conditions. More than 50 papers have been published over the last 90 years attempting experimentally, spectroscopically or theoretically to quantify gold solubility, and determine the stability of its major aqueous complexes in hydrothermal fluids (Pokrovski et al., 2014 and references therein). It follows from those works that two major Au aqueous complexes are gold(I) di-hydrosulfide, $Au(HS)_2^-$, and gold(I) di-chloride, $AuCl_2^-$. Their thermodynamic stability and molecular structure have been thoroughly constrained in a wide T-P range. The former is generally dominant in sulfide-bearing, near-neutral pH, low-to-moderate temperature hydrothermal fluids, whereas the latter may control Au transport in highly-saline, acidic, oxidized and higher-temperature magmatic-hydrothermal fluids. In addition, two other subordinate complexes, $AuHS^0$ and $AuOH^0$, have been identified in some laboratory solubility studies, but their contribution to Au solubility remains generally much lower than that of $Au(HS)_2$ and $AuCl_2^-$. In the recent years, following the discovery of the trisulfur radical ion in hydrothermal fluids (Pokrovski and Dubrovinsky, 2011; Pokrovski and Dubessy, 2015), another gold complex has been added to the gold speciation scheme, $Au(HS)S_3^-$(Pokrovski et al., 2015). The latter may account for Au transport in high-temperature sulfur-rich fluids (wt% level of S concentrations) in which sulfate and sulfide coexist. Such conditions can occur close to the magmatic-hydrothermal transition in porphyry Cu-Au-Mo deposits as well as in deep metamorphic settings of amphibolite

facies when pyrite breaks down to pyrrhotite producing high sulfur concentrations in the fluid. Thus, this complex may be an important player at the deep and high-temperature gold source.

In most Carlin, epithermal, and low-to-moderate temperature orogenic deposits settings related to sedimentary environments, sulfur concentrations are, however, not high enough to favor the large abundance of the trisulfur complex. The hydrothermal fluids in most these three types of deposits (except probably for some high sulfidation varieties in epithermal type deposits) have similar characteristics. They are low salinity fluids (<10 wt% NaCl), reduced (f_{O2} < hematite-magnetite buffer), with near neutral pH values (5-8), and containing hundreds ppm of H_2S (Hofstra et al., 2000; Simmons et al., 2020). Thus, Au^I hydrosulfide complexes dominate the transport of gold under these conditions. Fig. 8 shows the solubility of gold for typical conditions and compositions of epithermal fluids. It can be seen that such fluids are capable of transporting up to 1 ppm of Au at near-neutral pH, which is 1000 time more than its average crustal abundance. Such transporting capacities are in agreement with natural fluid inclusion analyses of Au discussed above (e.g., Kouzmanov and Pokrovski, 2012).
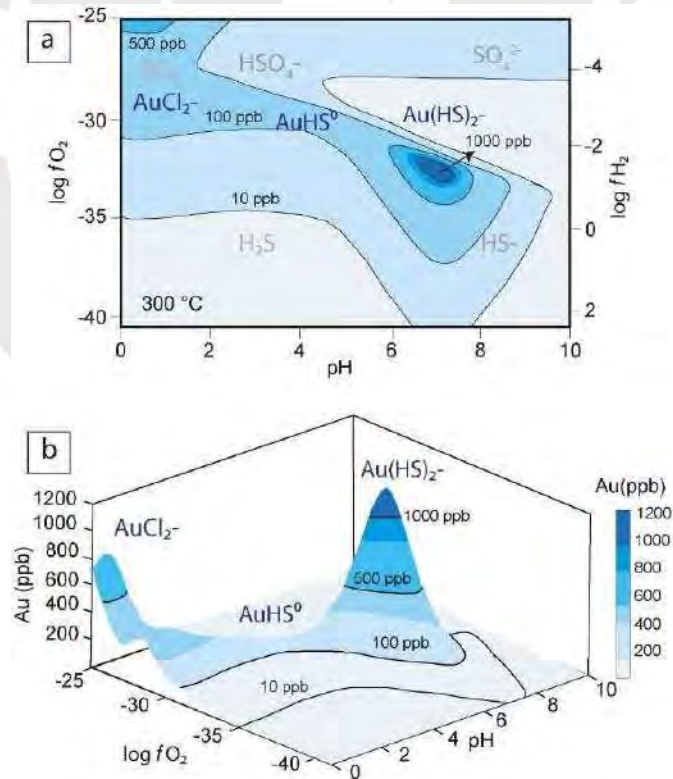
Fig. 8. Gold solubility and chemical speciation represented in plan (a) and three-dimensional (b) diagrams at 300 °C, 85 bar, as a function of oxygen fugacity and pH in an epithermal fluid with 0.01 m S (320 ppm S) and 1 m NaCl (adapted from Simmons et al., 2020).

The precipitation of gold carried by hydrothermal fluid requires the fluid to reach gold saturation upon the fluid movement and evolution in the crust. This precipitation process involves destabilization of the gold-bearing sulfide complexes due to changes in the key parameters of the hydrothermal fluid, in particular its sulfur content. These changes may occur through fluid unmixing or boiling (mainly removal of H_2S into the vapor phase), sulfidation of Fe-bearing host rocks (i.e., scavenging H_2S by pyrite), mixing with meteoric fluids (i.e., leading to H_2S oxidation and dilution), or reducing by organic matter (leading to Au(I) reduction to Au(0)), to name a few (Pokrovski et al., 2014; Simmons et al., 2020; references therein). However, as it will be shown in this work, because different fluid parameters change simultaneously during the fluid evolution, the final effect on gold solubility will be a fine interplay among all these factors. Thus, the effect of organic matter, for example, on gold transport and precipitation reveals itself to be far more complex than a simple gold reduction exemplified above (see chapter II).

Another possible mechanism of gold transport, different from true dissolved complexes, is in the form of colloids. Evidence of colloidal gold transported by hydrothermal fluids has been reported in active geothermal systems and high-temperature black smokers (Gartman et al., 2018; Hannington and Garbe-Schönberg, 2019), but also in fluid inclusions from an orogenic gold deposit intercepted by the Kola borehole (Northwest Russia; Prokofiev et al., 2020). These fluid inclusions contain gold nanoparticles. The total gold content of these fluid inclusions (up to 6,000 ppm) is higher than the amount predicted by thermodynamic modeling and previously reported in fluid inclusions (e.g., Kouzmanov and Pokrovski, 2012; Garofalo et al., 2014; Rauchenstein-Martinek et al., 2016), consistent with colloidal gold transported by hydrothermal fluids rather than gold nanoparticles precipitated after fluid entrapment. Gold nanoparticles associated with amorphous silica have been reported in high-grade Carlin and orogenic deposits (e.g., Saunders, 1990; Petrella et al., 2022), the authors propose that gold and silica colloids were nucleated at deeper levels and then transported to the site of deposition by hydrothermal fluids. Thus, the ability of the hydrothermal fluid to transport gold in colloidal form at some conditions might be greater than that of gold in dissolved form in solution, and probably may be responsible for the formation of high-grade mineralization in some places. However, robust experimental evidence of such gold-silica colloidal transport is yet lacking. It should be noted that efficient stabilization of gold nanoparticles in solution in industrial applications is often achieved in the presence of sulfide sulfur ligands binding the particles at their surface (e.g., Häkkinen, 2012). Thus, the role of sulfur in hydrothermal colloidal gold transport yet remains to be investigated.

Finally, a different mechanism of gold precipitation is the adsorption/scavenging of invisible gold in a chemically bound state by arsenian pyrite from the hydrothermal fluid (e.g., Reich et al., 2005; Kusebauch et al., 2019; Pokrovski et al., 2019, 2021; references therein). This mechanism does not require the fluid to be saturated with respect to gold metal and, therefore, may operate even at low Au concentrations. This process may particularly be important for sediment-hosted gold deposits where arsenic-rich pyrite hosting invisible gold is the major gold-bearing mineral, and should be considered along with other 'traditional' mechanisms, such as phase separation, sulfidation, and mixing common in orogenic and epithermal deposits, as discussed above. The exact knowledge of the nature and composition of surface or in-lattice complexes of gold in pyrite is key to understanding this important phenomenon. The research in this topic is yet in its infancy and requires in situ spectroscopic techniques that only recently became available (e.g., Pokrovski et al., 2021 and references therein).

I.3. The role of carbonaceous material and arsenian pyrite in sediment-hosted gold deposits.

I.3.1. Occurrence of carbonaceous material and arsenian pyrite in sediment-hosted gold deposits.

Carbonaceous material and arsenian pyrite hosting invisible gold are two key ingredients shared by Carlin, orogenic and epithermal sediment-hosted gold deposits, described above. Carbonaceous material refers to organic carbon deposited with the sediments, and its derivatives or modified products (e.g., hydrocarbons, graphite, etc.) after the organic carbon has been affected by processes such as diagenesis, metamorphism or hydrothermalism. In Carlin type gold deposits, arsenian pyrite hosting invisible gold is the main (if not exclusive) gold ore before it is affected by supergene alteration. In orogenic and epithermal sediment-hosted gold deposits, arsenian pyrite and arsenopyrite are also important gold-bearing minerals becoming the principal ore mineral in some deposits. Note that the famous gold deposits of the Witwatersrand basin also contain arsenian pyrite hosting invisible-gold, but its contribution to the total amount of gold has not been quantified. Some examples of sediment-hosted gold deposits and their association with carbonaceous material and arsenian pyrite are presented below.

In sediment- or metasediment-hosted orogenic gold deposits, the carbonaceous material is broadly present in the host rock and lodes. Fig. 9 shows a typical example of
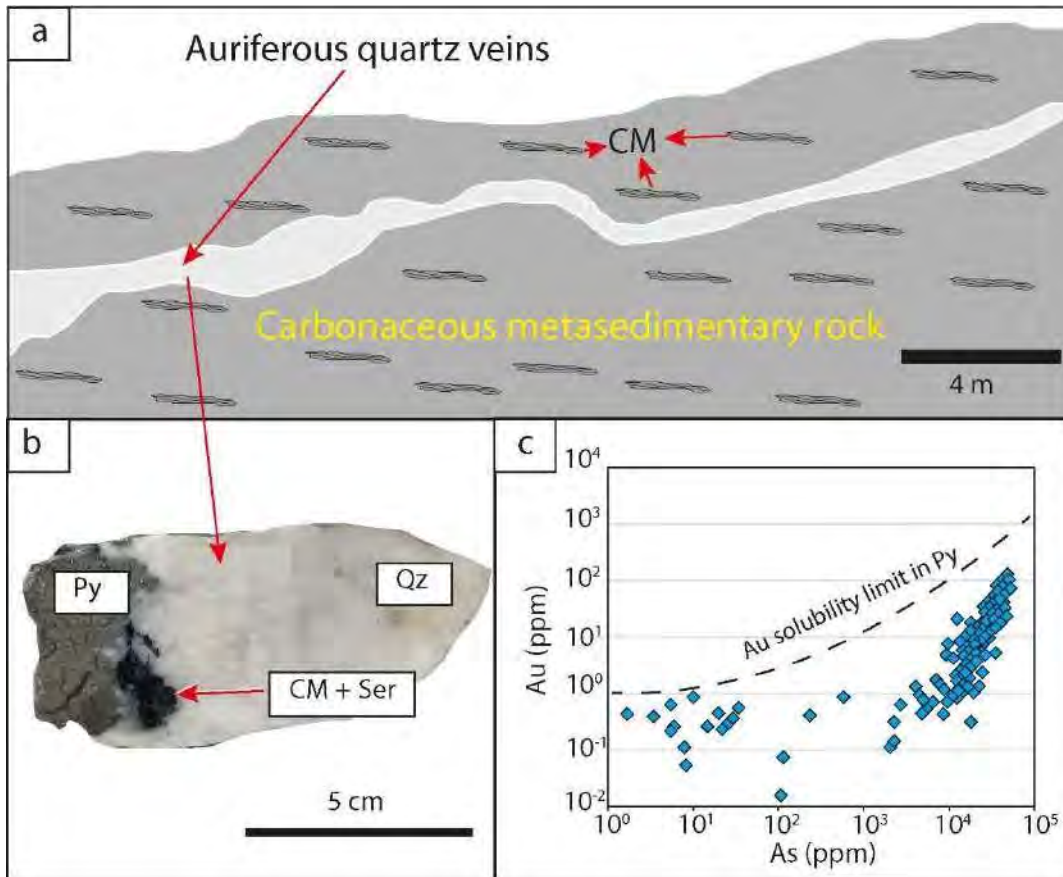
Fig. 9. Example of associations of carbonaceous material and arsenian pyrite in a sediment-hosted orogenic gold deposit (Bangbu deposit, China; Ding et al., 2023). a) Quartz vein hosted by a carbonaceous metasedimentary rock. b) Quartz vein with carbonaceous material, sericite and pyrite. c) Au vs. As concentration in different generations of arsenian pyrite from the Bangbu deposit; the dashed curve is an empirical gold solubility limit of Reich et al. (2005). Abbreviations: CM (carbonaceous material), Py (pyrite), Qz (quartz), Ser (sericite).

sediment-hosted orogenic deposits. The auriferous quartz vein is hosted by carbonaceous sediment rock (Fig. 9a). The quartz vein contains hydrothermally deposited carbonaceous material and arsenian pyrite hosting invisible gold (Fig. 9b, c). Recent studies show that different types of carbonaceous material were present, each type being likely associated with a particular sedimentary, metamorphic or mineralizing event.For example, four types of carbonaceous material (CM1, CM2, CM3 and CM4) have been identified in the Macraes orogenic gold deposit from the Otago Schist Belt (New Zealand): i) CM1 is of sedimentary origin; ii) and iii) CM2 and CM3 were transported and deposited by metamorphic fluids prior to gold deposition, and, finally, iv) CM4 is spatially associated with the mineralization, likely having been deposited by the same hydrothermal fluids responsible for gold deposition (Hu et al., 2015). Likewise, other

studies show that hydrothermally deposited carbonaceous material is closely associated with gold and sulfide minerals (e.g., Mirasol-Robert et al., 2017). This association was interpreted as a co-deposition of carbonaceous material, sulfides, and gold from the same carbonic ore fluid (e.g., Hu et al., 2016; Ding et al., 2023). Widely used tools to characterize the carbonaceous material are Raman spectroscopy, nano-scaling imaging (like STEM and HRTEM), and carbon isotope geochemistry.

In Carlin type gold deposits, the main gold ore is arsenian pyrite. The gold mineralization is also spatially associated with carbonaceous material. For example, the Screamer and Betze-Post deposits are mainly hosted by the Devonian Popovich Formation (Fig. 10a). This Formation corresponds to a sedimentary sequence with abundant organic carbon, especially in the Planar unit composed of carbonaceous limestone and calcareous mudstone with a very high organic carbon content (up to 14 wt %; Fig. 10b). However, organic carbon concentrations and gold grades do not show a clear correlation (Hofstra et al., 2000; Cline et al., 2005; De Alameda et al., 2010; Fig. 10b). In constast, Fig. 10c shows the Au and As concentrations in pyrite from the Screamer and Betze-Post deposits positively correlated. The ore pyrite from these deposits hosts up to 2,000 ppm Au with a mean value of 200 ppm Au (De Alameda et al., 2010).

Epithermal gold deposits can be hosted by sediments or volcano sedimentary sequences where organic carbon stems from the sediments: for example, epithermal gold deposits in southeast Asia as well as the American giants Pueblo Viejo (Dominican Republic) and Lagunas Norte (Peru) share several characteristics with Carlin type deposits. They are hosted by sediments both with high organic carbon content and refractory (invisible gold hosting) arsenian pyrite as the major gold-bearing mineral. The main difference from Carlin type deposits is their clear association with a Cu-Au porphyry deposit (e.g., Kirwin and Royle, 2017). At Pueblo Viejo, the Los Ranchos Formation that hosts part of the gold mineralization, presents a sedimentary sequence with high organic carbon content (Kettler et al., 1990). Figure 11a shows the location of the Monte Negro and Moore pits, which are spatially associated with the upper and lower carbonaceous units represented in light and dark grey respectively, hosting gold mineralization. The lower carbonaceous unit consists of interbedded mudstone, siltstone, and sandstone with <2% total organic carbon (Fig. 11b). The upper carbonaceous unit has less siltstone and sandstone, and contains > 2% total organic carbon (Fig. 11c, Vaughan et al., 2020).
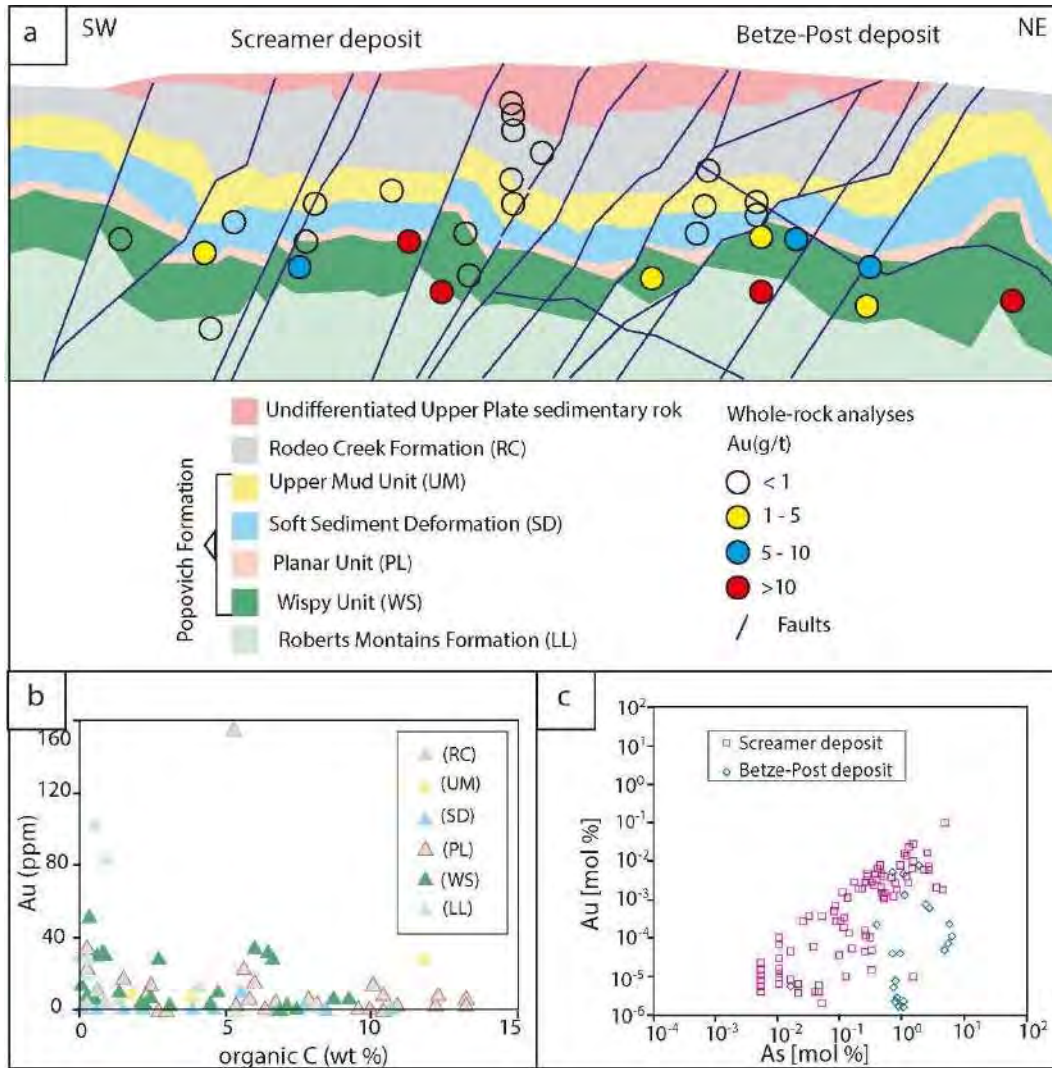
Fig. 10. Example of association of carbonaceous material and arsenian pyrite in Carlin type gold deposits (Screamer and Betze-Post deposits). a) Schematic southwest-northeast cross section showing the Screamer and Betze-Post deposits (Adapted from De Almeida et al., 2010). b) Gold grade vs. organic carbon concentration from different sedimentary rocks (Adapted from De Almeida et al., 2010). c) Au vs As concentration in pyrites from Screamer and Betze-Post Carlin type gold deposits (according to Reich et al., 2005).

The lower carbonaceous unit is mineralized whereas the upper carbonaceous unit contemporaneous with the latest mineralizing events is practically barren, likely because of its low permeability that may not have allowed fluid movement and resulting mineralization (Vaughan et al., 2020). Figure 11d shows arsenian pyrite with up to 1.7 wt % As concentration from Pueblo Viejo. At Pueblo Viejo, most of gold hypogene mineralization is present in arsenian pyrite with up to 1,000 ppm of gold (Deditius et al.,

2009; Vaughan et al., 2020). The Lagunas Norte, epithermal gold deposit in Peru, is mainly hosted by the Chimú Formation which consists of quartz-rich sandstones with levels of carbonaceous mudstone. Furthermore, the Chimú Formation overlies the Chicama Formation which consists of 1000 m of black shales with up to 2 % of total carbon (Vallance et al., 2024). In Lagunas Norte the gold is also mainly concentrated in pyrite (Montgomery, 2012; Cerpa et al., 2013), even though the concentrations values were not reported. To date, mining in Lagunas Norte is restricted to the oxidized zone. Lagunas Norte is located in the same metallogenetic belt that Algamarca and Shahuindo epithermal deposits, which will be examined in depth in chapters II and III.
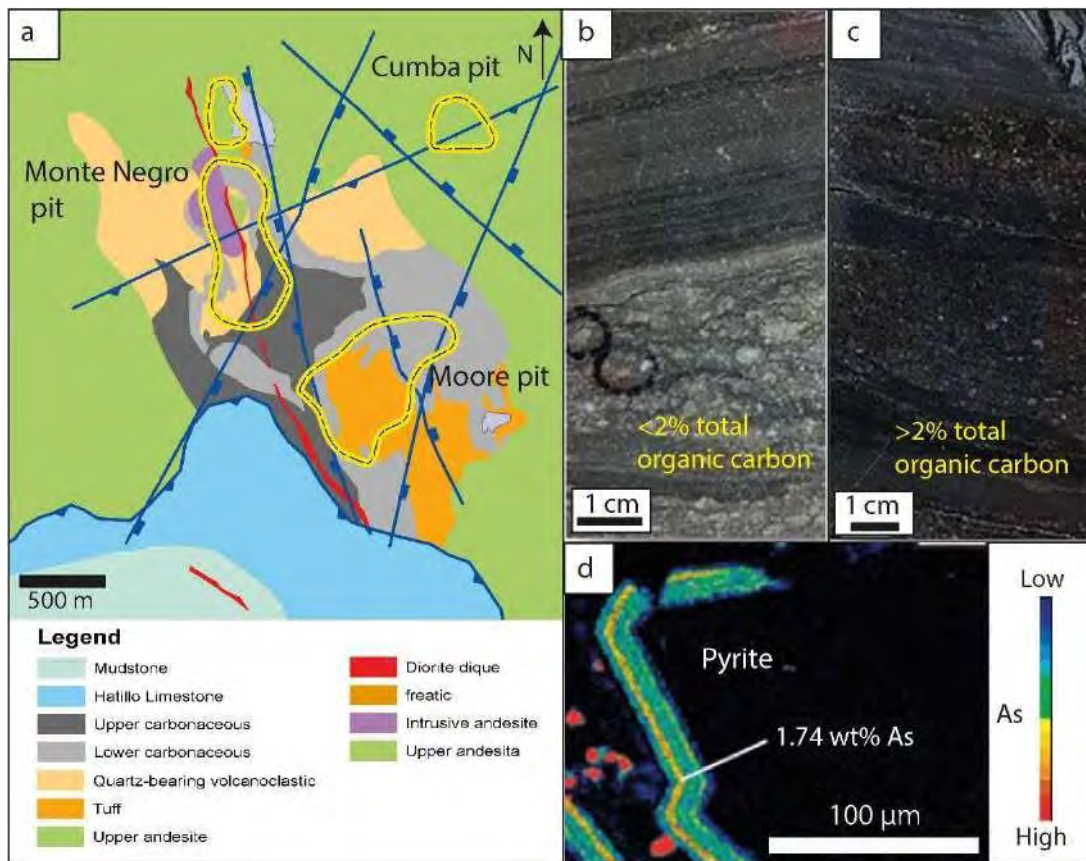
Fig. 11. Example of association of carbonaceous material and arsenian pyrite in sediment-hosted epithermal gold deposits (Pueblo Viejo of Dominican Republic; Deditius et al., 2009; Vaughan et al., 2020). a) Geological map of Pueblo Viejo. b) Mineralized lower carbonaceous sediment unit with abundant fragments of pyrite (black circles). c) Unmineralized upper carbonaceous unit. d) EPMA elemental maps for pyrite from Pueblo Viejo.

I.3.2. Role of carbonaceous material in the genesis of gold mineralization

The examples presented above are representative of orogenic, Carlin and epithermal sediment-hosted gold deposits, and unambiguously show that these types are intrinsically associated with carbonaceous material. The carbonaceous material may be already present in the sediments hosting the gold mineralization or precipitated from the fluid during the mineralization process. As a result of this close association, the role of the carbonaceous material in the genesis of sediment-hosted gold deposits has been attentively considered. However, a consensus on its exact contribution to the formation of sediment-hosted gold deposits is yet elusive. Major proposals regarding the role of carbonaceous material in the formation of sediment-hosted gold deposits are overviewed below.

Carbonaceous material as the source of gold. In this proposal, the source of gold is carbonaceous sediments with high metal contents, called metalliferous black shales (e.g., Nelson, 1989; Johnson et al., 2017). In this type of rock, metals and organic matter are often positively correlated. The organic matter deposited in the sediments by microorganisms such as phytoplankton may scavenge metals directly from seawater. High concentrations of organic carbon in the sediments coupled with their high absorption affinity and the availability of metals in seawater are the necessary prerequisits for enrichment of metals in the sediments. Therefore, the deposition of sediments with these characteristics is limited to geologic ages with favorable conditions for the proliferation of life (generating a greater amount of deposited organic matter), combined with intense tectonic plate activity favoring volcanism and supplying more metals to seawater (Johnson et al., 2017). In this model, the metalliferous black shales are fertile rocks capable of producing economic concentrations of gold after their metallic content has been leached and re-concentrated by hydrothermal fluids (e.g., Nelson, 1989; Large et al., 2011). During diagenesis, metals concentrated by organic carbon are transferred and concentrated into sedimentary pyrite (Large et al., 2011). The pyrite is then converted to pyrrhotite during greenschist and amphibolite facies metamorphism. This conversion provides Au, As and S to the mineralizing metamorphic fluids because pyrrhotite, unlike pyrite, does not have the ability to accommodate Au and As in its structure (Large et al., 2011). The key conditions of this model are numerous, however, spanning from the availability of a large gold-rich rock sedimentary source to the extreme efficiency of Au scavenging by pyrite and its concentrated release into the fluid during metamorphism - the conditions that may be hard to be fulfilled together and in the right sequence.

27

Carbonaceous material as a gold trap. The proposition of carbonaceous material being a chemical trap for gold was explored by several authors to explain the close association between gold mineralization and carbonaceous material. Here, the carbonaceous material acts as a reducing agent that promotes gold deposition (e.g., Gatellier and Disnar, 1989; Fuchs et al., 2016). For orogenic gold deposits in France, Gatellier and Disnar (1989), for example, proposed that interactions between the hydrothermal fluid and carbonaceous material led to a decrease in oxygen fugacity and caused sulfide precipitation with incorporation of gold into pyrite and arsenopyrite. In addition, interactions between a gold-bearing fluid and carbonaceous material reduced gold and promoted its deposition as nanoparticles in the organic matter. In the case of Witwatersrand, Fuchs et al. (2016) proposed that the change in redox state destabilized the $Au^I(HS)$ and $Au^I(HS)_2^-$ complexes, thereby causing gold deposition in the native state. The chemical trap model has been regarded to be responsible for gold deposition in Carlin, orogenic, and Witwatersrand gold deposits (e.g., Radtke and Scheiner, 1970; Gatellier and Disnar, 1989; Tan et al., 2015; Fuchs et al., 2016; Ding et al., 2023). However, the difficulty of the model is that changes in redox have a relatively small effect on Au solubility compared to those in H_2S content and fluid acidity that have not been considered in those models. In addition, if Au is incorporated in pyrite in a chemically bound state (as Au^I) from Au^I aqueous complexes, then there should be no effect of redox changes at all.

Gold transport by oil. A third, alternative or additional, proposal invoked in the literature is direct transport of gold by hydrocarbon liquids. Indeed, rare direct solubility and partitioning experiments show that oil can dissolve up to 2 ppb Au up 100 °C, and up to 50 ppb Au at 250 °C in equilibrium with gold metal (Migdisov et al., 2017; Crede et al., 2019). Gold solubility in oil is thus appears fairly modest compared to that in typical S-bearing aqueous solution from epithermal settings (>100s ppb and up to 100 ppm with S concentrations of few wt% S - typical of those in oil; e.g., Pokrovski et al., 2014; Simmons et al., 2020). In addition, oil is generally unstable at temperatures above 150°C transforming to pyrobitumen and graphite, and may be preserved only in rare occurrences. An example of petroleum preservation in fluid inclusions associated with gold mineralization occurs in the Carlin Type gold deposits of the Yankee Basin (Hulen and Collister, 1999). This example indicates that the temperature did not exceed 150°C in agreement with temperatures obtained by other geo-thermometers. The small size and low grade of Carlin type gold deposits of the Yankee Basin compared with the other Carlin type deposits of the district were attributed to the low temperature of hydrothermal fluids, <150°C, which are lower than the typical temperatures associated with gold

mineralizations (Hulen and Collister, 1999), and therefore such fluids have even lesser capacity for gold transport.

I.3.3. Role of arsenian pyrite in the genesis of gold mineralization

In sediment-hosted gold deposits, most of the hypogene gold mineralization is concentrated as invisible-gold in arsenian pyrite. The close association of Au and As in pyrite has been widely documented in several types of ore deposits, including sediment-hosted ones (Deditius et al., 2014; references therein). Numerous studies show that the amount of invisible-gold in pyrite is a function of As. Based on this premise, Reich et al. (2005) proposed an impirical solubility limit of gold that allows one to distinguish bound gold in pyrite from disseminated gold nanoparticles, as shown in Fig. 12 (solid curve).
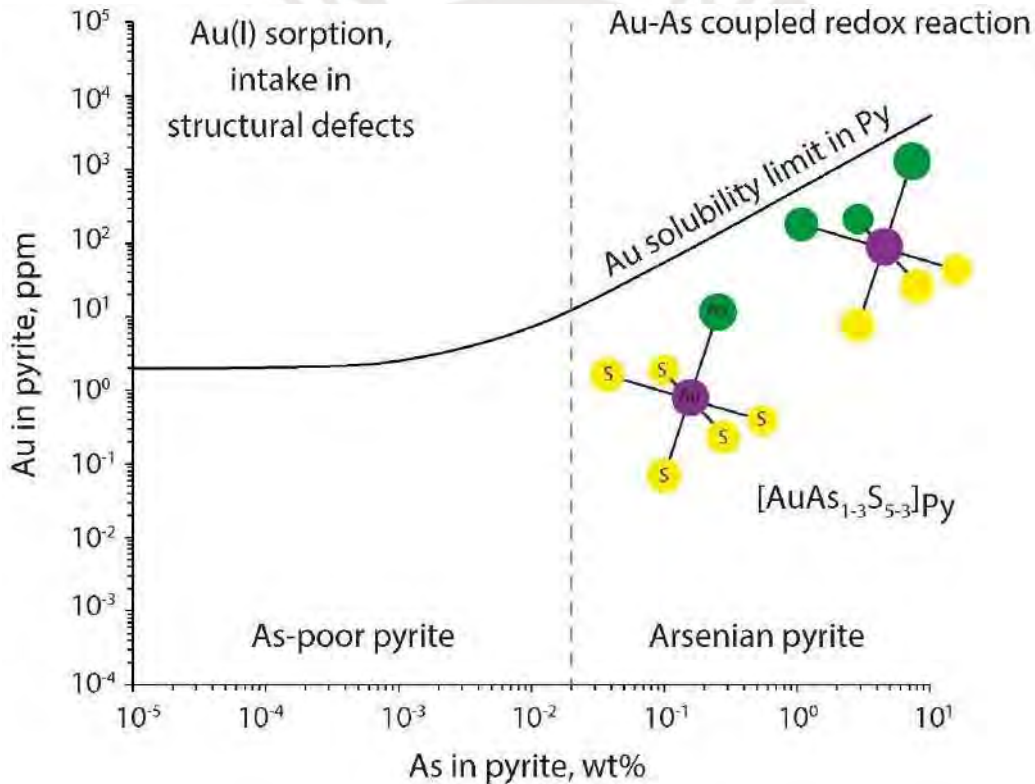
Fig. 12. Structural model for chemically bound Au in pyrite (not to scale). The Au coordination is shown by ball-and-stick atomic clusters (Au = purple, S = yellow, As = green). Empirical Au solubility limit in arsenian pyrite from Reich et al., 2005. Note a fundamental transition in the Au incorporation mechanism (vertical dashed line, indicative position), from chemisorption as Au(I)-polysulfide complexes at low As content in pyrite to coupled Au-As redox reactions driving Au entry in As-enriched Fe crystallographic sites of the pyrite (according to Pokrovski et al., 2021).

However, in some epithermal deposits, in which gold concentrations in pyrite are below the solubility limit, gold nanoparticles were identified by LA-ICPMS spiky signals of gold (e.g., Tanner et al., 2016). Inversely, chemically bound gold concentrations well above the solubility limit of Fig. 12 were measured in pyrite from gold deposit tailings (e.g., Merkulova et al., 2019). By combination of in-situ high-resolution x-ray absorption spectroscopic methods with experiments under controlled laboratory conditions and thermodynamic modeling, it has recently been demonstrated that the coupled incorporation of Au^{II} and As^{-I} in the Fe and S pyrite crystallographic sites, respectively, may be the key mechanism to explain the Au-As chemical association in arsenic-rich pyrite, arsenopyrite and löllengite (Pokrovski et al., 2021). In contrast, arsenic-poor pyrite has a very limited capacity of incorporating gold into the structure. In such pyrites, little gold may be incorporated into structural defects in the form of Au sulfide complexes and subsequently expelled from the structure as native metal during pyrite recrystallization (Pokrovski et al., 2019). Figure 12 illustrates how gold is incorporated into arsenic-rich pyrite. According to these recent findings, the extremely efficient partitioning of Au and As from a fluid (unsaturated with respect to metallic gold) into pyrite can lead to large tenors of Au and As chemically bound in pyrite at redox and pH conditions of Carlin and orogenic-type deposits (Kusebauch et al., 2018, 2019; Pokrovski et al., 2021).

These recent findings will further be tested and explored in this work on a natural case study of two epithermal gold deposits in northern Peru emplaced within a sedimentary basin, the Shahuindo and Algamarca deposits, which are representative of close association of gold with both organic matter and arsenian pyrite. These settings thus offer to us a great opportunity to explore in detail the yet enigmatic relationships of gold and associated metals with organic carbon and arsenic. In the following section, we introduce the geological and metallogenic context and identify gaps of our knowledge of these case deposits.

I.4. Geological and metallogenic setting of the present study

The Shahuindo and Algamarca deposits are located 22 km west of the town of Cajabamba (Cajamarca region) of northern Peru, within the Marañon Fold and Thrust Belt (MFTB). The MFTB hosts a suite of epithermal, porphyry and skarn deposits associated with intrusions from the Oligo-Miocene subduction-related magmatic arc (Noble and McKee, 1999; Scherrenberg et al., 2016). Remarkable deposits currently being mined within the belt include Yanacocha, Lagunas Norte and Shahuindo (all

epithermal-type), and Antamina (skarn-type), to name a few. In the northern part of the MFTB, several epithermal deposits are hosted by siliciclastic sedimentary sequences of the Goyllarisquizga Group. The permeable sandstones from the Chimú, Carhuaz, and Farrat formations are the main host rocks (Fig. 13a; Gauthier et al., 1999; Defilippi et al., 2016). This set of deposits is known as the XXIA metallogenic belt: Au-Ag epithermal deposits hosted in siliciclastic sequences of the lower Cretaceous Goyllarisquizga Group (Acosta et al., 2009). Representative Au-Ag epithermal deposits in this metallogenic belt include Shahuindo, Algamarca, La Arena, Lagunas Norte, Igor, El Toro, and La Virgen (Fig. 13a).
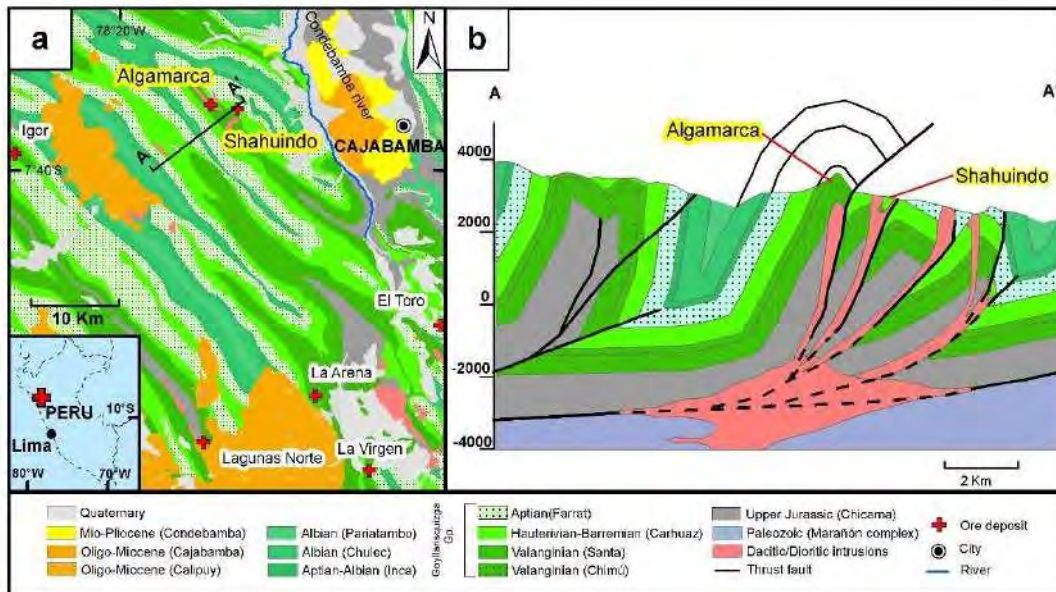
Fig. 13. (a) Regional geological map showing the principal ore deposits in the north of the Marañon Fold and Thrust Belt, and the A-A´ cross-section in Figure 1b (modified from INGEMMET, 2017). (b) Structural SW-NE cross section (modified from Vallance et al., 2024).

The MFTB is an east-verging thin-skinned thrust system composed of a succession of tight imbricates and associated folds, forming good structural traps and reflecting a significant amount of horizontal shortening. It propagated in a fluvio-deltaic and marine sedimentary series deposited in a back-arc basin from late Jurassic to late Cretaceous. These sediments overlie a basement formed by metamorphic rocks from Precambrian to lower-Ordovician, known as the Marañón complex (Mégard, 1984; Benavides-Cáceres, 1999; Chew et al., 2007; Scherrenberg et al., 2016). The MFTB

developed during the Peruvian and Incaic phases corresponding to the early period of the Andean orogeny, between the late Cretaceous and the middle Eocene (Noble et al., 1979; Mégard, 1984). The main décollement occurred at the interface between the thick black shales of the Chicama Formation and the basement (Mégard, 1984; Jaillard and Jacay, 1989; Eude et al., 2015). The MFTB is truncated by a middle Eocene regional unconformity sealed by volcanic and volcano-clastic sediments of the late Eocene to middle Miocene Calipuy plateau-basin to the West (Noble et al., 1990; Prudhomme et al., 2019), and the Cajabamba basin fluvial and lacustrine sediments to the East. The MFTB and the overlying Calipuy and Cajabamba basins were uplifted and exhumed as a result of the subduction of the Nazca Ridge during the late Neogene (Rosenbaum et al., 2005). In the study area, the MFTB is currently NW-SE oriented and segmented by NE-SW strike-slip and normal faults of apparently later age. Intrusions of Oligo-Miocene age outcrop, and form elongated bodies generally controlled by anticline axes, thrust faults, and transverse NE-SW faults. A more detailed description of the local geology can be found in Defilippi et al. (2016) and Prudhomme et al. (2019). Shahuindo and Algamarca are two epithermal deposits currently mined in the study area. The Shahuindo deposit comprises a zone of primary sulfide ore and an oxidized zone of supergene origin. Within the area of hypogene mineralization, the distribution of gold reflects permeability induced by favorable sedimentary facies (Carhuaz and Farrat sandstones), faults, breccia, and intrusion contacts. At Algamarca, the mineralization occurs as veins emplaced in the sandstones of the Chimú Formation, which constitutes the core of the most imposing anticline of the area (Fig. 13b). The two deposits are just ˜2 km apart, implying that they are likely to be related to a common magmatic-hydrothermal center (Hodder et al., 2010). Shahuindo and Algamarca are epithermal sediment-hosted gold deposits, showing a clear spatial association with carbonaceous material of the regional black shale levels (Chicama and Santa formations).

The late Jurassic and Cretaceous sedimentary series involved in the deformation of the MFTB constituted currently an overmature petroleum system. The source rocks correspond to the Chicama and Santa black shales, and reservoirs are the Chimú, Carhuaz and Farrat sandstones, which today host the gold deposits. The Santa and Inca black shales form the seal rocks of the sandstone reservoirs. The main HC source rock is clearly the Chicama thick black shales (1000 m), which belong to the late Jurassic stratigraphic interval considered to be a word-class hydrocarbon source rock (Klemme and Ulmishek, 1991). Basin modelling (Van de Vyver, 2021) showed that the Chicama source rock generated and expulsed hydrocarbons mainly between 110 and 25 Ma, in

part during the development of the MFTB, which probably allowed gas or oil to be trapped in the anticlinal structures. These hydrocarbons were not preserved during the tectonic uplift and Neogene erosion of the MFTB. The maximum burial depth of the Chicama black shales was reached between 100 and 157 Ma, at temperatures above 200°C. A second peak of gas generation was reached under the same conditions at 11 Ma.

This brief overview shows that the stratigraphy, general mineralogy, and global evolution of the Shahuindo and Algamarca sediment-hosted gold deposits are known and defined. However, many questions remain about the source and evolution of gold-bearing fluids and the role of carbonaceous material and arsenic in the genesis of these deposits. Integrated studies including structural analysis, detailed mineralogical and geochemical characterization of the hypogene ore, fluid inclusion study, and thermodynamic and chemical speciation modeling are lacking. Solving these questions will allow for improved exploration models for gold mineralization in sediment-hosted deposits in the Marañon Fold and Thrust Belt and worldwide.

I.5. Aims of the present study

The state-of-the-art overview above shows that despite extensive chronological, mineralogical, geochemical and isotopic characterization of sediment-hosted gold deposits due to their economic relevance, the source of gold and the role of organic matter and arsenian pyrite, – the two fundamental ingredients of sediment-hosted gold deposits, – yet remain unresolved. The resolution of these questions is complicated by the complex formation history of sediment-hosted gold deposits, the poor preservation of direct evidence such as fluid inclusions, and the lack of modeling of the interactions between hydrothermal fluids and sediments rich in organic carbon. Although the two key ingredients (carbonaceous material and arsenian pyrite hosting invisible gold) occur in association in sediment-hosted gold deposits, most of genetic models omit a link between them. In this work, we address these questions on a case study of the Shahuindo and Algamarca epithermal Au-Ag deposits, which are representative of sediment-hosted gold deposits worldwide.

The main objectives of the present study are the following:

- To analyze the tectonic and sedimentary context of the Algamarca and Shahuindo sediment-hosted gold deposits.

- To provide a detailed petrographic, mineralogical and geochemical study of ore and gangue minerals, host rocks and fluid inclusions in the Algamarca and Shahuindo epithermal deposits.

- To determine the source of gold for Algamarca and Shahuindo and identify the paragenetic sequence.

- To investigate the role played by the organic carbon and arsenian pyrite in the formation of both deposits.

- To propose a model of formation for the Algamarca and Shahuindo deposits that integrates both the role of carbonaceous material and arsenian pyrite.

I.6. Manuscript organization

The present manuscript is organized in four chapters. An Introduction (the present chapter I) and three following chapters whose content is briefly summarized below.

Chapter II: Combined effect of organic carbon and arsenic on the formation of sediment-hosted gold deposits: a case study of the Shahuindo epithermal deposit, Peru. This chapter presents a published article in Economic Geology (Vallance, Galdos et al., 2024), that describes an integrated structural, mineralogical, geochemical and modeling study of the Shahuindo deposit. Our objectives were to determine the source of gold-bearing fluids and the roles played by arsenic and organic carbon in the formation of sediment-hosted gold deposits. For this purpose, we have elaborated and applied the following methods: structural analysis, mineralogical and geochemical analyses of the ore and surrounding rocks, and thermodynamic and chemical speciation modeling of a gold-bearing magmatic fluid interacting with sediments rich in organic carbon. The results reveal the structural and lithological control of gold deposition, the source of the fluids, and the link between arsenic and organic matter that likely controls the formation of the Shahuindo sediment-hosted gold deposit.

Chapter III: Origin and evolution of gold-bearing fluids in a carbon-rich sedimentary basin: a case study of the Algamarca epithermal gold-silver-copper deposit, Northern Peru. This chapter presents a published article in Ore Geology Reviews (Galdos et al., 2024). This work is focused on mineral paragenesis and mineralizing fluid of the neighboring Algamarca deposit. Our objectives here were to determine the origin

of the mineralizing fluids and the role played by the organic matter and arsenic in the transport, concentration and deposition of gold. Mineralogical and geochemical data of ore and gangue minerals were determined by chemical etching, optical microscopy, scanning electron microscopy, X-ray powder diffraction, electron microprobe and LA-ICPMS analysis. Fluid inclusions were studied in quartz grains by cathodoluminescence imaging, microthermometric analyses, Raman spectroscopy, and in-situ analyses of single fluid inclusions by LA-ICPMS. The results allowed us to determine the origin of the mineralizing fluids and to integrate the role of organic matter and arsenic in the formation model of the Algamarca epithermal deposit.

Chapter IV: Conclusions and perspectives. The chapter summarizes the conclusions drawn from this work, discusses several near-future perspectives opened by our study, and provides some new clues for exploration strategies.

Annex: The annex contains the list of figures and tables, the electronic supplementary material for Chapters II and III, and two extended peer-reviewed abstracts that have been presented by Renzo Galdos at the ProExplo 2021 and 2023 Conferences. The first abstract is entitled "A common hydrothermal magmatic system generates different styles of gold mineralization at Algamarca and Shahuindo, Northern Peru" (Galdos et al., 2021) and the second abstract is entitled "Decoding hydrothermal fluids in organic carbon-rich basins: The case of the Algamarca Au-Ag-Cu deposit, Northern Peru. Implications for targeting hidden porphyry deposits" (Galdos et al., 2023). The oral presentation of this work by R. Galdos at this conference has been awarded by a prize for the best student talk.

References

Acosta, J., Rivera, R., Valencia, M., Chirif, H., Huanacuni, D., Rodríguez, I., Villareal, E., Paico, D., Santisteban, A., Santisteban, A., 2009. Memoria mapa metalogenético del Perú 2009. Instituto geológico minero y metalúrgico (INGEMMET), Perú, 17 p.

Akcil, A., Sun, Z., Panda, S., 2020. COVID-19 disruptions to tech-metals supply are a wake-up call. Nature 587, 365-367.

Albinson, T., Norman, D.I., Cole, D., Chomiak, B., 2001. Controls on formation of low sulfidation epithermal deposits in Mexico; constraints from fluid inclusion and stable isotope data. In: Albinson, T. and Nelson, C.E. (eds.) New Mines and Discoveries in Mexico and Central America. Soc. Econ. Geol. Spec. Publ. 8, 1-32.

Arehart, G.B., Chryssoulis, S.L., Kesler, S.E., 1993. Gold and arsenic in iron sulfides from sediment-hosted disseminated gold deposits; implications for depositional processes. Econ. Geol. 88, 171-185.

Arribas Jr., A., 1995. Characteristics of high-sulfidation epithermal deposits, and their relation to magmatic fluid. In: Thompson, J.F.H. (Ed.), Magmas, fluids, and ore deposits: Min. Assoc. of Canada Short Course, 23, 419-454.

Banco central de reservas del Perú (BCRP), 2023. Cotizaciones internacionales BCRP data. https://estadisticas.bcrp.gob.pe/estadisticas/series/mensuales/resultados/PN01654XM.

Barker, S.L., Hickey, K.A., Cline, J.S., Dipple, G.M., Kilburn, M.R., Vaughan, J.R., Longo, A.A., 2009. Uncloaking invisible gold: Use of nanoSIMS to evaluate gold, trace elements, and sulfur isotopes in pyrite from Carlin-type gold deposits. Econ. Geol. 104, 897-904.

Barton, P.B., Toulmin, P., 1966. Phase relations involving sphalerite in the Fe-Zn-S system. Econ. Geol. 61, 815-849.

Benavides-Cáceres, V., 1999. Orogenic evolution of the Peruvian Andes: The Andean cycle. Soc. Econ. Geol. Special Publ. 7, 61-107.

Bissing, T., Clark, A.H., Rainbow, A., Montgomery, A., 2015. Physiographic and tectonic settings of high-sulfidation epithermal gold-silver deposits of the Andes and their controls on mineralizing processes Ore. Geol. Rev. 65, 237-364.

Bodnar, R.J., Lecumberri-Sanchez, P., Moncada, D., Steele-MacInnis, M., 2014. Fluid inclusions in hydrothermal ore deposits, in: Holland, H.D., Turekian, K.K. (Eds.), Treatise on Geochemistry. second ed., 13 Elsevier, Oxford, pp. 119-142.

Camprubí, A., Ferrari, L., Cosca, M.A., Caredellach, E., Canals, A., 2003. Ages of epithermal deposits in Mexico: regional significance and links with the evolution of Tertiary volcanism. Econ. Geol. 98, 1029-1037.

Camprubí, A., Chomiak, B.A., Villanueva-Estrada, R.E., Canals, À., Norman, D.I., Cardellach, E., Stute, M., 2006. Fluid sources for the La Guitarra epithermal deposit (Temascaltepec district, Mexico): Volatile and helium isotope analyses in fluid inclusions. Chem. Geol. 231, 252-284.

Camprubí, A., Albinson, T., 2007. Epithermal deposits in Mexico - update of current knowledge, and an empirical reclassification. Geol. Soc. Am. Spec. Pap. 422, 377-415.

Cerpa, L.M., Bissig, T., Kyser, K. McEwan, C., Macassi, A., Hugo W. Rios, H.W., 2013. Lithologic controls on mineralization at the Lagunas Norte high-sulfidation epithermal gold deposit, Northern Peru. Miner. Deposita 48, 653-673.

Chew, D., Schaltegger, U., Košler, J., Whitehouse, M.J., Gutjahr, M., Spikings, R.A., and Mišković, A., 2007. U-Pb geochronologic evidence for the evolution of the Gondwanan margin of the north central Andes: Geol. Soc. Am. Bull. 119, 697-711.

Chiaradia, M., 2023. Radiometric dating applied to ore deposits: theory and methods, in: Huston, D., Gutzmer, J., (Eds.), Isotopes in Economic Geology, Metallogenesis and Exploration. Springer, International Publishing, pp. 15-35.

Clayton, R. N., 1961. Oxygen isotope fractionation between calcium carbonate and water. J. Chem. Phys. 34, 724-726.

Cline, J.S., Hofstra, A.A., 2000. Ore-fluid evolution at the Getchell Carlin-type gold deposit, Nevada, USA. Eur. J. Mineral. 12, 195-212.

Cline, J.S., Hofstra, A.H., Muntean, J.L., Tosdal, R.M., Hickey, K.A., 2005. Carlin-type gold deposits in Nevada: critical geologic characteristics and viable models. Econ. Geol. 100, 451-454.

Crede, L.S., Evans, K.A., Rempel, K.U., Grice, K., Sugiyama, I., 2019. Gold partitioning between 1-dodecanethiol and brine at elevated temperatures: implications of Au transport in hydrocarbons for oil-brine ore systems. Chem. Geol. 504, 28-37.

Corral, I., Cardellach, E., Corbella, M., Canals, À., Griera, A., Gómez-Gras, D., Johnson, C.A., 2017. Origin and evolution of mineralizing fluids and exploration of the Cerro Quema Au-Cu deposit (Azuero Peninsula, Panama) from a fluid inclusion and stable isotope perspective. Ore Geol. Rev. 80, 947-960.

Crocket, J.H., 1991. Distribution of gold in the Earth's crust, in: Foster, R.P. (Ed.), Gold Metallogeny and Exploration. Blackie, Glasgow, pp. 1-36.

De Almeida, C.M., Olivo, G.R., Chouinard, A., Weakly, C., Poirier, G., 2010. Mineralparagenesis, alteration, and geochemistry of the two types of gold ore and the Host rocks from the Carlin-type deposits in the southern part of the Goldstrike property, northern Nevada: implications for sources of ore-forming elements, ore genesis, and mineral exploration. Econ. Geol. 105, 971-1004.

Deditius, A., Utsunomiya, S., Ewing, R.C., Chryssoulis, S., Venter, D., Kesler, S.E., 2009. Decoupled geochemical behavior of As and Cu in hydrothermal systems. Geology 37, 707-710.

Deditius, A.P., Reich, M., Kesler, S.E., Utsunomiya, S., Chryssoulis, S.L., Walshe, J., Ewing, R.C., 2014. The coupled geochemistry of Au and As in pyrite from hydrothermal ore deposits. Geochim. Cosmochim. Acta 140, 644-670.

Deen, J.A., Rye, R.O., Munoz, J. L., Drexler, J. W., 1994. The magmatic hydrothermal system at Julcani, Peru; evidence from fluid inclusions and hydrogen and oxygen isotopes. Econ. Geol. 89, 1924-1938.

Defilippi, C., Muerhoff, C.V., Williams, T., 2016. Technical Report on the Shahuindo mine, Cajabamba, Peru: NI 43-101 Technical Report Tahoe Resources. 307 p.

Ding, Z.P., Sun, X.M., Hu, S.Y., Chen, H.J., Li, D.F., Fu, Y., Xu, L., Wu, Z.Y., Huang, F., 2023. Role of carbonaceous material in gold precipitation for orogenic gold deposits: A case study of the Bangbu gold deposit in southern Tibet, China. Ore. Geol. Rev. 152, 105231.

Emsbo, P., Hofstra, A.H., Lauha, E.A., Griffin, G.L., Hutchinson, R.W., John, D.A., Theodore, T.G., 2003. Origin of high- grade gold ore, source of ore fluid components, and genesis of the Meikle and neighboring Carlin-type deposits, northern Carlin Trend, Nevada. Econ. Geol. 98, 1069-1105.

Einaudi, M.T., Hedenquist, J.W., Inan, E.E., 2003. Sulfidation state of fluids in active and extinct hydrothermal systems: transitions from porphyry to epithermal environments, in: Simmons, S.F., Graham, I. (Eds.), Volcanic, Geothermal, and Ore-Forming Fluids: Rulers and Witnesses of Processes within the Earth. Soc. Econ. Geol. Spec. Publ. 10, 285−313.

Eude, A., Roddaz, M., Brichau, S., Brusset, S., Baby, P., Calderon, Y., and Soula J.C., 2015. Timing of exhumation and deformation in the Northern Peruvian Eastern Andean Wedge (5 - 8

S) as inferred from low temperature thermochronology and balanced cross section: Tectonics 34, 715-730.

Frimmel, H.E., 2008. Earth's continental crustal gold endowment. Earth Planet. Sci. Lett. 267, 45-55.

Fontboté, L., Kouzmanov, K., Chiaradia, M., Pokrovski, G.S., 2017. Sulfide minerals in hydrothermal deposits. Elements 13, 97-103.

Fuchs, Sebastian, Williams-Jones, Anthony E., Jackson, Simon E., Przybylowicz, Wojciech J., 2016. Metal distribution in pyrobitumen of the Carbon Leader Reef, Witwatersrand Supergroup, South Africa: Evidence for liquid hydrocarbon ore fluids. Chem. Geol. 426, 45-59.

Garofalo, P.S., Fricker, M.B., Gunther, D., Bersani, D., Lottici, P.P., 2014. Physical-chemical properties and metal budget of Au-transporting hydrothermal fluids in orogenic deposits, in: Garofalo, P., Ridley, J. (Eds.), Gold-transporting Hydrothermal Fluids in the Earth's Crust. Geol. Soc. London Spec. Publ. 402, 71-102

Gartman, A., Hannington, M., Jamieson, J.W., Peterkin, B., Garbe-Schönberg, D., Findlay, A.J., Fuchs, S., Kwasnitschka, T., 2018. Boiling-induced formation of colloidal gold in black smoker hydrothermal fluids. Geology, 46, 39-42.

Gatellier, J., Disnar, J., 1989. Organic matter and gold-ore association in a hydrothermal deposit, France. Appl. Geochem. 4, 143-149.

Gauthier A., Díaz N., Quirita V., 1999. Yacimientos la Arena-Virgen. ProEXPLO 1999, Lima, Perú. Primer volumen de monografías de yacimientos minerales peruanos. Historia, exploración y geología, 73-91.

Goldfarb, R.J., Groves, D.I., Gardoll, S., 2001. Orogenic gold and geologic time; a global synthesis. Ore Geol. Rev. 18, 1-75.

Goldfarb, R. J., Groves, D. I., 2015. Orogenic gold: Common or evolving fluid and metal sources through time. Lithos 233, 2-26.

Gopon, P., Douglas, J.O., Auger, M.A., Hansen, L., Wade, J., Cline, J.S., Robb, L.J., Moody, M. P., 2019. A nanoscale investigation of Carlin-type gold deposits: An atom-scale elemental and isotopic perspective. Econ. Geol. 114, 1123-1133.

Groff, J.A., 2018. Fluid mixing during late-stage Carlin-type mineralization in the Getchell and Twin Creeks deposits, Nevada. Ore. Geol. Rev. 101, 960-965.

Groves, D. I., Goldfarb, R. J., Gebre-Mariam, M., Hagemann, S. G., Robert, F., 1998. Orogenic gold deposits: a proposed classification in the context of their crustal distribution and relationship to other gold deposit types. Ore. Geol. Rev. 13, 7-27.

Groves, D.I., Santosh, M., Deng, J., Wang, Q., Yang, L., Zhang, L., 2020. A holistic model for the origin of orogenic gold deposits and its implications for exploration. Miner. Deposita 55, 275-292.

Günther, D., Audétat, A., Frischknecht, R., Heinrich, C.A., 1998. Quantitative analysis of major, minor and trace elements in fluid inclusions using laser ablation inductivelyCoupl ed plasma mass spectrometry. J. Anal. At. Spectrom. 13, 263-270.

Häkkinen H., 2012. The gold-sulfur interface at the nanoscale. Nat. Chem. 4, 443-455.

Hannington, M., Harðardóttir, V., Garbe-Schönberg, D., Brown, K.L., 2016. Gold enrichment in active geothermal systems by accumulating colloidal suspensions. Nat. Geosci. 9, 299-302.

Hannington, M., Garbe-Schönberg, D., 2019. Detection of gold nanoparticles in hydrothermal fluids. Econ. Geol. 114, 397-400.

Hedenquist, J.W., Lowenstern, J. B., 1994. The role of magmas in the formation of hydrothermal ore deposits. Nature 370, 519-527.

Hedenquist, J.W., Arribas, A., Reynolds, T.J., 1998. Evolution of an intrusion-centered hydrothermal system; Far Southeast-Lepanto porphyry and epithermal Cu-Au deposits, Philippines. Econ. Geol. 93, 373-404.

Hedenquist, J.W., Arribas, A., Gonzales-Urien, E., 2000. Exploration for epithermal gold deposits. Soc. Econ. Geol. Rev. 13, 245-277.

Hedenquist, J.W., Arribas, A., 2022. Exploration implications of multiple formation environments of advanced argillic minerals. Econ. Geol. 117, 609-643.

Hodder, R.W., Amireault, S., Arsenault, C., Huisa, F., 2010. The Shahuindo epithermal gold occurrence Cajabamba Province, Peru. Petrographic reconnaissance & interpretation of shape and size: Report Prepared for Sulliden Gold Corporation Ltd. 121 p.

Hofmann, A., Pitcairn, I., Wilson, A., 2017. Gold mobility during Palaeoarchaean submarine alteration. Earth Planet. Sci. Lett. 462, 47-54.

Hofstra, A.H., Cline, J.S., 2000. Characteristics and models for Carlin-type gold deposits. Soc. Econ. Geol. Rev. 13, 163-220.

Holley, E.A., Fulton, A., Jilly-Rehak, C., Johnson, C., Pribil, M., 2022. Nanoscale isotopic evidence resolves origins of giant Carlin-type ore deposits. Geology 50, 660-664.

Hu, S., Evans, K., Craw, D., Rempel, K., Bourdet, J., Dick, J., Grice, K., 2015. Raman characterization of carbonaceous material in the Macraes orogenic gold deposit and metasedimentary host rocks, New Zealand. Ore Geol. Rev. 70, 80-95.

Hu, S., Evans, K., Craw, D., Rempel, K., Grice, K., 2017. Resolving the role of carbonaceous material in gold precipitation in metasediment-hosted orogenic gold deposits. Geology 45, 167-170.

Hulen, J.B., Collister, J.W., 1999. The oil-bearing, carlin-type gold deposits of Yankee basin, Alligator Ridge district, Nevada. Econ. Geol. Bull. Soc. 94, 1029-1049.

Huston, D.L., Trumbull, R.B., Beaudoin, G., Ireland, T., 2023. Light Stable Isotopes (H, B, C, O and S) in Ore Studies–Methods, Theory, Applications and Uncertainties. In: Huston, D., Gutzmer, J. (Eds.), Isotopes in economic geology, metallogenesis and exploration. Springer International Publishing, Cham, pp. 209-244.

INGEMMET, 2017. Mapa Geológico del Perú, escala 1:100,000. https://geocatmin.ingemmet.gob.pe/geocatmin/.

Jaillard, E., Jacay, J., 1989. Les "Couches Chicama" du Nord du Pérou: colmatage d'un bassin né d'une collision oblique au tithonique. C.R. Acad. Sci. Paris 308, 1459-1465.

John, D.A., Hofstra, A.H., Fleck, R.J., Brummer, J.E., Saderholm, E.C., 2003. Geologic setting and genesis of the Mule Canyon low-sulfidation epithermal gold-silver deposit, north-central Nevada. Econ. Geol. 98, 425-463.

Johnson, S.C., Large, R.R., Coveney, R.M., Kelley, K.D., Slack, J.F., Steadman, J.A., Gregory, D.D., Sack, P.J., Meffre, S., 2017. Secular distribution of highly metalliferous black shales corresponds with peaks in past atmosphere oxygenation. Miner. Deposita 52, 791-798.

Jones, R.S., Fleischer, M., 1969. Gold in minerals and the composition of native gold. Geological survey circular 612, Washington, D.C., 17 p.

Kesler, S.E., Riciputi, L. C., Ye, Z., 2005. Evidence for a magmatic origin for Carlin-type gold deposits: isotopic composition of sulfur in the Betze-Post-Screamer Deposit, Nevada, USA. Miner. Deposita 40, 127-136.

Kettler, R.M., Waldo, G.S., Penner-Hahn, J.E., Meyers, P.A., Kesler, S.E., 1990. Sulfidation of organic matter associated with gold mineralization, Pueblo Viejo, Dominican Republic. Appl. Geochem. 5, 237-248.

Kirwin, D.J., Royle, D.Z., 2019. Sediment-hosted gold deposits in Southeast Asia. Resource Geol. 69, 125-147.

Klemme, H. D. and Ulmishek, G. F., 1991. Effective petroleum source rocks of the world: stratigraphic distribution and controlling depositional factors. Am. Assoc. Petrol. Geol. Bull. 75, 1809-1851.

Kouzmanov, K., Pettke, T., Heinrich, C.A., 2010. Direct analysis of ore-precipitating fluids: combined IR microscopy and LA-ICPMS study of fluid inclusions in opaque ore minerals. Econ. Geol. 105, 351-373.

Kouzmanov, K., Pokrovski, G.S., 2012. Hydrothermal controls on metal distribution in Cu(-Au-Mo) porphyry systems. Soc. Econ. Geol. Spec. Publ. 16, 573-618.

Kusebauch, C., Oelze, M., Gleeson, S.A., 2018. Partitioning of arsenic between hydrothermal fluid and pyrite during experimental siderite replacement. Chem. Geol. 500, 136-147.

Kusebauch, C., Gleeson, S. A., Oelze, M., 2019. Coupled partitioning of Au and As into pyrite controls formation of giant Au deposits. Sci. Adv. 5, eaav5891.

Large, R.R., Bull, S.W., Maslennikov, V.V., 2011. A carbonaceous sedimentary source-rock model for carlin-type and orogenic gold deposits. Econ. Geol. 106, 331-358.

Large, S.J.E., Bakker, E.Y.N., Weis, P., Wälle, M., Ressel, M., Heinrich, C.A., 2016. Trace elements in fluid inclusions of sediment-hosted gold deposits indicate a magmatic-hydrothermal origin of the Carlin ore trend. Geology 44, 1015-1018.

Li, H., Wang, Q., Yang, L., Dong, C., Weng, W., Deng, J., 2022. Alteration and mineralization patterns in orogenic gold deposits: Constraints from deposit observation and thermodynamic modeling. Chem. Geol. 607, 121012.

Matsuhisa, Y., Goldsmith, J.R., Clayton, R.N., 1979. Oxygen isotopic fractionation in the system quartz-albite-anorthite-water. Geochim. Cosmochim. Acta 43, 1131-1140.

McDonough, W.F., 2003. Compositional model for the Earth's core, in: Holland, H.D., Turekian, K.K. (Eds.), Treatise on geochemistry. Elsevier, Amsterdam, pp. 547-568.

Mégard, F., 1984. The Andean orogenic period and its major structures in central and Northern Perú. J. Geol. Soc. Lond. 141, 893-900.

Merkulova, M., Mathon, O., Glatzel, P., Rovezzi, M., Batanova, V., Marion, P., Boiron, M.- C., Manceau, A., 2019. Revealing the chemical form of "invisible" gold in natural arsenian pyrite and arsenopyrite with high Energy-Resolution X-ray Absorption Spectroscopy. ACS Earth Space Chem. 3, 1905-1914.

Migdisov, A.A., Guo, X., Xu, H., Williams-Jones, A.E., Sun, C.J., Vasyukova, O., Sugiyama, I., Fuchs, S., Pearce, K., Roback, R., 2017. Hydrocarbons as ore fluids. Geochem. Persp. Lett. 5, 47-52.

Mirasol-Robert, A., Grotheer, H., Bourdet, J., Suvorova, A., Grice, K., McCuaig, T.C., Greenwood, P.F., 2017. Evidence and origin of different types of sedimentary organic matter from a Paleoproterozoic orogenic Au deposit. Precambrian Res. 299, 319-338.

Montgomery, A.T., 2012. Metallogenetic Controls on Miocene High-sulphidation Epithermal Gold Mineralization, Alto Chicama District, La Libertad, Northern Perú. Queen's University, Kingston, Ontario, Canada, 381 p. (Unpublished PhD thesis).

Morishita, Y., Shimada, N., Shimada, K., 2018. Invisible gold in arsenian pyrite from the high grade Hishikari gold deposit, Japan: Significance of variation and distribution of Au/As ratios in pyrite. Ore Geol. Rev. 95, 79-93.

Nelson, C.E., 1990. Comparative geochemistry of jasperoids from Carlin-type gold deposits of the western United States. J. Geochem. Explor. 36, 171-195.

Noble, D.C., McKee, E.H., Mégard, F., 1979. Early Tertiary "Incaic" tectonism, uplift, and volcanic activity, Andes of central Peru. Geol. Soc. Am. Bull. 90, 903-907.

Noble, D.C., McKee, E.H., Mourier, T., Mégard, F., 1990. Cenozoic stratigraphy, magmatic activity, compressive deformation and uplift in Northern Peru. Geol. Soc. Am. Bull. 102, 1105-1113.

Noble, D.C., McKee, E.H., 1999. The Miocene metallogenic belt of Central and Northern Peru. in: Skinner, B.J. (Ed.), Geology and Ore Deposits of the Central Andes. Soc. Econ. Geol. Spec. Publ. 7, 155-193.

O'Neil, J. R. & Taylor, H. P., 1967. The oxygen isotope and cation exchange chemistry of feldspars. Am. Mineral. 52, 1414-1437.

Palyanova, G.A., 2020. Gold and silver minerals in sulfide ore. Geol. Ore Deposits 62, 383-406.

Petrella, L., Thébaud, N., Fougerouse, D., Tattitch, B., Martin, L., Turner, S., Suvorova, A., Gain, S., 2022. Nanoparticle suspensions from carbon-rich fluid make high-grade gold deposits. Nat. Comm. 13, 3795.

Pitcairn, I.K., 2013. Background concentrations of gold in different rock types. Appl. Earth Sci. 120, 31-38.

Pokrovski, G.S., Dubrovinsky, L.S., 2011. The S_3^- ion is stable in geological fluids at elevated temperatures and pressures. Science 331, 1052-1054.

Pokrovski, G.S., Akinfiev, N.N., Borisova, A.Y., Zotov, A.V., Kouzmanov, K., 2014. Gold speciation and transport in geological fluids: insights from experiments and physical-chemical modeling, in: Garofalo P, Ripley E (Eds.), Gold-Transporting Fluids in the Earth's Crust. Geol. Soc. London Spec. Publ. 402, 9-70.

Pokrovski, G.S., Dubessy, J., 2015. Stability and abundance of the trisulfur radical ion S3- in hydrothermal fluids. Earth Planet. Sci. Lett. 411, 298-309.

Pokrovski, G.S., Kokh, M.A., Guillaume, D., Borisova, A.Y., Gisquet, P., Hazemann, J.-L., Lahera, E., DelNet, W., Proux, O., Testemale, D., Haigis, V., Jonchière, R., Seitsonen, A.P., Ferlat, G., Vuilleumier, R., Saitta, A.M., Boiron, M.-C., Dubessy, J., 2015. Sulfur radical species form gold deposits on Earth. Proc. Nat. Acad. Sci. USA 112, 13484-13489.

Pokrovski, G.S., Kokh, M.A., Proux, O., Hazemann, J.L., Bazarkina, E.F., Testemale, D., Escoda, C., Boiron, M.C., Blanchard, M., Aigouy, T., Gouy, S., de Parseval, P., Thibaut, M., 2019. The nature and partitioning of invisible gold in the pyrite-fluid system. Ore Geol Rev. 109, 545-563.

Pokrovski, G. S., Escoda, C., Blanchard, M., Testemale, D., Hazemann, J.L., Gouy, S., Kokh, M. A., Boiron, M. C., Parseval F., Aigouy, T., et al., 2021. An arsenic-driven pump for invisible gold in hydrothermal systems. Geochem. Persp. Let. 17, 39-44.

Prokofiev, V.Y., Banks, D.A., Lobanov, K.V., Selektor, S.L., Milichko, V.A., Akinfiev, N. N., Borovikov, A.A., Lüders, V., Chicherov, M.V., 2020. Exceptional concentrations of gold nanoparticles in 1, 7 Ga fluid inclusions from the Kola superdeep Borehole, Northwest Russia. Sci. Re. 10, 1108.

Prudhomme, A., Baby, P., Robert, A., Brichau, S., Cuipa, E., Eude, A., Calderon, Y., O'Sullivan, P., 2019. Western thrusting and uplift in Northern Central Andes (Western peruvian margin), in: Horton, B.K., Folguera, A. (Eds.), Andean Tectonics. Elsevier, Amsterdam, pp. 299-331.

Quesnel, Q., Scheffer, C., Beaudoin, G., 2023. The light stable isotope (hydrogen, boron, carbon, nitrogen, oxygen, silicon, sulfur) composition of orogenic gold deposits. In: Huston, D., Gutzmer, J. (Eds.), Isotopes in economic geology, metallogenesis and exploration. Springer International Publishing, Cham, pp. 283-328.

Radtke, A.S., Scheiner, B.J., 1970. Studies of hydrothermal gold deposition (I). Carlin gold deposit, Nevada, the role of carbonaceous materials in gold deposition. Econ. Geol. 65, 87-102.

Rauchenstein-Martinek, K., Wagner, T., Wälle, M., Heinrich, C.A., Arlt, T., 2016. Chemical evolution of metamorphic fluids in the Central Alps, Switzerland: insight from LA-ICPMS analysis of fluid inclusions. Geofluids 16, 877-908.

Reich, M., Kesler, S.E., Utsunomiya, S., Palenik, C.S., Chryssoulis, S.L., Ewing, R., 2005. Solubility of gold in arsenian pyrite. Geochim. Cosmochim. Acta 69, 2781-2796.

Rosenbaum, G., Giles, D., Saxon, M., Betts, P.G., Weinberg, R.F., Duboz, C., 2005. Subduction of the Nazca Ridge and the Inca Plateau: insights into the formation of ore deposits in Peru. Earth Planet. Sci. Lett. 239, 18-32.

Rottier, B., Kouzmanov, K., W¨alle, M., Bendezú, R., Fontbot´e, L., 2016. Sulfide replacement processes revealed by textural and LA-ICP-MS trace element analyses: Example from the early mineralization stages at Cerro de Pasco. Peru. Econ. Geol. 111, 1347-1367.

Rottier, B., Kouzmanov, K., Casanova, V., Wälle, M., Fontboté, L., 2018. Cyclic dilution of magmatic metal-rich hypersaline fluids by magmatic low-salinity fluid: A major process generating the giant epithermal polymetallic deposit of Cerro de Pasco, Peru. Econ. Geol. 113, 825-856.

Rudnick R., Gao S., 2014. Composition of the Continental Crust, in: Holland, H.D., Turekian, K.K. (Eds.), Treatise on Geochemistry. second ed., Elsevier, Oxford, pp.1-51.

Saunders, J.A., 1990. Colloidal transport of gold and silica in epithermal precious-metal systems: Evidence from the Sleeper deposit, Nevada. Geology 18, 757-760.

Saunders, J.A., Hofstra, A.H., Goldfarb, R.J., Reed, M.H., 2014. Geochemistry of Hydrothermal Gold Deposits, in: Holland, H.D., Turekian, K.K. (Eds.), Treatise on Geochemistry. second ed., Elsevier, Oxford, pp. 383-424.

Saunders, J.E., Pearson, N.J., O′Reilly, S.Y., Griffin, W.L., 2018. Gold in the mantle: a global assessment of abundance and redistribution processes. Lithos 322, 376-391.

Scherrenberg, A. F., Kohn, B. P., Holcombe, R. J., Rosenbaum, G., 2016. Thermotectonic history of the Marañón Fold-Thrust Belt, Peru: Insights into mineralisation in an evolving orogen. Tectonophysics. 667, 16-36.

Schirra, M., Laurent, O., Zwyer, T., Driesner, T., Heinrich, C.A., 2022. Fluid evolution at the Batu Hijau porphyry Cu-Au deposit, Indonesia: hypogene sulfide precipitation from a single-phase aqueous magmatic fluid during chlorite-white-mica alteration. Econ. Geol. 117, 979-1012.

Shahzad, U., Mohammed, K.S., Tiwari, S., Nakonieczny, J., Nesterowicz, R., 2023. Connectedness between geopolitical risk, financial instability indices and precious metals markets: Novel findings from Russia Ukraine conflict perspective. Res. Policy, 80, 103190.

Sillitoe, R.H., Bonham Jr, H.F., 1990. Sediment-hosted gold deposits: Distal products of magmatic-hydrothermal systems. Geology 18, 157-161.

Sillitoe, R.H., Hedenquist, J.W., 2003. Linkages between volcanic tectonic settings, ore fluid compositions, and epithermal precious metals deposits. Soc. Econ. Geol. Spec. Publ. 10, 315-343.

Sillitoe, R.H., 2010. Porphyry copper systems. Econ. Geol. 105, 3-41.

Simmons, S.F., White, N., John, D., 2005. Geological characteristics of epithermal precious and base metal deposits. Econ. Geol.100th anniversary 1905-2005, 485-522.

Simmons, S.F., Brown, K.L., Tutolo, B.M., 2016. Hydrothermal transport of Ag, Au, Cu, Pb, Te, Zn, and other metals and metalloids in New Zealand geothermal systems: spatial patterns, fluid-mineral equilibria, and implications for epithermal mineralization. Econ. Geol. 111, 589-618.

Simmons, S.F., Tutolo, B.T., Barker, S.L.L., Goldfarb, R.J., Robert, F., 2020. Hydrothermal gold deposition in epithermal, carlin, and orogenic deposits. Soc. Econ. Geol. Spec. Publ. 23, 823-845.

Sillitoe, R.H., 2020. Gold deposit types: an overview. Soc. Econ. Geol. Spec. Publ. 23, 1-28.

Sykora, S., Cooke, D., Meffre S., Stephanov, A., Gardner, K., Scott, R., Selley, D., Harris, A., 2018. Evolution of pyrite trace element compositions from porphyry-style and epithermal conditions at the Lihir gold deposit: Implications for ore genesis and mineral processing. Econ. Geol. 113, 193-208.

Tan, Q. P., Xia, Y., Xie, Z. J., Yan, J., 2015. Migration paths and precipitation mechanisms of ore-forming fluids at the Shuiyindong Carlin-type gold deposit, Guizhou, China. Ore Geol. Rev. 69, 140-156.

Tanner, D., Henley, R. W., Mavrogenes, J. A., Holden, P., 2016. Sulfur isotope and trace element systematics of zoned pyrite crystals from the El Indio Au-Cu-Ag deposit, Chile. Contrib. Mineral Petrol. 171, 1-17.

Tomkins, A.G., 2010. Windows of metamorphic sulfur liberation in the crust: Implications for gold deposit genesis. Geochim. et Cosmochim. Acta 74, 3246-3259.

USGS, 2023. Mineral commodity summaries of the US Geological Survey.https://www.usgs.gov/publications/mineral-commodity-summaries-2023.

Vallance, J., Cathelineau, M., Boiron, M., Fourcade, S., Shepherd, T., Naden, J., 2003. Fluid-rock interactions and the role of late Hercynian aplite intrusion in the genesis of the Castromil gold deposit, Northern Portugal. Chem. Geol. 194, 201-224.

Vallance, J., Galdos, R., Balboa, M., Berna B., Cabrera O., Huisa F., Baya C., Van De Vyver C., Viveen W., Béziat D., Salvi, S., Brusset, S., Baby, P., Pokrovski G.S., 2024. Combined effect of organic carbon and arsenic on the formation of sediment-hosted gold deposits: a case study of the Shahuindo epithermal deposit, Peru. Econ. Geol. 119, 85-112.

Van de Vyver C., 2021. Le rôle des systèmes pétroliers dans les minéralisations des bassins sédimentaires en contexte orogénique (Nord Pérou). Université de Lorraine, Lorraine, France, 51 p. (Unpublished master thesis).

Vaughan, J., Nelson, C.E., Polanco, J., Garcia, V., Macassi, A., Garrido, G., 2020. The Pueblo Viejo Au-Ag-Cu-(Zn) deposit, Dominican Republic. Soc. Econ. Geol. Spec. Publ. 23, 415-430.

Warr, L.N., 2021. IMA-CNMNC approved mineral symbols. Mineral. Mag. 85, 291-320.

White, N.C., Hedenquist, J.W., 1995. Epithermal gold deposits: styles, characteristics and exploration. Soc. Econ. Geol. Newsletter. 23, 1-13.

Vho, A., Lanari, P., Rubatto, D., 2019. An internally-consistent database for oxygen isotope fractionation between minerals. J. Petrol. 60, 2101-2129.

Wilkinson, J.J., Simmons, S.F., Stoffell, B., 2013. How metalliferous brines line Mexican epithermal veins with silver. Sci. Rep. 3, 2057.

Yakubchuk, A., 2023. Russian gold mining: 1991 to 2021 and beyond. Ore Geol. Rev. 153, 105287.

Zhai, W., Sun, X., Sun, W., Su, L., He, X., Wu, Y., 2009. Geology, geochemistry, and genesis of Axi: a Paleozoic low-sulfidation type epithermal gold deposit in Xinjiang, China. Ore Geol. Rev. 36, 265-281.

Chapter II. COMBINED EFFECT OF ORGANIC CARBON AND ARSENIC ON THE FORMATION OF SEDIMENT-HOSTED GOLD DEPOSITS: A CASE STUDY OF THE SHAHUINDO EPITHERMAL DEPOSIT, PERU

Chapter II

This chapter presents a published article in the journal Economic Geology (Vallance J., Galdos R., Balboa M., Berna B., Cabrera O., Huisa F., Baya C., Van De Vyver C., Viveen W., Béziat D., Salvi S., Brusset, P., Baby P., and Pokrovski G. S., 2024. "*Combined effect of organic carbon and arsenic on the formation of sediment-hosted gold deposits: a case study of the Shahuindo epithermal deposit, Peru*". Econ. Geol. 119, 85–112. https://doi.org/10.5382/econgeo.5040). Here we present a brief introduction to contextualize the article in the framework of the thesis; followed by the full text of this article.

Introduction

In this chapter, we present an integrated structural, mineralogical, geochemical, and modeling study of the enigmatic relationships between gold, arsenic and organic carbon in sedimentary rocks. These rocks host the epithermal Shahuindo deposit, our first case study. The structural analysis revealed that gold deposition occurred in structural and stratigraphic traps, very similar to those found in petroleum systems. Our detailed mineralogical and geochemical analyses of ore and surrounding rocks allowed us to constrain the major events of gold deposition, the distribution of gold in the deposit, and the sources of gold and other metals. These novel data are further supported by thermodynamic and chemical speciation modeling of fluid-rock interactions.

Our findings have significant implications for genetic formation models of sediment-hosted gold deposits. In particular, novel thermodynamic modeling results reveal that the interactions between the hydrothermal fluid and the organic carbon from sedimentary rocks in the Shahuindo context strongly enhance gold solubility. Furthermore, the geometry and distribution of the orebodies present analogies to both "classic" magmatic hydrothermal deposits and petroleum systems. This similarity highlights the importance of using petroleum exploration tools (such as balanced cross sections and basin analysis) when they are combined with numerical modeling of fluid-rock interactions and detailed geochemical analyses for fingerprint trace elements for mineral exploration.

Combined Effect of Organic Carbon and Arsenic on the Formation of Sediment-Hosted Gold Deposits: A Case Study of the Shahuindo Epithermal Deposit, Peru

Jean Vallance,[1,2,†] Renzo Galdos,[1] Macneill Balboa,[1] Brigitte Berna,[1] Omar Cabrera,[3] Freddy Huisa,[3] Camille Baya,[4] Caroline Van De Vyver,[4] Willem Viveen,[5] Didier Béziat,[4] Stefano Salvi,[4] Stéphane Brusset,[4] Patrice Baby,[4,5] and Gleb S. Pokrovski[4]

[1]*Grupo de investigación en Geología de Yacimientos, Especialidad de Ingeniería Geológica, Departamento de Ingeniería, Pontificia Universidad Católica del Perú, avenida Universitaria 1801, San Miguel, Lima 15088, Peru*

[2]*Thin Section Lab, 1223 Rue du Bois la ville, F-54200 Toul, France*

[3]*Pan American Silver Peru S.A.C., Av. de la Floresta 497, Lima 15037, Peru*

[4]*Géosciences Environnement Toulouse, Université Toulouse III - Paul Sabatier, Centre National de la Recheche Scientifique (CNRS), Institut de Recherche pour le Développement (IRD), Centre National d'Etudes Spatiales (CNES), Observatoire Midi Pyrénées (OMP), 14 avenue Edouard Belin, F-31400 Toulouse, France*

[5]*Grupo de investigación en Geología Sedimentaria, Especialidad de Ingeniería Geológica, Departamento de Ingeniería, Pontificia Universidad Católica del Perú, avenida Universitaria 1801, San Miguel, Lima 15088, Peru*

Abstract

Sediment-hosted gold deposits represent a significant portion of the world's gold resources. They are characterized by the ubiquitous presence of organic carbon (C_{org}; or its metamorphosed product, graphite) and the systematic occurrence of invisible gold-bearing arsenian pyrite. Yet the role played by these features on ore formation and the distribution of gold remains a long-standing debate. Here, we attempt to clarify this question via an integrated structural, mineralogical, geochemical, and modeling study of the Shahuindo deposit in northern Peru, representative of an epithermal gold deposit contained in a sedimentary basin. The Shahuindo deposit is hosted within Lower Cretaceous fluvio-deltaic carbon-bearing sandstone, siltstone, and black shale of the Marañón fold-and-thrust belt, where intrusions of Miocene age are also exposed. The emplacement of the auriferous orebodies is constrained by structural (thrust faults, transverse faults) as well as lithological (intrusion contacts, permeable layers, anticlinal hinge in sandstone) features. The defined gold reserves (59 tons; t) are located in the supergene zone in the form of native gold grains. However, a primary mineralization, underneath the oxidized zone, occurs in the form of invisible gold in arsenian pyrite and arsenopyrite. Here, four subsequent pyrite generations were identified—namely, pyI, pyII, pyIII, and pyIV. PyI has mean Au concentrations of 0.3 ppm, contains arsenic that is not detectable, and is enriched in V, Co, Ni, Zn, Ag, and Pb compared to the other pyrite generations. This trace element distribution suggests a diagenetic origin in an anoxic to euxinic sedimentary basin for pyI. Pyrite II and pyIV have comparable mean Au (1.1 and 0.7 ppm, respectively) and As (2.4 and 2.9 wt %, respectively) concentrations and precipitated under conditions evolving from lower (pyrrhotite, chalcopyrite, sphalerite) to higher (enargite, digenite, chalcocite) sulfidation, respectively. The pyIII generation is the major gold event in the primary mineralization, with pyrite reaching 110 ppm Au (mean ~7 ppm) and 5.6 wt % As (mean ~1.8 wt %), while coeval arsenopyrite attains 460 ppm Au. Pyrite III is also enriched in other trace elements such as Se, Ge, Mo, In, Ga, and Bi compared to the other pyrite generations, which is indicative of a magmatic source. Bulk analyses of the surrounding unmineralized rocks show only parts per billion levels of Au and less than 25 ppm As. These data, combined with mass balance considerations, demonstrate that the sedimentary rocks could not be the sole source of gold, as they could only contribute a minor portion of arsenic and sulfur (and iron) to the deposit. Conversely, fluids exsolved from a pluton crystallizing at depth likely provided the great part of the gold endowment. Equilibrium thermodynamics simulations, using geochemical constraints established in this study, demonstrate that interaction between Au-As-S-Fe–bearing fluids and organic carbon-bearing rocks strongly enhanced the fluid ability to transport gold by maximizing its solubility as Au^I hydrosulfide complexes via a combined increase of pH and aqueous sulfide concentration. This finding challenges the traditional qualitative view of organic matter acting exclusively as a reducing agent for Au^I that should promote gold deposition in its native state (Au^0) rather than enhance its solubility in the fluid. Our results have significant implications for the exploration of carbonaceous sedimentary environments. Such settings may provide a very effective mechanism for focusing gold transport. Subsequent scavenging of Au^I from solution in a chemically bound form is promoted by the precipitation of arsenian pyrite in permeable structural and lithologic traps, bound by more impermeable units, similar to what occurs in petroleum systems. Our integrated study underlines the important potential of sedimentary C_{org}-bearing rocks in the formation and distribution of gold and associated metal resources.

[†]Corresponding author: e-mail, jeanvallance@hotmail.com

46

Introduction

Sediment-hosted deposits represent an important part of gold resources on Earth. Examples of mineralization in siliciclastic sedimentary rocks that contain gold as the main product or by-product can be found in at least six (orogenic, porphyry, epithermal, Carlin-type, reduced intrusion-related, and volcanogenic massive sulfide) out of the 11 gold deposit classes proposed by Sillitoe (2020). Notwithstanding the classification and exact source of gold (e.g., magmatic, metamorphic, sedimentary, or biogenic), the most characteristic features of sediment-hosted gold deposits are the systematic presence of organic carbon (C_{org}, i.e., bitumen, pyrobitumen, or their metamorphosed product, graphite) and arsenian pyrite (e.g., Cline et al., 2005; Large et al., 2009; Muntean et al., 2011; Gaboury, 2013; Gregory et al., 2016; Percival et al., 2018; Xie et al., 2018). The respective roles of these ubiquitous features as a possible gold source and their impact on the processes of metal concentration and/or remobilization are long-standing subjects of debate. Some authors consider the carbonaceous sediments to be both the source and trap for mineralization, which was produced by hydrothermal processes at local to regional scale within the crust (e.g., Phillips et al., 1987; Large et al., 2011; Hofstra and Cline, 2000). Other studies defend a magmatic source and vapor-phase transport of gold, with carbonaceous sediments acting exclusively as a metal trap (e.g., Muntean et al., 2011; Large et al., 2016; Muntean and Cline, 2018).

There exist multiple instances of close spatial and temporal associations of gold with organic matter, such as in the renowned Witwatersrand basin, where the precipitation of native gold and uraninite was suggested to have occurred by reduction at the interface between a hydrothermal sulfide-bearing fluid and hydrocarbon liquids or solids (Disnar and Sureau, 1990; Robb and Meyer, 1995; Drennan et al., 1999; Drennan and Robb, 2006; Fuchs et al., 2016). The close spatial association of gold and carbonaceous-bearing formations (including hydrocarbons) in the Carlin trend deposits has triggered the foundation for the carbonaceous trap model (Radtke and Scheiner, 1970). However, more recent work on Carlin deposits has shown that organic carbon contents and ore grades do not correlate, thus suggesting that C_{org} likely played only a minor role (if any) in gold concentration and precipitation, compared to the major gold precipitation mechanism through sulfidation of ferroan carbonates (Hofstra and Cline, 2000; Cline et al., 2005; Kusebauch et al., 2019; Muntean, 2020). Gold transport and concentration are known to result from a complex interplay of different parameters (temperature [T], pressure [P], pH, redox, S content) of the fluid during its evolution and interactions with the host rock (e.g., Seward, 1973; Heinrich, 2005; Pokrovski et al., 2014). However, quantification of the respective contributions of these parameters is lacking for sedimentary deposit settings. It also remains unclear whether gold may be transported to a significant degree by the liquid hydrocarbon phases as opposed to the aqueous phase. Rare experimental data on a wide range of crude oil samples at temperatures of 150° to 300°C show that gold solubilities are too low (e.g., <50 ppb; Migdisov et al., 2017) to allow for massive gold transport. Indeed, these low values contrast with thermodynamic predictions, multiple

experimental studies, and extensive data from natural fluid inclusions, all of which demonstrate that an aqueous S-rich epithermal fluid (>0.1 wt % S), at equivalent temperatures, is capable of dissolving tens to hundreds of parts per million of Au, at favorable pH and redox conditions (e.g., Seward, 1973; Heinrich, 2005; Kouzmanov and Pokrovski, 2012; Pokrovski et al., 2014, 2022a; references therein). Thus, our current view on the mechanisms of formation of sedimentary gold deposits lacks a quantitative physicochemical understanding of the interactions that take place between a fluid and the rocks it flows through. This understanding is now possible by coupling the robust up-to-date knowledge of the chemical speciation and solubility of Au in aqueous fluids with a well-constrained geologic framework based on detailed studies of the ores and their host rocks.

Another serious limitation in understanding the transport and deposition of gold in sedimentary deposits is the role of arsenic, since arsenian pyrite and arsenopyrite are systematically enriched in invisible gold in these settings (e.g., Cathelineau et al., 1989; Reich et al., 2005; Deditius et al., 2014). Even though the redox and chemical state of gold and its incorporation mechanisms in these sulfides remain subjects of debate (e.g., Arehart et al., 1993; Pokrovski et al., 2019; references therein), recent experimental data attest to an enhanced Au partitioning from a hydrothermal fluid to As-bearing pyrite with increasing As content in the system (e.g., Kusebauch et al., 2019; Pokrovski et al., 2019, 2021). This partitioning data, together with the recent spectroscopic knowledge of the structural and redox state of invisible Au in sulfarsenides (e.g., Pokrovski et al., 2021; references therein) as well as improved thermodynamic and structural models of the incorporation of As into pyrite (e.g., Xing et al., 2019; Manceau et al., 2020), allow at present more quantitative modeling of the arsenic-gold relationships during fluid-rock interaction.

In this study, we attempt to unravel fundamental questions of the roles played by arsenic and organic carbon in the formation of sediment-hosted gold deposits. Here, we explore the Au-As-C_{org} relationships using, as a case study, the Shahuindo gold deposit in northern Peru, characterized by the presence of invisible gold associated with arsenian pyrite and organic matter in a sedimentary basin (Defilippi et al., 2016; Vallance et al., 2018). To interpret these features, we have combined detailed structural investigations of the formation and evolution of this sedimentary sequence with in situ microanalyses of ore and gangue minerals, followed by physicochemical modeling of fluid-mineral-organic carbon interactions. Our results provide new constraints on the controls exerted both by arsenic and C_{org} on gold transport and deposition. Our findings may be applicable to many other sediment-hosted deposits and thus contribute to improving exploration strategies for this important resource of gold and associated metals.

Geologic Background and Samples

Regional geology

The thousand-kilometer-long NNW-SSE–trending Marañón fold-and-thrust belt of central to northern Peru hosts a variety of ore deposits, including Cu-Mo-Au porphyry (e.g., Toromocho), polymetallic and Cu-Fe skarn (e.g., Antamina), and epithermal precious and base metals deposits (e.g.,

Yanacocha and Cerro de Pasco), genetically linked to Oligocene to Miocene subduction-related calc-alkaline magmatism (Noble and McKee, 1999; Bissig et al., 2008; Scherrenberg et al., 2016; Fontboté, 2018). This belt hosts, respectively, 40, 30, 75, and 65% of the Au, Cu, Zn, and Ag production of the country (Noble and McKee, 1999; Scherrenberg et al., 2016; Fontboté, 2018). In the study area, the rocks building the Marañón belt correspond to fluvio-deltaic and marine sediments of Late Jurassic to Late Cretaceous age, deposited in a back-arc basin on a basement of Precambrian to Lower Ordovician metamorphic rocks known as the Marañón Complex (Mégard, 1984; Benavides-Cáceres, 1999; Chew et al., 2007; Eude et al., 2015; Scherrenberg et al., 2016). The Marañón belt is truncated by a middle Eocene regional unconformity capped by volcanic and volcaniclastic sediments of the late

Eocene to Middle Miocene Calipuy plateau basin to the west (Noble et al., 1990; Prudhomme et al., 2019) and the Cajabamba basin fluvial and lacustrine sediments to the east (Figs. 1, 2). The base of the Cajabamba deposits has recently been dated at ~23 Ma (Prudhomme et al., 2019). Therefore, the belt is considered to have developed during an early period of the Andean orogeny (traditionally known as Peruvian and Incaic phases; Noble et al., 1979; Mégard, 1984), between the Late Cretaceous and the middle Eocene. The Marañón belt is a thin-skinned thrust system related to a detachment located at the base of the Late Jurassic black shale and sandstone rocks of the Chicama Formation and composed by a succession of tight imbricates and associated folds, reflecting a significant amount of horizontal shortening. The post-Incaic orogenic period is characterized by the development of the
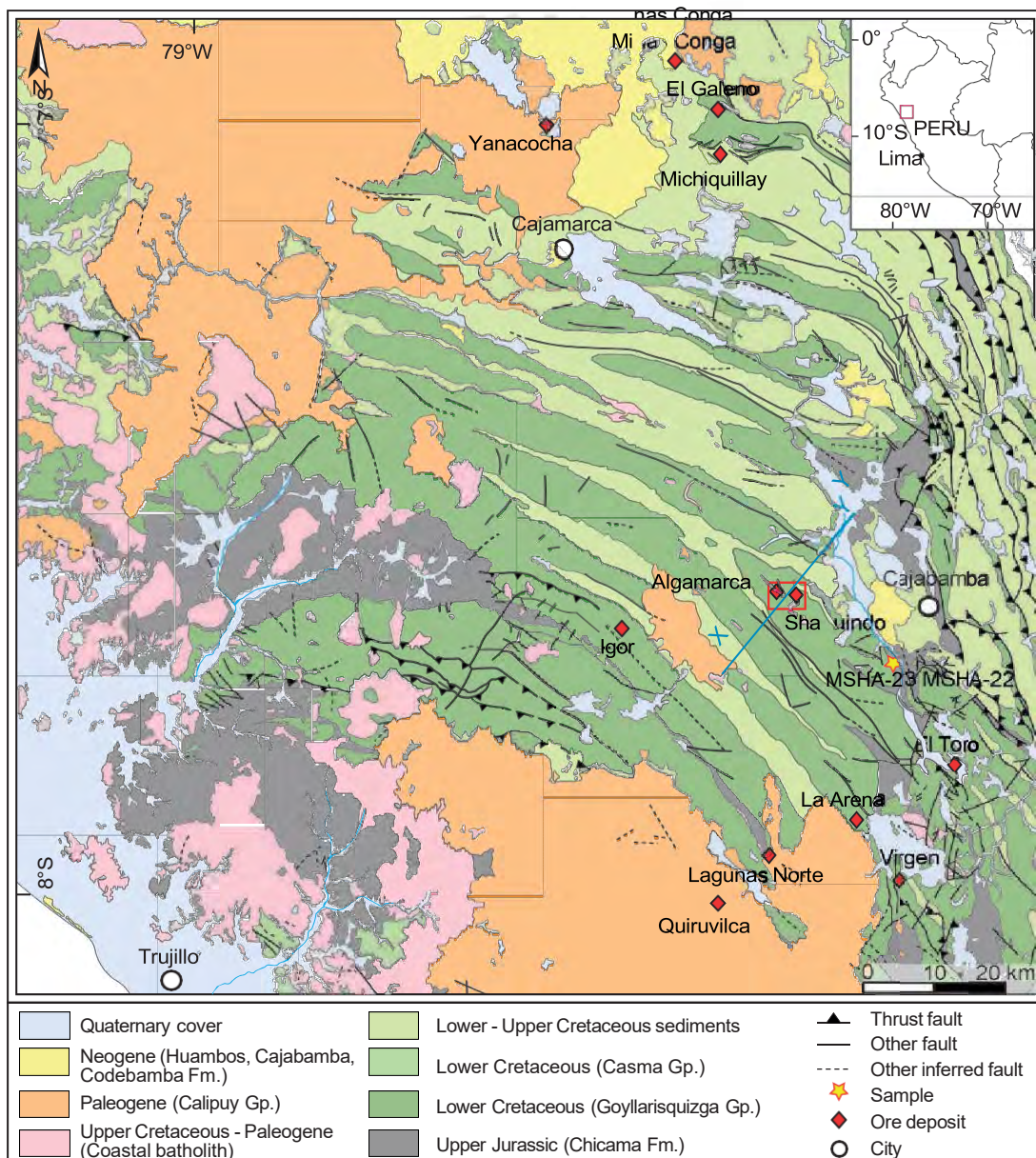
Fig. 1. Geologic map of the Marañón fold-and-thrust belt in northern Peru showing the location of major deposit and projects and the X-Y cross section shown in Figure 4 (modified from Eude, 2014).

48

VALLANCE ET AL.
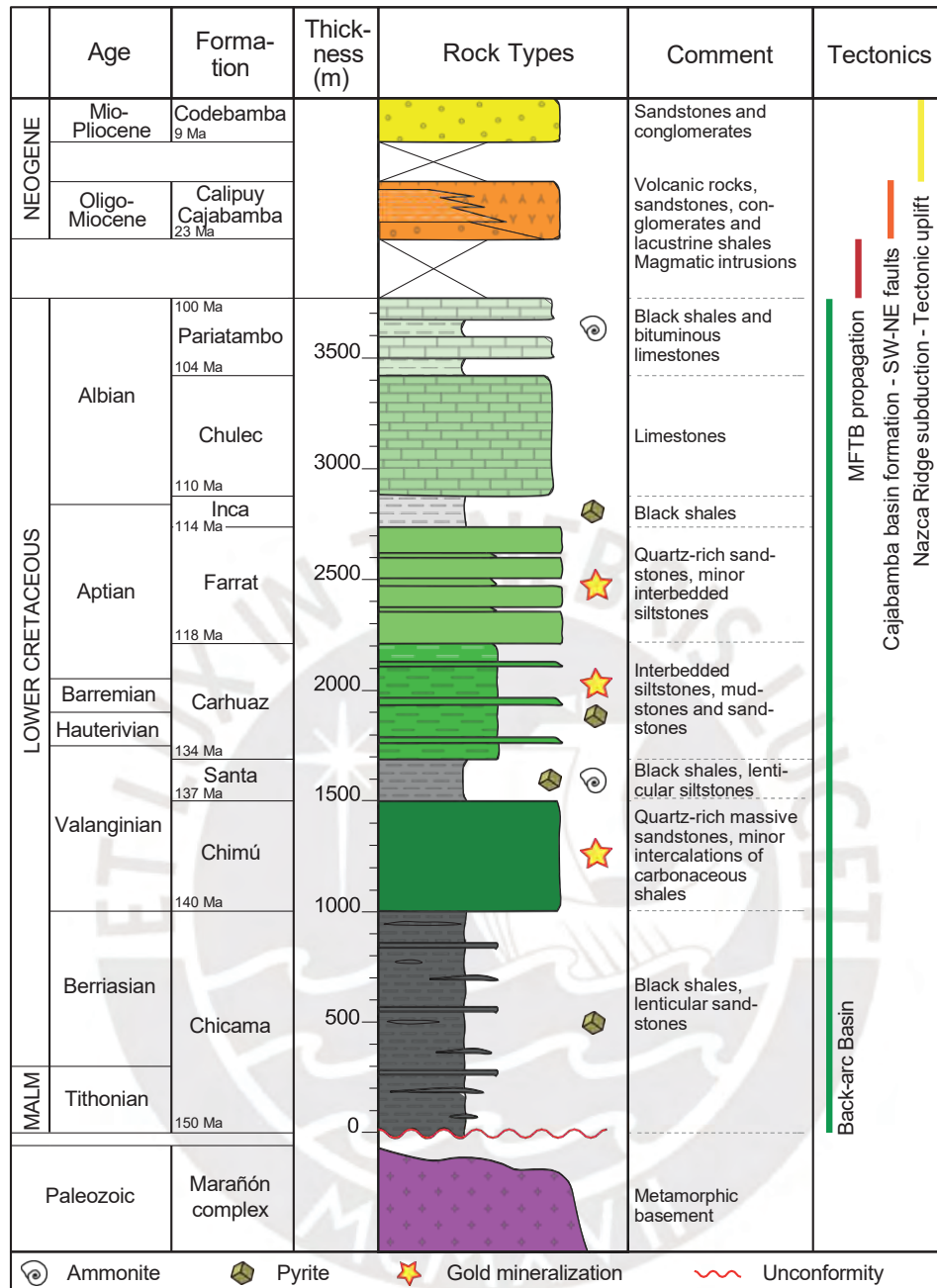
Fig. 2. Stratigraphical column of the Marañón fold-and-thrust belt in the study area (compiled and revised from Jaillard and Jacay, 1989; Defilippi et al., 2012, 2016; Eude, 2014; Prudhomme et al., 2019). MFTB = Marañón fold-and-thrust belt.

Calipuy and Cajabamba basins above the middle Eocene regional unconformity and the intrusion of igneous stocks in the subjacent folded and thrusted Cretaceous sediments (Benavides-Cáceres, 1999; Scherrenberg et al., 2016; Prudhomme et al., 2019; Fig. 1). These relatively weakly deformed basins are associated with normal faulting (Bellier et al., 1989; Prudhomme et al., 2019) and likely have recorded the postorogenic period of tectonic quiescence and relaxation. From the Late Miocene, the Marañón belt and the Calipuy and Cajabamba basins were uplifted and exhumed as a result of the Nazca Ridge subduction (Hampel, 2002; Rosenbaum et al., 2005).

Deposit geology and host-rock lithology

The oldest rocks exposed in the area of the Shahuindo deposit are marine graphite-bearing pyritic shale, silt, and sandstone, with intercalations of coal seams of the Late Jurassic Chicama Formation of ~1,000 m in thickness (Navarro Colque et al., 2010; Figs. 2, 3). The shale and coal layers at the base of the Chicama Formation, at the contact with the Paleozoic basement, are considered to be the detachment plane common to all thrusts in the Marañón belt (Mégard, 1984). The Chicama Formation is overlain by siliciclastic fluvio-deltaic and shallow-marine sequences of the Lower Cretaceous Goyllarisquizga
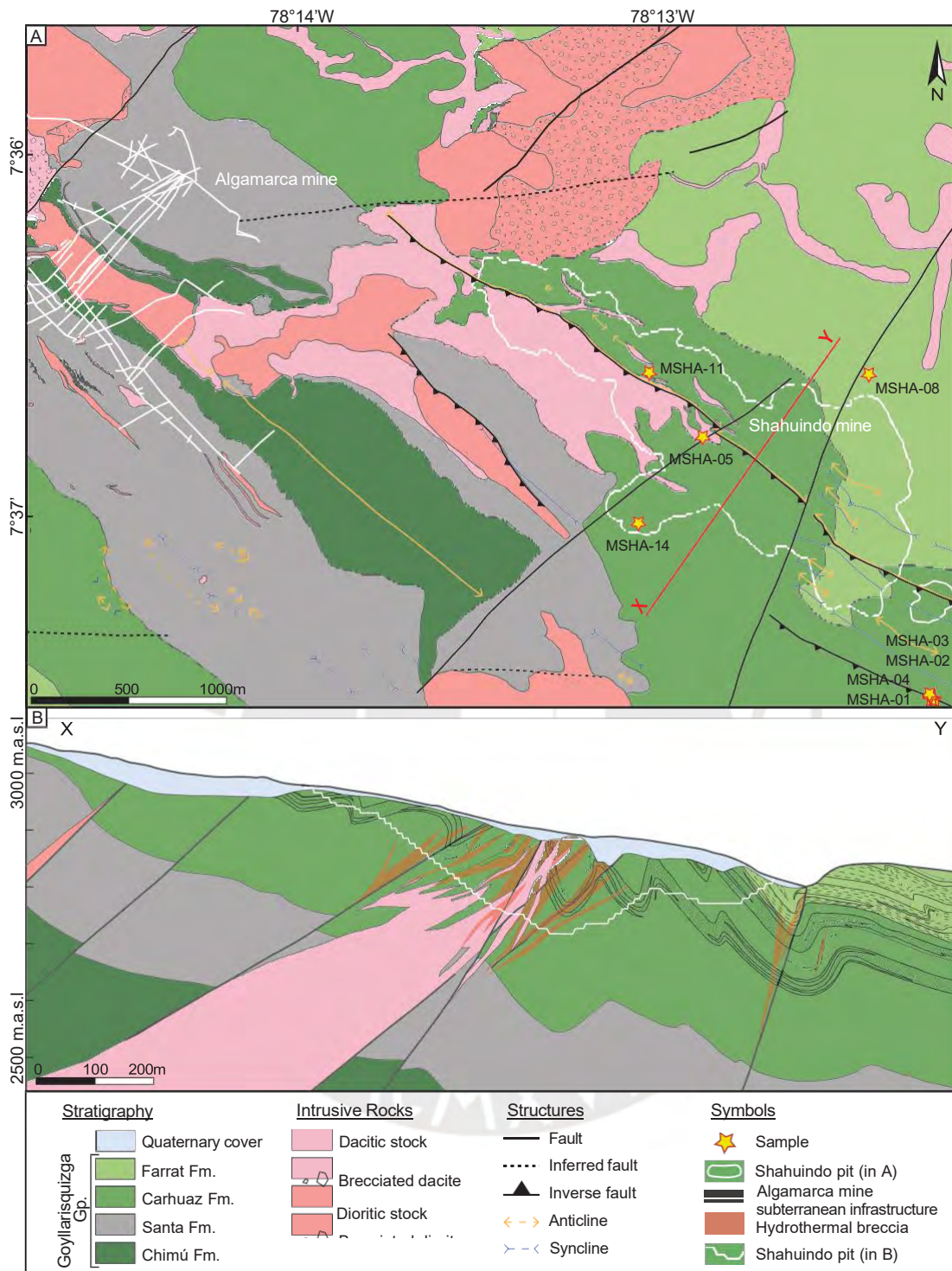
Fig. 3. A. Geologic map of the study area showing the location of the Shahuindo open pit, the former Algamarca mine, and the X-Y cross section shown in B (modified from Defilippi et al., 2016). B. Southwest-northeast cross section of the central part of the Shahuindo deposit (modified from Defilippi et al., 2016). m.a.s.l. = meters above sea level.

Group. The base of the Goyllarisquizga Group comprises ~500 m of fluvial fine- to medium-grained (63–250 and 250–500 μm, respectively) sandstones with occasional coal seams of the Chimú Formation (Jacay, 2005; Navarro Colque et al., 2010). The deposit lithology is described in detail by Defilippi et al. (2016). Briefly, the Chimú Formation forms the core of

the Algamarca anticline, which defines the highest elevation of the Shahuindo area (Fig. 3). The Santa Formation lies on the Chimú Formation and is composed of pyritic black shales with local intercalations of limestone. The Santa Formation is strongly deformed and therefore precludes more accurate thickness estimations, which actually range between 150 and

50

200 m in the mine area. The Santa Formation is covered by ~500 m of gray siltstone interbedded with fine- to medium-grained sandstone, pyritic black shale, and rare bioclastic limestone named the Carhuaz Formation. The uppermost formation of the Goyllarisquizga Group, named the Far- rat Formation, is of ~500 m total thickness and includes up to 2-m-thick beds of yellow to white fine- to coarse-grained sandstone and quartzite with minor interbedded siltstone. The Goyllarisquizga sedimentary sequence crops out in the cores of the fault propagation anticlines, northwest-southeast oriented and segmented by northeast-southwest strike-slip and normal faults apparently posterior to the Marañón belt. These northeast-southwest faults segment the Shahuindo deposit into three blocks (western, central, and eastern; see Fig. 3). The eastern and central blocks were down-dropped by hundreds of meters, and the western block is likely to rep-resent the deepest part of the deposit (R.W. Hodder, unpub. report, 2010). Stocks of andesitic (also locally named "diorite porphyry") and later dacitic (or quartz-feldspar porphyry) intrusions of Oligo-Miocene age crop out and are inter-sected by diamond drilling mostly in the western, deeper part of the deposit (Defilippi et al., 2016). Their emplacement as elongated bodies was generally controlled by anticline axes, thrust faults, and transverse northeast-southwest faults

(Fig. 3). Longitudinal fractures in the outer arcs of the hinge zones of the competent unit, like Farrat sandstone, axial planes of anticline (mainly in the San José anticline), thrust faults, transverse faults, intrusion contacts, and permeable layers in sandstone, are all presumably preferred sites for emplacement of mineralization as will be confirmed by the structural analysis in this study (Fig. 4).

Mineralization

The Shahuindo deposit comprises a zone of primary sulfide ore and an oxidized zone of supergene origin. In the latter, gold is found as native metal particles of <5 µm in size, asso-ciated with goethite (FeOOH), hematite (Fe_2O_3), jarosite ($KFe_3(SO_4)_2(OH)_6$), and scorodite ($FeAsO_4 \cdot 2H_2O$). Gold reserves in the supergene zone are of 59 t Au at 0.46 g/t, and extraction is currently conducted by heap-leach process (C. Alvarez, pers. commun., 2019). The primary sulfide miner-alization does not crop out. Gold reserve estimates for this zone are not currently available, because exploration has not yet been completed. Pyrite is the main sulfide mineral hosting invisible gold in the primary ore, in addition to minor amounts of arsenopyrite, chalcopyrite, galena, sphalerite, tetrahedrite, and stibnite. This assemblage points to an epithermal, so-called intermediate-sulfidation type of deposit for Shahuindo,

Codebamba	Chulec	Carhuaz	Chicama
Calipuy/Cajabamba	Inca	Santa	Marañón complex
Pariatambo	Farrat	Chimú	Dacitic/dioritic intrusions
Thrust fault			

51

Fig. 4. A. A 2017 view of the Algamarca anticline to the left and the Shahuindo open pit to the right. B. Structural southwest to northeast cross section across the Marañón fold-and-thrust belt reconstructed in this study.

according to Defilippi et al. (2016). Gold grades in the sulfide ore are typically <2 g/t; however, higher grades, up to 33 g/t, were locally measured (R.W. Hodder, unpub. report, 2010; Defilippi et al., 2016). Within the area of endogenic mineralization, the distribution of gold reflects both primary and secondary permeability. The former is induced by favorable sedimentary facies, while the latter occurs because of faults, breccia, and intrusion contacts, with notable paucity of veins and open-space-filling features. In the sedimentary rocks, gold occurs preferentially in the coarse-grained sandstone that is capped by less permeable horizons, and it is hosted within pyrite. Less permeable, graphite-bearing, fine-grained pyrite-rich shale horizons rarely show gold grades in excess of 0.2 g/t, except in the proximity of faults or breccia related to extended fracture networks. In the shale, gold is also spatially associated with pyrite, even though the bulk pyrite content in the rock does not display a direct correlation with gold grades. This can be attributed to the diverse occurrences and origins of pyrite, including fine-grained disseminations of diagenetic origin and/or partial replacement of graphitized vegetal fragments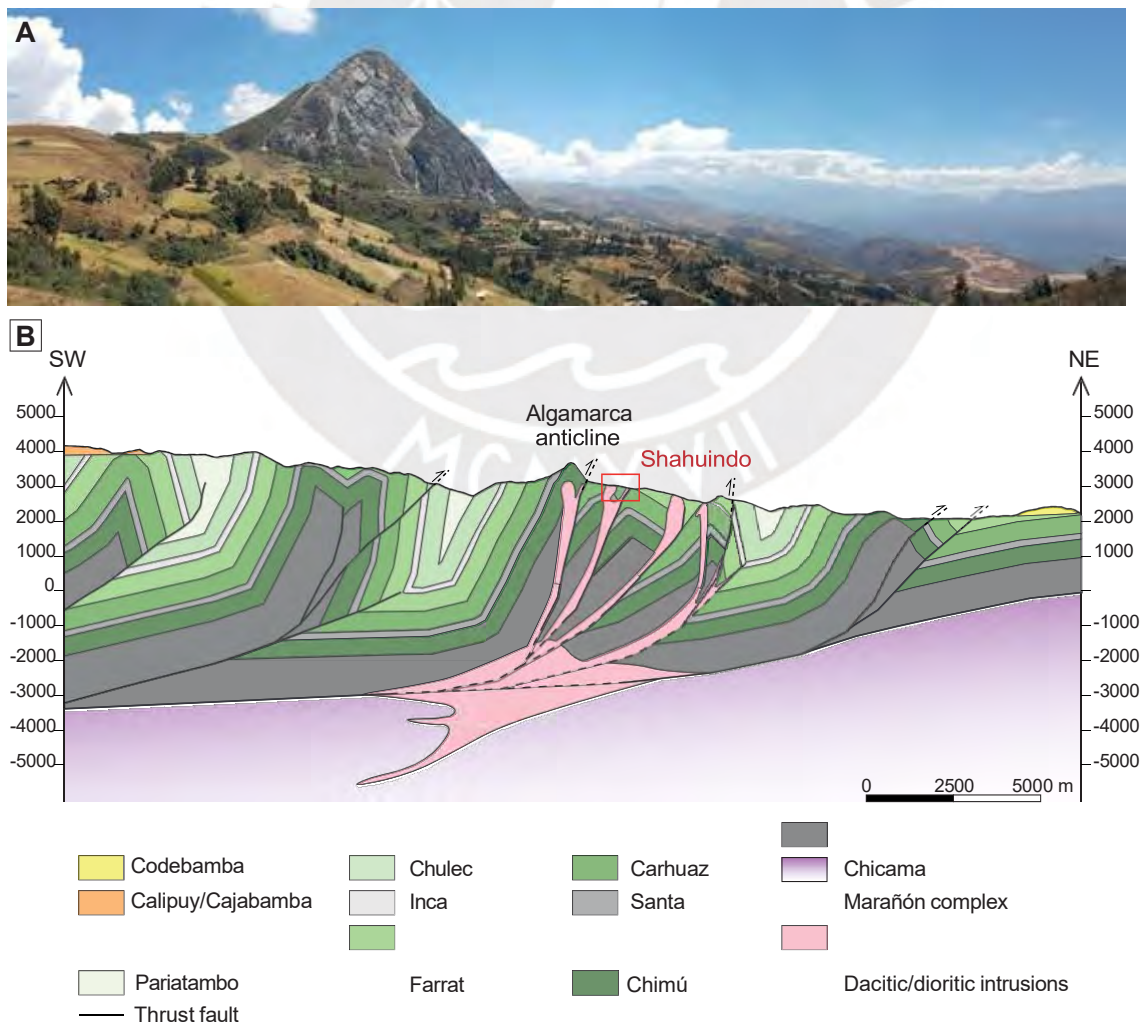 and bioclasts in shale and fine-grained sandstone horizons (Fig. 5A, B), euhedral pyritohedra in medium-grained sandstone (Fig. 5C), bioclast replacement in the rare limestone beds, and filling in <1-cm-thick veinlets (Fig. 5D). Massive coarse-grained pyrite bodies formed locally at the contact between the intrusion and sedimentary host rock are surrounded by a gray-beige silicification halo (Fig. 5E). These pyrite bodies are weakly mineralized, with grades <0.5 g/t Au. The highest gold grades (up to 33 g/t) were found in polyphasic breccia in thrust and transverse faults, within sedimentary rocks.

Multiple porphyritic igneous bodies of andesitic to dacitic composition have intruded the Cretaceous sedimentary rocks in the Shahuindo deposit and the adjacent Algamarca mine area (Fig. 3). Field observations, drill core data, and a preliminary geochronological study (S. Bussey and E. Nelson, unpub. report, 2011, cited by Defilippi et al., 2012) suggest that the oldest intrusions have andesitic composition. Zircon U-Pb dating yielded an age of ~26 Ma, while the youngest dacitic intrusions were dated at ~16 Ma (no error margins reported). In the intrusive rocks, gold mineralization is scarce, only occurring in <5-cm-thick veins and locally in stockworks and breccia cement (Fig. 5F), as well as disseminations in strongly sericitized andesite and dacite. The occurrence of gold in both andesitic and dacitic intrusions provides therefore an upper age limit of 16 Ma for the mineralization at Shahuindo (Defilippi et al., 2016; Vallance et al., 2018; this study). This age is consistent with a K-Ar age value of 15.5 ± 0.4 Ma reported by Noble and McKee (1999) from hydrothermal muscovite bordering a polymetallic vein that crosscuts a quartz monzonite porphyry at Algamarca. These results confirm a value of 16 to 15 Ma for the age of the mineralization at Shahuindo, assuming that both deposits belong to the same magmatic-hydrothermal system.

Methods

Construction of a regional structural cross section

To better understand the stratigraphic and structural architecture of the Marañon fold-and-thrust belt and the tectonic framework of the Shahuindo Au deposit, a regional structural cross section (see Fig. 1 for location) has been constructed following the classic thrust-tectonics concepts (Dahlstrom, 1969; Boyer and Elliott, 1982; Elliott, 1983) and using the structural geology modeling MOVE software (Petroleum Experts, 2022). The structural construction results from the integration of surface data, as structural dips, faults, and stratigraphic contacts in line with the stratigraphic synthesis presented in Figure 2. Surface data were obtained from our own field surveys and 1:100,000 geologic maps available from the Instituto Nacional Geológico, Minero y Metalúrgico del Perú (INGEMMET). In order to validate our construction, the final cross section has been forward modeled based on the MOVE flexural-slip algorithm and assuming constant bed length and thickness. The results are presented in Figure 4.

Analytical techniques

Thirty polished sections from sulfide ore sampled in drill cores were examined using a LEICA DM2500 optical microscope. A selection of key samples was examined on an environmental scanning electron microscope (SEM) Quanta 650 FEI, equipped with an EDAX-Octane Pro energy dispersive spectrometry (EDS) microanalysis system at Centro de Caracterización de Materiales of the Pontifical Catholic University of Peru (CAM-PUCP). Operating conditions were 20-kV accelerating voltage and 5-nA current in backscattered electron (BSE) mode. Bulk contents of carbon, sulfur, other major elements, and a suite of 36 trace elements from 10 host-rock and mineralized samples were determined at ALS Loughrea-Geochemistry, Ireland, and Lima, Peru. Analytical instruments, digestion methods, numerical results, and their corresponding detection limits are given in the Appendix (Table A1).

Major elements (>0.1 wt %) in sulfide minerals were quantified using a CAMECA SXFive electron probe microanalyzer (EPMA) equipped with five wavelength dispersive spectrometers at the Raimond Castaing Microanalysis Centre of the University of Toulouse, France. Analyses were conducted at 25-kV acceleration voltage and 20-nA electron beam current, with a beam diameter of <2 μm and 10 s of counting time at the fluorescence peak and 5 s at the left- and right-side background around the peak. The elements analyzed were S (Kα), As (Lβ), Au (Lα), Fe (Kα), Cu (Kα), and Sb (Lα). Mineral standards included natural chalcopyrite for calibration of Fe, Cu, and S, arsenopyrite for As, and native metals for Au and Sb. The detection limits for each element and the obtained numerical data are reported in Table 1 and Appendix Table A2.

Laser ablation-inductively coupled plasma-mass spectrometry (LA-ICP-MS) analyses of 21 trace elements in sulfide minerals (^{51}V, ^{57}Fe, ^{59}Co, ^{60}Ni, ^{63}Cu, ^{66}Zn, ^{71}Ga, ^{74}Ge, ^{75}As, ^{77}Se, ^{95}Mo, ^{107}Ag, ^{115}In, ^{121}Sb, ^{130}Te, ^{187}Re, ^{189}Os, ^{195}Pt, ^{197}Au, ^{208}Pb, ^{209}Bi) were performed at the GET laboratory using a Thermo Finnigan MAT Element HR quadrupole ICP-MS coupled with a ultraviolet femtosecond laser (New Wave) (energy 0.003 mJ, fluency 0.94 J/cm^2, power 12%, frequency 5 Hz). The laser ablation spot size was ~20 μm for most analyses, with additional spots of ~60 μm for large-grain samples to increase the signal to noise ratio. The counting time for each ablation spot analysis was 140 s, including 30 s of preablation
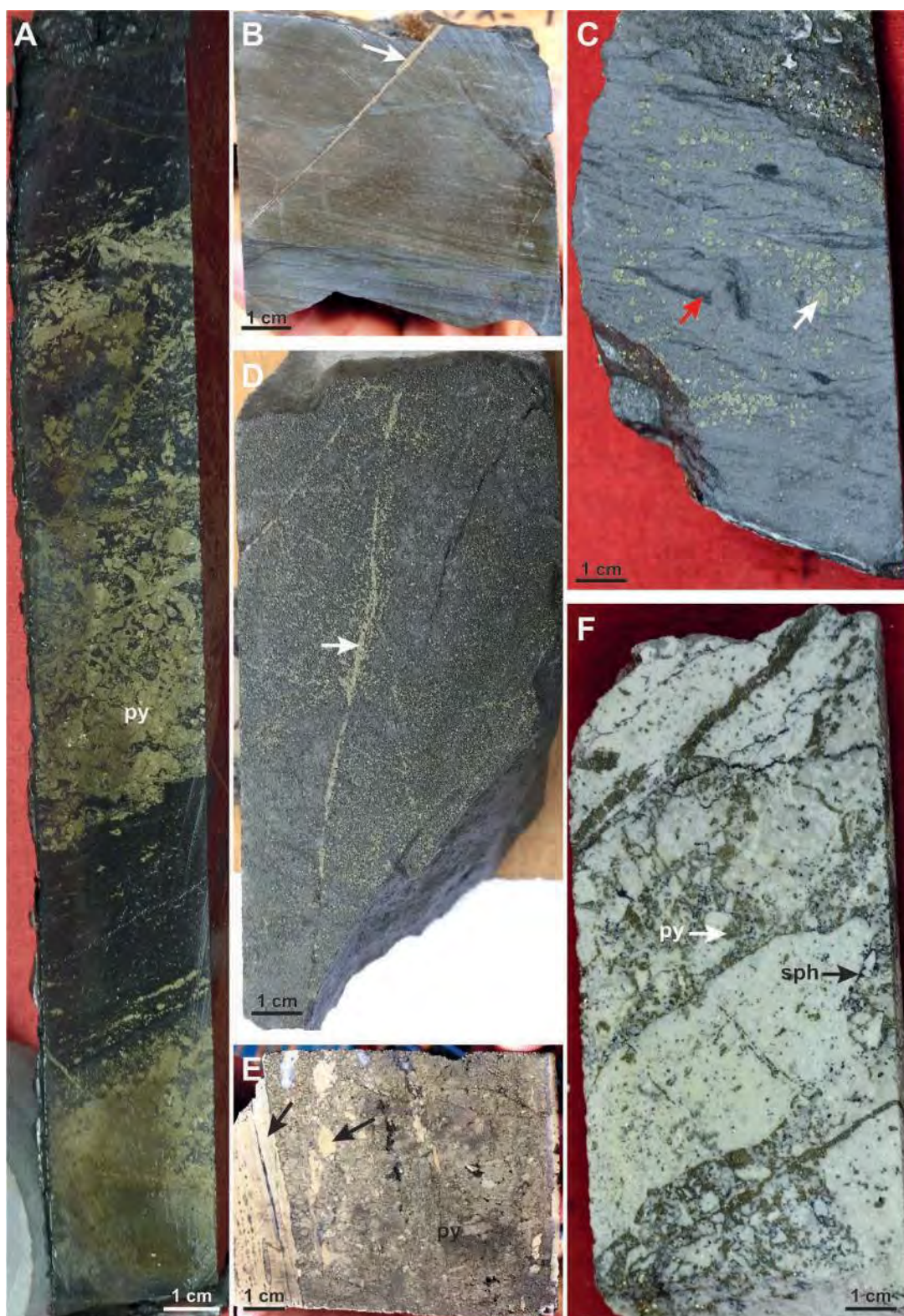
Fig. 5. Photographs of representative samples of the host rocks at the Shahuindo deposit. A. Pyritized vegetal fragments and bioclasts in shale; sample BSHA-05. B. Pyrite (py) I dissemination and late pyII vein (white arrow) in shale; sample MSHA-13. C. Pyrite I overgrown by euhedral coarse-grained pyII (white arrow) in medium-grained sandstone rich in shale clasts (red arrow); sample BSHA-09b. D. Pyrite II dissemination in carbonaceous fine-grained sandstone cut by a pyII-III vein; sample MSHA-08. E. Brecciated and altered medium-grained sandstone (black arrow) cemented by pyII and pyIII; sample MSHA-14. F. Strongly sericitized and brecciated dacite showing abundant pyrite as disseminations (pyII > pyIII), filling veinlets and aggregates in the breccia cement, with local presence of sphalerite (sph); sample BSHA-20.

Table 1. Pyrite and Arsenopyrite Generations, with As and Au Concentration Range and Average Content, for the Shahuindo Mine, as Analyzed by EPMA and LA-ICP-MS

Pyrite / arsenopyrite type	Morphology and spatially associated minerals	EPMA As (wt %) Range **Mean** *Number of points*	LA-ICP-MS Au (ppm) Range **Mean** *Number of points*	Stage
pyI	10- to 200-µm aggregates of subhedral to euhedral cubic microcrysts and framboids; no other sulfides associated	<0.2 **<0.2** *11*	0.1–4.5 **0.3** *56*	Diagenetic/syngenetic
pyII	<2-mm subhedral to euhedral crystals in sandstone, replacing organic detritus and/or bioclasts; dissemination, vein filling, and local breccia cement in intrusions; massive bodies at the contact between igneous intrusions and sedimentary wall rocks; <30-µm pyrrhotite and chalcopyrite inclusions	<0.2–2.4 **0.5** *51*	0.1–9.9 **1.0** *45*	Hydrothermal pre-ore, low As and Au
pyIII	Rims on and/or partial replacement of pyII; massive bodies and breccia cement at the contact between igneous intrusions and sedimentary wall rocks; filling <5-cm-thick veins in dacitic intrusions; oscillatory zoning with As-rich and As-poor bands; in part coeval with arsenopyrite; frequent occurrence of <50-µm inclusions of chalcopyrite, sphalerite, tetrahedrite-tennantite, galena, and stannite	<0.2–5.6 **1.8** *107*	0.1–110.0 **7.0** *129*	Hydrothermal main ore stage, high Au and As
apyIII	Subhedral to euhedral <0.3-mm strongly zoned grains along fracture walls rimmed by pyIII; accompanied by chalcopyrite, sphalerite, tetrahedrite-tennantite, galena, and minor quartz and carbonate	40.9–46.8 **42.3** *23*	1.8–460.0 **55.0** *11*	Hydrothermal main ore stage, high Au and As
pyIV	Only observed in a vein cutting andesitic intrusion and in a contact pyrite body as rims on pyIII; oscillatory zoning with As-rich and As-poor bands; no inclusions observed; accompanied by enargite and minor digenite	<0.2–2.9 **1.8** *12*	0.1–2.6 **0.7** *8*	Hydrothermal late ore stage, medium As and low Au

Abbreviations: EPMA = electron probe microanalysis, LA-ICP-MS = laser ablation-inductively coupled plasma-mass spectrometry

background, 80 s of laser ablation, and 30 s of postablation background. Iron (as ^{57}Fe) was used as the internal standard; its content in arsenian pyrite was determined by EPMA and found to be fairly constant and independent of As content (±0.1 wt %). The external calibration reference materials were Po-726 (Sylvester et al., 2005), NIST610 (Norman et al., 1996), MASS-1 (Wilson et al., 2002), and a natural arsenopyrite (Pokrovski et al., 2002, 2021).

Thermodynamic modeling of fluid-rock interactions

Chemical speciation and mineral solubility in simplified fluid-rock systems relevant to the geologic context of the deposit were modeled using available robust thermodynamic data. The goal was to better constrain the major compositional fluid and ore-forming parameters to help validate the proposed model of formation. In particular, the major focus in this study was on evaluating the role of organic matter on Fe, Au, and As transport and precipitation. Other accompanying trace elements were not considered in detail by the modeling, because of the paucity of both analytical and thermodynamic data on their content, distribution, and speciation in the fluid and major host ore mineral (pyrite).

Calculations were performed using the HCh software package and associated Unitherm database, allowing chemical equilibrium simulations in multicomponent fluid-mineral systems based on the minimization of the Gibbs energy of the system (Shvarov, 2008, 2015), and accounting for nonideality

of the fluid using the extended Debye-Hückel equation (Helgeson et al., 1981). The selection of thermodynamic data sources and their consistency for Au, S, and Fe were discussed in detail elsewhere (Pokrovski et al., 2015, 2019, 2022a, b; Kokh et al., 2016, 2017) and are only briefly overviewed here. The thermodynamic properties of the minerals were taken from the Joint Army-Navy-Air Force (JANAF; Chase, 1998) and the U.S. Geological Survey (USGS; Robie and Hemingway, 1995) databases, whereas major fluid components (salts) and most sulfur aqueous species were adopted from the updated SUPCRT database (Johnson et al., 1992) or its recently extended equivalent, SUPCRTBL (Zimmer et al., 2016) and were complemented by recent data for important ionic sulfur forms including S^- (Pokrovski and Dubessy, 2015)

using the revised and extended Helgeson-Kirkham-Flowers equation of state (HKF; Oelkers et al., 2009; Sverjensky et al., 2014; references therein). A large set of organic aqueous ions and molecules (hydrocarbons, carboxylic acids, thiols) whose thermodynamic coefficients are available in the SUPCRT database was also tested in the calculations, but their equilibrium concentrations were found to be too low (<0.001 m, where m is number of moles per kg of water) to significantly affect the fluid properties (pH, redox) and mineral solubility, compared to the dominant CO_2 and CH_4. The data for ferrous iron species (Fe^{2+}, $FeCl^+$, and $FeCl^0$) were taken from the SUPCRT database, whereas those for $FeCl_2^-$ from Testemale et al. (2009). Both $FeCl^0$ and $FeCl_2^-$ dominantly contribute to

VALLANCE ET AL.

the Fe speciation at our conditions. The properties of aqueous As[III] and As[V] oxyhydroxide complexes and iron (sulfo)arsenide minerals (FeAsS, FeAs$_2$, and FeAs) were adopted from Perfetti et al. (2008). The major arsenic aqueous species over the entire range of our conditions is arsenious acid, As(OH)$_3^0$. We also incorporated and examined the recent model of As solid solutions in marcasite and arsenopyrite recently proposed by Xing et al. (2019) based on the data for those pure phases from Perfetti et al. (2008) and density functional theory and Monte Carlo theoretical calculations of As substitution for S in the FeS$_2$ and FeAsS structures by Reich and Becker (2006). This model yielded As tenors in pyrite (0.5–1.0 wt %) right in the middle of the analyzed range of our samples and thus was judged to be adequate to account for the general arsenic distribution and mass balance between fluid and rock. The thermodynamic properties of the molecular sulfur aqueous forms, H$_2$S, SO$_2$, and dissolved H$_2$, O$_2$, CO$_2$ and CH$_4$, were adopted according to the Akinfiev and Diamond (2003) model for aqueous nonelectrolytes, which allows a more accurate description than the HKF model over the T-P range relevant to our study (<350°C; <1 kbar; Pokrovski and Dubessy, 2015). Note that the thermodynamic data from Akinfiev and Diamond (2003) have also been used in derivation of the thermodynamic properties of the Au species and thus were chosen here to maintain thermodynamic consistency. The thermodynamic properties of traditional hydrogen sulfide (AuHS^0, Au(HS)$_2^-$) and hydroxide (AuOH^0) species were taken from the compilation of Pokrovski et al. (2014), consistent with existing robust experimental data (e.g., Stefansson and Seward, 2004; Tagirov et al., 2005), whereas those for the dichloride species (AuCl$_2^-$) were taken from Zotov et al. (2018) and those for the recently discovered gold complex with the trisulfur ion, Au(HS)S$_3^-$, from Pokrovski et al. (2015). Species such as AuCl^0, AuCl$_3^{2-}$, and Au(OH)$_2^-$ tentatively suggested in some previous compilations, were ignored in the present modeling because of the large uncertainties associated with predictions of their stability constants at elevated temperatures as well as the lack of direct spectroscopic evidence of their existence. Among the chosen Au species, AuHS^0 and Au(HS)$_2^-$ are the dominant complexes at acidic (<4) and neutral to basic pH (>6), respectively, in the S-bearing epithermal fluids considered in this study (e.g., Tagirov et al., 2005). In addition, Au(HS)S$_3^-$ also contributes to the gold solubility at intermediate pH values (4–5) at redox conditions of the sulfate-sulfide coexistence in the fluid. The precision of our predictions of Au, Fe, and As concentrations at a given model fluid composition at the T-P conditions of this study (150°–350°C, <1,000 bar) is typically better than 50% of the concentration value, as conditioned by the intrinsic uncertainties of the thermodynamic data and activity coefficient models chosen here. The input HCh files of representative models are supplied as an electronic supplement (App. 1).

Results

Structural analysis

The structural framework, reconstructed in this study, is illustrated by the regional structural cross section in Figure 4. It shows the geometry of the imbricated thrusts and associated folds of the E-verging Marañón belt, which has been partly eroded during the middle Eocene postorogenic period (Noble et al., 1990; Prudhomme et al., 2019). The belt is covered to the west by the Calipuy volcaniclastic sediments and to the east by the Codebamba lacustrine and fluvial deposits (Figs. 2, 4). Both formations are poorly deformed, indicating that the Neogene reactivations of thrusts structures were rather weak. Imbricated thrusts and folds are tight and accommodated a large degree of shortening. They are connected to a sole thrust that developed at the interface between the Chicama black shales and the metamorphic basement. The entire thickness of the Chicama black shales (~1,000 m) was deformed, and the shales occupy the cores of imbricates and anticlines, which form excellent structural traps when preserved. The Chicama base décollement developed between 7 km deep in the west and 2 km in the east, with a steep slope in the east.

Our structural analysis shows that the Shahuindo deposit is located in a system of four imbricate thrusts where the related anticlines are preserved. The most spectacular of these anticlines is the Algamarca anticline, which marks the landscape of the region with an outcropping fold made of Chimú sandstones (Fig. 4). The Algamarca imbricate is the most western and uplifted and thus the first to have been formed in accordance with the in-sequence thrusting propagation evidenced by the normal stacking of the four imbricates. The Shahuindo gold deposit has been trapped in the reservoir sandstones (Carhuaz and Farrat Formations) of the anticlines of the second and third imbricates. It is possible that similar deposits could also exist in the Chimú sandstones, but these have not yet been revealed by the mine drill holes. In the Algamarca-Shahuindo imbricate system, elongated bodies of andesitic and dacitic intrusions are emplaced at the intersection of the northwest-southeast thrust faults and later northeast-southwest transverse faults. In our structural interpretation, these intrusions are connected to an upper crustal laccolith installed at the interface between the basement and the Chicama black shales, following the model of Vigneresse et al. (1999) and Richards (2003), and resulting from magma migration along deeper and later northeast-southwest transverse faults clearly identified at the surface (Fig. 3). As a result of this analysis, the obtained structural cross section allows us to circumscribe the Algamarca-Shahuindo imbricate system that likely fed the Shahuindo deposit. The migration of ore fluids was guided by the thrust geometries up to the reservoir sandstones of the anticlines, showing analogies with processes typically observed in petroleum systems (e.g., Magoon and Dow, 1994; Calderon et al., 2017; Baby et al., 2021). Moreover, the Lower Cretaceous Shahuindo stratigraphic series comprise essential elements as black shales, sandstone reservoirs, and overburden rocks (Fig. 2) that all contributed to the processes of trap formation and fluid migration and accumulation linked to thrust tectonics of the Marañón belt.

Host-rock and ore geochemistry

Thirty-seven samples were collected in the Shahuindo area, most of them (*n* = 32) selected from drill core to avoid the influence of supergene alteration. Barren and gold-rich samples were collected from both sedimentary and igneous rock types of the Shahuindo area in order to characterize all facies of the deposit. Additionally, two fresh outcrop samples

of graphite-bearing sandstone from the Chicama Formation were collected about 20 km southeast of the deposit, where no igneous and/or hydrothermal activity was detected, to assess the host rock unaffected by hydrothermal fluids. The location of the 10 samples from mineralized and barren sedimentary rocks as well as their mineralogical and geochemical characteristics are given in Figures 1 and 3, Appendix Figure A1A, Tables 2 and 3, and Appendix Table A1. Locations of graphite-rich sandstone samples from the Chicama Formation (MSHA-22 and MSHA-23) are shown in Figure 1. The Chimú Formation was not sampled, because it was not intersected by exploration drilling, and all exposed occurrences are affected by strong supergene alteration. The Santa Formation was sampled from core drilled in the deposit (MSHA-05). The Carhuaz Formation was sampled from surface outcrops

(samples MSHA-01 to MSHA-04; Fig. 3A) as well as from drill core (MSHA-08; MSHA-11). Sample MSHA-14 is from a breccia with pyrite cement at the contact between a dacitic intrusion and fine-grained sandstone of the Carhuaz Formation (Fig. 5E).

Based on their chemical and mineralogical compositions, the rock samples were separated into two groups. The first consists of three barren samples, including MSHA-22 and MSHA-23 from outside the deposit and MSHA-01 collected within the deposit. They do not show any Au, As, or Cu enrichment compared to typical black shales (Johnson et al., 2017). These samples have major element compositions within the range of typical barren black shales (Johnson et al., 2017; App. Fig. A1). Their gold and arsenic contents (<1–2 ppb and 12–23 ppm, respectively) are at the lower end of the range of

Table 2. Description and Key Element Bulk Composition of Selected Rock Samples from the Shahuindo Mine

Sample identity	Sample type and location	Geographical coordinates	Description	C (wt %)	S (wt %)	Fe[1] (wt %)	Cu (ppm)	As (ppm)	Au (ppm)
MSHA-01	Surface outcrop	7°37'30.02"S 78°12'19.04"W	Carhuaz Formation; light-gray siltstone with flaser bedding; black organic matter accompanied by fine-grained pyrite is abundant in mud layers	0.43	0.22	5.31	30	12	0.002
MSHA-02	Surface outcrop	7°37'30.14"S 78°12'18.31"W	Carhuaz Formation; light-gray siltstone with flaser bedding; black organic matter accompanied by fine-grained pyrite is abundant in mud layers	0.94	0.44	3.84	130	16	0.02
MSHA-03	Surface outcrop	7°37'30.14"S 78°12'18.31"W	Carhuaz Formation: light-gray siltstone with flaser bedding; black organic matter accompanied by fine-grained pyrite is abundant in mud layers	0.93	0.53	4.15	124	21	0.02
MSHA-04	Surface outcrop	7°37'29.27"S 78°12'19.60"W	Carhuaz Formation, SW-NE fault zone; strongly deformed black shale accompanied by coarse-grained pyrite	0.13	7.15	6.81	31	743	0.18
MSHA-05	Drill core within the deposit	7°36'35.94"S 78°12'53.54"W	Santa Formation; black shale rich in carbonaceous material with dissemination of fine-grained pyrite	0.65	0.75	3.74	37	41	0.03
MSHA-08	Drill core within the deposit	7°36'23.52"S 78°12'27.80"W	Fine-grained dark-gray sandstone of the Carhuaz Formation; dissemination of abundant subidiomorphic pyrite (>0.5 mm); yellow fine-grained pyrite fills sinuous veinlets (<1 mm)	0.03	19.3	16.71	8250	1,000	0.95
MSHA-11	Drill core within the deposit	7°36'24.39"S 78°13'01.73"W	Fine-grained dark-gray sandstone of the Carhuaz Formation with abundant carbonaceous matter including plants fragments and dissemination of fine-grained pyrite	1.43	5.09	4.70	64	237	0.03
MSHA-14	Drill core within the deposit	7°36'49.36"S 78°13'02.87"W	Matrix-supported breccia with ~30% subangular to subrounded clasts of altered medium-grained sandstone; the cement is mainly pyrite with minor amounts of arsenopyrite, tetrahedrite-tennantite, Bi and Te minerals, aluminum phosphate-sulfate minerals, and quartz; sample collected at a sandstone/intrusion contact	0.20	21.9	18.81	57	2,460	0.25
MSHA-22	Surface outcrop 20 km SE of the deposit	7°41'39"S 78°05'07"W	Chicama Formation; light-gray fine-grained sandstone with flaser bedding; black organic matter accompanied by fine-grained pyrite is abundant in mud layers; left side of the Rio Condebamba River	1.91	0.44	2.78	21	12	0.001
MSHA-23	Surface outcrop 20 km SE of the deposit	7°41'39"S 78°05'07"W	Chicama Formation; light-gray fine-grained sandstone with flaser bedding; black organic matter accompanied by fine-grained pyrite is abundant in mud layers; left side of the Rio Condebamba River	2.27	0.37	3.35	26	23	<0.001

[1]Calculated on the basis of the oxide analysis; see also Appendix Table A1

Table 3. Comparison of Element Content Along a 50-m-Long Profile Perpendicular to a Roof Branch of the Thrust that Controls Mineralization at the Deposit Scale

Sample	Location	Au (ppb)	As (ppm)	Ag (ppm)	S (wt %)	Fe excess[1] (mol/kg)
MSHA-01	50 m SW of the thrust	2	12	0.1	0.22	0.09
MSHA-02	25 m SW of the thrust	17	16	0.1	0.44	0.06
MSHA-03	25 m SW of the thrust	17	21	0.2	0.53	0.06
MSHA-04	0 m from the thrust	180	743	0.7	7.15	0.01

[1]Fe excess, in moles per 1 kg of rock, relative to the FeS_2 stoichiometry, that all S is in pyrite

whole-rock analyses of black shales compiled for the Sukhoi Log, Carlin, and Bendigo Au-As provinces (Large et al., 2011). Mass balance calculations, assuming all sulfur to be in pyrite, show iron to be in excess compared to sulfur (i.e., mole ratio Fe/S > 0.5; App. Fig. A1B) for samples that contain less than 1 wt % S, thereby suggesting an additional contribution from other Fe-bearing minerals (silicates, carbonates). In contrast, hydrothermal pyrite-bearing samples enriched in gold (0.02–1.0 ppm) show a mole Fe/S ratio close to 0.5 (App. Fig. A1C), indicating that almost all of the iron and sulfur are hosted by pyrite. Assuming all carbon to be from carbonaceous matter (traces of carbonate were only found in sample MSHA-14), there is no correlation between carbonaceous matter contents

and gold concentrations. Samples MSHA-02, MSHA-03, and MSHA-04 belong to the above-mentioned 50-m-long profile starting with MSHA-01 (Fig. 3A). While samples MSHA-02 and MSHA-03 do not differ in mineralogy and texture from sample MSHA-01 (Table 3), they show significantly higher Au, S, and As concentrations and much smaller Fe excess. These compositional differences are even more pronounced in sample MSHA-04 taken from the fault zone itself.

Pyrite paragenetic sequence

Pyrite is by far the major sulfide mineral associated with gold at Shahuindo, accompanied by subordinate amounts of arsenopyrite, pyrrhotite, chalcopyrite, sphalerite, tetrahedrite-tennantite, enargite, chalcocite, and galena and minor stibnite, bismuthinite, tellurobismuthite, kobellite, stannite, boulangerite, and greenockite. Gangue minerals comprise, in decreasing abundance, white micas, quartz, kaolinite, carbonates, pyrophyllite, and aluminum phosphate-sulfate minerals. In contrast to samples affected by oxidation from the supergene zone (the defined gold resource), in the endogenous sulfide ore no visible gold was detected by optical microscopy nor SEM, even in samples with grades as high as 30 g/t Au. Figure 6 shows the paragenetic sequence comprising four successive stages as defined by four generations of pyrite identified in this study based on morphological characteristics, chemical composition, and mineral assemblages as summarized in Table 1 and detailed below.

Pyrite I: The earliest pyrite (pyI) occurs as aggregates of subhedral to euhedral cubic-shaped microcrysts and framboids of 10 to 200 μm in size, which are only observed in the

Mineral	Stage I	Stage II	Stage III	Stage IV
Pyrrhotite				
Arsenopyrite				
Chalcopyrite				
Pyrite	pyI	pyII	pyIII	pyIV
Gold *				
Sphalerite				
Tetrahedrite-tennantite				
Stibnite				
Galena				
Bismuthinite				
Tellurobismuthite				
Russellite				
Boulangerite				
Kobellite				
Carbonates				
Enargite				
Digenite				
Chalcocite				
Kaolinite				
APS minerals **				

* Gold chemically bound in pyrite and arsenopyrite

** Aluminum-phosphate-sulfate minerals

Fig. 6. Paragenetic sequence of the Shahuindo gold deposit as established in this study. The bar thickness is roughly indicative of the relative mineral abundance. Stage I corresponds to the deposition of diagenetic pyI; pyrrhotite, chalcopyrite, and sphalerite of stage II occur as inclusions within coarse-grained pyII; gold precipitated within pyIII and arsenopyrite during stage III, and the other sulfides fill open space between their euhedral terminations, with evidence of local replacement; pyrite IV forms overgrowths on pyIII and is accompanied by enargite, minor digenite, and aluminum phosphate-sulfate minerals, partially replacing stage III chalcopyrite and tetrahedrite-tennantite.

sedimentary rocks of the Santa and Carhuaz Formations (Fig. 7A, B). This pyrite type is not accompanied by other sulfide minerals and occurs as disseminations at a regional scale, strongly suggesting a diagenetic origin.

Pyrite II: Stage II pyrite (pyII) is the most abundant of the four types. It is spatially associated with intrusive bodies and occurs both in the igneous rocks and nearby sediments. Pyrite II occurs mainly as pyritohedral crystals up to 5 mm in size, filling porosity in sandstone, (Fig. 6C-E), replacing organic detritus and/or bioclasts in siltstone and shales (Fig.

6F), or filling veinlets. Pyrite II is also the main constituent of pyrite bodies formed at the contact between igneous intrusions and sedimentary wall rocks. In the igneous rocks, disseminated pyII occurs together with sericite as replacement of mafic minerals. It also fills thin veinlets (<5 mm thick) that are locally interconnected and form a stockwork array and is an important constituent of the breccia matrix. In both igneous and sedimentary rocks, SEM analyses do not show compositional zoning of pyII (Fig. 6E) but reveal the presence of <30-μm-size inclusions of pyrrhotite and, less commonly,
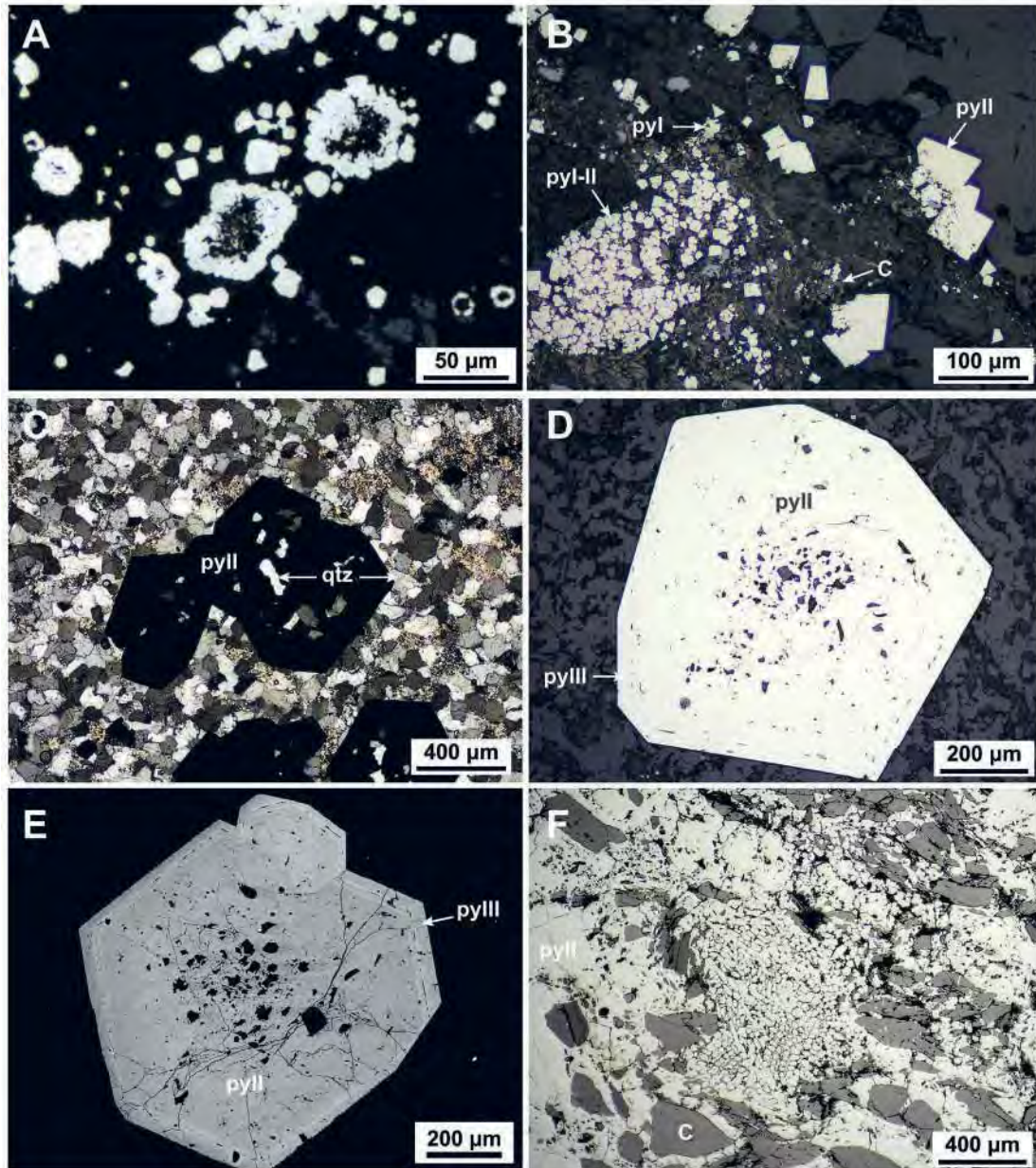
Fig. 7. Textural features of pyrite I and pyrite II from the Shahuindo deposit. A. Cluster of subhedral to euhedral pyrite microcrysts. Reflected light. B. Spatial association between framboidal pyrite (pyI) and graphitic organic detritus (C). Pyrite II (pyII) nucleation on pyrite I, making it difficult to distinguish between pyI and pyII. Reflected light. C. Subhedral pyritohedron (py) in sandstone that encloses detrital quartz (qtz). Transmitted light, crossed polars. D. Euhedral pyrite II grain with As-rich pyrite III (pyIII) overgrowths. E. Backscattered electron image of coarse euhedral pyrite II grain with pyrite III overgrowths showing alternating As-rich (lighter color) and As-poor bands. F. Partial replacement of graphitic organic detritus (C) by pyrite II (pyII), locally infilling plant cells (center of the picture). Reflected light.

intergrowths of pyrrhotite, chalcopyrite, and sphalerite with local chalcopyrite disease.

Pyrite III: Similar to pyrite II, pyrite III (pyIII) was observed both in sedimentary and igneous rocks as well as in massive pyrite bodies. Pyrite III typically forms rims on pyII (Fig. 6E) and, less frequently, fracture and crystallographically controlled replacement zones (Fig. 7A). The key distinguishing feature of pyIII is an oscillatory zoning with an alternation of As-rich and As-poor bands (Fig. 7B, D). As-rich bands often contain <50-μm inclusions of chalcopyrite, sphalerite, tetrahedrite-tennantite, galena, and stannite (Fig. 7D) and, more rarely, bismuthinite, tellurobismuthite, kobellite, and russellite. Arsenopyrite (apyIII) is coeval with pyIII and forms strongly zoned subhedral to euhedral grains (<0.3 mm; Fig. 7B, C, E). Locally, arsenopyrite occurs as euhedral crystals along fracture walls rimmed by pyIII within pyII (Fig. 6B, E). In these fractures, chalcopyrite, sphalerite, tetrahedrite-tennantite, galena, and minor quartz and carbonate fill open space between euhedral terminations with evidence of local replacement (Fig. 7E).

Pyrite IV: The fourth generation of pyrite (pyIV) was only identified in a vein cutting an andesitic porphyry body and in a massive pyrite contact body. Pyrite IV occurs as inclusion-free overgrowths on pyIII with alternation of As-rich and As-poor bands (Fig. 7F), and is accompanied by enargite, minor digenite, and aluminum phosphate-sulfate minerals, partially replacing chalcopyrite and tetrahedrite-tennantite.

Pyrite and arsenopyrite composition

The EPMA analyses of pyrite I show a close to ideal stoichiometry, $FeS_{2.00}$, and no As, Sb, and Cu were detected (<0.05–0.1 wt %; Fig. 8; App. Table A2). Pyrite II is also close to stoichiometric ($FeS_{1.98–2.00}$), with detectable As (up to 2.4 wt %). Pyrite III is more enriched in both As and Cu (up to ~5.6 and ~0.9 wt %, respectively). The latest pyrite type, pyrite IV, contains up to 2.9 wt % As. There are no significant correlations between S and As in pyII, whereas in pyIII and pyIV both elements display negative correlations (Fig. 9A), implying an isomorphic substitution by As in the –I formal oxidation state for S in the pyrite structure (e.g., Fleet and Mumin, 1997; Simon et al., 1999; Deditius et al., 2008; Manceau et al., 2020; references therein). The strongest As enrichment in pyIII was observed in grains hosted by sedimentary rocks, whereas the lowest concentrations were found in grains occurring in transverse faults (Fig. 9B). Arsenopyrite, belonging to the pyIII stage, is generally depleted in As ($Fe_{0.98–1.01}As_{0.85–1.00}S_{1.13–1.00}$) compared to the ideal FeAsS stoichiometry, and it is zoned, with cores having lower As (~41 wt %) than the rims (~47 wt %). Sulfur correlates negatively with As plus Sb supporting an (As + Sb) to S substitution mechanism, typical of most arsenopyrites (e.g., Boiron et al., 1989; Pokrovski et al., 2021).

Trace element composition of pyrite and arsenopyrite

Pyrite (from the four paragenetic stages; Fig. 6) and arsenopyrite (from the pyIII stage) were analyzed for trace elements using LA-ICP-MS in 10 representative samples collected in sandstone, andesite, contact sedimentary rocks/dacitic bodies, dacitic bodies, and the northeast-southwest fault (Fig. 10; Table 4; App. Tables A3, A4). Gold contents in pyI range from 0.1 to 1.7 ppm (with a single data point of 4.5 ppm). Gold correlates positively with Ge, Se, and Te and negatively with V, Ga, and In but shows no statistically meaningful pattern with As (Fig. 11A). In pyII, gold ranges from 0.03 to 9.9 ppm (mean value ~1 ppm) with a generally positive correlation with As, depending on the host lithology (App. Table A4). Gold concentrations in pyIII range from ~0.1 to 110 ppm, with the highest concentrations measured in pyrite bodies at the contact of dacitic intrusions with the sedimentary rocks (Fig. 11B). Conversely, the lowest values were observed in pyrite from the andesitic intrusion. The correlations between gold and other elements in pyIII vary greatly depending on the host lithology. Gold and arsenic are strongly correlated in pyrite samples from transverse faults and intrusions but uncorrelated in pyrite from samples from sedimentary rocks. Other minor/trace elements such as Ni, Cu, Zn, Ag, In, Sb, Te, Pb, and Bi locally show relatively high tenors and often strong intercorrelations (App. Fig. A2; App. Tables A2, A4). Such correlations suggest that some spot analyses may include microparticles of minerals like chalcopyrite, kobellite, or tetrahedrite-tennantite. Indeed, the presence of such mineral inclusions is confirmed by SEM analyses (see Fig. 7D-F) as well as by observation of spikes in some laser ablation spectra of pyrite. The presence of arsenic-rich mineral phases (such as tetrahedrite-tennantite) that do not contain significant gold (e.g., George et al., 2017) would, at least partly, obscure correlations between As and Au in sediment-hosted pyIII samples. Gold in arsenopyrite from the pyIII generation exhibits a large range of concentrations (2–460 ppm) independent of the lithology (Fig. 11C, D; App. Table A3). LA-ICP-MS signals of Cu, Zn, Ag, Ga, Ge, Sb, and In in arsenopyrite often show spikes and/or irregular patterns, which are suggestive of the presence of tetrahedrite-tennantite and/or chalcopyrite inclusions enriched in those elements (App. Fig. A3). This interpretation is in accordance with the textures of pyIII and apyIII indicating replacement by these Cu-bearing minerals. Pyrites III and IV show similar alternation of As-rich and As-poor zones, but pyIV is almost free of inclusions and has a lower average content of trace elements than pyIII (Fig. 10; Table 3). Gold concentrations in pyIV range from 0.1 to 2.6 ppm (mean = 0.7 ppm), weakly correlating with arsenic.

Discussion

Evolution of the ore-forming conditions and succession of the mineralization events

The structural reconstruction analysis and the paragenetic sequence established above provide key constraints on the evolution of ore-forming conditions during the Shahuindo deposit formation. The earliest ore mineral assemblage, identified both in sedimentary and intrusive rocks, is only evidenced by residual inclusions of pyrrhotite, chalcopyrite, and sphalerite within the abundant pyII mineralization. This assemblage is consistent with deposition under relatively reducing and sulfur-poor conditions, indicative of pyrrhotite stability. Extensive hydrothermal alteration of the intrusions that accompanies pyII deposition suggests acidic pH conditions, as sericitization is typically associated with percolation of acidic fluids (Hemley and Jones, 1964; Hemley and Hunt, 1992; Seedorff et al., 2005). The occurrence, in the following
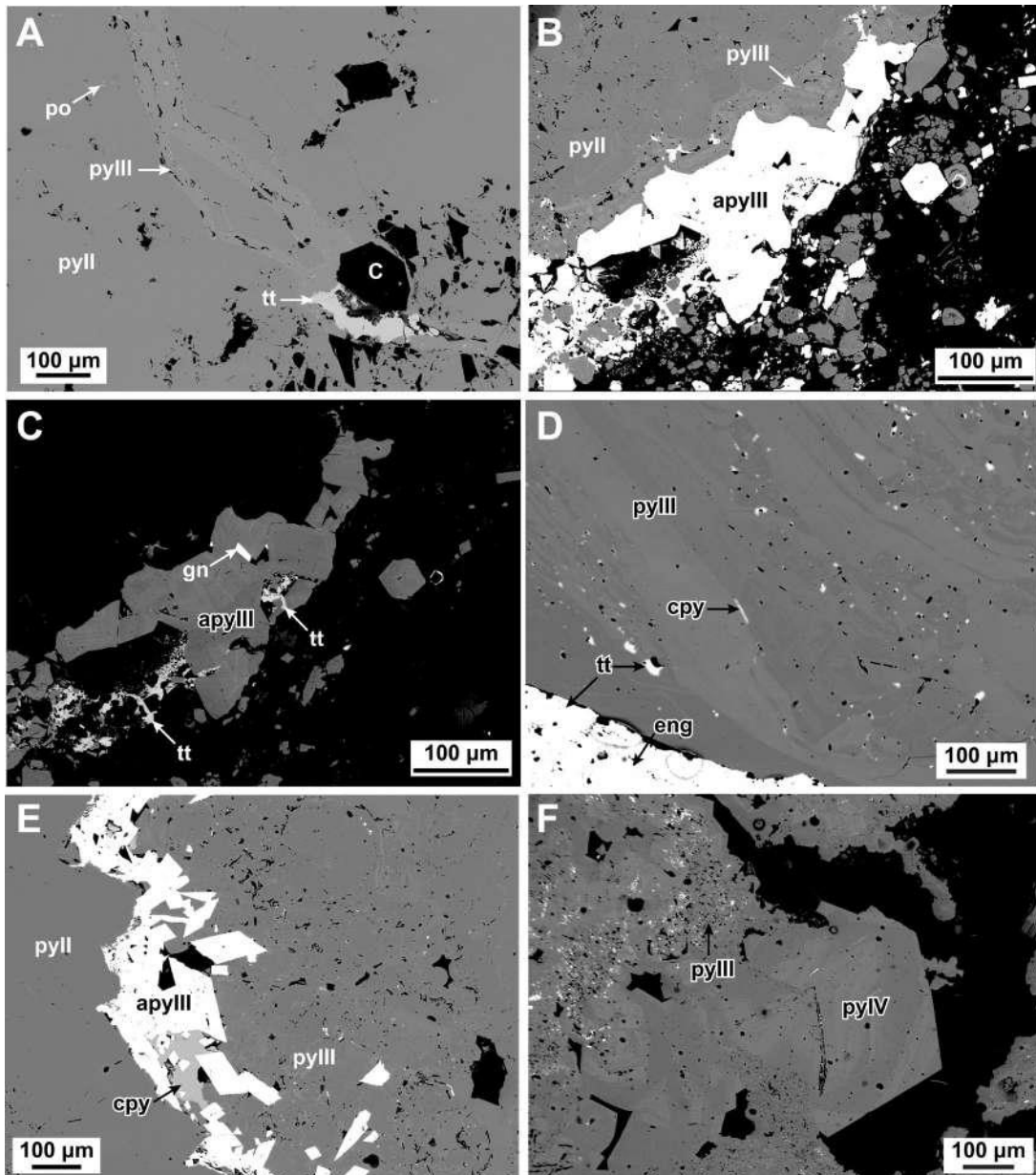
Chapter II

99

Fig. 8. Scanning electron microscope (SEM) photomicrographs (in backscattered electron mode) of ore samples from the Shahuindo deposit. A. Replacement zone of pyrite II (pyII) by pyrite III (pyIII) and tetrahedrite-tennantite (tt). C = graphite, po = pyrrhotite inclusion in pyrite II. B. Pyrite II (pyII) rimmed by oscillatory-zoned pyrite III (pyIII) and arsenopyrite (apyIII). C. Same view as in B, with different contrast enhancing the arsenopyrite zoning and the later tetrahedrite-tennantite (tt) and galena (gn). D. Details of the oscillatory zoning in pyrite III (pyIII); tetrahedrite-tennantite (tt) and chalcopyrite (cpy) inclusions are preferentially located at the limit between bands; later enargite (eng) partially replacing tetrahedrite-tennantite. E. Arsenopyrite (apyIII) precipitated at the contact between coarse pyrite II (pyII) and finer pyrite III (pyIII) grains with local replacement of the latter; chalcopyrite (cpy) filling spaces between arsenopyrite euhedral terminations. F. Late subhedral oscillatory-zoned and inclusion-free pyrite IV (pyIV) occurring as overgrowth on oscillatory-zoned inclusion-bearing pyrite III (pyIII).

pyIII stage, of Au-rich highly arsenian pyIII and arsenopyrite with the presence of later Ca-Mg-Fe carbonate minerals indicates less acidic fluid pH, more favorable for stabilizing the carbonate mineral phases. The chalcopyrite-tetrahedrite-tennantite assemblage that postdates Au-bearing pyIII and arsenopyrite points to an evolution toward higher sulfidation conditions, as also suggested by late pyIV together with digenite, enargite, kaolinite, and aluminum phosphate-sulfate

minerals within the magmatic intrusions and at their contacts with sedimentary rocks (Einaudi et al., 2003; Fontboté et al., 2017). This assemblage of enargite, chalcocite, and digenite is indicative of magmatic fluids (Einaudi et al., 2003). The transition from low- to intermediate- and to high-sulfidation stages has been documented in other Cordilleran deposits of Central Peru, such as Morococha, Cerro de Pasco, and Ayawilca (Catchpole et al., 2015; Rottier et al., 2016; Fontboté, 2020;

62
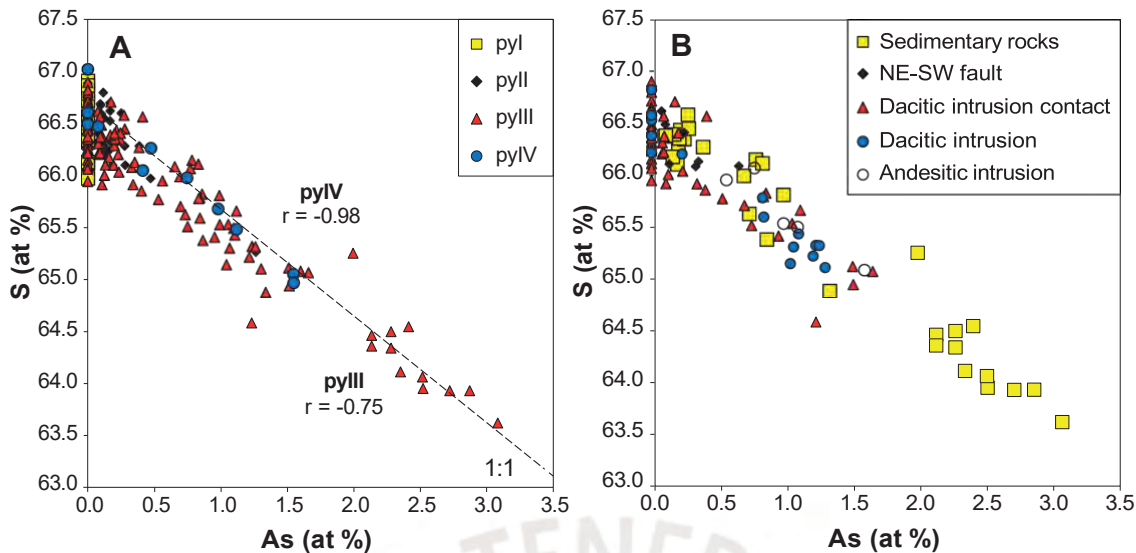
Fig. 9. Electron probe microanalyses (in at %) of pyrite from the Shahuindo deposit. A. As versus S for the indicated pyrite generations. Dashed lines represent 1:1 correlation; r is the Pearson correlation coefficient. B. As versus S for the pyIII generation from different host-rock types or tectonic position.

Benites et al., 2022). Indeed, the different sulfidation stages identified in our study are rather similar to stages A to C of most Cordilleran-type deposits that are generally explained by decreasing temperature (Fontboté, 2018, 2020). However, the fundamental reasons for this evolution of sulfidation state may be different at Shahuindo and reflect the particularities of interaction of magmatic fluids with C_{org}-rich rocks, as will be shown below. Due to high reactivity of sedimentary organic matter, initially acidic, oxidized magmatic-derived fluids may have completely lost their acidic and oxidizing properties by interacting with fresh portions of C_{org}-bearing rocks, resulting in the low-sulfidation mineral assemblages at early stages. Subsequent portions of fluids may have passed through progressively more and more altered rocks having less and less buffering capacity and resulted in an apparent increase in sulfidation state conditions from pyII to pyIV generations. This interpretation is consistent with the thermodynamic modeling that will be discussed further below.

Gold-arsenic relationships in pyrite

Gold and arsenic contents in diagenetic pyrite (pyI) from the Shahuindo deposit are similar to those observed in sedimentary pyrite from other provinces worldwide such as Sukhoi Log (Russia), Bendigo (Australia), and the Otago schist in New Zealand (Large et al., 2009, 2012). At Shahuindo, no clear correlation emerges between gold and arsenic at this early stage, suggesting that these elements were decoupled at the time of diagenesis, before ore formation. Hydrothermal pyII, pyIII, and pyIV display, in contrast, positive correlations between Au and As with the maximum of Au-As enrichment attained during pyIII deposition. The maximum As concentration value of 5.6 wt % in pyIII is consistent with theoretical predictions of As-S solid-solution range in pyrite, which may extend to ~6 wt % As incorporated in the pyrite structure, without formation of arsenopyrite domains (Reich and Becker, 2006). This As saturation limit in pyrite is also in agreement with the paragenetic sequence showing

that arsenopyrite and pyIII were coeval. A maximum content of 460 ppm Au analyzed by LA-ICP-MS in arsenopy- rite of the pyIII stage is consistent with both natural and experimental data, which indicate that arsenopyrite incorporates much higher Au contents than coexisting pyrite (up to 1–2 wt %; Boiron et al., 1989; Wu and Delbove, 1989; Fleet and Mumin, 1997; Pokrovski et al., 2021). The arsenic-gold coupling in hydrothermal pyrite evidenced in our study is consistent with the common As-Au associations and As control on Au incorporation in pyrite, initially identified in Carlin-type deposits (e.g., Radtke et al., 1972; Wells and Mullens, 1973; Fleet and Mumin, 1997; Simon et al., 1999; Cline, 2001; Cline et al., 2005; Muntean et al., 2011) and later recognized in many other gold deposit types such as orogenic (e.g., Cook and Chryssoulis, 1990; Large et al., 2007; Velasquez et al., 2014; Belousov et al., 2016), intrusion-related (e.g., Voute et al., 2019), porphyry Cu-Au (e.g., Deditius et al., 2014), and volcanogenic massive sulfide (e.g., Deditius et al., 2014; Belousov et al., 2016). More recently, the key role of arsenic in invisible gold incorporation into pyrite has been demonstrated by direct laboratory experiments coupled with in situ X-ray absorption spectroscopy (e.g., Kusebauch et al., 2019; Pokrovski et al., 2019, 2021). Our findings thus confirm the recent proposition, based on experimental and spectroscopic evidence, that incorporation of gold in pyrite and arsenopyrite from gold-undersaturated fluids during pyritization of the host rock occurs through a redox-driven reaction of Au binding to As in the structures of pyIII and apyIII (Pokrovski et al., 2021). In contrast, gold occurring in much lower concentrations in As-poor diagenetic pyrite (pyI) is decoupled from arsenic and is likely being chemisorbed on the pyrite surface and/or incorporated in structural defects in the form of Au sulfide complexes (e.g., Pokrovski et al., 2019). Gold concentrations increase in pyIII that is enriched in arsenic, which is also in line with the coexistence of Au-rich apyIII. The formation of both As-rich phases is likely favored by an increase in As
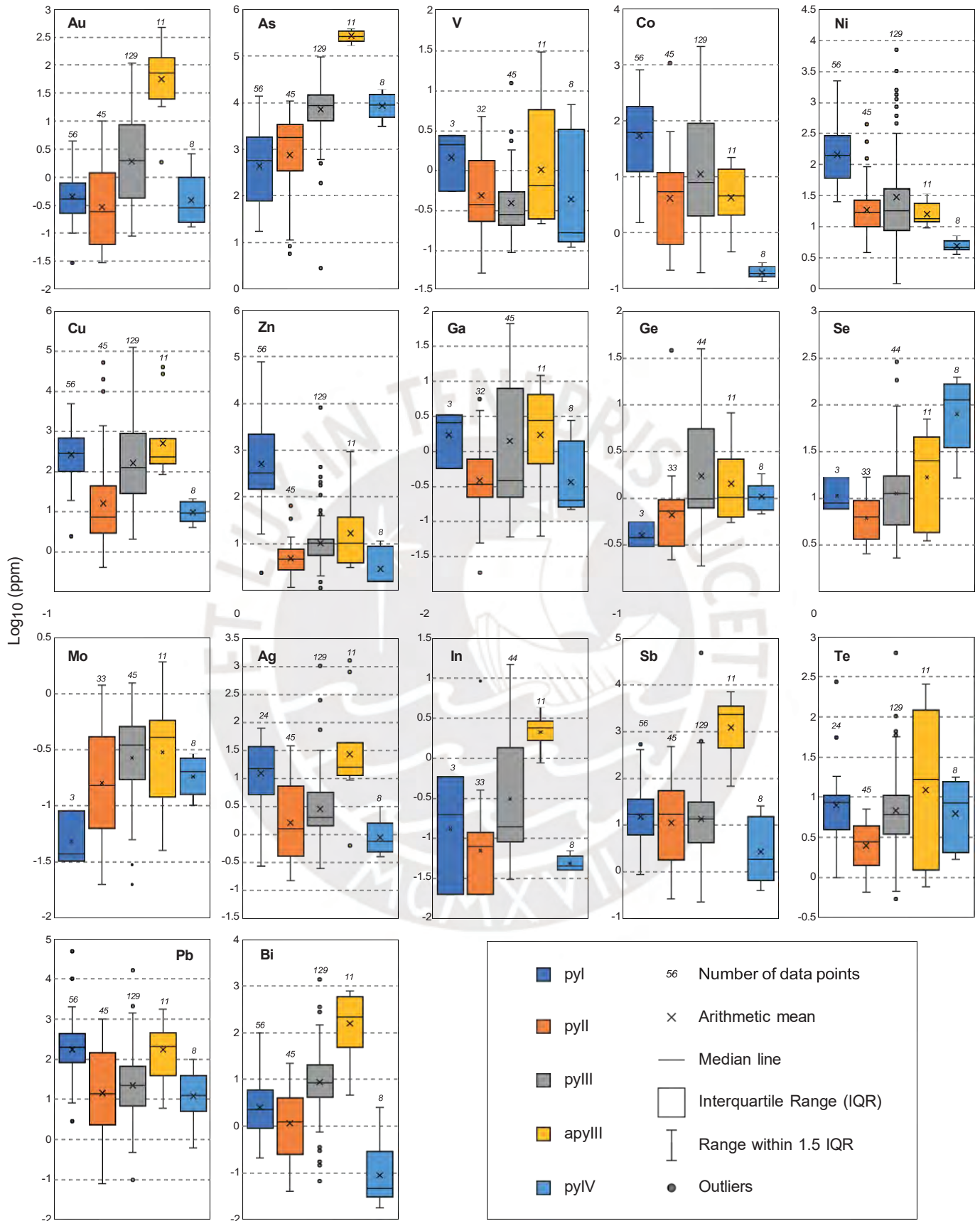
Fig. 10. Box plots showing the contents of 17 trace elements (in log₁₀ units of ppm) analyzed by laser ablation-inductively coupled plasma-mass spectrometry in the four pyrite generations (pyI to pyIV) and in arsenopyrite (apyIII, belonging to pyIII generation).

Table 4. Summary of LA-ICP-MS Analyses (in ppm) of Selected Arsenopyrite and Pyrite Grains from the Shahuindo Mine

| Mineral		V	Co	Ni	Cu	Zn	Ga	Ge	As	Se	Mo	Ag	In	Sb	Te	Au	Pb	Bi
pyI	Min	0.5	1.5	25	2.5	2.4	0.6	0.3	17	7.7	0.03	0.3	0.02	0.9	1.0	0.03	2.8	0.2
n = 56	Max	2.6	790	2,250	4,970	77,860	3.3	0.56	13,670	17	0.09	78	0.6	530	270	4.5	48,520	99
	Mean	1.4	53	145	264	499	1.7	0.40	43	10	0.05	12	0.11	15	7.8	0.3	177	2.5
pyII	Min	0.05	0.2	3.9	0.4	1.2	0.02	0.2	6	2.6	0.02	0.15	0.02	0.27	0.65	0.03	0.08	0.04
n = 45	Max	4.6	1,070	450	53,660	65	5.5	1.74	10,610	17	1.2	38	0.4	480	7.1	9.9	1,010	23
	Mean	0.5	4.0	19	16	4.9	0.4	0.5803	729	6.0	0.16	1.6	0.06	11	2.5	1.0	14	1.1
pyIII	Min	0.09	0.2	1.2	2.1	1.1	0.06	0.2	3	2.3	0.02	0.2	0.03	0.2	0.5	0.09	0.1	0.07
n = 129	Max	11.9	2,070	7,020	125,500	8,270	66.1	40	94,270	290	1.3	1,030	14.8	48,740	620	110	16,210	1,380
	Mean	0.4	11	30	166	10	1.4	1.9	6,950	11	0.27	2.9	0.3	14	6.8	7.0	23	8.9
apyIII	Min	0.2	0.5	9.5	84	3.1	0.06	0.6	163,150[1]	3.5	0.04	0.6	0.9	70	0.8	1.8	6.0	4.7
n = 11	Max	29	22	33.6	40,320	940	12.3	8.2	377,170[1]	70.8	1.9	1,260	4.3	7,280	250	460	1,780	790
	Mean	1.0	4.2	16	520	17	1.7	1.4	263,070[1]	17	0.3	27	2.1	1,249	12	55	171	158
pyIV	Min	0.1	0.1	3.6	4.0	1.5	0.2	0.7	2,970	17	0.1	0.4	0.04	0.4	1.7	0.1	0.6	0.02
n = 8	Max	6.4	0.3	7.2	21	12	2.8	1.8	18,870	200	0.3	3.2	0.07	26	18	2.6	100	2.6
	Mean	0.4	0.2	4.9	9.5	2.9	0.4	1.0	8,140	80	0.2	0.9	0.05	2.7	6.2	0.7	12	0.09

Abbreviations: n = number of LA spot analyses, LA-ICP-MS = laser ablation-inductively coupled plasma-mass spectrometry, Mean = arithmetic mean value

[1]Absolute values underestimated because of lack of external standard

concentration in the fluid together with an increase in pH, as may be inferred by the change from sericitic-type alteration (pyII stage, acidic pH) to carbonate mineral deposition (pyIII stage, near-neutral pH).

In summary, gold was likely deposited from a metal-undersaturated fluid and incorporated in a chemically bound state mainly into arsenian pyIII and arsenopyrite from reducing (H_2S-dominating) fluids of near-neutral pH—conditions that likely generated from the interaction of magmatic-derived fluid with organic-bearing sediments. At a somewhat later time, upon (partial) exhaustion of the organic sediment buffering capacities, conditions evolved to more oxidizing and acidic. Circulation of oxidizing (at the sulfate-sulfide coexistence boundary), acidic magmatic fluids with deposition of alunite and enargite indicate an environment typical of the upper part of a porphyry system (White and Hedenquist, 1990; Hedenquist and Lowenstern, 1994; Einaudi et al., 2003; Sillitoe and Hedenquist, 2003; Fontboté et al., 2017). The change from low- to intermediate- and to high-sulfidation states observed in most Peruvian Cordilleran-type deposits is commonly attributed to hydrolysis of SO_2 from magmatic acidic fluids progressively interacting with Paleozoic graphite-bearing phyllites, which have lesser abundance and weaker buffering capacities than C_{org} rocks at Shahuindo (Kouzmanov and Pokrovski, 2012; Fontboté, 2018, 2020; Benites et al., 2022). Further evidence for a magmatic origin of the gold-bearing fluid is provided by the presence of other trace elements such as Se, Ge, Mo, In, Ga, and Bi in pyIII. These elements are commonly found in pyrite formed in epithermal deposits hosted in volcanic rocks (Sykora et al., 2008; Ishida et al., 2022). This signature is in agreement with the elevated volatility and solubility of these elements in hydrothermal-magmatic fluids or vapor phases, produced during porphyry stages by magmatic fluid unmixing (e.g., Kouzmanov and Pokrovski, 2012; Pokrovski et al., 2013; Large et al., 2016).

Source of elements and mass balance considerations

Gold concentrations above 20 ppb were systematically analyzed in samples showing either direct (hydrothermal pyrite with or without other sulfides) or indirect (Fe excess compared to FeS_2 assuming all S in pyrite; Table 3) evidence of hydrothermal mineralization. In contrast, barren host-rock samples collected outside and within the deposit show gold content below 1 ppb. This value is lower than those suggested by Large et al. (2011) in a compilation of black shale compositions from Sukhoi Log, Carlin, and Bendigo. Our Au values in unmineralized samples also fall in the lower part of the concentration range of the typical black shales (0.2–11 ppb Au) of Johnson et al. (2017) and are far below the mean Au content of 7 ppb of carbonaceous black shales reported by Crocket (1991). The elevated Au values in sedimentary rocks cited in the previous work above might partly be due to higher detection limits of the analytical techniques used in those studies. Therefore, a value of 1 ppb Au can be used as a more realistic background value for the sediments of the Chicama Formation and the Goyllarisquizga Group that host part of the Shahuindo gold mineralization. The other part of gold at Shahuindo is hosted by strongly altered andesitic and dacitic intrusions. The gold content for andesitic to dacitic rocks is estimated to be 6 to 9 ppb (Moss et al., 2001; Chiaradia,
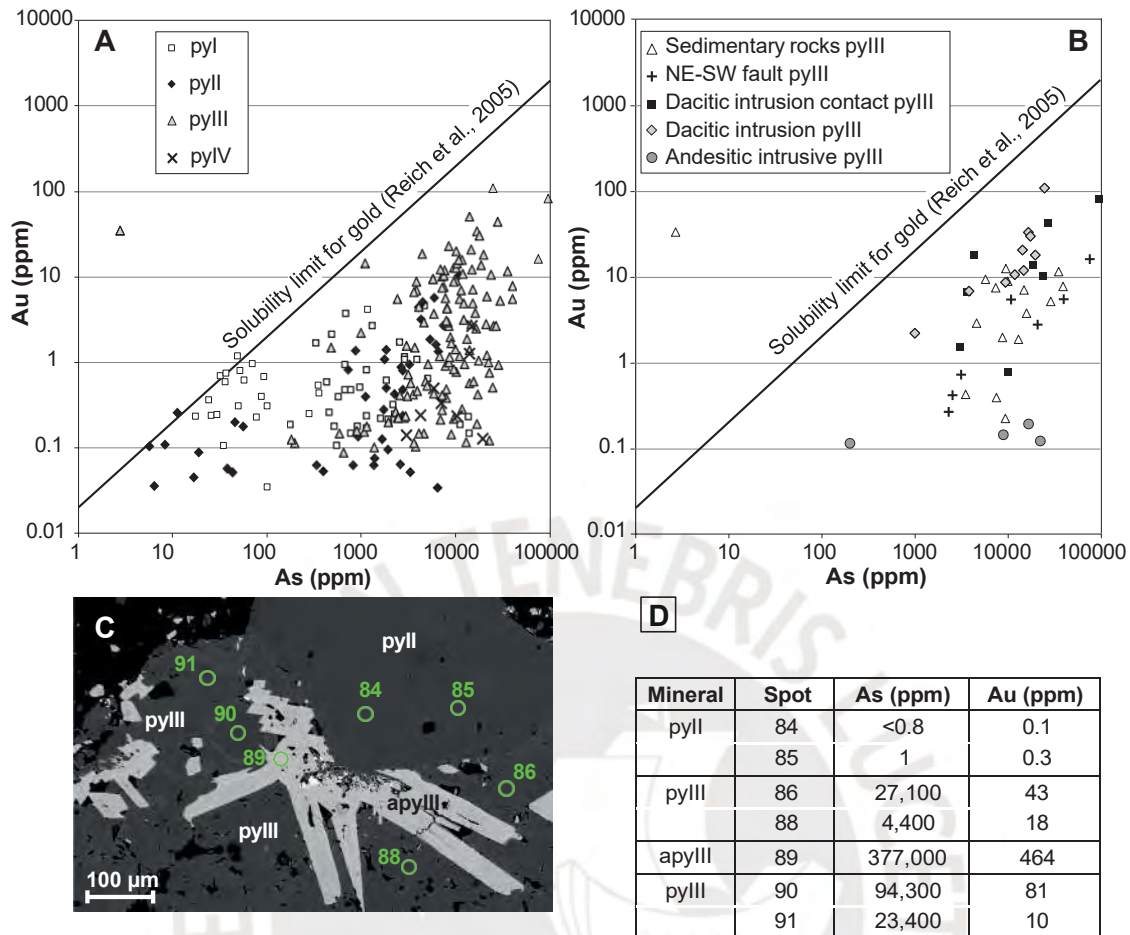
65

Fig. 11. Results of laser ablation-inductively coupled plasma-mass spectrometry (LA-ICP-MS) analyses of gold and arsenic concentrations in representative pyrite (py I to pyIV) and arsenopyrite samples from the Shahuindo deposit. A. Logarithmic plot of As versus Au for all pyrite generations. B. Logarithmic plot of As versus Au for pyIII from different host rocks. C. Scanning electron microscope photomicrograph of an Au-poor pyII grain with later Au- and As-bearing pyIII and coexisting arsenopyrite (apyIII); green circles show the position of LA-ICP-MS laser spots. D. As and Au concentrations obtained in the laser ablation spots indicated in C.

2020). We therefore adopted a value of 4 ppb Au as the most plausible background level for the global source rock, composed of sediments crosscut by intrusions, and we used this value in the mass balance analysis that follows.

Reserves estimates at Shahuindo are 59 t Au in the oxidized currently exploited part of the deposit. Considering a similar amount of the underlying primary sulfide ore, a total endowment of 100 t Au would be a reasonable estimate. Assuming 4 ppb Au in the source rock (density of 2.6 g/cm^3), with 50% efficiency for gold mobilization from the rock and 50% efficiency for subsequent Au deposition, 38.4 km^3 (3.4 × 3.4 × 3.4 km) of source rock would be necessary to supply 100 t of gold. This estimated volume is conservative because of the presence of numerous impermeable shale horizons, particularly in the Santa and Carhuaz Formations, which show no evidence of hydrothermal alteration. This mass balance analysis indicates that the host sedimentary rock alone cannot be regarded as the only source for gold in the deposit. This is because the potential size of the Shahuindo hydrothermal system, as estimated by the exploration drilling program (Defilippi et al., 2016) (Fig. 3), is less than ~2 km (≤8 km^3), which is almost five times smaller than the necessary volume

calculated above to account for the known Au tonnage. In addition, there is no evidence of massive release of gold from diagenetic pyrite related to a regional metamorphic event as in orogenic gold settings. The iron content of the host rock is also a key parameter, as its abundance and reactivity partly controls the H$_2$S fluid content and the resulting Au dissolved concentration in the form of sulfide complexes. The analyzed sedimentary rocks show an excess of iron compared to FeS$_2$, which decreases when approaching the mineralized zones. In the case of the intrusions, sericitic alteration is accompanied by iron sulfidation of mafic minerals. Iron sourced from magmatic minerals is sufficient to account for the abundance of pyrite in the system. However, an additional contribution of iron directly from magmatic fluids is also possible and would be in line with the large amount of pyrite observed within the massive contact bodies. Note that low-salinity aqueous fluids of magmatic origin, typical of porphyry-epithermal settings, are able to transport as much as tens of parts per million Au, 100 to 1,000 ppm As, and 10,000 ppm Fe, as demonstrated by the large body of direct fluid inclusion analyses available (e.g., Kouzmanov and Pokrovski, 2012). Our statistical sample is, however, not

sufficiently large to provide a more quantitative estimate of the amounts of the different pyrite types and their respective gold contributions compared to the whole mineralized rock. Nevertheless, our rough mass balance assessment above, combined with the observed mineral assemblages, and independent geochemical evidence from trace element patterns in pyrite, strongly suggests that a magmatic-hydro-

thermal source was the major metal supplier to the deposit

for both Au and As and partly for Fe. In-depth understanding of the mechanisms of Au transport and precipitation and

the effects of organic carbon and arsenic may be helped by physical-chemical modeling, as discussed below.

Thermodynamic modeling of mechanisms of gold and arsenic transport and precipitation

Based on the constraints detailed above, we simulated interactions of an Au-As-Fe–bearing hydrothermal fluid with an organic carbon-bearing rock, in an attempt to model gold transport and concentration mechanisms as they may have occurred in the Shahuindo deposit. In these simulations, gold and arsenic were assumed to be transported by moderate-salinity (7 wt % NaCl equiv; Na/K = 10) S-bearing (0.6 wt % total S) acidic fluids (pH < 3), such as typically exsolved in magmatic systems (Heinrich, 2005; Fontboté et al., 2017; references therein). We chose a wide range of redox potential (from strongly oxidized, sulfate-dominated, to strongly reduced, hydrogen sulfide-dominated), between 150°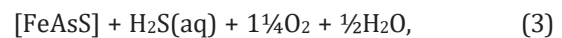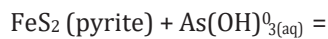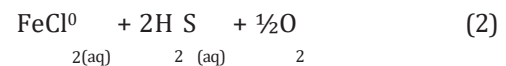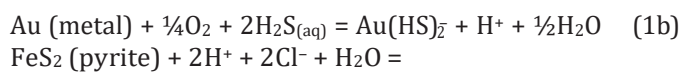 and 350°C at pressures of 100 to 1,000 bar. These conditions are consistent with the temperatures and sulfidation stages inferred in this study from mineral assemblages and with the general epithermal-like setting of the deposit (Defilippi et al., 2016). The fluid was assumed to interact with hydrocarbon-bearing sandstone/shale such as the host rocks of the sedimentary basin. In order to best evaluate the maximum potential for the fluid to transport Au and Fe, we assumed saturation with respect to metallic gold and pyrite. Arsenic was also added to the initial fluid at a level of 100 ppm, a typical concentration inferred from published fluid inclusion analyses from epithermal deposits (e.g., Kouzmanov and Pokrovski, 2012). Figure 12 shows the evolution of Au, Fe, and As, as well as sulfate, sulfide, trisulfur ion, methane, carbonate, and hydrogen concentrations, oxygen fugacity, and pH in two initially acidic (pH ~2.5) S-bearing (0.6 wt % total S) fluids of contrasting redox potential. One fluid is reduced (oxygen fugacity in log f_{O_2} relative to the conventional hematite-magnetite [HM] buffer, HM – 3) and the other is oxidized (log f_{O_2} = HM + 3). Each fluid type was allowed to interact at 300°C and 500 bar with a hydrocarbon-bearing rock (C_{org}, with a molal C/H ratio of 1) with progressively increasing modal C_{org} abundance (Fig. 12). Calculations at other T-P values within the chosen epithermal range (150°–350°C, 100–1,000 bar), and for rocks with different types of organic matter ranging from oil-like compositions (C/H ratio ~½) to matured kerogen (C/H ratio ~2) and to graphite (C/H ratio ∞), yielded very similar solubility trends and thus are not reported here in detail.

Our results show that the effect of organic matter on Au, As, and Fe solubility is strongly conditioned by the initial redox state of the fluid, yielding highly contrasting solubility trends for the three metals. These trends are driven by changes in three key parameters—redox potential, pH, and sulfide

activity—as they affect the solubility reactions for native gold and pyrite as well as the degree of arsenic and gold incorporation in pyrite:

$$Au\ (metal) + \tfrac{1}{4}O_2 + H_2S_{(aq)} = AuHS^0_{(aq)} + \tfrac{1}{2}H_2O \qquad (1a)$$

$$Au\ (metal) + \tfrac{1}{4}O_2 + 2H_2S_{(aq)} = Au(HS)_2^- + H^+ + \tfrac{1}{2}H_2O \qquad (1b)$$

$$FeS_2\ (pyrite) + 2H^+ + 2Cl^- + H_2O =$$

$$FeCl_2^0{}_{(aq)} + 2H_2S_{(aq)} + \tfrac{1}{2}O_2 \qquad (2)$$

$$FeS_2\ (pyrite) + As(OH)^0_{3(aq)} =$$

$$[FeAsS] + H_2S(aq) + 1\tfrac{1}{4}O_2 + \tfrac{1}{2}H_2O, \qquad (3)$$

where [FeAsS] denotes arsenopyrite or arsenian pyrite solid solution for simplicity. All reaction constituents other than pyrite, arsenopyrite, and gold metal are aqueous species in the single-phase liquid-like fluid. In these reactions, we have chosen O_2 because oxygen fugacity is the most widely admitted redox parameter and is conveniently referenced to common mineral buffers typical of hydrothermal systems (e.g., HM, or pyrite-pyrrhotite-magnetite [PPM]). Note that equivalent reactions may be written with any other oxidizing or reducing component, such as H_2, CH_4, CO_2, or CO, with no effect on the thermodynamic equilibrium relationships.

Figure 12 shows that the changes in f_{O_2}, pH, and sulfide activity are rather minor for an initial strongly reduced H_2S-dominated fluid interacting with organic carbon. This is because both fluid and rock have similar redox potential. In addition, the dissolution of hydrocarbon in water, leading to the formation of uncharged dominant species, CO_2, CH_4, and graphite, cannot generate significant changes in fluid acidity (Fig. 12A, B). As a result, the solubility of Fe increases only slightly and that of Au and As decreases slightly when the fluid reacts with the first portions of sedimentary rock. Such H_2S-rich acidic fluid can thus transport significant concentrations of Fe (~1,000 ppm) but rather low concentrations of Au (0.1 ppm) and As (<10 ppm), the latter being preferentially incorporated in arsenian pyrite (up to 10,000 ppm in the mineral). Thus, such fluids cannot transport significant amounts of As and Au together. Furthermore, they would rapidly lose their contents in the presence of reactive ferrous iron (FeO) present in carbonates and mafic silicates. These reactions altogether would lead to both a decrease in pH and consumption of H_2S through precipitation of pyrite (inverse of reaction 2), and concomitant gold deposition, mostly via decrease in H_2S activity in the fluid (inverse of reaction 1a, b).

A different scenario occurs for a more oxidized fluid containing sulfate upon interaction with the carbonaceous rock (Fig. 12C, D). Such a fluid, which initially transports Fe, As, and Au with concentrations of up to 1,000, 100, and 1 ppm, respectively, similar to the reduced fluid above, exhibits drastic changes when interacting with organic carbon. It can be seen in Figure 12C that Fe concentrations drop as much as six orders of magnitude even in the presence of quite low contents of C_{org} in the rock (<2 mol %), whereas As concentrations remain constant in the fluid, and only a small As fraction is incorporated into pyrite at tenors of few parts per million As. It is only when the aqueous sulfate is mostly consumed by reduction by organic carbon (C_{org} in rock >3 mol %) that As is incorporated into pyrite in amounts comparable to the naturally observed levels as found in this study (>10–100 ppm
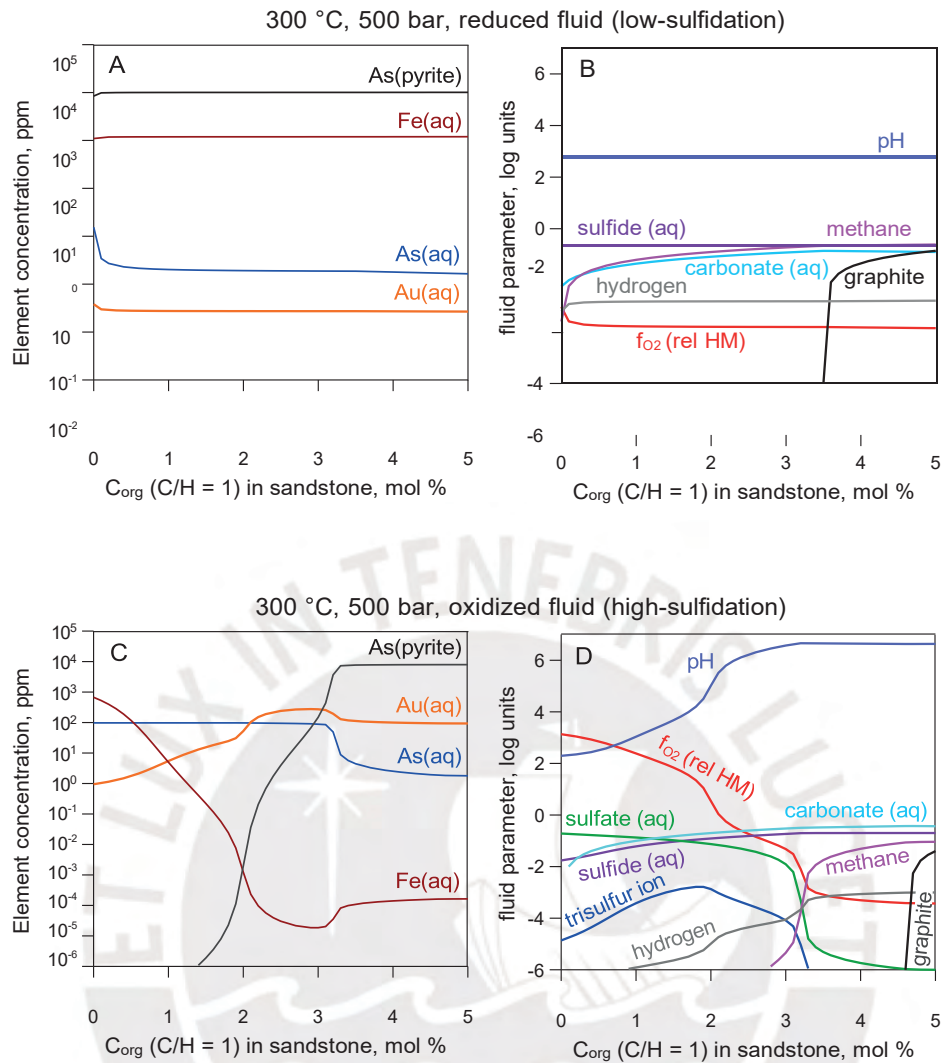
300 °C, 500 bar, reduced fluid (low-sulfidation)

300 °C, 500 bar, oxidized fluid (high-sulfidation)

Fig. 12. Diagrams showing the results of thermodynamic modeling of fluid-rock interactions in the context of the Shahuindo deposit. Two contrasting cases of the initial S-Au-As-Fe–bearing epithermal fluid are monitored: (A, B) reduced (H_2S-dominated) and (C, D) oxidized (sulfate-dominated). The low-salinity acidic (7 wt % NaCl equiv; 1 m NaCl + 0.1 m KCl + 0.05 HCl, pH = 2.5) magmatic-derived fluid containing 100 ppm As and saturated with pyrite and metallic gold was allowed to react at 300°C and 500 bar with a hydrocarbon-bearing shale at a mass fluid/rock ratio of 1:1 as a function of organic carbon content in the rock (C_{org}, with C/H atomic ratio of 1). A and C. Concentrations of dissolved Au, Fe, and As in the fluid (aq) and of As in pyrite as a function of CH content for a reduced (f_{O_2} is close to the conventional pyrite-pyrrhotite-magnetite redox buffer, PPM ≈ HM – 3) and an oxidized (f_{O_2} is above that of the hematite-magnetite buffer, HM + 3) initial fluid. B and D. Corresponding evolution of the fluid-phase concentrations (in log10 units of molality) of sulfide, sulfate, the S^{3-} ion, dissolved hydrogen, and carbon-bearing species, pH, and oxygen fugacity (relative to the HM buffer). It can be seen that organic carbon may exert a contrasting effect on the transport of different metals, depending on the initial fluid properties and the organic carbon (C_{org}) content. In particular, organic matter may promote, rather than limit, gold fluid transport in C_{org}-bearing sedimentary/metamorphic rocks (see text for discussion).

As in pyIII and apyIII). Gold shows a spectacular increase in its solubility, attaining several hundreds of parts per million Au at C contents in the system comparable to that of S (at C_{org} >2–3 mol %), followed by a slight decrease (to 10s ppm Au) when approaching the graphite saturation. These contrasting changes are fundamentally driven by the evolution of pH and redox of the sulfate-bearing fluid, which are controlled by thermochemical sulfate reduction (TSR) reactions:

$$SO_4^{2-} + CH_4 + 2 H^+ = H_2S_{(aq)} + CO_2 + 2H_2O \qquad (4)$$

$$CH_4 + 2O_2 = CO_2 + 2H_2O. \qquad (5)$$
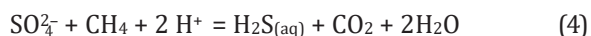
It can be seen in Figure 12D that proton-consuming reaction (4) induces a pH increase of >4 units (from ~2 to >6) upon fluid infiltration into the carbonaceous rock. At the same time, reaction (5), which consumes oxygen, leads to an f_{O2}

decrease of five to six orders of magnitude. Note that reaction (1b) imposes Au solubility to be linearly proportional to the H^+ activity, i.e., inverse of pH, but to be proportional only to the power of one-fourth of f_{O_2}. Likewise, pyrite solubility (reaction 3) is proportional to the square-power of H^+, but to only the power of one-half of f_{O_2}. Although changes in H_2S upon fluid interaction with organic matter are relatively small compared to those in pH (1 log unit H_2S concentration vs. >4 log units in pH; Fig. 12D), they do contribute to favoring Au solubility, in particular for reaction (1b). Therefore, increase in pH (and partly in H_2S) upon sulfate reduction by organic carbon appears to exert the major control on Au solubility for a typical epithermal fluid in a high-sulfidation regime. Thus, independently of the exact scenario of Fe and Au fluid-phase transport, whose details would depend on a fine interplay

VALLANCE ET AL.

between the exact fluid initial redox, S and C_{org} contents of the system, and the fluid/rock ratio, the effect of pH increase on Au solubility is generally much greater than the opposite effect of f_{O2} decrease. Thus, our modeling quantitatively demonstrates that TSR reactions of epithermal fluids may strongly enhance gold mobility and focused transfer from a magmatic source to a sedimentary organic-bearing rock sequence and its subsequent deposition in favorable structures such as anticlines. Hence, our findings question common belief that organic matter would be unfavorable for gold transport and therefore act as trap for this metal in hydrothermal systems (Radtke and Scheiner, 1970; Bierlein et al., 2001; Zhou et al., 2010; Phillips and Powell, 2013).

Gold incorporation in arsenian pyrite and arsenopyrite

Our quantitative thermodynamic modeling demonstrates that parts per million-level Au concentrations can be transported by moderately reduced to moderately oxidized (sulfate-sulfide coexistence) S-bearing epithermal fluids through organic-rich sedimentary rocks, without reaching saturation with the metal. Such gold metal-undersaturated fluids may lose their dissolved gold content by Au incorporation to arsenian pyrite in a chemically bound state. Although quantitative thermodynamic models of chemically bound Au incorporation in arsenian pyrite are not available at present, direct X-ray absorption spectroscopy data show Au to substitute for Fe in the octahedral sites by forming As-rich $[Au(As,S)_6]$ arsenopyrite-like moieties (Pokrovski et al., 2021). Combining this speciation data with a recent thermodynamic model proposed for arsenopyrite (Pokrovski et al., 2021), the following formal reaction may be considered for Au incorporation in arsenian pyrite:

$$Au(HS)_2^- + H^+ + As(OH)_{3(aq)}^0 =$$
$$[AuAsS]_{pyrite} + \tfrac{1}{2}O_2 + H_2S_{(aq)} + 2H_2O, \qquad (6)$$
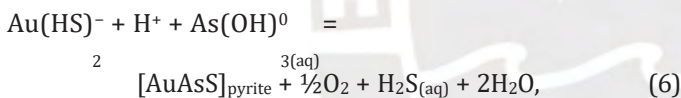
where $[AuAsS]_{pyrite}$ is the mole fraction of the fictive Au end member in the arsenian pyrite solid solution, and $Au(HS)_2^-$ and $As(OH)_3$ are the activities of the major Au and As aqueous species in the fluid. It can be seen from reaction (6) that the incorporation of Au in pyrite is directly favored by (1) higher Au and As dissolved concentrations, (2) more reducing conditions, (3) lower H_2S contents in the fluid, and (4) near-neutral pH at which Au is the most soluble as dihydrosulfide complexes. These trends are in good qualitative agreement with the increase of invisible Au concentrations in pyrite from the As-poor pyII of the low-sulfidation stage to As-rich pyIII (intermediate-sulfidation) and subsequent decrease in the more oxidized pyIV generation (high-sulfidation stage). More quantitative analysis of reaction (6) would require numerical values of its thermodynamic constant at a given T-P, coupled with more direct knowledge of the fluid composition gained from fluid inclusions, which are not presently available at Shahuindo. In the meantime, recent pyrite-fluid gold partitioning coefficients, experimentally measured by Kusebauch et al. (2019) at 200°C and Pokrovski et al. (2019, 2021) at 300° to 450°C, may be used for first-order estimations. Using an Au partition coefficient range of 100 to 1,000 between an arsenian pyrite with 0.1 to 1.0 wt % As and an S-bearing fluid carrying 0.1 to 1 ppm of Au (i.e., the typical Au concentration in epithermal porphyry-related fluids; Kouzmanov

and Pokrovski, 2012), it can be estimated that such a pyrite would incorporate 10 to 1,000 ppm of Au in a bound state. Remarkably, such predicted tenors are of the same order of magnitude as those measured in arsenian pyrites and arsenopyrites of this and many previous studies (Cathelineau et al., 1989; Cook and Chryssoulis, 1990; Fleet and Mummin, 1997; Simon et al., 1999; Reich et al., 2005; Muntean et al., 2011; Deditius et al., 2014; Belousov et al., 2016; Voute et al., 2019). As a conclusion, our thermodynamic analysis attests for the large potential capacity of As- and S-bearing fluids for focused Au transfer from magmatic settings and subsequent Au intake in arsenian pyrite in structural traps in organic carbon-bearing sedimentary basins.

Formation model for the Shahuindo deposit

The structural analysis, coupled with geochronological data, paragenetic sequence, mineralization and host-rock geochemistry, and thermodynamic modeling presented here, allows us to propose a new model for the Au-bearing magmatic-hydrothermal fluid evolution in the sedimentary setting of the Shahuindo deposit (Fig. 13). A magmatic source for Au, As, and partly Fe is supported by the solubility of these elements in fluids typical of the epithermal conditions that prevailed in the system (Fig. 12) as well as by mass balance constraints attesting that the amount of gold initially present in the sedimentary host rocks is insufficient to account for the total tonnage of the deposit. Dacitic intrusions rooted in a laccolith at depth were emplaced along thrust faults, anticline axial planes, and northeast-southwest transverse faults of the Algamarca-Shahuindo imbricate system. Gold- and arsenic-bearing aqueous fluids (possibly of variable sulfidation state) exsolved at depth from the crystallizing igneous complex and ascended into the sedimentary basin along the same paths as the intrusions. During the fluid ascent, its interactions with the sedimentary formations rich in organic carbon allowed for efficient and focused dissolved gold transport, without reaching saturation with metallic gold. This gold transfer occurred through the sedimentary sequence to structural (e.g., fractured anticline hinges, brecciated intrusion-sediment contact) or lithological (e.g., layers of permeable rock between less permeable strata) traps that resemble those commonly observed in oil systems. Entrapment of the Au-As-H_2S(-Fe)–bearing fluid in zones of reduced permeability, followed by its eventual cooling, favored invisible chemically bound gold incorporation in arsenian pyrite, thereby resulting in the formation of the orebodies.

The enhancement of hydrothermal gold transport by pH neutralization produced by feldspar alteration in igneous rocks or by calcite dissolution in sediments has been predicted thermodynamically in the literature to account for the large gold mobility in epithermal settings hosted within organic carbon-poor altered volcanic rocks (Heinrich, 2005). The chemical-level control of the enhancement of gold solubility is fundamentally similar in our model, as driven by reaction (1b), which is favored by both increasing pH and H_2S content. However, in our case the cause of this enhancement is the interaction of the fluid with carbonaceous matter, followed by subsequent gold incorporation in arsenian pyrite. Such a new combined mechanism of gold transport and precipitation in a sedimentary setting has not yet been documented.
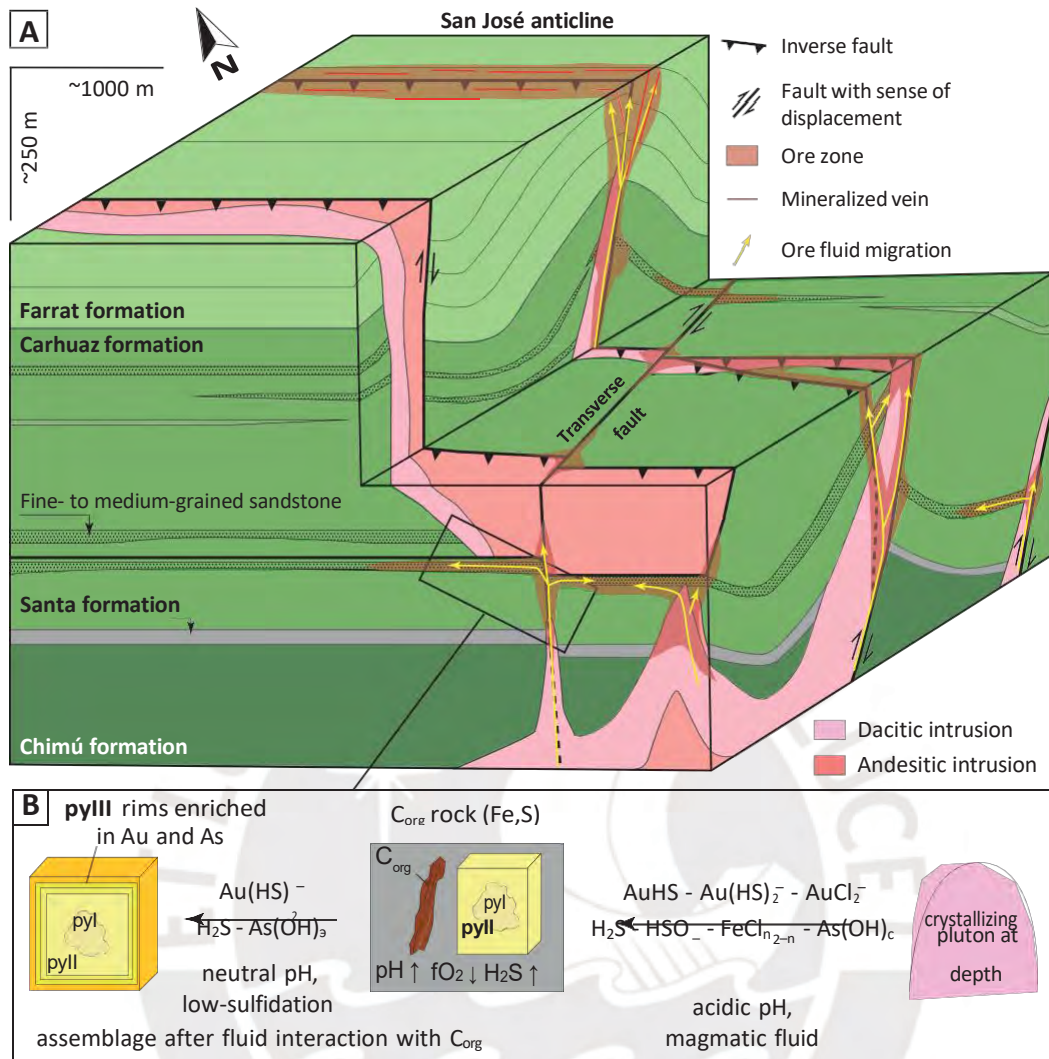
Fig. 13. A. Block diagram model of the Shahuindo deposit showing the location of the San José anticline, thrust and transverse faults, intrusion contacts, and permeable fine- to medium-grained sandstone horizons that control the location of gold ore. B. Schematic representation of the mineralization process, with gold transport by a magmatic fluid during its interaction with organic carbon (C_{org})-bearing sedimentary rocks, and subsequent gold scavenging from the fluid by arsenian pyrite. The key aqueous species of gold and associated elements are indicated.

This scenario is also different from the one generally assumed for Carlin-type deposits, where Au-bearing arsenian pyrite is formed by direct sulfidation of Fe-bearing carbonate rocks (Cline et al., 2005; Muntean et al., 2011; Kusebauch et al., 2019). Our mechanism is also different from those invoked in many other types of epithermal gold deposits, where boiling and fluid mixing in rock types lacking organic carbon are considered to be the dominant processes for gold deposition (e.g., Simmons et al., 2005, 2020). Although invisible gold in arsenian pyrite has been also recognized in different types of ore deposits such as orogenic (e.g., Large et al., 2007; Velasquez et al., 2014; Belousov et al., 2016; Simmons et al., 2020), intrusion-related (e.g., Voute et al., 2019), some porphyry Cu-Au (e.g., Deditius et al., 2014), and volcanogenic massive sulfide (e.g., Deditius et al., 2014; Belousov et al., 2016), its fraction appears to be small compared to the predominant visible metallic gold in those settings. In addition, the molecular state of invisible gold in pyrite from those settings

(nanoparticulate metal vs. chemically bound) is not well established. In contrast, chemically bound gold incorporation in arsenian pyrite is clearly the main gold depositional process at Shahuindo and suggests a new, previously disregarded mechanism for gold transport and deposition in organic carbon-rich sedimentary rocks in an epithermal setting.

Comparison with other gold deposits

The Shahuindo deposit shares some common features with Carlin-type deposits (Hofstra and Cline, 2000; Cline et al., 2005; Muntean et al., 2011; Rhys et al., 2015; Muntean and Cline, 2018; Henry et al., 2023), including (1) significant stratigraphic and structural ore control, (2) rarity of veins, (3) gold in a chemically bound state in arsenian pyrite, and (4) similar temperature and pressure conditions (150°–300°C, 100–1,000 bar). Conversely, Shahuindo differs from Carlin-type deposits by the following features: (1) apparently lower tonnages and grades (however, exploration in this area of the

VALLANCE ET AL.

Marañon fold-and-thrust belt is far more immature compared to the area of the Carlin trend), (2) a clearer genetic association between mineralization and coeval felsic magmatism as source of fluids and metals, (3) an episode of polymetallic mineralization, (4) high-sulfidation conditions reached locally, and (5) rarity of carbonates and lack of evidence of their sulfidation.

Shahuindo also displays some structural similarities with orogenic gold deposits hosted in carbonaceous sedimentary sequences. However, these deposits are believed to be formed through release of gold from diagenetic pyrite during regional metamorphism and associated compression. Gold deposition in such deposits occurred in anticlinal and/or thrust structures in higher and less metamorphosed portions of the sequence in response to sulfidation of the wall rock under relatively reducing conditions corresponding to the PPM mineral buffer (Mikucki, 1998; Goldfarb et al., 2005; Pitcairn et al., 2006; Large et al., 2011; Gaboury, 2013; Tomkins, 2013; Pokrovski et al., 2015). At Shahuindo, no evidence of regional metamorphism has been identified. Furthermore, the changing sulfidation conditions and the resulting hydrothermal alteration types are not compatible with a metamorphic model.

At Shahuindo, the presence of a significant magmatic-hydrothermal component of the fluids, the spatial association with intrusions, and the polymetallic stage are features in common with the distal disseminated gold ± silver deposit type (Cox, 1992; Muntean and Cline, 2018). In contrast, an important difference is the absence of a proximal zone that is typical in porphyry/skarn mineralization. Other notable differences from these distal deposits are the abundance of invisible gold mineralization and a large range of sulfidation conditions.

Gold association with low-sulfidation mineral assemblages at Shahuindo makes it similar to the low-sulfidation type of epithermal deposits. In addition, some low-sulfidation epithermal deposits contain auriferous pyrite, even though the gold speciation is not clear (John et al., 2003; Morishita et al., 2018). In contrast, in most classic low-sulfidation epithermal deposits, gold-bearing pyrite represents only a small fraction of the mineralization, in which gold occurs mainly as electrum (Au-Ag alloy). Furthermore, metal deposition in such deposits is usually accompanied by precipitation of large amounts of silica, carbonate, and adularia with textures indicative of boiling. Such features are not observed at Shahuindo.

The transition from low- to intermediate- and to high-sulfidation stages detected at Shahuindo may reflect the continued interaction of the magmatic fluids with the reactive C_{org}-bearing sedimentary rocks, with later fluid portions passing through already altered rocks, partly losing their chemical reactivity and buffering capacity. Alternatively, or in parallel, the evolution of the magmatic fluid itself from low-sulfidation to high-sulfidation might have contributed to this sequence. The latter is also a typical feature of many porphyry-related Zn-Pb-(Ag) deposits of central Peru known as Cordilleran-type deposits formed in an epithermal environment (Catchpole et al., 2015; Rottier et al., 2016; Fontboté, 2020; Benites et al., 2022). These deposits are believed to be formed via cooling of a metal-bearing fluid of magmatic origin in contact with silica-alumina-carbonate–bearing rocks. The Cordilleran-type deposits are, however, typically polymetallic (Cu, Zn, Pb, Ag) and relatively poor in gold. Thus, the Shahuindo deposit may represent a gold-rich end member where a previously disregarded very efficient mechanism of gold transport, concentration, and deposition in carbon-rich sedimentary setting played the major role.

Concluding Remarks

At Shahuindo, gold was transported and deposited after andesitic and dacitic bodies intruded into the sedimentary rocks. The shape of these bodies was controlled by thrusts that were imbricated in a northwest-southeast direction, along with associated folds and transverse faults that ran in a northeast-southwest direction. The auriferous orebodies were emplaced under similar structural control as the igneous bodies, with a strong influence from the anticlines, intrusion contacts, and permeable layers situated between impermeable horizons. This is a typical pattern seen in the formation of petroleum systems.

A thorough mineralogical and geochemical examination of the primary sulfide ore at Shahuindo has revealed that the majority of the gold is present in a chemically bound form in arsenian pyrite and arsenopyrite. These minerals were primarily deposited in a sedimentary environment under relatively low sulfidation conditions.

Additional geochemical analyses of the surrounding rock formations, coupled with mass balance constraints, have indicated that the sedimentary rocks alone did not contain sufficient gold, arsenic, and sulfur to be considered as the main source of the metals and ligands. Our results collectively support an igneous source of these metals, which may have been introduced via magmatic fluids exsolved from a plutonic complex crystallizing at depth.

The formation of the primary orebody could be envisaged by the following sequence of events. The ascent of magmatic aqueous fluids, likely acidic and rich in Au-As(-Fe) sulfate-sulfide, led to their interaction with the organic matter in the sedimentary sequence through TSR reactions. This process facilitated (or at least maintained) efficient transport of dissolved gold, enabling its deposition in structural and lithological traps in a chemically bound state within coprecipitating arsenian pyrite.

Implications for Exploration

These findings have significant implications for exploration, as invisible gold may be the main potential source of gold production in many countries (Berger et al., 2014; Volkov and Sidorov, 2017; Velasquez et al., 2020) despite the common a priori exclusion of refractory gold ores due to extraction difficulties. At the deposit scale, dating igneous intrusions, identifying arsenic, carbon, and gold geochemical anomalies in the rock and soil, and obtaining detailed trace element signatures in sulfide ore are of primary importance. At the regional scale, imbricated thrusts and folds should be targeted because they can provide pathways for magma and fluid migration to entrapment sites. Intersection of these structures with transverse faults may provide the necessary structural connectivity for an efficient flow of metal-bearing fluids sourced from crystalizing plutonic complexes at depth. This connectivity also makes it more probable for gold deposition to focus at such locations, which should be targeted during exploration. In

addition, anticlines, such as those in the thick, brittle Chimú and Farrat sandstones, are preferential zones for fluid entrapment between more impermeable rock types. Theses structural factors highlight the interest for constructing balanced cross sections in mineral exploration analogous to those extensively used by the oil industry for petroleum exploration in fold-and-thrust belts. These analogies with petroleum systems should prove helpful for developing mineral exploration strategies in sedimentary basins. Overall, our integrated structural, mineralogical, geochemical, and modeling study highlights an important potential of sedimentary carbon-bearing rocks in the formation and distribution of gold and associated critical metal resources.

Acknowledgments

REFERENCES

Akinfiev, N.N., and Diamond, L.W., 2003, Thermodynamic description of aqueous nonelectrolytes at infinite dilution over a wide range of state parameters: Geochimica et Cosmochimica Acta, v. 67, p. 613–627.

Arehart, G.B., Chryssoulis, S.L., and Kesler, S.E., 1993, Gold and arsenic in iron sulfides from sediment-hosted disseminated gold deposits: Implications for depositional processes: Economic Geology, v. 88, p. 171–185.

Bellier, O., Sébrier, M., Gasse, F., Fourtanier, E., and Robles, I., 1989, Evolution géodynamique mio-pliocène et quaternaire des bassins de la cordillère occidentale du Nord-Pérou: Les bassins de Cajabamba, San Marcos et Namora (département de Cajamarca): Géodynamique, v. 4, p. 93–118.

Belousov, I., Large, R.R., Meffre, S., Danyushevsky, L.V., Steadman, J., and Beardsmore, T., 2016, Pyrite compositions from VHMS and orogenic Au deposits in the Yilgarn craton, Western Australia: Implications for gold and copper exploration: Ore Geology Reviews, v. 79, p. 474–499.

Benavides-Cáceres, V., 1999, Orogenic evolution of the Peruvian Andes: The Andean cycle: Society of Economic Geologists, Special Publication 7, p. 61–107.

Benites, D., Torró, L., Vallance, J., Laurent, O., Quispe, P., Rosas, S., Uzieda, M.F., Holm-Denoma, C.S., Pianowski, L.S., Camprubí, A., et al., 2022, Geology, mineralogy, and cassiterite geochronology of the Ayawilca Zn-Pb-Ag-In-Sn-Cu deposit, Pasco, Peru: Mineralium Deposita, v. 57, p. 481–507.

Berger, V.I., Mosier, D.L., Bliss, J.D., and Moring, B.C., 2014, Sediment-hosted gold deposits of the world—database and grade and tonnage models: U.S. Geological Survey, Open-File Report 2014-1074, 51 p.

Bierlein, F.P., Cartwright, I., and McKnight, S., 2001, The role of carbonaceous "indicator" slates in the genesis of lode gold mineralization in the western Lachlan orogen, Victoria, southeastern Australia: Economic Geology, v. 96, p. 431–451.

Bissig, T., Ullrich, T., Tosdal, R., Friedman, R., and Ebert, S., 2008, The time-space distribution of Eocene to Miocene magmatism in the central Peruvian polymetallic province and its metallogenic implications: Journal of South American Earth Sciences, v. 26, p. 16–35.

Boiron, M.C., Cathelineau, M., and Trescases, J.J., 1989, Conditions of gold-bearing arsenopyrite crystallization in the Villeranges basin,

Marche-Combrailles shear zone, France: A mineralogical and fluid inclusion study: Economic Geology, v. 84, p. 1340–1362.

Boyer, S.E., and Elliott, D., 1982, The geometry of thrust systems: American Association of Petroleum Geologists, AAPG Bulletin, v. 66, p. 1196–1230.

Calderon, Y., Baby, P., Vela, C., Hurtado, A., Eude, A., Roddaz, M., Brusset, S., Calvés, G., and Bolaños, R., 2017, Petroleum systems restoration of the Huallaga-Marañon Andean retroforeland basin, Peru: Petroleum systems analysis-case studies: American Association of Petroleum Geologists (AAPG), Memoir 114, p. 95–116.

Catchpole, H., Kouzmanov, K., Putlitz, B., Seo, J.H., and Fontboté, L., 2015, Zoned base metal mineralization in a porphyry system: Origin and evolution of mineralizing fluids in the Morococha district, Peru: Economic Geology, v. 110, p. 39–71.

Cathelineau, M., Boiron, M.C., Holliger, P., Marion, P., and Denis, M., 1989, Gold-rich arsenopyrites: Crystal-chemistry, gold location and state, physical and chemical conditions of crystallization: Economic Geology Monograph 6, p. 328–341.

Chase, M.W., Jr., 1998, NIST-JANAF thermochemical tables, 4th ed.: The Journal of Physical Chemistry, Monograph 9, http://webbook.nist.gov/chemistry.

Chew, D., Schaltegger, U., Košler, J., Whitehouse, M.J., Gutjahr, M., Spikings, R.A., and Miškovic´, A., 2007, U-Pb geochronologic evidence for the evolution of the Gondwanan margin of the north central Andes: Geological Society of America Bulletin, v. 119, p. 697–711.

Chiaradia, M., 2020, Gold endowments of porphyry deposits controlled by precipitation efficiency: Nature Communications, v. 11, p. 1–10.

Cline, J.S., 2001, Timing of gold and arsenic sulfide mineral deposition at the Getchell Carlin-type gold deposit, north-central Nevada: Economic Geology, v. 96, p. 75–89.

Cline, J.S., Hofstra, A.H., Muntean, J.L., Tosdal, R.M., and Hickey, K.A., 2005, Carlin-type gold deposits in Nevada: Critical geological characteristics and geologic models: Economic Geology 100th Anniversary Volume, p. 451–484.

Cook, N.J., and Chryssoulis, S.L., 1990, Concentrations of "invisible gold" in the common sulfides: The Canadian Mineralogist, v. 28, p. 1–16.

Cox, D.P., 1992, Descriptive model of distal disseminated Ag-Au deposits: U.S. Geological Survey, Bulletin 2004, p. 19–22.

Crocket, J.H., 1991, Distribution of gold in the Earth's crust, *in* Foster, R.P., ed., Gold metallogeny and exploration: London, New York, Chapman and Hall, p. 1–36.

Dahlstrom, C.D.A., 1969, Balanced cross-sections: Canadian Journal of Earth Sciences, v. 6, p. 743–757.

Deditius, A.P., Utsunomiya, S., Renock, D., Ewing, R.C., Ramana, C.V., Becker, U., and Kesler, S.E., 2008, A proposed new type of arsenian pyrite: Composition, nanostructure and geological significance: Geochimica et Cosmochimica Acta, v. 72, p. 2919–2933.

Deditius, A.P., Reich, M., Kesler, S.E., Utsunomiya, S., Chryssoulis, S.L., Walshe, J., and Ewing, R.C., 2014, The coupled geochemistry of Au and As in pyrite from hydrothermal ore deposits: Geochimica et Cosmochimica Acta, v. 140, p. 644–670.

Defilippi, C.E., Dyer, T., and Tietz, P., 2012, Technical report on the Shahuindo heap leach project Cajabamba, Peru: Sulliden Gold Corporation, Ltd, NI 43-101 Technical Report 420 p.

Defilippi, C.E., Muerhoff, C.V., and Williams, T., 2016, Technical report on the Shahuindo mine, Cajabamba, Peru: Tahoe Resources, NI 43-101 Technical Report, 307 p.

Disnar, J.R., and Sureau, J.F., 1990, Organic matter in ore genesis: Progress and perspectives: Organic Geochemistry, v. 16, p. 577–599.

Drennan, G.R., and Robb, L.J., 2006, The nature of hydrocarbons and related fluids in the Witwatersrand basin, South Africa: Their role in metal redistribution: Geological Society of America, Special Paper 405, p. 353–385.

Drennan, G.R., Boiron, M.C., Cathelineau, M., and Robb, L.J., 1999, Characteristics of post-depositional fluids in the Witwatersrand basin: Mineralogy and Petrology, v. 66, p. 83–109.

Einaudi, M.T., Hedenquist, J.W., and Inan, E.E., 2003, Sulfidation state of fluids in active and extinct hydrothermal systems: Transitions from porphyry to epithermal environments: Society of Economic Geologists, Special Publication 10, p. 285–313.

Elliott, D., 1983, The construction of balanced cross-sections: Journal of Structural Geology, v. 5, p. 101.

Eude, A., 2014, La croissance des Andes centrales du nord du Pérou (5-9°S): Propagation d'un prisme orogénique dans un contexte d'héritage tectonique

et de subduction plane: Unpublished Ph.D. thesis, Toulouse, France, Paul Sabatier University, 323 p., https://tel.archives-ouvertes.fr/tel-01080498.

Eude, A., Roddaz, M., Brichau, S., Brusset, S., Baby, P., Calderon, Y., and Soula, J.C., 2015, Timing of exhumation and deformation in the northern Peruvian eastern Andean wedge as inferred from low temperature thermochronology and balanced cross section: Tectonics, v. 34, p. 715–730.

Fleet, M.E., and Mumin, A.H., 1997, Gold-bearing arsenian pyrite and marcasite and arsenopyrite from Carlin trend gold deposits and laboratory synthesis: American Mineralogist, v. 82, p. 182–193.

Fontboté, L., 2018, Ore deposits of the central Andes: Elements, v. 14, p. 257–261.

——2020, Systematic trends in the evolution of porphyry-related Zn-Pb-(Ag) deposits: Swiss Geoscience Meeting, Zurich, 2020, Abstracts, p. 40–41.

Fontboté, L., Kouzmanov, K., Chiaradia, M., and Pokrovski, G.S., 2017, Sulfide minerals in hydrothermal deposits: Elements, v. 13, p. 97–103.

Fuchs, S., Williams-Jones, A.E., Jackson S.E., and Przybylowicz, W.J., 2016, Metal distribution in pyrobitumen of the Carbon Leader reef, Witwatersrand supergroup, South Africa; evidence for liquid hydrocarbon ore fluids: Chemical Geology, v. 426, p. 45–59.

Gaboury, D., 2013, Does gold in orogenic deposits come from pyrite in deeply buried carbon-rich sediments? Insight from volatiles in fluid inclusions: Geology, v. 41, p. 1207–1210.

George, L.L., Cook, N.J., and Ciobanu, C.L., 2017, Minor and trace elements in natural tetrahedrite-tennantite: Effects of element partitioning among base metal sulphides: Minerals, v. 7, article 17.

Goldfarb, R.J., Baker, T., Dube, B., Groves, D.I., Hart, C.J.R., and Gosselin, P., 2005, Distribution, character, and genesis of gold deposits in metamorphic terranes: Economic Geology 100th Anniversary Volume, p. 407–450.

Gregory, D.D., Large, R.R., Bath, A.B., Steadman, J.A., Wu, S., Danyush- evsky, L., Bull, S.W., Holden, P., and Ireland, T.R., 2016, Trace element content of pyrite from the Kapai slate, St. Ives gold district, Western Aus- tralia: Economic Geology, v. 111, p. 1297–1320.

Gregory, D.D., Kovarik, L., Taylor, S.D., Perea, D.E., Owens, J.D., Atienza, N., and Lyons, T.W., 2022, Nanoscale trace-element zoning in pyrite framboids and implications for paleoproxy applications: Geology, v. 50, p. 736–740.

Hampel, A., 2002, The migration history of the Nazca ridge along the Peruvian active margin: A re-evaluation: Earth and Planetary Science Letters, v. 203, p. 665–679.

Hedenquist, J.W., and Lowenstern, J.B., 1994, The role of magmas in the formation of hydrothermal ore deposits: Nature, v. 370, p. 519–527.

Heinrich, C.A., 2005, The physical and chemical evolution of low-salinity magmatic fluids at the porphyry to epithermal transition: A thermodynamic study: Mineralium Deposita, v. 39, p. 864–889.

Helgeson, H.C., Kirkham, D.H., and Flowers, G.C, 1981, Theoretical prediction of the thermodynamic behavior of aqueous electrolytes at high pressures and temperatures: IV. Calculation of activity coefficients, osmotic coefficients and apparent molal and relative partial molal properties to 600°C and 5 kb: American Journal of Science, v. 281, p. 1249–1516.

Hemley, J.J., and Hunt, J.P., 1992, Hydrothermal ore-forming processes in the light of studies in rock-buffered systems: II. Some general geologic applications: Economic Geology, v. 87, p. 23–43.

Hemley, J.J., and Jones, W.R., 1964, Chemical aspects of hydrothermal alteration with emphasis on hydrogen metasomatism: Economic Geology, v. 59, p. 538–569.

Hofstra, A.H., and Cline, J.S., 2000, Characteristics and models for Carlin-type gold deposits: Reviews in Economic Geology, v. 13, p. 163–220.

Ishida, M., Romero, R., Leisen, M., Yasukawa, K., Nakamura, K., Barra, F., Reich, M., and Kato, Y., 2022, Auriferous pyrite formed by episodic fluid inputs in the Akeshi and Kasuga high-sulfidation deposits, Southern Kyushu, Japan: Mineralium Deposita, v. 57, p. 129–145.

Jacay, J., 2005, Análisis de la sedimentación del sistema cretáceo de los Andes del Perú Central: Revista del Instituto de Investigación-FIGMMG, Universidad Nacional Mayor de San Marcos, Peru, v. 8, p. 49–59.

Jaillard, E., and Jacay, J., 1989, Les Couches Chicama du Nord du Pérou: Colmatage d'un bassin né d'une collision oblique au tithonique: Comptes rendus de l'Académie des sciences. Série 2, Mécanique, Physique, Chimie, Sciences de l'univers, Sciences de la Terre, v. 308, p. 1459–1465.

John, D.A., Hofstra, A.H., Fleck, R.J., Brummer, J.E., and Saderholm, E.C., 2003, Geologic setting and genesis of the Mule Canyon low-sulfidation epithermal gold-silver deposit, north-central Nevada: Economic Geology, v. 98, p. 425–463.

Johnson, J.W., Oelkers, E.H., and Helgeson, H.C., 1992, SUPCRT92: A software package for calculating the standard molal thermodynamic properties of minerals, gases, aqueous species, and reactions from 1 to 5000 bar and 0 to 1000°C: Computers and Geoscience, v. 18, p. 899–947, updated version based on a series of subsequent papers reporting HKF parameters for most ions and aqueous complexes available online at http://geopig3.la.asu.edu:8080/GEOPIG/index.html.

Johnson, S.C., Large, R.R., Coveney, R.M., Kelley, K.D., Slack, J.F., Stead- man, J.A., Gregory, D.D., Sack, P.J., and Meffre, S., 2017, Secular distri- bution of highly metalliferous black shales corresponds with peaks in past atmosphere oxygenation: Mineralium Deposita, v. 52, p. 791–798.

Kokh, M.A., Lopez, M., Gisquet, P., Lanzanova, A., Candaudap, F., Besson, P., and Pokrovski, G.S., 2016, Combined effect of carbon dioxide and sulfur on vapor-liquid partitioning of metals in hydrothermal systems: Geochimica et Cosmochimica Acta, v. 187, p. 311–333.

Kokh, M.A., Akinfiev, N.N., Pokrovski, G.S., Salvi, S., and Guillaume, D., 2017, The role of carbon dioxide in the transport and fractionation of metals by geological fluids: Geochimica et Cosmochimica Acta, v. 197, p. 433–466.

Kouzmanov, K., and Pokrovski, G.S., 2012, Hydrothermal controls on metal distribution in Cu(-Au-Mo) porphyry systems: Society of Economic Geologists, Special Publication 16, p. 573–618.

Kusebauch, C., Gleeson, S.A., and Oelze, M., 2019, Coupled partitioning of Au and As into pyrite controls the formation of giant Au deposits: Science Advances, v. 5, article eaav5891.

Large, R.R., Maslennikov, V.V., Robert, F., Danyushevsky, L., and Chang Z., 2007, Multistage sedimentary and metamorphic origin of pyrite and gold in the giant Sukhoi Log deposit, Lena gold province, Russia: Economic Geology, v. 102, p. 1233–1267.

Large, R.R., Danyushevsky, L., Hollit, C., Maslennikov, V., Meffre, S., Gil- bert, S., Bull, S., Scott, R., Emsbo, P., Thomas, H., Singh, B., and Foster, J., 2009, Gold and trace element zonation in pyrite using a laser imaging technique: Implications for the timing of gold in orogenic and Carlin-style sediment-hosted deposits: Economic Geology, v. 104, p. 635–668.

Large, R.R., Bull, S.W., and Maslennikov, V.V., 2011, A carbonaceous sedi- mentary source-rock model for Carlin-type and orogenic gold deposits: Economic Geology, v. 106, p. 331–358.

Large, R.R., Thomas, H., Craw, D., Henne, A., and Henderson, S., 2012, Diagenetic pyrite as a source for metals in orogenic gold deposits, Otago schist, New Zealand: New Zealand Journal of Geology and Geophysics, v. 55, no. 2, p. 137–149.

Large, S.J.E., Bakker, E.Y.N., Weis, P., Wälle, M., Ressel, M., and Heinrich C.A., 2016, Trace elements in fluid inclusions of sediment-hosted gold deposits indicate a magmatic-hydrothermal origin of the Carlin ore trend: Geology, v. 44, p. 1015–1018.

Magoon, L.B., and Dow, W.G., 1994, The petroleum system: American Asso- ciation of Petroleum Geologists (AAPG), Memoir 60, p. 3–24.

Manceau, A., Merkulova, M., Mathon, O., Glatzel, P., Murdzek, M., Batanova, V., Simionovici, A., Steinmann, S.N., and Paktunc, D., 2020, The mode of incorporation of As(-I) and Se(-I) in natural pyrite revisited: ACS Earth Space Chemistry, v. 4, p. 379–390.

Mégard, F., 1984, The Andean orogenic period and its major structures in central and northern Peru: Journal of the Geological Society of London, v. 141, p. 893–900.

Migdisov, A.A., Guo, X., Williams-Jones, A.E., Sun, C.J., Vasyukova, O., Sugi- yama, I., Fuchs, S., Pearce, K., and Roback, R., 2017, Hydrocarbons as ore fluids: Geochemical Perspectives Letters, v. 5, p. 47–52.

Mikucki, E.J., 1998, Hydrothermal transport and depositional processes in Archean lode-gold systems: A review: Ore Geology Reviews, v. 13, p. 307–321.

Morishita, Y., Shimada, N., and Shimada, K., 2018, Invisible gold in arsenian pyrite from the high-grade Hishikari gold deposit, Japan: Significance of variation and distribution of Au/As ratios in pyrite: Ore Geology Reviews, v. 95, p. 79–93.

Moss, R., Scott, S.D., and Binns, R.A., 2001, Gold content of Eastern Manus basin volcanic rocks: Implications for enrichment in associated hydrother- mal precipitates: Economic Geology, v. 96, p. 91–107.

Muntean, J.L., 2020, Carlin-type gold deposits in Nevada: Geologic charac- teristics, critical processes, and exploration: Society of Economic Geolo- gists, Special Publication 23, p. 775–795.

Muntean, J.L., and Cline, J.S., 2018, Diversity of Carlin-style gold deposits: Reviews in Economic Geology, v. 20, p. 1–5.

Muntean, J.L., Cline, J.S., Simon, A.C., and Longo, A.A., 2011, Magmatic hydrothermal origin of Nevada's Carlin-type gold deposits: Nature Geosci- ence, v. 4, p. 122–127.

Navarro Colque, P., Rivera Porras, M., and Monge Miguel, R., 2010, Geología y metalogenia del Grupo Calipuy (Volcanismo Cenozoico) Segmento Santiago de Chuco, Norte del Perú: Ministerio de Energía y Minas e INGEMMET, Boletín 28 Serie D, Estudios Regionales, 201 p.

Noble, D.C., and McKee, E.H., 1999, The Miocene metallogenic belt of central and northern Perú: Society of Economic Geologists, Special Publication 7, p. 155–193.

Noble, D.C., McKee, E.H., and Mégard, F., 1979, Early tertiary "Incaic" tectonism, uplift, and volcanic activity, Andes of Central Peru: Geological Society of America Bulletin, v. 90, p. 903–907.

Noble, D.C., McKee, E.H., Mourier, T., and Mégard, F., 1990, Cenozoic stratigraphy, magmatic activity, compressive deformation, and uplift in northern Peru: Geological Society of America Bulletin, v. 102, p. 1105–1113.

Norman, M.D., Pearson, N.J., Sharma, A., and Griffin, W.L., 1996, Quantitative analysis of trace elements in geological materials by laser ablation ICP-MS: Instrumental operating conditions and calibration values of NIST glasses: Geostandards Newsletter, v. 20, p. 247–261.

Oelkers, E.H., Benezeth, P., and Pokrovski, G.S., 2009, Thermodynamic databases for water-rock interaction: Reviews in Mineralogy and Geochemistry, v. 70, p. 1–46.

Percival, T.J., Hofstra, A.H., Gibson, P.C., Noble, D.C., Radtke, A.S., Bagby, W.C., Pickthorn, W.J., and McKee, E.H., 2018, Sedimentary rock-hosted gold deposits related to epizonal intrusions, Bau district, Island of Borneo, Sarawak, East Malaysia: Reviews in Economic Geology, v. 20, p. 259–297.

Perfetti, E., Pokrovski, G.S., Ballerat-Busserolles, K., Majer, V., and Gibert, F., 2008, Densities and heat capacities of aqueous arsenious and arsenic acid solutions to 350°C and 300 bar, and revised thermodynamic properties of $As(OH)_{3(aq)}^0$, $AsO(OH)_{3(aq)}^0$ and iron sulfarsenide minerals: Geochimica et Cosmochimica Acta, v. 72, p. 713–731.

Petroleum Experts, 2022, Petroleum engineering and structural geology software: www.petex.com/products/move-suite/.

Phillips, G.N., and Powell, R., 2013, Origin of Witwatersrand gold: A metamorphic devolatilization-hydrothermal replacement model: Applied Earth Science, v. 120, no. 3, p. 112–129.

Phillips, G.N., Groves, D.I., and Brown, I.J., 1987, Source requirements for the Golden Mile, Kalgoorlie—significance to the metamorphic replacement model for Archean gold deposits: Canadian Journal of Earth Sciences, v. 24, p. 1643–1651.

Pitcairn, I.K., Teagle, D.A.H., Craw, D., Olivo, G.R., Kerrich, R., and Brewer, T.S., 2006, Sources of metals and fluids in orogenic gold deposits: Insights from the Otago and Alpine schists, New Zealand: Economic Geology, v. 101, p. 1525–1546.

Pokrovski, G.S., and Dubessy, J., 2015, Stability and abundance of the trisulfur radical ion S_3^- in hydrothermal fluids: Earth and Planetary Sciences Letters, v. 411, p. 298–309.

Pokrovski, G.S., Kara, S., and Roux, J., 2002, Stability and solubility of arsenopyrite, FeAsS, in crustal fluids: Geochimica et Cosmochimica Acta, v. 66, p. 2361–2378.

Pokrovski, G.S., Borisova, A.Y., and Bychkov, A.Y., 2013, Speciation and transport of metals and metalloids in geological vapors: Reviews in Mineralogy and Geochemistry, v. 76, p. 165–218.

Pokrovski, G.S., Akinfiev, N.N., Borisova, A.Y., Zotov, A.V., and Kouzmanov, K., 2014, Gold speciation and transport in geological fluids: Insights from experiments and physical-chemical modelling: Geological Society of London, Special Publication 402, p. 9–70.

Pokrovski, G.S., Kokh, M.A., Guillaume, D., Borisova, A.Y., Gisquet, P., Hazemann, J.-L., Lahera, E., Del Net, W., Proux, O., Testemale, D., et al., 2015, Sulfur radical species form gold deposits on Earth: Proceedings of the National Academy of Sciences of the United States of America, v. 112, p. 13,484–13,489.

Pokrovski, G.S., Kokh, M.A., Proux, O., Hazemann, J.L., Bazarkinac, E.F., Testemale, D., Escoda, C., Boiron, M.C., Blanchard, M., Aigouy, T., Gouy, S., de Parseval, P., and Thibaut, M., 2019, The nature and partitioning of invisible gold in the pyrite-fluid system: Ore Geology Reviews, v. 109, p. 545–563.

Pokrovski, G.S., Escoda, C., Blanchard, M., Testemale, D., Hazemann, J.L., Gouy, S., Kokh, M.A., Boiron, M.C., de Parseval, F., Aigouy, T., et al., 2021, An arsenic-driven pump for invisible gold in hydrothermal systems: Geochemical Perspectives Letters, v. 17, p. 39–44.

Pokrovski, G.S., Desmaele, E., Laskar, C., Bazarkina, E.F., Testemale, D., Hazemann, J.-L., Vuilleumier, R., Seitsonen, A.P., Ferlat, G., and Saitta, A.M., 2022a, Gold speciation in hydrothermal fluids revealed by in situ high

energy resolution X-ray absorption spectroscopy: American Mineralogist, v. 107, p. 369–376.

Pokrovski, G.S., Sanchez-Valle, C., Guillot, S., Borisova, A.Y., Muñoz, M., Auzende, A-L., Proux, O., Roux, J., Hazemann, J-L., Testemale, D., and Shvarov, Y.V., 2022b, Redox dynamics of subduction revealed by arsenic in serpentinite: Geochemical Perspectives Letters, v. 22, p. 36–41.

Prudhomme, A., Baby, P., Robert, A., Brichau, S., Cuipa, E., Eude, A., Calderon, Y., and Sullivan, P., 2019, Western thrusting and uplift in the northern Central Andes (Western Peruvian margin), *in* Horton, B.K., and Folguera, A., eds., Andean tectonics: Amsterdam, Elsevier, p. 299–331.

Radtke, A.S., and Scheiner, B.J., 1970, Studies of hydrothermal gold deposition (I); Carlin gold deposit, Nevada: The role of carbonaceous materials in gold deposition: Economic Geology, v. 65, p. 87–102.

Radtke, A.S., Taylor, C.M., and Christ, C.L., 1972, Chemical distribution of gold and mercury at the Carlin deposit, Nevada [abs.]: Geological Society of America Abstracts with Programs, v. 4, p. 632.

Reich, M., and Becker, U., 2006, First-principles calculations of the thermodynamic mixing properties of arsenic incorporation into pyrite and marcasite: Chemical Geology, v. 225, no. 3–4, p. 278–290.

Reich, M., Kesler, S.E., Utsunomiya, S., Palenik, C.S., Chryssoulis, S.L., and Ewing, R.C., 2005, Solubility of gold in arsenian pyrite: Geochimica et Cosmochimica Acta, v. 69, p. 2781–2796.

Rhys, D., Valli, F., Burgess, R., Heitt, D., Griesel, G., and Hart, K., 2015, Controls of fault and fold geometry on the distribution of gold mineralization on the Carlin trend, *in* Pennell, W.M., and Garside, L.J., eds., New concepts and discoveries: 2015 Symposium proceedings: Reno, Nevada, Geological Society of Nevada, p. 333–389.

Richards, J.P., 2003, Tectono-magmatic precursors for porphyry Cu-(Mo-Au) deposit formation: Economic Geology, v. 98, p. 1515–1533.

Robb, L.J., and Meyer, F.M., 1995, The Witwatersrand basin, South Africa: Geological framework and mineralization processes: Ore Geology Reviews, v. 10, p. 67–94.

Robie, R.A., and Hemingway, B.S., 1995, Thermodynamic properties of minerals and related substances at 298.15 K and 1 bar (10^5 Pascals) pressure and at higher temperatures: U.S. Geological Survey, Bulletin 2131, 461 p.

Rosenbaum, G., Giles, D., Saxon, M., Betts, P.G., Weinberg, R.F., and Duboz, C., 2005, Subduction of the Nazca Ridge and the Inca Plateau: Insights into the formation of ore deposits in Peru: Earth and Planetary Science Letters, v. 239, p. 18–32.

Rottier, B., Kouzmanov, K., Wälle, M., Bendezú, R., and Fontboté, L., 2016, Sulfide replacement processes revealed by textural and LA-ICP-MS trace element analyses: Example from the early mineralization stages at Cerro de Pasco, Peru: Economic Geology, v. 111, p. 1347–1367.

Rottier, B., Kouzmanov, K., Casanova, V., Wälle, M., and Fontboté, L., 2018, Cyclic dilution of magmatic metal-rich hypersaline fluids by magmatic low-salinity fluid: A major process generating the giant epithermal polymetallic deposit of Cerro de Pasco, Peru: Economic Geology, v. 113, p. 825–856.

Scherrenberg, A.F., Konh, B.P., Holcombe, R.J., and Rosenbaum, G., 2016, Thermotectonic history of the Marañón fold-thrust belt, Peru: Insights into mineralisation in an evolving orogeny: Tectonophysics, v. 667, p. 16–36.

Seedorff, E., Dilles, J.H., Proffett J.M., Jr., Einaudi, M.T., Zurcher, L., and Stavast, W.J.A., 2005, Porphyry deposits: Characteristics and origin of hypogene features: Economic Geology 100th Anniversary Volume, p. 251–298.

Seward, T.M., 1973, Thio complexes of gold and the transport of gold in hydrothermal ore solutions: Geochimica et Cosmochimica Acta, v. 37, p. 379–399.

Shvarov, Y.V., 2008, HCh: New potentialities for the thermodynamic simulation of geochemical systems offered by Windows: Geochemistry International, v. 46, p. 834–839.

——2015, A suite of programs, OptimA, OptimB, OptimC, and OptimS, compatible with the Unitherm database, for deriving the thermodynamic properties of aqueous species from solubility, potentiometry and spectroscopy measurements: Applied Geochemistry, v. 55, p. 17–27, www.geol.msu.ru/deps/geochems/soft/index_e.html.

Sillitoe, R.H., 2020, Gold deposit types: An overview: Society of Economic Geologists, Special Publication 23, p. 1–28.

Sillitoe, R.H., and Hedenquist, J.W., 2003, Linkages between volcanotectonic settings, ore-fluid compositions, and epithermal precious metal deposits: Society of Economic Geologists, Special Publication 10, p. 315–343.

Simmons, S.F., White, N.C., and John, D.A., 2005, Geological characteristics of epithermal precious and base metal deposits: Economic Geology 100th Anniversary Volume, p. 485–522.

Simmons, S.F., Tutolo, B., Barker, S.L., Goldfarb, R., and Robert, F., 2020, Hydrothermal gold deposition in epithermal, Carlin, and orogenic deposits geothermal resources: Society of Economic Geologists, Special Publication 23, p. 823–845.

Simon, G., Kesler, S.E., and Chryssoulis, S., 1999, Geochemistry and textures of gold-bearing arsenian pyrite, Twin Creeks, Nevada; implications for deposition of gold in Carlin-type deposits: Economic Geology, v. 94, p. 405–421.

Stefánsson, A., and Seward, T.M., 2004, Gold(I) complexing in aqueous sulphide solutions to 500°C at 500 bar: Geochimica et Cosmochimica Acta, v. 68, p. 4121–4143.

Sverjensky, D.A., Harrison, B., and Azzolini, D., 2014, Water in the deep Earth: The dielectric constant and the solubilities of quartz and corundum to 60 kb and 1200°C: Geochimica et Cosmochimica Acta, v. 129, p. 125–145.

Sykora, S., Cooke, D.R., Meffre, S., Stephanov, A.S., Gardner, K., Scott, R., Selley, D., and Harris, A.C., 2018, Evolution of pyrite trace element compositions from porphyry-style and epithermal conditions at the Lihir gold deposit: Implications for ore genesis and mineral processing: Economic Geology, v. 113, p. 193–208.

Sylvester, P., Cabri, L.J., Tubrett, M., McMahon, G., Laflamme, J., and Peregoedova, A., 2005, Synthesis and evaluation of a fused pyrrhotite standard reference material for platinum group elements and gold analysis by laser ablation-ICP-MS: 10th International Platinum Symposium, Oulu, Finland, August 8–11, 2005, Proceedings, p. 16–20.

Tagirov, B.R., Salvi, S., Schott, J., and Baranova, N.N., 2005, Experimental study of gold-hydrosulphide complexing in aqueous solutions at 350–500°C, 500 and 1000 bars using mineral buffers: Geochimica et Cosmochimica Acta, v. 69, p. 2119–2132.

Testemale, D., Brugger, J., Liu, W., Etschmann, B., and Hazemann, J.-L., 2009, In-situ X-ray absorption study of iron (II) speciation in brines up to supercritical conditions: Chemical Geology, v. 264, p. 295–310.

Tomkins, A.G., 2013, On the source of orogenic gold: Geology, v. 41, p. 1255–1256.

Vallance, J., Balboa, M., Berna, B., Cabrera, O., Baya, C., Baby, P., and Pokrovski, G.S., 2018, Oro y material orgánico en el depósito de Shahuindo (Cajamarca, Peru): XIX Congreso Peruano de Geología, Lima, Peru, 2018, Conference Abstract, 4 p.

Velásquez, G., Béziat, D., Salvi, S., Siebenaller, L., Borisova, A.Y., Pokrovski, G.S., and de Parseval, P., 2014, Formation and deformation of pyrite and implications for gold mineralization in the El Callao district, Venezuela: Economic Geology, v. 109, p. 457–486.

Velásquez, G., Estay, H., Vela, I., Salvi, S., and Pablo, M., 2020, Metal-selective processing from the Los Sulfatos porphyry-type deposit in Chile: Co, Au, and Re recovery workflows based on advanced geochemical characterization: Minerals, v. 10, article 531.

Vigneresse, J.L., Tikoff, B., and Améglio, L., 1999, Modification of the regional stress field by magma intrusion and formation of tabular granitic plutons: Tectonophysics, v. 302, p. 203–224.

Volkov, A.V., and Sidorov, A.A., 2017, Invisible gold: Herald of the Russian Academy of Sciences, v. 87, p. 40–48.

Voute, F., Hagemann, S.G., Evans, N.J., and Villanes, C., 2019, Sulfur isotopes, trace element, and textural analyses of pyrite, arsenopyrite and base metal sulfides associated with gold mineralization in the Pataz-Parcoy district, Peru: Implication for paragenesis, fluid source, and gold deposition mechanisms: Mineralium Deposita, v. 54, p. 1077–1100.

Wells, J.D., and Mullens, T.E., 1973, Gold-bearing arsenian pyrite determined by microprobe analysis, Cortez and Carlin gold mines, Nevada: Economic Geology, v. 68, p. 187–201.

White, N.C., and Hedenquist, J.W., 1990, Epithermal environments and styles of mineralization: Variations and their causes, and guidelines for exploration: Journal of Geochemical Exploration, v. 36, p. 445–474.

Wilson, S.A., Ridley, W.I., and Koenig, A.E., 2002, Development of sulfide calibration standards for the laser ablation inductively-coupled plasma mass spectrometry technique: Journal of Analytical Atomic Spectrometry, v. 17, p. 406–409.

Wu, X., and Delbove, F., 1989, Hydrothermal synthesis of gold-bearing arsenopyrite: Economic Geology, v. 84, p. 2029–2032.

Xie, Z.J., Xia, Y., Cline, J.S., Koenig, A., Wei, D.T., Tan, Q.P., Wang, Z.P., and Muntean, J.L., 2018, Are there Carlin-type gold deposits in China? A comparison of the Guizhou, China, deposits with Nevada, USA, deposits: Reviews in Economic Geology, v. 20, p. 187–233.

Xing, Y., Brugger, J., Tomkins, A., and Shvarov, Y., 2019, Arsenic evolution as a tool for understanding formation of pyritic gold ores: Geology, v. 47, p. 335–338.

Zhou, T., Phillips, G.N., Denn, S., and Burke, S., 2010, Woodcutters goldfield: Gold in an Archaean granite, Kalgoorlie, Western Australia: Australian Journal of Earth Sciences, v. 50, p. 553–569.

Zimmer, K., Zhang, Y.L., Lu, P., Chen, Y.Y., Zhang, G.R., Dalkilic, M., and Zhu, C., 2016, SUPCRTBL: A revised and extended thermodynamic dataset and software package of SUPCRT92: Computers and Geosciences, v. 90, p. 97–111.

Zotov, A.V., Kuzmin, N.N., Reukov, V.L., and Tagirov, B.R., 2018, Stability of AuCl⁻ from 25 to 1000°C at pressure to 5000 bar and consequences for hydrothermal gold mobilization: Minerals, v. 8, article 286, p. 1–15.

Jean Vallance received his Ph.D. degree from the University of Nancy, France, in 2001. In 2002 he joined the Geneva University (Switzerland) as a postdoc. From 2007 to 2013, he worked in the mineral industry as an exploration geologist in the Morococha and San Rafael deposits, Peru. In 2014, he was appointed associate professor at the Pontifical Catholic University of Peru. He currently is a part-time profesor in economic geology at the Pontifical Catholic University of Peru and teaches earth and life sciences in secondary schools in France. His research focuses on orogenic, skarn, and epithermal gold deposits.

Chapter III. ORIGIN AND EVOLUTION OF GOLD-BEARING FLUIDS IN A CARBON-RICH SEDIMENTARY BASIN: A CASE STUDY OF THE ALGAMARCA EPITHERMAL GOLD-SILVER-COPPER DEPOSIT, NORTHERN PERU

Chapter III

This chapter presents a published article in the journal Ore Geology Reviews (Galdos R., Vallance J., Baby P., Salvi S., Schirra M., Velasquez G., Viveen W., Soto R., and Pokrovski G. S., 2024. "*Origin and evolution of gold-bearing fluids in a carbon-rich sedimentary basin: a case study of the Algamarca epithermal gold-silver-copper deposit, Northern Peru*". Ore Geol. Rev. 166, 105857. https://doi.org/10.1016/j.oregeorev.2023.105857). Here we present a brief introduction to contextualize the article in the framework of the thesis; followed by the full text of this article.

Introduction

The origin and evolution of mineralizing fluids in a carbon-rich sedimentary basin are poorly understood topics (see Chapter I). The main obstacle to their unambiguous interpretation is the small size of fluid inclusions in sediment-hosted gold deposits. In contrast, at Algamarca quartz-hosted fluid inclusions are abundant and have adequate size (between ~2 and 50 μm) to be accurately studied by a variety of analytical methods, such as microthermometry analyses, Raman spectroscopy, and LA-ICPMS in-situ analyses of individual fluid inclusions. Therefore, the Algamarca deposit, our second case study, located ~2 km from the Shahuindo deposit, provides an excellent opportunity to study mineralizing fluids within an organic carbon-rich sedimentary basin.

The ensemble of mineralogical, geochemical, and fluid inclusion data obtained in this work complements the results of the regional-scale structural and basin analysis and thermodynamic modeling at Shahuindo presented in Chapter II. Our results point to a possible presence of porphyry-style mineralization underneath the sediments hosting the Algamarca deposit, and allow us to propose a metallogenetic model for the Algamarca sediment-hosted gold deposit, integrating the roles of carbonaceous material and arsenian pyrite in gold transport, distribution, and concentration. The results of this study improve exploration models for sediment-hosted gold deposits and their associated porphyry-style mineralization in northern Peru and worldwide.

Origin and evolution of gold-bearing fluids in a carbon-rich sedimentary basin: A case study of the Algamarca epithermal gold-silver-copper deposit, northern Peru

Renzo Galdos [a,b], Jean Vallance [a], Patrice Baby [b,c], Stefano Salvi [b], Michael Schirra [d], German Velasquez [e], Willem Viveen [c], Rodrigo Soto [a], Gleb S. Pokrovski [b,*]

[a] Grupo de investigaci´on en Geología de Yacimientos, Especialidad de Ingeniería Geol´ogica, Departamento de Ingeniería, Pontificia Universidad Cato´lica del Perú, avenida Universitaria 1801, San Miguel, Lima 15088, Peru

[b] G´eosciences Environnement Toulouse, Universit´e Toulouse III – Paul Sabatier, CNRS, IRD, CNES, OMP, 14 avenue Edouard Belin, F-31400 Toulouse, France

[c] Grupo de investigaci´on en Geología Sedimentaria, Especialidad de Ingeniería Geolo´gica, Departamento de Ingeniería, Pontificia Universidad Cato´lica del Perú, avenida Universitaria 1801, San Miguel, Lima 15088, Peru

[d] Department of Earth Sciences, University of Geneva, 1205 Geneva, Switzerland

[e] Instituto de Geología Econ´omica Aplicada, Universidad de Concepci´on, casilla 160-C, Concepci´on, Chile

ABSTRACT

Sediment-hosted gold deposits account for the major part of economic gold in the Earth's crust. However, the origin of the gold-bearing fluid and its evolution in sedimentary basins in the presence of organic carbon and its metamorphosed products such as graphite are poorly known. In an attempt to clarify these issues, we performed an integrated mineralogical, geochemical, and fluid-inclusion study of the Algamarca epithermal Au-Ag-Cu deposit, hosted by Mesozoic sediments corresponding to an over-mature petroleum system within the Maran˜o´n fold and thrust belt (northern Peru). Results show that mineralization started with a pre-gold stage characterized by quartz veins containing gold-poor pyrite and chalcopyrite. Most gold was deposited afterwards, during the main gold stage in an "invisible" form within arsenian pyrite, followed by minor visible native gold with sulfosalts and chalcopyrite at a later stage. Fluid inclusions in quartz from the pre-gold and gold stages show features analogous to those observed in porphyry Cu-Au systems such as vapor–liquid immiscibility, enrichment in K, Rb, Cu, As, and Sb, a wide range of salinity (5–35 wt% NaCl eq.), and similar elemental (atomic) ratios (Zn/Pb ~ 4, $0.1 < K/Na < 5$, Br/Cl ~ 0.06), all consistent with a fluid of magmatic origin. In addition, the fluid inclusions from the pre-gold stage are highly enriched in CO_2 (~60 mol% in gas phase), CH_4 (~10 mol%) and H_2S (~30 mol%). Such high volatile contents are rather unusual for typical porphyry-epithermal systems and likely reflect reactions between the magmatic fluid and carbon-bearing sediments. This conclusion is independently supported by the temperature values of graphite metamorphic peak determined by Raman spectroscopy, which are similar to those derived by fluid-inclusion microthermometry in quartz veins. Our findings imply that strong interactions of magmatic fluid with carbonaceous matter favored gold transport through the sedimentary basin and its subsequent concentration in arsenian pyrite. Furthermore, our results point to a possible presence of porphyry-style mineralization beneath the sedimentary sequence hosting the epithermal Algamarca deposit, thereby providing new potential for exploration.

1. Introduction

The ubiquitous presence of carbonaceous material, such as graphite, bitumen, pyrobitumen, and hydrocarbons, and their close association with gold-rich arsenian pyrite are two key ingredients shared by many types of sedimentary-hosted gold deposits including Carlin, orogenic, and some epithermal types, not to mention the largest gold anomaly on Earth - Witwatersrand (Arehart, 1996; Cline et al., 2005; Large et al., 2011, 2013; Agangi et al., 2013, 2015; Vaughan et al., 2020; Wu et al., 2020; Fuchs et al., 2021; Gaboury et al., 2021; Ge et al., 2022; Ding

et al., 2023; Vallance et al., 2024). These deposits correspond to the major world's known gold endowments; a single deposit or province can contain tens to hundreds million ounces of gold (e.g., Muntean et al., 2011; Frimmel and Nwaila, 2020). Consequently, these deposits have been in the focus of a large volume of scientific literature, leading to their structural, petrological, and mineralogical frameworks being well characterized. In contrast, considerably less effort has been allocated to delving into the genesis of mineralizing fluids and their evolution within sedimentary basins. The major enigmatic issue is the involvement of carbonaceous material and arsenic-rich pyrite in the transportation and concentration of gold, ultimately promoting its deposition. Despite various proposed models aiming to address this issue, the role played by both parameters is still controversial and subject of ongoing debate. Some of these models suggest that metamorphic or basinal fluids may reconcentrate gold from sedimentary or metasedimentary rocks (e.g., Hofstra and Cline, 2000; Large et al., 2011; Large et al., 2013), while others emphasize the importance of an external mineralizing input, such as magmatic fluids (e.g., Sillitoe and Bonham, 1990; Barker et al., 2009; Muntean et al., 2011; Large et al., 2016; Vallance et al., 2024). The consensus regarding the role played by carbonaceous material equally remains elusive. While it is generally assumed that interactions of hydrothermal fluids with organic matter trigger gold precipitation due to reduction (e.g., Radtke and Scheiner, 1970), other studies have demonstrated that such interactions actually enhance gold solubility (Vallance et al., 2024). Likewise, gold transport by organic fluids, such as petroleum, has received limited attention, with only a handful of studies dedicated to this subject demonstrating fairly modest gold solubility compared to that in S-bearing aqueous solution (e.g., Pokrovski et al., 2014; Crede et al., 2019). The resolution of this debate is hindered by several factors. Firstly, the intricate metallogenic evolution observed in the majority of deposits, characterized by the superimposition of various mineralization events, poses difficulties in establishing a clear sequence of ore-forming stages solely through mineralogical observation and geochronological dating (e.g., Groves et al., 2003; Cline et al., 2005; Emsbo et al., 2006; Vikentyev et al., 2019; Seltmann et al., 2020; Vursiy et al., 2020). Secondly, direct evidence from fluid inclusions remains rare for sediment-hosted gold deposits. This scarcity can be attributed to the limited presence of quartz, as well as its fine-grained texture in many sediment-hosted hydrothermal settings that results both in overly small size (e.g., <2–10 μm in Carlin type deposits from Nevada; Hofstra and Cline, 2000; Large et al., 2016; references therein) and limited availability of fluid inclusions (e.g., Cline et al., 2005; Pinet et al., 2023; Vallance et al., 2024). Although quartz is much more abundant in orogenic-type deposits, good preservation state of fluid inclusions is unusual (Zhang and Audétat, 2023), and in many cases fluid inclusions are also very small (typically < 5 μm; e.g., Velásquez et al., 2014). These conditions pose analytical challenges for in-situ LA-ICPMS analyses of fluid inclusions (e.g., Cline et al., 2005; Deditius et al., 2014). This paucity of direct information on the ore-forming fluid in sedimentary basins contrasts with the large amount of fluid-inclusion data available from magmatic-hydrothermal porphyry systems (e.g., Kouzmanov and Pokrovski, 2012; references therein). Alternatively, certain sulfide minerals, such as pyrite, sphalerite, enargite, wolframite and stibnite, which are opaque when observed under transmitted light in the visible spectral region, can be examined using infrared microscopy to identify any fluid inclusions they may contain (e.g., Campbell and Robinson-Cook, 1987; Richards and Kerrich, 1993; Moritz, 2006; Kouzmanov et al., 2002; Ortelli et al., 2018). Such study can be combined with in-situ LA-ICPMS analyses to determine their bulk composition (e.g., Kouzmanov et al., 2010; Rottier et al., 2018). However, analyzing fluid inclusions in opaque As-bearing minerals presents significant challenges, primarily due to the considerable infrared radiation absorption caused by arsenic, a prevalent element commonly found in pyrite associated with these gold deposits.

In light of the above challenges, our study offers a unique opportunity to investigate mineralizing hydrothermal fluids within an organic

carbon-rich sedimentary basin, focusing on the Algamarca epithermal deposit. Consisting of Au-Ag-Cu veins of Miocene age, this relatively young deposit offers a simplified sequence of mineralization events, encompassing only three hypogene stages of ore deposition. The veins consist predominantly of quartz, which serves as the primary host for abundant fluid inclusions of suitable size for a range of analyses (microthermometry, Raman spectroscopy and LA-ICPMS). While extensive research has been conducted on other epithermal Au-Ag deposits hosted by Cretaceous sedimentary rocks like Lagunas Norte, Shahuindo and La Arena in the Marañón fold and thrust belt (MFTB) of northern Peru, these studies were primarily focused on geochronological dating, mineralogical and geochemical characterization and stable isotope analyses (e.g., Montgomery, 2012; Cerpa et al., 2013; Santos et al., 2023; Vallance et al., 2024). To the best of our knowledge, no studies have been published specifically targeting the characterization of mineralizing fluids in these deposits.

In this paper, we present a comprehensive analysis of the properties and composition of the mineralizing fluids, textural and compositional characteristics of pyrite and quartz, a detailed paragenetic sequence, as well as a metallogenic model for the Algamarca deposit. Our work is based on meticulous sampling campaigns, systematic mineralogical studies, and rigorous in-situ analyses of minerals and fluid inclusions. The outcomes of our investigation offer novel insights into the origin and evolution of the mineralizing fluids within an organic carbon-rich basin. Additionally, our findings demonstrate the efficiency of detailed in-situ determination of major and trace elements as a viable approach for identifying concealed porphyry-style mineralization beneath the epithermal mineralization.

1.1. Geological setting

1.1.1. Regional geology

The Algamarca Au-Ag-Cu deposit is situated in the Marañón fold and thrust belt, in the Andes of northern Peru. The MFTB hosts a suite of epithermal, porphyry and skarn deposits associated with subduction-related Oligo-Miocene magmatic arc intrusions and belongs to the Miocene metallogenic belt of central and northern Peru (Noble and McKee, 1999; Scherrenberg et al., 2016). Remarkable deposits currently being mined include Yanacocha, Lagunas Norte, and Shahuindo (all epithermal-type), and Antamina (skarn-type), to name a few. The fertility of the belt has been attributed to a change in the subduction geometry (from normal to flat slab) triggered by the subduction of the Nazca ridge and Inca plateau (topographic anomalies) between 15 Ma and 13 Ma (Rosenbaum et al., 2005; Cooke et al., 2005).

The MFTB is an essential structural component of the western Cordillera of the Andes. It corresponds to an east-verging thin-skinned thrust system, which propagated in a fluvio-deltaic and marine sedimentary series, late Jurassic to late Cretaceous in age. The sediments were deposited in a back-arc basin on a basement formed by metamorphic rocks from Precambrian to lower-Ordovician, known as the Marañón complex (Mégard, 1984; Benavides-Cáceres, 1999; Chew et al., 2007; Scherrenberg et al., 2016). The MFTB developed during an early period of the Andean orogeny (traditionally known as the Peruvian and Incaic phases; Noble et al., 1979; Mégard, 1984), between the late Cretaceous and the middle Eocene. The main décollement occurred at the interface between the Mesozoic series and the basement, in the late Jurassic black shales of the Chicama Formation (Mégard, 1984; Jaillard and Jacay, 1989; Eude et al., 2015). The MFTB is truncated by a middle Eocene regional unconformity sealed by volcanic and volcano-clastic sediments of the late Eocene to middle Miocene Calipuy plateau-basin (Cossio and Jaen, 1967; Noble et al.,1990; Prudhomme et al., 2019). The western Cordillera and MFTB have been uplifted at their current altitude (from ~3000 to 4000 m a.s.l.) during the Neogene orogenic period.

2

1.1.2. Geology of the Algamarca deposit

The Algamarca deposit is hosted by the Algamarca anticline, a well-preserved and prominent structure situated in the northern part of the MFTB (Fig. 1a, b), 22 km west of Cajabamba town and ~1 km northwest of the Shahuindo deposit (Fig. 1a-c), at a current elevation of 3100 m a.s. l. It consists of veins trending perpendicularly or obliquely to the anticline axis. Stratigraphically, the Algamarca anticline is composed by the late Jurassic black shales with intercalations of fine-grained sandstone of the Chicama Formation and the overlying lower Cretaceous fluvio-deltaic and shallow-marine sequences of the Goyllarisquizga Group (Benavides-Cáceres, 1956; Navarro et al., 2010; Defilippi et al., 2016). The Goyllarisquizga Group includes, from bottom to top, quartz-rich massive sandstone with minor intercalations of shale, siltstone and coal bed of the Chimú Formation, black shales with lenticular siltstones, minor mudstones and limestones of the Santa Formation, interbedded siltstone, mudstone, and sandstone of the Carhuaz Formation, and quartz-rich sandstone with minor interbedded siltstone of the Farrat Formation (Fig. 2). Sandstones from the Chimú, Carhuaz, and Farrat formations are the main country rocks for the epithermal mineralization in the district including the Algamarca deposit (Fig. 1a; Gauthier et al., 1999; Defilippi et al., 2016). Oligocene-Miocene andesitic and dacitic intrusive stocks were emplaced at the intersection of NW-SE thrust faults and later NE-SW transverse faults, or along the axis of the Algamarca anticline (Fig. 1b, c; Defilippi et al., 2016; Vallance et al., 2024). They outcrop in the area and were intercepted by underground workings of the Algamarca mine. The Algamarca deposit has been exploited since Spanish colonial times. Later, Minera Algamarca SA operated an underground mine between 1945 and 1989 (Wright et al., 2009; Tietz and Defilippi, 2012). Some veins are currently mined on a small scale by AMASBA artisanal miners' association.

The Algamarca deposit is composed by seven veins labelled as Descubridora, San Blas, Los Alisos, Rosario, Lucy, Concepción, and
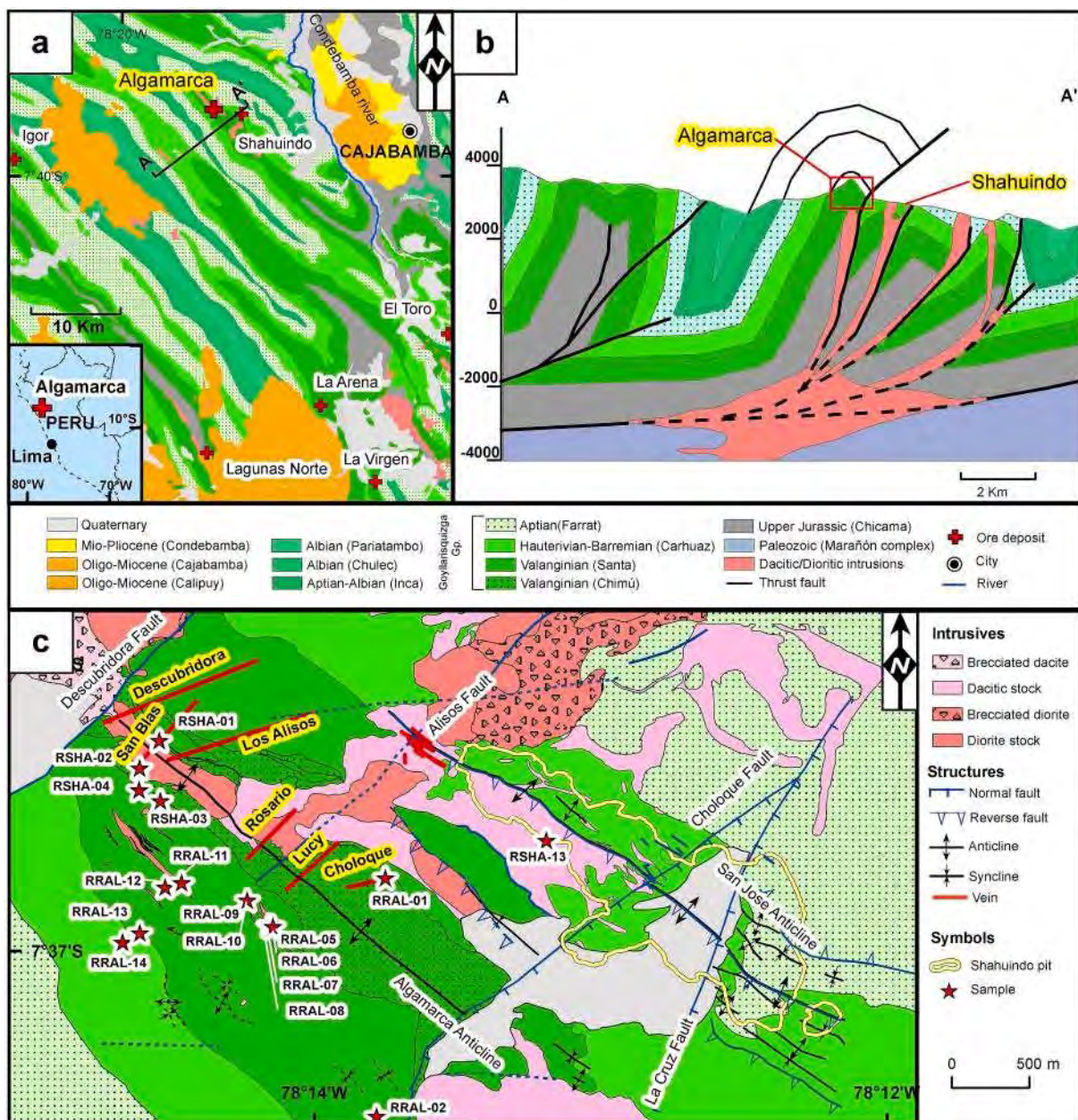
Fig. 1. (a) Regional geological map showing the principal ore deposits in the north of the Marañón fold and thrust belt, and location of the A-Á cross section depicted in 1b (modified after INGEMMET, 2017). (b) Structural SW-NE cross section (modified after Vallance et al., 2024). (c) Local geology of the Algamarca deposit. Note that the Lucy and Concepción veins overlap on the map. The location of the Shahuindo open pit is also shown (modified after Defilippi et al., 2016).

3
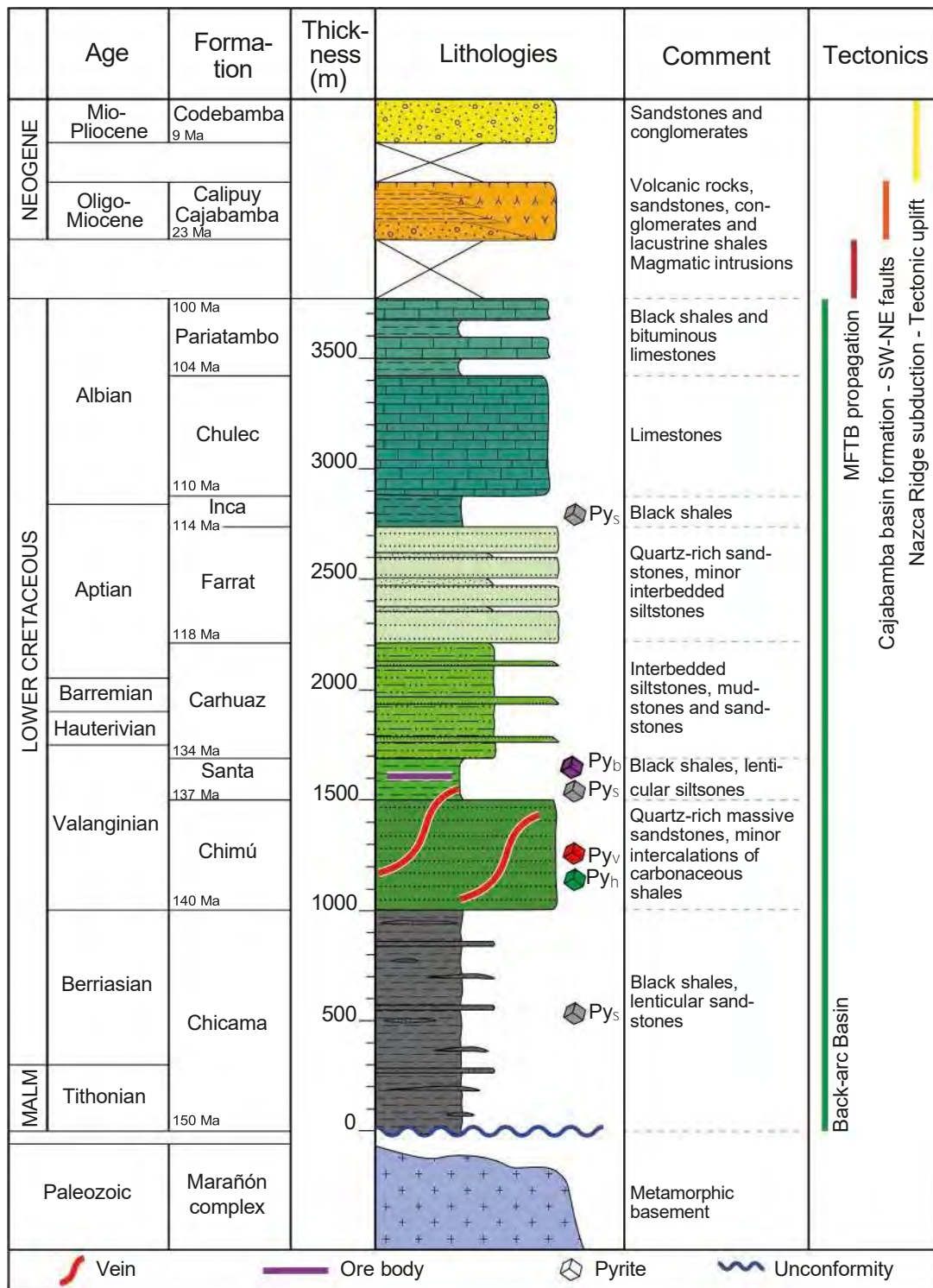
Fig. 2. Stratigraphical column of the Marañón fold and thrust belt in the study area (modified after Vallance et al., 2024), also showing the position of the Algamarca veins, ore bodies and different pyrite types. Abbreviations for pyrites types are as in Table 2.

Choloque, all of them of thicknesses varying from 0.1 to 2 m, up to more than 600 m in length, and extending over about 200 m in the vertical direction. The veins strike northeast and dip 60° to 70° to southeast (Fig. 1c; Defilippi et al., 2016). Maximum vein thicknesses are observed in the more competent lithologies such as quartzite of the Chimú Formation and andesitic intrusive stocks. In contrast, in less competent rocks, like coal beds of the Chimú Formation and shales of the Santa Formation, veins tend to split into fine branches of less than 1 cm thick

(Defilippi et al., 2016). Grades of up to 14 g/t Au, 2700 g/t Ag, and 25 wt % Cu were reported from one-sampling analyses in the Descubridora vein (the most exploited at Algamarca), which is hosted by quartz-rich sandstones of the Chimú Formation (Defilippi et al., 2016). In addi- tion, to the southwest part of the deposit, stratabound ore bodies composed of pyrrhotite, marcasite and pyrite are emplaced into the Santa Formation. The ore bodies are described for the first time in this study. The Algamarca deposit was dated at 15.5 ± 0.4 Ma by the K-Ar

Table 1
Location and description of samples from the Algamarca deposit.

Sample	Sample type and location	Geographical coordinates	Elevation (m a.s.l.)	Description
RSHA-01	Underground "Dump" Halcon gallery	7° 36′ 15.78″ S, 78° 14′ 33.33″ W	3297	San Blas vein. Quartz with pyrite, chalcopyrite and fahlore. Cut argilized pre mineral intrusive with abundant disseminated pyrite.
RSHA-02	Underground "Dump" Capuli gallery	7° 36′ 21.57″ S, 78° 14′ 37.41″ W	3163	San Blas vein. Massive pyrite with interstitial baryte.
RSHA-03	Underground "Dump" Alisos gallery	7° 36′ 28.41″ S, 78° 14′ 32.99″ W	3131	Alisos vein. Tennantite, chalcopyrite and pyrite with lesser euhedral quartz.
RSHA-04	Underground "Stockpile" Nivel 0 gallery	7° 36′ 26.13″ S, 78° 14′ 37.50″ W	3086	San Blas vein. Chalcopyrite, pyrite, tetrahedrite and euhedral quartz.
RSHA-13	Drill core SH-11–232, from 446.8 to 446.9 m	7° 36′ 36.14″ S, 78° 13′ 12.05″ W	n.a.	Santa Formation. Black shale with disseminated fine-grained pyrite.
RRAL-01A	Underground "In situ" Choloque gallery	7° 36′ 44.11″ S, 78° 13′ 44.44″ W	3261	Chimú Formation. Disseminated euhedral pyrite up to 0.5 cm in sandstone.
RRAL-01B	Underground "In situ" Choloque gallery	7° 36′ 44.11″ S, 78° 13′ 44.44″ W	3261	Choloque vein. Breached texture, clasts of quartzite and matrix of quartz and pyrite (vein width 8 cm).
RRAL-02	Surface outcrop 1 km SE of the veins	7° 37′ 34.10″ S, 78° 13′ 47.22″ W	3318	Santa Formation. Intercalations of siltstone and shale.
RRAL-03	Surface outcrop 1.4 km SE of the veins	7° 37′ 46.65″ S, 78° 13′ 51.42″ W	3352	Santa Formation. Black shale with intercalations of sandstone.
RRAL-04	Surface outcrop 1.4 km SE of the veins	7° 37′ 44.81″ S, 78° 13′ 47.95″ W	3349	Coarse-grained intrusive.
RRAL-05	Underground "In situ" Esperanza gallery	7° 36′ 54.309″ S, 78° 14′ 10.070″ W	3071	Lucy vein. Pyrite-quartz-tennantite- tetrahedrite as matrix and clasts of quartzite from Chimú Formation (vein width 45 cm).
RRAL-06	Underground "In situ" Esperanza gallery	7° 36′ 54.74″ S, 78° 14′ 9.47″ W	3063	Concepción vein. Centimetric hydrothermal quartz crystals with minor pyrite and tennantite- tetrahedrite (vein width 35 cm).
RRAL-07	Underground "In situ" Esperanza gallery	7° 36′ 54.573″ S, 78° 14′ 9.281″ W	3064	Concepción vein. Fine pyrite-quartz veinlets (0.5 cm) cutting the coal beds of Chimú Formation.
RRAL-08	Underground "In situ" Esperanza gallery	7° 36′ 54.518″ S, 78° 14′ 9.206″ W	3064	Coal beds of Chimú Formation with disseminated pyrite.
RRAL-09	Underground "In situ" Esperanza gallery	7° 36′ 49.10″ S, 78° 14′ 14.68″ W	3015	Post-mineral intrusive strongly argilized.
RRAL-10	Underground "In situ" Esperanza gallery	7° 36′ 49.08″ S, 78° 14′ 14.66″ W	3015	Iron oxides, chalcocite and covellite in the contact between a vein and post-mineral intrusive.
RRAL-11	Underground "In situ" Esperanza gallery	7° 36′ 45.49″ S, 78° 14′ 28.44″ W	3081	Sill of porphyry quartz diorite intrusive in Santa Formation.
RRAL-12A	Underground "Stockpile" Esperanza gallery	7° 36′ 46.47″ S, 78° 14′ 37.15″ W	3086	Lucy vein. Fahlore, pyrite and quartz with minor chalcopyrite, covellite and chalcocite. Cut by alunite veins.
RRAL-12B	Underground "Stockpile" Esperanza gallery	7° 36′ 46.47″ S, 78° 14′ 37.15″ W	3086	Gangue white minerals (alunite, pyrophyllite, nacrite).
RRAL-13A	Underground "In situ" CX-126 gallery	7° 36′ 56.07″ S, 78° 14′ 43.75″ W	2898	Algamarca ore bodies. Massive pyrrhotite partially replaced by marcasite and pyrite.
RRAL-13B	Underground "In situ" CX-126 gallery	7° 36′ 56.07″ S, 78° 14′ 43.75″ W	2898	Calcite-marcasite veinlets with fine halos of chlorite.
RRAL-014	Underground "In situ" CX-126 gallery	7° 36′ 58.00″ S, 78° 14′ 40.74″ W	2898	Fault with abundant carbonaceous material, minor pyrite and quartz.

m a.s.l. = meters above sea level; n.a. = not available.

R. Galdos et al.

method on hydrothermal muscovite found bordering a vein (Noble and McKee,1999). The deposit was classified as intermediate-sulfidation epithermal based on sulfide and gangue mineral assemblages (Defilippi et al., 2016; Galdos et al., 2021). Due to the proximity to the Shahuindo Au-Ag deposit (~1 km; Fig. 1c) and general similarities in ore mineralogy (Vallance et al., 2024), the Algamarca deposit was inferred to be part of the same magmatic-hydrothermal system as Shahuindo (Hodder et al., 2010; Galdos et al., 2021).

2. Samples and methods

2.1. Samples investigated in this study

Samples for this study were collected from underground mining works on the Algamarca veins, drill core, as well as from outcrops surrounding the veins. The San Blas, Alisos, Lucy, Concepción, and Choloque veins were sampled on site, in stockpiles or dumps, depending on underground access authorization. Weathered surfaces were avoided during sampling. In total, 22 samples from 19 different locations were obtained from these veins and their sedimentary and intrusive host rocks (e.g., Fig. A1). Sample locations are identified in Fig. 1c, and their coordinates and brief description are reported in Table 1. A selection of 30 polished sections (2.5 cm in diameter) and 8 doubly-polished thick sections (from 100 to 150 μm thick) were prepared.

2.2. Methods

2.2.1. Optical microscopy and etching

The 30 polished sections from the Algamarca deposit were examined under a reflected-light polarizing microscope to identify the sulfide paragenesis. Based on petrographic descriptions, pyrite crystals were selected for detailed observation to investigate compositional zonation in a single crystal. For that, the polished face of selected sections, containing mainly pyrite, was etched with commercially available bleach solution (4 wt% sodium hypochlorite, NaOCl, in water) for five minutes; then the sections were rinsed under tap cold water and left to dry, following the procedure described by Tanner et al. (2016) and Sykora et al. (2018).

2.2.2. Scanning electron microscopy (SEM) and X-ray powder diffraction (XRD)

Sulfides and gangue minerals were studied using a JEOL JSM 6360LV scanning electron microscope (SEM) equipped with an energy dispersive X-ray spectrometer (EDS) at the GET laboratory, Toulouse, France. Pyrites were observed in backscattered electron mode (BSE) at an acceleration voltage of 20 kV. The BSE images were compared and correlated with images of both pristine and etched pyrite obtained with a conventional optical microscope. X-ray powder diffraction (XRD) analyses of gangue minerals were performed with a Bruker D8 Advance A25 diffractometer at the GET laboratory. The step size was 0.01° and
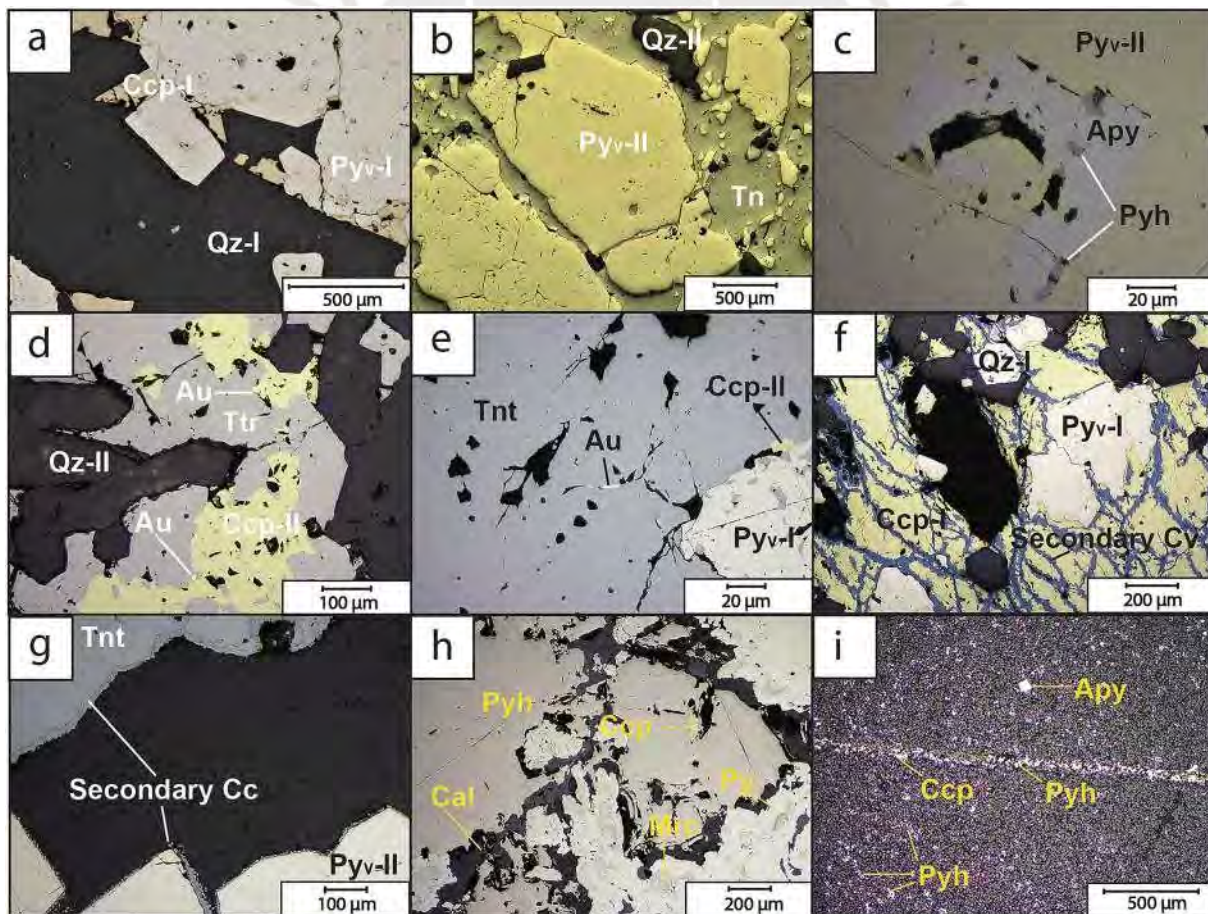
Fig. 3. Photomicrographs in reflected light showing representative textures of ore mineral assemblages in the Algamarca veins (a–g) and ore bodies (h, i). (a) Quartz, pyrite and chalcopyrite from stage A. (b) Tennantite replacing and filling fractures in pyrite. (c) Pyrite including arsenopyrite and pyrrhotite. (d) Native gold at the contact between chalcopyrite and tetrahedrite. (e) Native gold filling microfractures in tennantite. (f) Incipient replacement of chalcopyrite by secondary covellite along fractures and mineral boundaries. (g) Chalcocite replacing tennantite along mineral boundaries and as patina on euhedral pyrite. (h) Marcasite replacing pyrrhotite, partially replaced by pyrite. (i) Disseminated pyrrhotite and arsenopyrite and a narrow vein of pyrrhotite, with local occurrence of chalcopyrite. In all figures, mineral abbreviations follow Warr (2021).

6
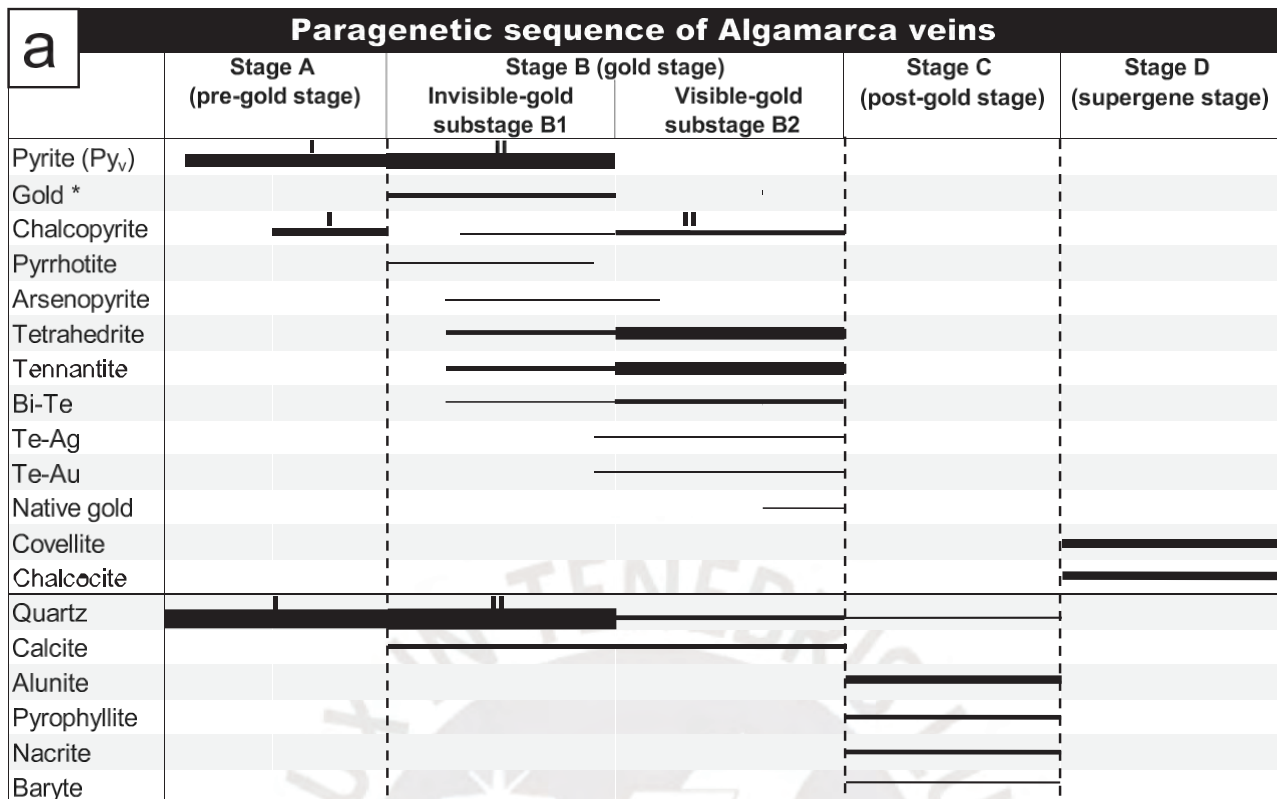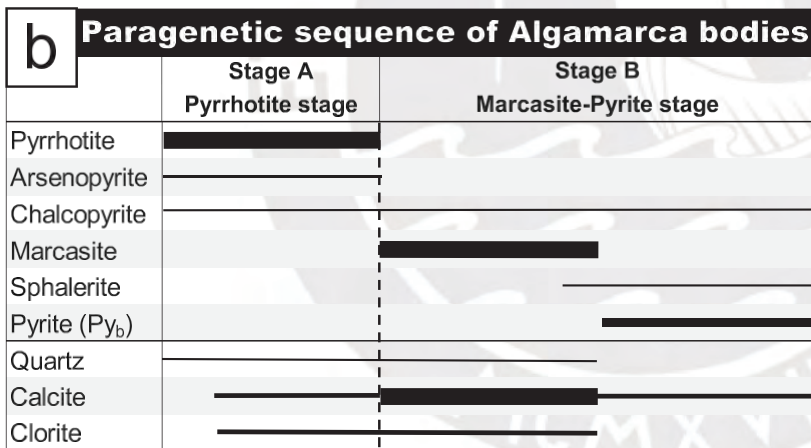
Fig. 4. Paragenetic sequence of the Algamarca veins (a) and ore bodies (b). Lines thickness is proportional to abundance.

the 2Θ range from 2° to 80°, with an acquisition time of 30 to 60 min per spectrum.

2.2.3. Electron microprobe analyses

Wavelength-dispersive X-ray spectroscopy (WDS) analyses of pyrite, marcasite, pyrrhotite, arsenopyrite, chalcopyrite, tetrahedrite, tennan-tite and native gold were performed on twelve polished sections with a CAMECA SXFive electron probe micro analyzer (EPMA) at the Raimond Castaing Microanalysis Centre of the University of Toulouse (France) using the following analytical conditions: 25 kV electron gun tension, 20 nA electron current, and 2 μm diameter beam size. The standards were chalcopyrite for S, Fe and Cu; arsenopyrite for As; sphalerite for Zn; and native gold, silver, bismuth and antimony for Au, Ag, Bi and Sb, respectively. The detection limits are reported in Tables A1 and A2.

2.2.4. Laser ablation - inductively coupled plasma mass spectrometry analyses of sulfide minerals

Laser ablation – inductively coupled plasma mass spectrometry (LA-ICPMS) analyses of the same samples and minerals analyzed with EPMA (except native gold) were performed using a Thermo Finnigan HR quadrupole ICP-MS coupled with a UV femtosecond laser at the GET laboratory. The laser ablation was performed under an argon atmosphere and the ablated material was carried by an Ar-He flow from the ablation cell to the spectrometer. Point analyses, a total of 150 data-points, were obtained with a laser spot size of 25 μm, a pulse frequency of 5 Hz and a 4.5 J.cm^{-2} fluence. Calibrations were performed using Po-726 (Sylvester et al., 2005), MASS-1 (Wilson et al., 2002) and natural arsenopyrite (Pokrovski et al., 2002, 2021) as external standards, and iron as an internal standard whose content was determined by EPMA. Each analysis comprised 30 s of background acquisition and 80 s of
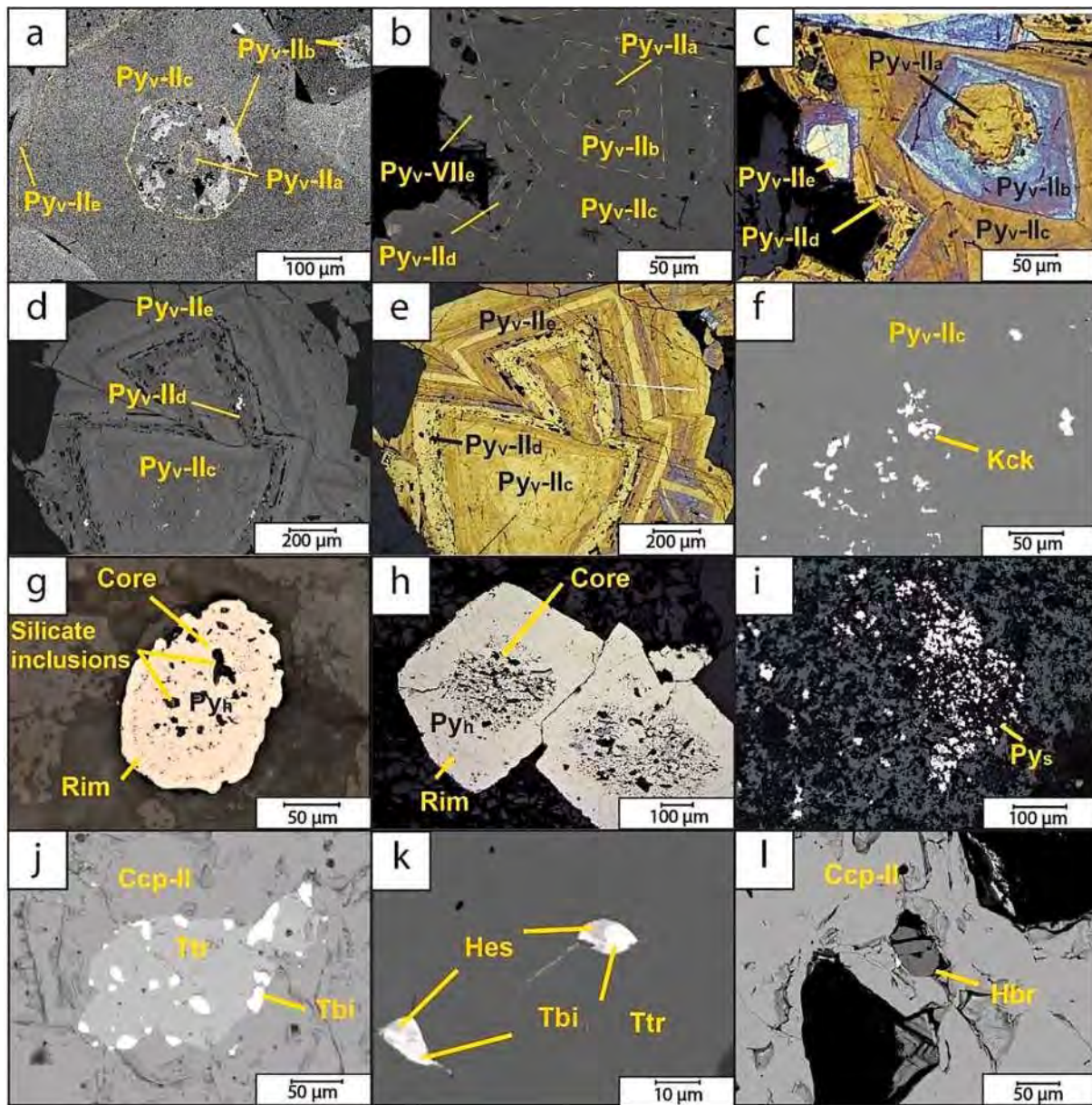
Fig. 5. SEM images in back-scattered electron mode (a, b, d, f, j, k and l), photomicrographs of NaOCl-etched pyrite (c and e) in veins, and photomicrographs in reflected light showing different types of pyrite in the Algamarca deposit (g, h and i). (a) Relics of Py$_v$-II$_a$ and Py$_v$-II$_b$ in Py$_v$-II$_c$, Py$_v$-II$_c$ is rimmed by Py$_v$-II$_e$ (San Blas vein). (b) Five overgrowth zones of pyrite from stage B (Concepció n vein). (c) Etching highlights the contacts between the different overgrowth zones of pyrite from (b). (d) Py$_v$-II$_c$, Py$_v$-II$_d$ and Py$_v$-II$_e$ (Concepció n vein); Py$_v$-II$_d$ showing cavities parallels to growth bands. (e) Same pyrite crystal as (d) etched with NaOCl. (f) Small crystals of kiddcreekite as inclusions in Py$_v$-II$_c$. (g) Hydrothermal pyrite in the intrusive host rock (Py$_h$) with a porous core with silicate inclusions (host rock relics) and a more compact rim. (h) Hydrothermal pyrite in sedimentary host rock (Py$_h$), showing a rounded porous core with silicate inclusions rimmed by a massive euhedral growth zone. (i) Anhedral to subhedral synsedimentary to diagenetic disseminated pyrite (Py$_s$) forming a mosaic of spongy crystals. (j) Association of Bi-Te minerals and tetrahedrite surrounded by chalcopyrite. (k) Small inclusions of telluride in tetrahedrite. (l) Hübnerite embedded in chalcopyrite.

ablation. The following isotopes were measured ^{34}S, ^{33}S, ^{51}V, ^{55}Mn, ^{57}Fe, ^{59}Co, ^{60}Ni, ^{62}Ni ^{63}Cu, ^{65}Cu, ^{66}Zn, ^{68}Zn, ^{69}Ga, ^{75}As, ^{77}Se, ^{82}Se, ^{95}Mo, ^{107}Ag, ^{111}Cd, ^{115}In, ^{118}Sn, ^{121}Sb, ^{125}Te, ^{182}W, ^{197}Au, ^{201}Hg, ^{202}Hg, ^{205}Tl, ^{208}Pb, and ^{209}Bi. Data reduction was carried out using the SILLS software (Guillong et al., 2008).

2.2.5. Raman spectroscopy

Raman spectra of carbonaceous material (CM) and fluid inclusions were acquired at the Centre d'E´laboration de Mat´eriaux et d'Etudes Structurales (CEMES) laboratory in Toulouse, France, using an XploRA PLUS instrument equipped with an Andor CCD detector, and using 1800 lines/mm grating, a confocal hole of 300 µm, and a 532 nm laser passing through a confocal microscope (Olympus, BX51, equipped with a 100x

objective with a numerical aperture of 0.90). Laser power was varied from 0.5 to 10 mW on the sample using optical filters. Acquisition time was 20 s per spectral window for CM and 60 s per window for fluid inclusions, with at least two scans per sample. The data were collected from 100 to 4200 cm^{-1} to cover both first- and second-order C-C and C-H bands wavenumber regions of the CM and the whole range of sulfur, carbon and water vibrations in the fluid inclusions. The spectra were processed using the Fityk program (Wojdyr, 2010). The CM Raman spectra were baseline subtracted and peak fitted following the procedure proposed by Kouketsu et al. (2014), to obtain the following band parameters: peak wavenumber position, intensity, area, and full width at half maximum (FWHM). In these fits, a pseudo-Voigt function (with Gaussian/Lorentzian ratio from 0 to 1) was used for all bands, and the

Table 2
Different types of pyrite present in the Algamarca deposit.

Pyrite type	Origin, location, shape	Size(μm)	Features	Mean concentration	
				EPMA As (wt%)	LA-ICPMS Au (ppm)
Py$_s$	Synsedimentary/diagenetic, sedimentary host rock, anhedral to subhedral	<20	Distinguished by its fine-grained crystals showing framboidal or spongy texture. Found in the Santa and Chicama formations.	0.2	0.1
Py$_v$-I	Hydrothermal veins (Stage A), anhedral to subhedral	200–1000	Compact crystals, BSE and etched sample images do not reveal internal textures.	0.4	1.3
Py$_v$-II	Hydrothermal veins (Stage B), subhedral to euhedral	20–500	Distinguished by its complex texture and zoning in BSE and etched sample images.	0.5	5.1
Py$_h$	Hydrothermal sedimentary and intrusive host rock, subhedral to euhedral	100–500	Occurring immediately next to the Algamarca veins as disseminated crystals, and displaying a porous core and a compact rim.	0.5	1.4
Py$_b$	Hydrothermal ore bodies and veinlets, anhedral to euhedral	50–200	Occurring as euhedral grains surrounding marcasite with bird's eye texture in ore bodies, and in calcite-marcasite-pyrite veinlets.	b.d.l.	b.d.l.

b.d.l. = below detection limit.

position of so-called G-band was fixed at 1593 cm^{-1} (Kouketsu et al., 2014).

2.2.6. Fluid inclusion petrography, microthermometry, and LA-ICPMS analyses

Quartz from the Algamarca veins contains a plethora of fluid inclusions that were investigated as detailed below. Prior to analyses, careful fluid inclusion petrography was carried out using a petrographic microscope, assisted by scanning electron microscopy-cathodoluminescence (SEM-CL), in order to distinguish different generations in the quartz host. SEM-CL images were acquired at the GET laboratory, using a TESCAN VEGA S5122 equipped with a Rainbow CL detector. The acceleration voltage and current applied were 10 kV and 10 nA, respectively. Microthermometry measurements were carried out at the GET laboratory on seven doubly polished sections (about 150 μm thick), using a Linkam THMSG-600 heating-freezing stage mounted on a BX51 Olympus microscope. The temperature was calibrated using the ice melting temperature (Tm$_{ice}$) and the homogenization temperature (Th) of pure H$_2$O synthetic fluid inclusions at 220 bar (0 and 374.1 °C) and the melting temperature of solid CO$_2$ (Tm$_{CO2}$) of pure CO$_2$-bearing inclusions from Camperio (−56.6 °C). The accuracy of temperature measurements on the calibrators was ±0.2 °C (at −56.6 and 0 °C) and ±2 °C (at 374.1 °C). The measurements were conducted on fluid inclusion assemblages (FIAs), i.e. groups of synchronously trapped inclusions with a similar phase ratio, according to the criteria defined by Goldstein and Reynolds (1994). The salinity was estimated from i) the ice melting temperature (Tm$_{ice}$) according to the equation of Bodnar (1993) in liquid-rich and vapor-rich fluid inclusions; ii) the halite dissolution temperature (Tm$_{hal}$) following the equation of Potter and Brown (1977) in multiphase-solid fluid inclusions. Pressure values were estimated from the equations of Zhang and Frantz (1987) and Bodnar and Vityk (1994) for the PVTX properties of water-salt-gas systems, using the Loner38 and Fluids software, respectively (Bakker, 2003).

Individual element concentrations of single fluid inclusions were analyzed using a COMPex nanosecond excimer laser coupled to an Agilent 8900 triple quadrupole ICP mass spectrometer at the University of Geneva. The beam diameter was varied from 15 to 65 μm in order to ensure complete ablation of the fluid inclusion depending on its size while minimizing the addition of the host to the signal. The analyzed isotopes for all fluid inclusions were [11]B, [23]Na, [25]Mg, [34]S, [35]Cl, [39]K, [44]Ca, [55]Mn, [57]Fe, [65]Cu, [66]Zn, [75]As, [88]Sr, [107]Ag, [121]Sb, [133]Cs, [197]Au, and [208]Pb, with addition of [79]Br, [85]Rb, [95]Mo, [137]Ba, and [209]Bi for multiphase-solid fluid inclusions. A dwell time of 10 ms was used for all elements except Au (40 ms), S, Cl and Ag (30 ms), Mo (20 ms), and Si (5 ms). Calibrations were performed using the NIST glass standard SR-610 (Norman et al., 1996) and an in-house andesitic glass standard doped with Cl and S (for chlorine and sulfur) as external calibrators, and the Na concentration in

the fluid inclusion as an internal standard. This concentration was assessed from the bulk salinity (wt % NaCl eq.) calculated from the ice melting and halite dissolution temperatures and corrected for the presence of the other major salts such as KCl, CaCl$_2$, FeCl$_2$, MnCl$_2$ from the LA-ICPMS analyses of the corresponding metal cations and using an iterative algorithm of Heinrich et al. (2003) implemented in the SILLS software (Guillong et al., 2008). For the quartz host, SiO$_2$ was used as internal standard, assuming nearly pure quartz (99.99 % SiO$_2$).

3. Results

3.1. Mineralogy, pyrite types and paragenetic sequence

3.1.1. Algamarca veins

Most Algamarca veins display crustiform, colloform and breccia textures, which are typical textures of open space precipitation (Fig. A1a-d; Echavarria et al., 2006). Most veins consist essentially of quartz (~40 %), pyrite (~30 %), tetrahedrite-tennantite (~10 %), and chalcopyrite (~10 %; Fig. A1c-h), the latter being much less abundant (<2%) in the Lucy, Concepció'n, and Choloque veins located southeast of the deposit. Pyrite occurring in the veins is hereafter termed (Py$_v$). The sulfides listed above, along with secondary chalcocite and covellite, are the only phases visible at the macroscopic scale (by naked eye or with the help of a hand lens). The veins also contain minor arsenopyrite (FeAsS), Bi-Te alloys, galena (PbS), sphalerite (ZnS), pyrrhotite (Fe$_{1-x}$S), hübnerite (MnWO$_4$), tungstenite (WS$_2$), kiddcreekite (Cu$_6$SnWS$_8$), stannite (Cu$_2$FeSnS$_4$), Ag and Au tellurides, and native gold (e.g., Fig. 3c-e), which were detected using an optical microscope or SEM. Calcite, alunite, nacrite, pyrophyllite, and baryte are minor gangue phases. Based on crosscutting relationships and replacement textures identified in the field, hand samples, and observations under the microscope, the following paragenetic sequence with four stages (A, B, C, and D) has been established (Fig. 4a).

Stage A (pre-gold stage). The assemblage consists of quartz (Qz-I), pyrite (Py$_v$-I) and chalcopyrite (Ccp-I; Fig. 3a). These minerals mainly occur as clasts in a matrix of minerals from later stages. Py$_v$-I presents a simple texture, without overgrowth zones, and etching and SEM images did not reveal any internal textures. The pyrite has subangular to sub-rounded edges, 0.1–5.0 mm size. Stage A was only identified in the Descubridora, San Blas, and Alisos veins.

Stage B (gold stage). Stage B represents the main event of gold mineralization in Algamarca veins. At this stage, it is common to see breached textures, where the clasts are fragments of the host rock (quartzite of the Chimú Formation; Fig. A1c, d) and/or minerals from stage A. This stage can be divided in two substages, B1 and B2. An invisible gold substage, B1, is characterized by an arsenic-rich pyrite hosting invisible-gold (labelled as Py$_v$-II), accompanied by euhedral
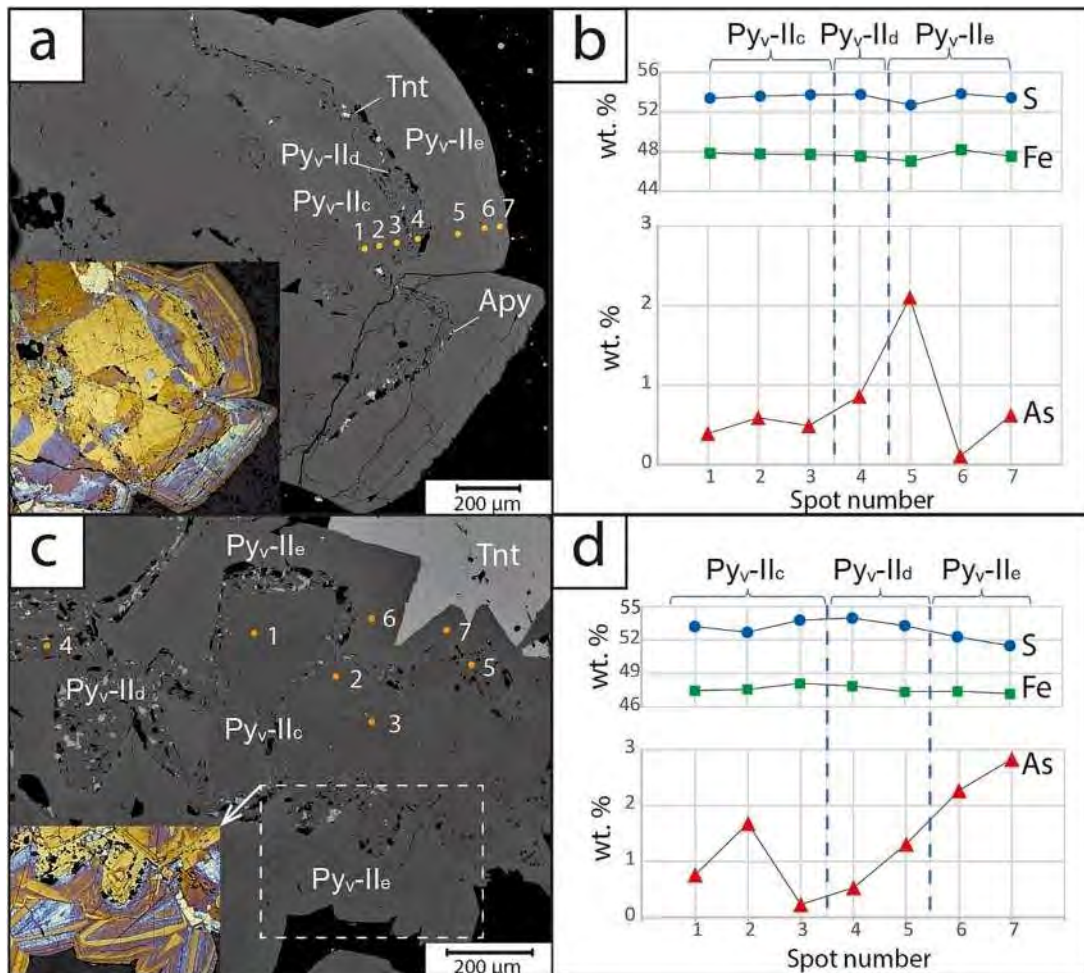
Fig. 6. Back scattered electron images of Py$_v$-II from the Lucy vein (a and c). Py$_v$-II$_d$ overgrowing Py$_v$-II$_c$ and showing porosity and abundant inclusions of arsenopyrite (Apy) and tennantite (Tnt). Euhedral Py$_v$-II$_e$ overgrowing Py$_v$-II$_d$ and presenting distinctive oscillatory zoning. The images of NaOCl-etched pyrite on the lower-left corners highlight high arsenic content in blue and white tints. (b and d) Concentration of S, Fe and As, obtained from EPMA analysis; analytical spots are located by orange dots in (a) and (c).
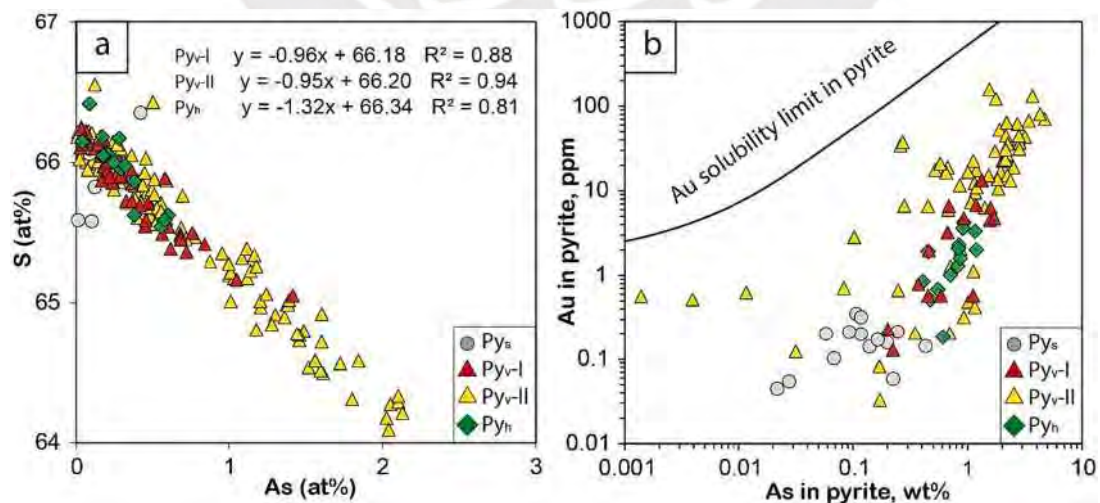
Fig. 7. EPMA (a) and LA-ICPMS (b) data on pyrites from the Algamarca deposit. (a) Distribution of As vs. S. (b) Au-As log–log plot. Abbreviations for pyrites types are from Table 2. The black curve of Au solubility limit is according to Reich et al. (2005).

9
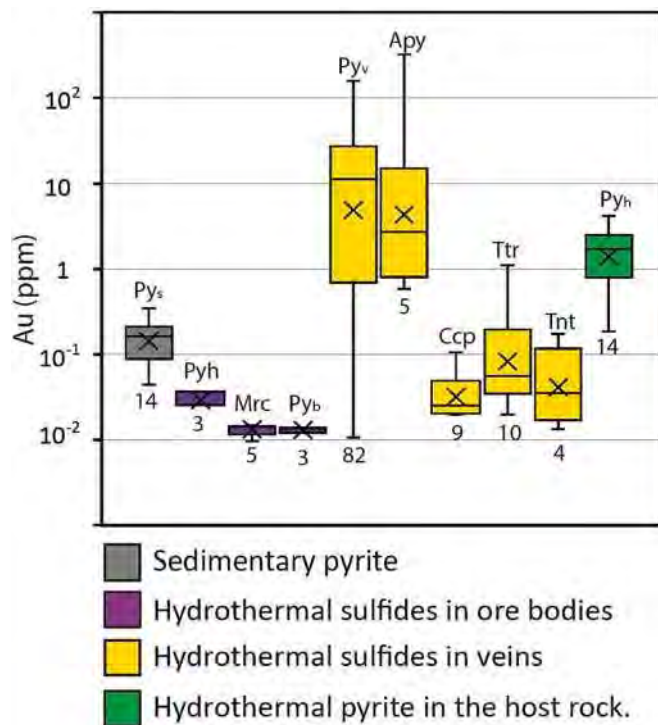
Fig. 8. Box plot comparing Au concentrations (in ppm) in different sulfides from the Algamarca deposit. Values below detection limit (DL, 0.03–0.05 ppm Au, depending on the mineral) are shown as half their DL value. Crosses denote the geometric mean. The host sulfide and the number of analyses are indicated, respectively, above and below each box. Pyrites are labelled as in Table 2.

quartz (Qz-II). A visible-gold substage, B2, is characterized by the ubiquitous presence of up to 30 µm native gold microparticles, commonly found as inclusions and filling microfractures in tetrahedrite-tennantite crystals, or at the boundary between this mineral and chalcopyrite (Fig. 3d, e). Both sub-stages are described in more detail as follows.

Substage B1 – invisible-gold mineralization – is characterized by the following features. The ore mineral is the arsenian pyrite, i.e. Py_v-II, which is characterized by several overgrowth zones (Fig. 5a-e). In a single Py_v-II crystal, we have been able to identify up to five distinct pyrite zones (labelled as "a" to "e") by clear cross-cutting relationships, which likely indicate the different precipitation steps during the invisible-gold substage. These overgrown zones are distinguished as follows. i) Py_v-II$_a$ has irregular boundaries due to corrosion, and it is dark in BSE images and yellow to orange in etched sample images (Fig. 5a-c). ii) Py_v-II$_b$ is euhedral and usually shows sharp contacts with earlier and later generations, it is bright in BSE images and blue after being etched (Fig. 5a-c). iii) Py_v-II$_c$ is the most abundant and is crosscut or overgrown by Py_v-II$_d$ and/or Py_v-II$_e$, it is dark to bright in BSE images and yellow to orange in etched sample images (Fig. 5a-e). The Py_v-II$_c$ type occasionally contains inclusions of galena, sphalerite, chalcopyrite, stannite and kiddcreekite (e.g., Fig. 5f). iv) Py_v-II$_d$ is porous, and its pores are elongated and parallel to the growth bands. Py_v-II$_d$ is dark in BSE images and yellow to orange in etched sample images (Fig. 5c-e). Py_v-II$_d$ overgrowth zones present abundant anhedral inclusions of arsenopyrite, tetrahedrite-tennantite, chalcopyrite, and pyrrhotite. v) Py_v-II$_e$, is euhedral in form and shows an oscillatory zoning. It is mainly found overgrowing to Py_v-II$_d$ or Py_v-II$_c$ (Fig. 5a-e and 6a, c). It also occurs as tiny crystals of less than 200 µm in size. This pyrite type also hosts scarce inclusions of arsenopyrite, pyrrhotite and chalcopyrite (Fig. 3c). Py_v-II$_e$ is dark to bright in BSE images and yellow to orange to blue in etched samples (Fig. 5a-e); these variations are due to differences in As content in the lattice of Py_v-II$_e$. The identified overgrowth types in

pyrite are associated with successive crystallization events, in which earlier precipitated cores were corroded, replaced, or overgrown by a successive pyrite. These zones are interpreted as dissolution-reprecipitation textures and are typically exhibited by pyrite in ore deposits (e.g., Sykora et al., 2018; Wu et al., 2019; Ishida et al., 2021). In the invisible-gold substage (B1), pyrite also is found as disseminated grains in the sedimentary and intrusive host rocks that surround the veins (Fig. 5g, h). These pyrite crystals (labelled as Py_h) present a porous core, containing relicts of the host rock as inclusions and overgrown by more compact rims without pores (Fig. 5g, h). This Py_h type is easily distinguishable from the regionally distributed *syn*-sedimentary or diagenetic pyrite (Py_s), as it is characterized by framboidal or spongy textures and does not display overgrowths (Fig. 5i). The main characteristics of the different types of pyrite present in the Algamarca deposit are reported in Table 2, and their position in the sedimentary sequence is represented in Fig. 2.

Substage B2 – visible-gold mineralization – is distinguished by the following features. Tetrahedrite and tennantite are the most abundant sulfides to have precipitated during this mineralization event, accompanied by minor chalcopyrite (Ccp-II). Tetrahedrite, tennantite and chalcopyrite locally fill (micro)fractures in Qz-II and Py_v-II from the invisible-gold substage (Fig. 3b). Bismuth-bearing minerals (e.g., tellurobismuthite) are common; they occur as anhedral inclusions in tetrahedrite-tennantite and as minor phases associated with chalcopyrite (Fig. 5j). Bismuth-bearing minerals inclusions are spatially associated with silver and gold telluride inclusions (Fig. 5k). Arsenopyrite occurs as euhedral crystals of less than 20 µm, or as larger anhedral crystals (up to 200 µm) partly replaced by tennantite-tetrahedrite and chalcopyrite. Tungsten and tin minerals (e.g., kiddcreekite, Kck and hübnerite, Hbr) are present as inclusions in pyrite, chalcopyrite, tennantite, and tennantite (e.g., Fig. 5f, l).

Stage C (post-gold stage). Stage C is recognized by the presence of nacrite, pyrophyllite, alunite, and baryte (Fig. A1b), which were iden- tified by XRD analyses (Fig. A2). These minerals fill reopened veins or form veinlets that crosscut all previous stages (Fig. A1h). Stage C was recognized in the Concepció´n, Lucy, and San Blas veins.

Stage D (supergene stage). The last stage, termed D, reflects supergene processes occurring after the deposit formation. It is clearly seen near the surface where the sulfides from stages A and B are replaced by goethite and hematite (Fig. A1d). In deeper parts, secondary Cu-bearing sulfides (chalcocite and covellite) replace chalcopyrite, tetrahedrite, and tennantite (Fig. 3f, g). Chalcocite is also found as a patina on pyrite (Fig. 3g).

3.1.2. Ore bodies

In addition to the veins described above, several <10 cm thick stratabound ore bodies replace carbonate beds in the Santa Formation. This type of mineralization was only observed in the CX-126 gallery and, as far as we know, has not been reported before in the Algamarca deposit. The ore bodies consist of massive pyrrhotite (stage A), crosscut and replaced by marcasite (Fig. A1j), which is subsequently replaced by pyrite (stage B; Fig. 3h). Pyrite in the ore bodies is hereafter referred to as Py_b. Minor chalcopyrite (stages A and B) and sphalerite (stage B) are also present. The rock immediately next to the orebodies is strongly chloritized and two types of veinlets are present: veinlets < 0.5 cm wide consisting of pyrrhotite and scarce chalcopyrite, corresponding to stage A (Fig. 3i), and veinlets up to 2 cm wide bearing calcite, marcasite, and minor pyrite (Py_b) with a narrow chlorite halo (Fig. A1k), corresponding to stage B. Euhedral to subhedral quartz crystals up to 0.7 mm in size occur in association with chlorite, both in ore bodies and veinlets. Fine disseminations of pyrrhotite with sporadic crystals of arsenopyrite (up to 100 µm) appear next to the ore bodies and pyrrhotite veinlets (Fig. 3i). The paragenetic sequence of Algamarca ore bodies is shown in Fig. 4b.
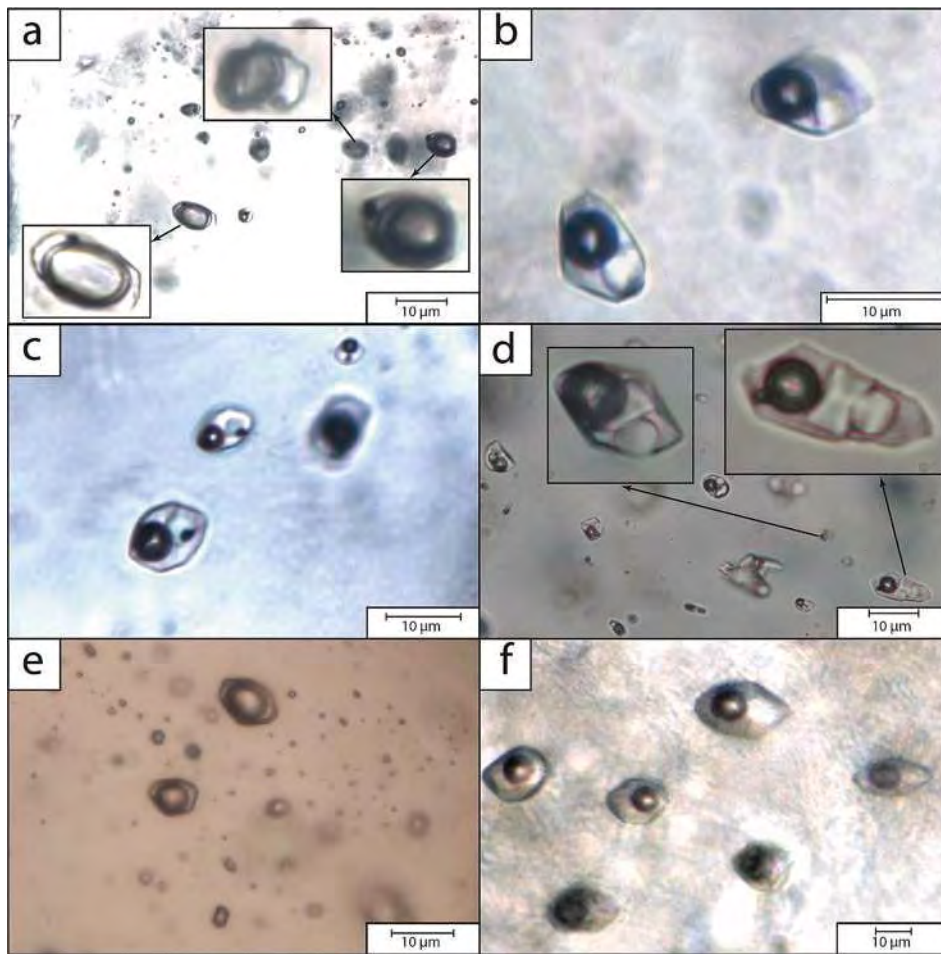
Fig. 9. Photomicrographs of fluid inclusions and fluid inclusion assemblages (FIAs) in quartz from stage A (Qz-I; a-e) and stage B (Qz-II; f), from the San Blas and Concepcio´n veins. (a) An immiscible-liquid (four-phase) FIA along a healed fracture. (b) A multiphase solid (three-phase) FIA. (c) A multiphase solid (four-phase) FIA. (d) Close-up of two fluid inclusions from a multiphase solid (five-phase) FIA. (e) A vapor-rich (two-phase) FIA. (f) A liquid-rich (two-phase) FIA.
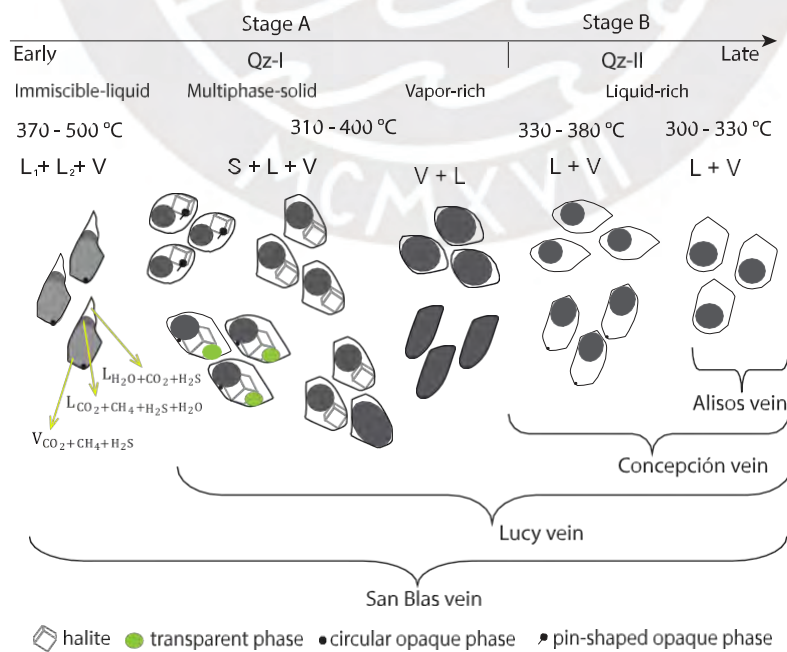
Fig. 10. Schematic representation of the different types of fluid inclusions identified in quartz from the Algamarca veins. The sketches respect the actual shapes of fluid inclusions and the proportions among the different phases.

12
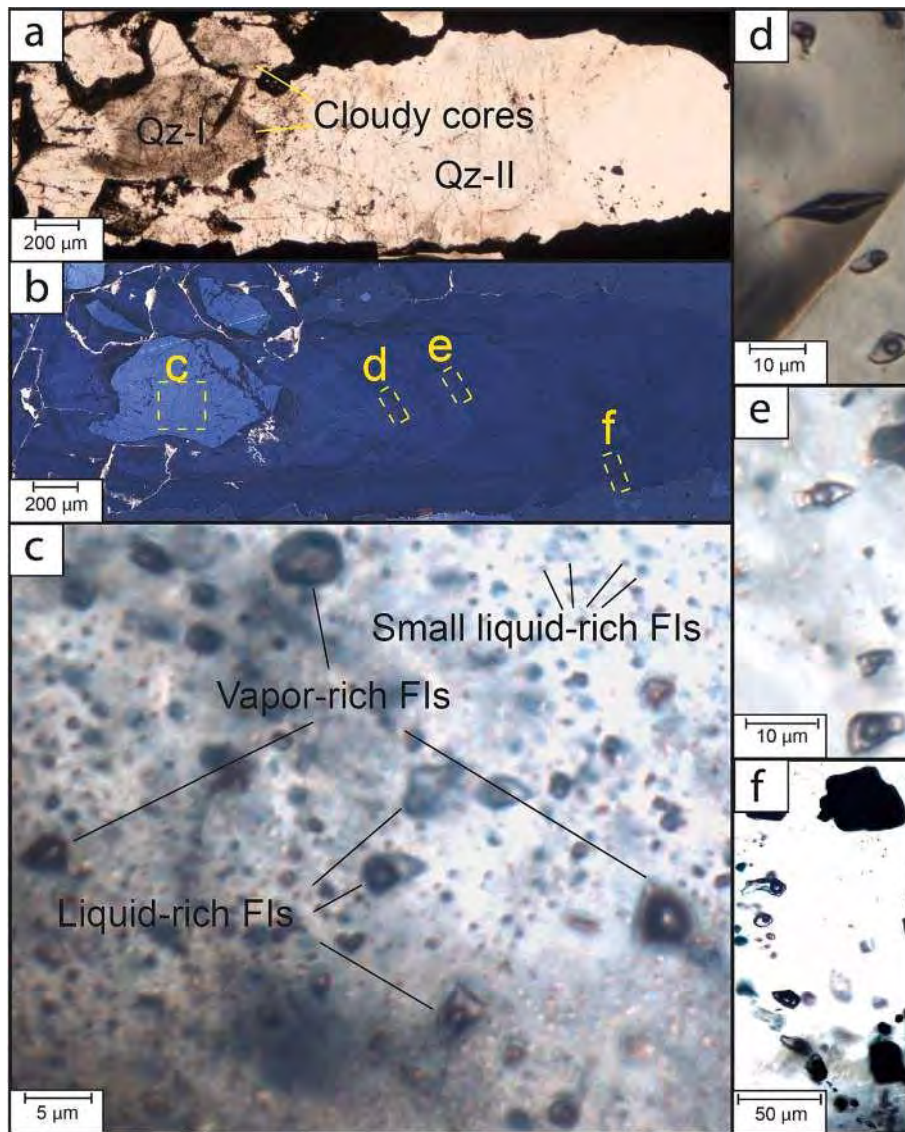
Fig. 11. (a) Transmitted-light photomicrograph of a quartz crystal from the Lucy vein. (b) Scanning electron microscopy-cathodoluminescence (SEM-CL) image of the same crystal from (a), with highly luminescent cloudy cores (Qz-I). Yellow rectangles locate the images in (c–f). (c) Cloudy cores consist of abundant randomly distributed liquid-rich, vapor-rich and multiphase-solid fluid inclusions, mostly smaller than 2 µm. (d) Fluid inclusions from a primary liquid-rich FIA hosted in a growth zone in quartz. (e) Detail of a primary liquid-rich FIA in a growth zone in quartz. (f) Detail of a pseudosecondary liquid-rich FIA in quartz.

3.2. Pyrite composition

3.2.1. EPMA major element analyses

The major-element content of pyrite ranges from 50.7 to 54.0 wt% for S (i.e. from 64.1 to 66.5 at%) and from 46.0 to 48.2 wt% for Fe (i.e. from 33.1 to 34.4 at%). Except As, Cu, and Sb, all other trace element concentrations in pyrite are below the detection limit (Sb was only detected in one point at 0.04 wt%). Copper was detected in <25 % of the points, at values of <0.1 wt% (except one point at 0.2 wt%). The As content in pyrite is variable, ranging from the detection limit (<0.06 wt %) to 4 wt% (Figs. 6, 7a, A5; Tables 2, A1, A2). Sedimentary pyrite (Py$_s$) shows up to 0.3 wt% As (with one point at 0.8 wt%), with half of the datapoints being below the detection limit (<0.06 wt%). The hydrothermal pyrite disseminated in the host rock (Py$_h$) presents moderate As concentrations (Fig. 7a), with cores from 0.1 to 0.4 wt%, and rims between 0.3 and 1.1 wt% As (Table A1). Hydrothermal pyrite in veins (Py$_v$) generally displays the highest values (up to 4.0 wt% in stage B, and up to 2.6 wt% in stage A; Fig. 7a; Table A1), but As concentration variations are substantial depending on the zones. Py$_v$-II$_a$ shows low As

concentrations, <0.3 wt%, while Py$_v$-II$_b$ shows consistently higher As contents, between 2.1 and 3.9 wt%. In the later pyrite zones, the As content is variable. Py$_v$-II$_e$ exhibits the strongest variations due to its oscillatory zoning between bands with As contents below detection limit (yellow in etched pyrite and dark in BSE image) and bands with up to 3.0 wt% As (red and blue in etched pyrite and bright in BSE image; Fig. 6a-d). The As content in hydrothermal pyrites from veins and disseminated in the sedimentary host rock (Py$_v$ and Py$_h$) shows a clearly negative correlation with S, with slope values close to 1 (in at %) indicating a stoichiometric substitution of As for S in the pyrite structure (Fig. 7a). In contrast, pyrite from orebodies (Py$_b$) displays As concentrations below the detection limit (<0.06 wt%).

3.2.2. LA-ICPMS trace element analyses

Pyrite is the most ubiquitous sulfide mineral in the Algamarca deposit. LA-ICPMS in situ analyses were performed on the different pyrite types recognized in the deposit. Crystals containing too many inclusions, or exhibiting strong porosity and/or fracture density, were carefully avoided. Most of the analyses were performed on hydrothermal pyrite

Table 3

Results of microthermometry from fluid inclusion assemblages (FIAs) in quartz from the Algamarca veins and orebodies. For each parameter, the average values are given; the number of analyzed fluid inclusions is in brackets.

Sample	Inclusion appearance	Daughter mineral	Th (°C)	Nb pts	Tm(ice) or Tm(hal) (°C)	Nb pts	wt% NaCl eq.	Density (g/cm³)[1]	Minimum pressure (bars)[2]
			Ore bodies, liquid-rich type						
RRAL-13	C	—	270 ± 8	(5)	−10.8 ± 0.7	(4)	14.8 ± 0.7	0.92 ± 0.01	48 ± 8
RRAL-13	I	—	247	(1)	−9.4	(1)	13.3	0.93	34
RRAL-13	PS	—	289	(1)	−12.3 ± 0.5	(2)	16.4 ± 0.5	0.91	69
			Lucy vein, liquid-rich type						
RRAL-05	C	—	309 ± 1	(5)	−3.4 ± 0.5	(2)	5.6 ± 0.7	0.76 ± 0.01	92 ± <1
RRAL-05	P	—	311 ± 5	(3)	−2.8 ± 0.5	(3)	4.7 ± 0.7	0.74 ± <0.01	96 ± 7
RRAL-05	P	—	321 ± 10	(3)	−2.3 ± 0.2	(3)	3.9 ± 0.4	0.7 ± 0.02	111 ± 15
RRAL-05	PS	—	308 ± 5	(2)	−5.0 ± 0.4	(3)	7.9 ± 0.6	0.8 ± 0.01	87 ± 6
RRAL-05	C	—	308 ± 8	(4)	−5.0 ± 0.5	(3)	7.9 ± 0.6	0.8 ± 0.02	88 ± 7
RRAL-05	PS	—	299 ± 3	(4)	−6.0 ± 0.4	(4)	9.2 ± 0.5	0.82 ± 0.01	81 ± 4
RRAL-05	C	—	302	(1)	−11.5 ± 0.5	(2)	15.4 ± 0.5	0.89	84
RRAL-05	RD	—	349 ± 15	(9)	−5.1 ± 0.5	(3)	8.0 ± 0.7	0.74 ± 0.02	140 ± 40
RRAL-05	RD	—	329 ± 11	(3)	−10.1 ± 1.7	(3)	14.0 ± 1.8	0.84 ± 0.04	121 ± 17
RRAL-05	RD	—	352 ± 22	(2)	−5.4 ± 0.3	(2)	8.4 ± 0.4	0.72 ± 0.05	164 ± 42
			Alisos vein, liquid-rich type						
RSHA-03	P	—	307 ± 3	(7)	−2.5 ± 0.6	(5)	4.2 ± 0.9	0.74 ± 0.01	89 ± 3
RSHA-03	C	—	316 ± 6	(6)	−2.2 ± 0.4	(4)	3.7 ± 0.7	0.71 ± 0.02	103 ± 10
RSHA-03	I	—	314 ± 4	(2)	−1.9 ± 0.4	(2)	3.2 ± 0.7	0.71 ± <0.01	100 ± 6
RSHA-03	P	—	321 ± 4	(2)	−3.0 ± 1.3	(2)	5 ± 2.1	0.72 ± 0.04	110 ± 5
RSHA-03	P	—	323 ± 2	(3)	−3.5	(1)	5.7	0.73	114
			Concepcio n vein, liquid-rich type						
RSHA-06	C	—	295 ± 1	(6)	−3.2 ± 0.3	(6)	5.3 ± 0.5	0.78 ± 0.01	76 ± 2
RSHA-06	C	—	298 ± 3	(3)	−3.1 ± 0.1	(2)	5.1 ± 0.1	0.77	77
RSHA-06	I	—	273 ± 2	(2)	−2.5 ± 0.2	(2)	4.1 ± 0.3	0.8 ± 0.01	56 ± 2
RSHA-06	PS	—	280 ± 5	(3)	−4.5 ± 0.2	(3)	7.2 ± 0.2	0.83 ± 0.01	60 ± 4
RSHA-06	P	—	377 ± 1	(3)	−3.1 ± 0.3	(3)	5.1 ± 0.5	0.6 ± 0.01	213 ± 2
RSHA-06	P	—	345 ± 3	(5)	−3.8 ± 0.3	(3)	6.2 ± 0.5	0.7 ± 0.02	146 ± 4
RSHA-06	C	—	288 ± 2	(3)	−2.3 ± 0.4	(2)	3.9 ± 0.6	0.77 ± 0.01	67 ± 3
RSHA-06	P	op	371 ± 14	(3)	−4.1 ± 0.3	(4)	6.6 ± 0.5	0.64 ± 0.04	202 ± 30
RSHA-06	C	—	289 ± 1	(5)	−4.1 ± 0.2	(3)	6.6 ± 0.2	0.8 ± 0.01	69 ± 1
RSHA-06	I	—	283	(1)	−3.0	(1)	5.0	0.79	63
RSHA-06	C	—	281 ± 7	(2)	−2.5 ± 1.0	(2)	4.2 ± 2.0	0.79 ± 0.04	61 ± 7
RSHA-06	I	—	312 ± 3	(2)	−1.8 ± 0.3	(2)	3.1 ± 0.5	0.71 ± 0.01	97 ± 4
RSHA-06	I	—	311 ± 1	(2)	−1.5 ± 0.1	(2)	2.6 ± 0.1	0.71 ± 0.01	96 ± 1
RSHA-06	C	—	283 ± 2	(3)	−3.6 ± 1.0	(3)	5.9 ± 1.4	0.81 ± 0.02	63 ± 2
RSHA-06	C	op	351 ± 2	(7)	−3.7 ± 0.3	(7)	6.0 ± 0.4	0.67 ± 0.01	160 ± 3
RSHA-06	C	—	290 ± 9	(3)	−3.5 ± 0.1	(3)	5.7 ± 0.2	0.79 ± 0.02	70 ± 10
RSHA-06	C	—	256 ± 9	(3)	−7.1 ± 0.3	(3)	10.6 ± 0.3	0.89 ± 0.01	40 ± 6
RRAL-06_2	C	op	348 ± 2	(6)	−1.9 ± 0.1	(6)	3.2 ± 0.1	0.63 ± 0.01	154 ± 3
RRAL-06_2	C	op	349 ± 1	(7)	−3.6 ± 0.1	(7)	5.9 ± 0.1	0.68 ± 0.01	156 ± 1
RRAL-06_2	P	op	357 ± 1	(13)	−3.3 ± 0.1	(13)	5.4 ± 0.2	0.65 ± 0.01	171 ± 1
RRAL-06_2	P	—	358 ± 6	(4)	−2.5 ± 0.1	(4)	4.2 ± 0.2	0.63 ± 0.02	174 ± 13
RRAL-06_2	C	op	291 ± 1	(6)	−3.1 ± 0.1	(6)	5.2 ± 0.1	0.79 ± 0.01	71 ± 2
RRAL-06_2	PS	—	360 ± 1	(7)	−3.6 ± 0.1	(6)	5.8 ± 0.2	0.65 ± 0.01	177 ± 3
RRAL-06_2	PS	—	365 ± 3	(6)	−7.4 ± 0.1	(6)	11 ± 0.2	0.74 ± 0.01	187 ± 6
RRAL-06_2	P	—	308 ± 2	(4)	−6.6 ± 1.0	(2)	9.9 ± 2.0	0.82 ± 0.01	91 ± 2
RRAL-06_2	P	—	308 ± 1	(4)	−6.2 ± 0.2	(4)	9.4 ± 0.2	0.81 ± 0.01	91 ± 1
RRAL-06_2	P	—	309 ± 1	(4)	−6.0 ± 0.1	(4)	9.1 ± 0.1	0.81 ± 0.01	93 ± 1
RRAL-06_2	P	—	307 ± 3	(7)	−6.2 ± 0.2	(6)	9.4 ± 0.3	0.81 ± 0.01	89 ± 2
RRAL-06_2	P	—	305 ± 1	(4)	−6.7 ± 0.1	(4)	10.0 ± 0.2	0.82 ± 0.01	88 ± 1
RRAL-06_2	C	—	299 ± 9	(4)	−10.5 ± 0.1	(4)	14.4 ± 0.1	0.88 ± 0.01	82 ± 11
RRAL-06_2	PS	—	378 ± 1	(8)	−2.8 ± 0.1	(7)	4.6 ± 0.2	0.58 ± 0.01	215 ± 1
RRAL-06_2	C	—	347 ± 2	(7)	−2.1 ± 0.1	(5)	3.5 ± 0.1	0.64 ± 0.01	151 ± 1

Table 3 (*continued*)

Sample	Inclusion appearance	Daughter mineral	Th (°C)	Nb pts	Tm(ice) or Tm(hal) (°C)	Nb pts	wt% NaCl eq.	Density (g/cm³)[1]	Minimum pressure (bars)[2]
RRAL–06_2	C	—	306 ± <1	(3)	−7.0 ± 0.1	(3)	10.5 ± 0.1	0.83 ± 0.01	89 ± 1
San Blas vein, liquid-rich type									
RSHA-04_2	C	—	309 ± 5	(8)	−1.9 ± 0.6	(8)	3.3 ± 1.0	0.72 ± 0.01	93 ± 7
RSHA-04_2	C	—	322 ± 5	(7)	−3.4 ± 0.1	(2)	5.5 ± 0.1	0.73 ± 0.01	111 ± 5
San Blas vein, vapor-rich type									
RSHA-04	PS	—	369 ± 9	(3)		n.m.	n.m.	n.m.	n.m.
RSHA-04	PS	—	377 ± 9	(2)		(2)	3.1 ± 0.3	n.m.	n.m.
San Blas vein, multiphase-solid type[3]									
RSHA-04	PS	Hl + op	310 ± 12	(3)	176 ± 14	(3)	30.8 ± 0.6	1.01 ± 0.02	76 ± 14
RSHA-04	PS	Hl + op	294 ± 5	(2)	232 ± 3	(2)	33.6 ± 0.2	1.06 ± 0.01	59 ± 4
RSHA-04	PS	Hl + op	394 ± 12	(4)	206 ± 27	(4)	32.3 ± 1.4	0.93 ± 0.02	200 ± 16
RSHA-04	PS	Hl + op	351 ± 26	(2)	263 ± 10	(2)	35.4 ± 0.6	1.01 ± 0.02	124 ± 37
RSHA-04	PS	Hl + op	325 ± 15	(3)	154 ± 1	(2)	29.8 ± 0.1	1.00 ± 0.01	86 ± 7
RSHA-04	PS	Hl + op	333 ± 2	(3)	274 ± 3	(3)	36.1 ± 0.2	1.04 ± 0.01	97 ± 2
RSHA-04	PS	Hl + op	323 ± 15	(2)	184 ± 27	(2)	31.2 ± 1.2	1.00 ± 0.01	92 ± 17
RSHA-04_2	C	Hl + op	328 ± 11	(6)	230 ± 30	(4)	33.5 ± 1.7	1.02 ± 0.02	96 ± 17
RSHA-04_2	C	Hl + op	307 ± 23	(7)	172 ± 11	(7)	30.6 ± 0.5	1.02 ± 0.02	76 ± 24
RSHA-04_2	C	Hl + op	326 ± 32	(5)	214 ± 16	(5)	32.6 ± 0.8	1.01 ± 0.05	99 ± 45
RSHA-04_2	I	Hl + op + tp	338 ± 28	(2)	235 ± 8	(2)	33.7 ± 0.5	1.01 ± 0.03	110 ± 36
RSHA-04_2	PS	Hl + op + tp	353 ± 24	(3)	294 ± 7	(3)	37.5 ± 0.5	1.04 ± 0.02	124 ± 32

Th = homogenization temperature, Tm(ice) = ice melting temperature, Tm(hal) = halite melting temperature, Nb pts = number of measurements, P = primary, PS = pseudosecondary, C = cluster, I = isolated, RD = randomly distributed in cloudy cores, Hl = halite, op = opaque phase, tp = transparent phase, — = not detected, n.m. = not measured.
[1] Calculated density of homogenized fluid in inclusions.
[2] Calculated minimum pressure value of entrapment.
[3] Tm(hal) for this type of inclusions instead of Tm(ice).

from the veins (Py$_v$). They show up to 50,000 ppm As, 1,000 ppm Co, Ni, and Cu; 100 ppm Mn, Zn, Ag, Sn, Sb, Te, Au, Pb, and Bi, and < 10 ppm V, Ga, Cd, In, and W (Table A3). Sedimentary pyrite (Py$_s$) is enriched in Co, Ni, Mo, V, Mn, Tl, Sb and Pb and depleted in Au and As, compared with hydrothermal pyrite from veins (Py$_v$) and hydrothermal pyrite disseminated in the host rock (Py$_h$) (Figs. 7, 8, A3, and A4). Pyrites from ore bodies (Py$_b$) are depleted in all trace elements, except Co and Ni, compared to sedimentary pyrite or hydrothermal pyrites in veins and disseminated in the sedimentary host rock (Figs. 8, A3, A4).

A statistical summary of gold concentrations in sulfides from the Algamarca deposit is illustrated in Fig. 8. All analyses on sedimentary pyrite (Py$_s$) are above the limit of detection (>0.03 ppm Au) with an average of 0.1 ppm Au. Gold concentrations in sulfides from ore bodies (pyrite, pyrrhotite and marcasite) are close to or below the limit of detection. In contrast, gold concentrations in hydrothermal pyrite from veins (Py$_v$) are well above the detection limit for most analytical points (96 %), with an average of 5 ppm Au and a maximum value of 160 ppm Au. Arsenopyrite shows an average of 4 ppm Au, with maximum of 320 ppm Au, which is the highest Au concentration among the analyzed sulfides. The 70 % of the Au analyses in chalcopyrite are below detection limit (<0.05 ppm), with a maximum value of 0.1 ppm. In tetrahedrite and tennantite, 30 % of the analyses are below detection limit (<0.05 ppm), most of the significant values are less than 0.2 ppm (with two exceptions of 0.5 ppm and 1.1 ppm in tetrahedrite). Pyrite disseminated in sedimentary host rocks (Py$_h$) has an average of 1.4 ppm Au with all datapoints above the detection limit; rims generally display higher Au concentrations than cores.

The analyses show that hydrothermal arsenian pyrite and arsenopyrite are the two sulfides with the highest invisible Au content (Fig. 8). Together with native gold, they are the major hosts of gold in the deposit. In arsenian pyrite, Au and As contents display a wedge-shape pattern below the empirical Au metal solubility limit (Reich et al., 2005) and a significant positive Au-As correlation at As contents in pyrite above 0.1 wt% (Fig. 7b). LA-ICPMS patterns from these pyrites generally show smooth and flat signals for Au suggesting the absence of nanoparticles of gold metal and/or other gold-bearing minerals (Fig. A5a, b). It is only in few cases that the Au signal presents a spiky pattern parallel to that of Te, corresponding to gold telluride inclusions (Fig. A5c, d). Bismuth signals in the LA-ICPMS patterns show matching sharp peaks with Te and positive correlations indicating that most of the Bi and Te in pyrite are contained in Bi-Te inclusions (Fig. A5a, b; Table A4). Elements such as Zn, Ga, Cd, In, and Sn show positive correlations between each other (Fig. A4g, h; Table A4). Similarly, positive correlations are shown by Co with Ni and Ag with Pb (Fig. A4a, f; Table A4).

The pyrite in veins from stage B (Py$_v$-II) shows higher As and invisible-gold contents than those in stage A (Py$_v$-I). Most of the gold contents in Py$_v$-II exceed 10 ppm Au, whereas they are consistently below 10 ppm in Py$_v$-I (Fig. 7b). Lead content exhibits the same trend as Au and As, with concentrations systematically higher in Py$_v$-II than in Py$_v$-I (Fig. A4f).

3.3. Fluid inclusion analyses

3.3.1. Fluid inclusion petrography and microthermometry

Four different types of fluid inclusions in quartz were identified in the Algamarca veins and ore bodies. Based on the major phases observed at room temperature, they were classified, according to the criteria of Shepherd et al. (1985), as i) immiscible-liquid (containing volatile phases, mostly carbonic, accompanied by H$_2$O), ii) multiphase-solid (H$_2$O plus solid phases), iii) vapor-rich (H$_2$O), and iv) liquid-rich (H$_2$O) (Figs. 9 and 10). Cathodoluminescence imaging reveals different quartz generations within the Algamarca veins. The Qz-I generation from stage A is brighter luminescing compared with the dark luminescing Qz-II generation from stage B (Fig. 11a, b). The results of microthermometry analyses are reported in Table 3, 4, and A5, and
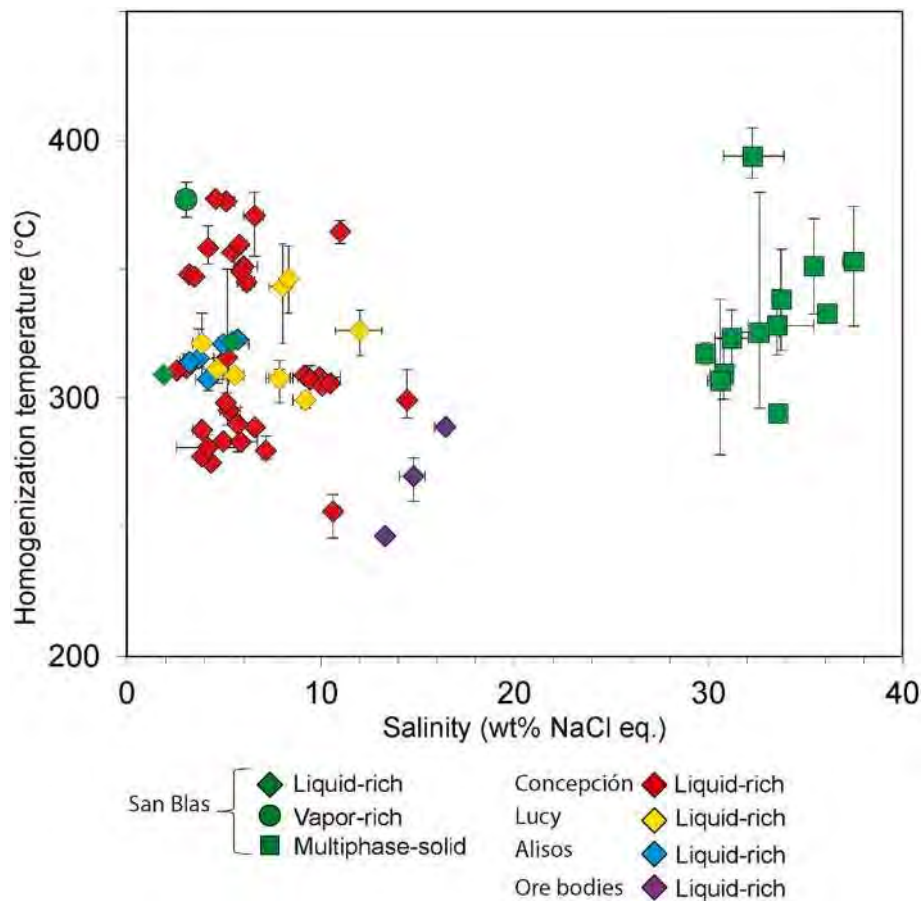
Fig. 12. Homogenization temperature (Th) vs. salinity for FIAs in quartz from stages A and B, from the Algamarca veins and ore bodies. Each point represents an average value of Th and salinity in a FIA; error bars correspond to the minimum and maximum value for each FIA (no error bars are shown where they are smaller than the symbol size).
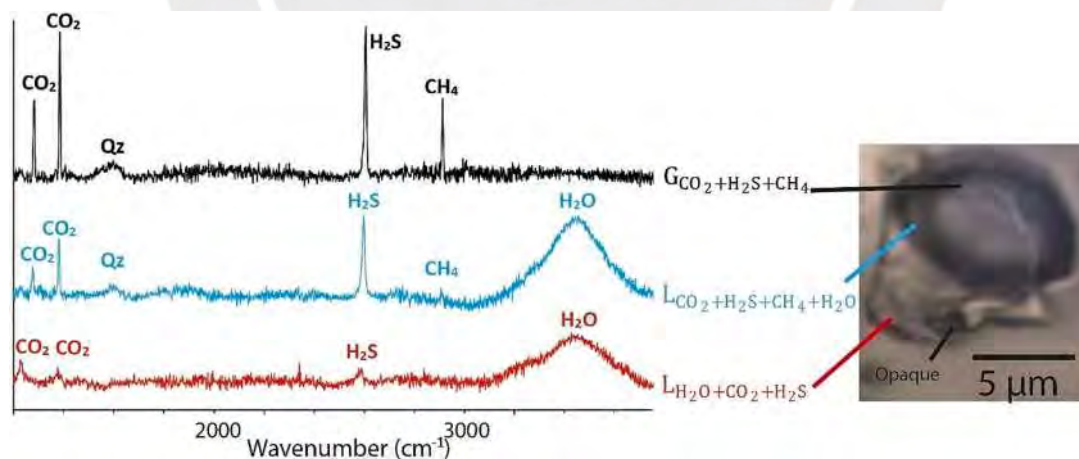
Fig. 13. Raman spectra of the different phases in a fluid inclusion representative of the immiscible-liquid type.

shown in Fig. 12 and A6. The composition of the different phases was determined by Raman spectroscopy (see section 4.3.2).

Pre-gold stage (Stage A). In Qz-I from Stage A of Algamarca veins three types of FIAs were recognized (i, ii, and iii; Fig. 10), which are described as follows. The immiscible-liquid type fluid inclusions (i) contain four phases at ambient conditions, including a CO_2-H_2S-CH_4 gas bubble, a CO_2-H_2S-CH_4-H_2O liquid, an aqueous liquid, and a small opaque daughter mineral (Fig. 9a). These fluid inclusions were found only in the San Blas vein, have an oval to irregular shape and a size of up

to 10 μm. They appear as clusters, pseudosecondary trails, or isolated individuals (e.g., Fig. 9a). The immiscible-liquid FIAs predate the multiphase-solid FIAs (see the following paragraph). Clusters of immiscible-liquid fluid inclusions are present in the core of quartz crystals (Qz-I) and are cross-cut by pseudosecondary and secondary trails of multiphase-solid fluid inclusions (not shown). Immiscible-liquid FIAs homogenize to vapor with homogenization temperature values (Th) from 404 to 498 °C (with one exception of 327 °C in an isolated fluid inclusion; Table A5), the opaque daughter mineral does not change

Table 4

Chemical composition acquired by Raman spectroscopy and corresponding microthermometric data for selected fluid inclusions of the immiscible-liquid fluid type in sample RSHA-04, from stage A (invisible-gold stage) in the San Blas vein.

Inclusion	Microthermometry				Raman data (mole % of volatile component)		
	$Tm_{(CO_2)}$ (°C)	$Th_{(CO_2)}$ (°C)	$Tm_{(clath)}$ (°C)	Th (°C)	CO_2	H_2S	CH_4
1	−67.1	30.9	10.2	460	63.2	26.8	10.0
2	−66.0	30.9	—	449	61.9	28.0	10.1
3	−66.3	31.0	12.5	484	60.3	31.7	8.0
4	−66.5	31.0	9.3	423	67.2	26.4	6.4

Th = homogenization temperature, $Tm_{(CO2)}$ = melting temperature of solid CO_2, $Tm_{(clath)}$ = melting temperature of clathrate, $Th_{(CO2)}$ = homogenization temperature of liquid CO_2, — = not measured.

during heating runs. The salinity, bulk composition and pressure values for this type of fluid inclusions could not be calculated from microthermometry or Raman data due to their high H_2S concentrations (revealed by Raman spectroscopy), which strongly affect the clathrate melting temperature (Touray and Guilhaumou, 1984), but are not accounted for in the model of Bakker (1997).

The second type of FIAs present in Qz-I, classified as multiphase-solid type (ii), contains multiple solid phases. They comprise a brine, a cubic crystal (halite), a vapor bubble, an opaque mineral, and a rounded greenish to transparent and slightly anisotropic mineral. The opaque mineral in these FIAs has a rounded shape or, less frequently, a pin-lke shape (Fig. 10). Multiphase-solid fluid inclusions have rounded or negative crystal shapes with sizes up to 20 μm. They occur as pseudosecondary and secondary trails and clusters. The multiphase-solid fluid inclusions homogenize to liquid, and show previous halite dissolution. Other solids dissolve at lower temperatures than halite, except the opaque mineral that remains unchanged during heating. This type of FIAs has Th values from 294 to 353 °C (with a single outlier of 394 °C), and salinities from 30 to 38 wt% NaCl eq. (Table 3).

The third type of FIAs present in Qz-I consists of vapor-dominated fluid inclusions, referred to as vapor-rich (iii). These fluid inclusions were observed in Qz-I from San Blas vein and Lucy vein (cloudy cores; Fig. 9e, 10 and 11c). The vapor bubble occupies more than 60 % of the fluid inclusion volume, with remaining liquid and an opaque mineral sporadically observable in some inclusions. Vapor-rich fluid inclusions occur as clusters or, less frequently, associated with multiphase-solid fluid inclusions forming a boiling assemblage (Fig. 9e and 10). Because the liquid phase in vapor-rich fluid inclusions is scarce or visually absent, only few microthermometry measurements could be conducted (Table 3), yielding Th values of 369 and 377 °C (from 2 FIAs) and a salinity of 3 wt% NaCl eq. (from 1 FIA).

Gold-stage (Stage B). In Qz-II from Stage B of Algamarca veins, fluid inclusions are exclusively liquid-rich (type iv), with liquid occupying more than 60 % of the volume, accompanied by a vapor bubble (<40 %) and a tiny opaque daughter mineral (locally present in the Conception vein; Table 3). The liquid-rich fluid inclusions are present in quartz from Lucy, Concepcioń, Alisos, and San Blas veins and have oval, rounded or negative crystal shapes with sizes between ~2 and 20 μm (exceptionally reaching up to 50 μm in size). They occur as primary fluid inclusions parallel to growth bands and along pseudosecondary trails, as well as clusters, isolated individuals and along secondary trails (e.g., Fig. 9f and 11d-f). In addition, randomly distributed liquid-rich fluid inclusions were identified in cloudy cores of quartz in the Lucy vein (Fig. 11 c). These cores (Qz-I) are bright luminescing under cathodoluminescence imaging compared to the host quartz (Qz-II; Fig. 11b). The liquid-rich fluid inclusions in these cloudy cores correspond to an early genera- tion that is "secondary" in origin with respect to the cloudy cores (Qz-I), and were formed before the liquid-rich fluid inclusions trapped in Qz-II. The latter are hereinafter referred to as late liquid-rich type.

All liquid-rich fluid inclusions homogenize to liquid. Liquid-rich FIAs from the Alisos, San Blas and Lucy veins homogenize at 300–320 °C and have salinities of 3–10 wt% NaCl eq. However, the early FIAs in the cloudy quartz core (Qz-I) of the Lucy vein present higher Th values and

salinities, 330–350 °C, and 8–14 wt% NaCl eq., respectively (Fig. A6). The Concepcioń vein has two populations of liquid-rich FIAs based on their Th. The first population presents Th values ranging from 260 to 310 °C and salinities from 3 to 14 wt% NaCl eq., not notably different from FIAs from the Alisos, San Blas and Lucy veins (late liquid-rich FIAs) veins. The second population presents higher Th values, of 350–380 °C and salinities of 3–11 wt% NaCl eq., comparable with the values in early liquid-rich FIAs from the cloudy cores in the Lucy vein (Fig. A6). The similarity in Th and salinity strongly suggests the presence of similar early liquid-rich FIAs in the Concepcioń vein (second population of FIAs), even though a clear temporal relationship between the two populations of FIAs in the Concepcioń vein could not be confirmed by petrographic features. Sedimentary clastic quartz grains, found in sandstones from the Chimú Formation, are distinguishable by their round shapes and high luminescence, present small liquid-rich fluid inclusions (<5 μm) with Th values around 285 °C, as measured in a single quartz grain.

In the San Blas vein that contains all four fluid inclusion types, the earlier immiscible-liquid fluid inclusion type (present in Qz-I) shows the highest Th values, up to 500 °C; however, pressure correction could not be applied. In this quartz type, the multiphase-solid fluid inclusions show Th values of 300–400 °C and coexist with vapor-rich fluid inclusions, which suggests boiling. Hence, no pressure correction is required for obtaining the actual entrapment temperature of these types of fluid inclusions. Finally, liquid-rich fluid inclusions found in Qz-II (Stage B) record Th values of ~315 °C. At this stage, shallow deposition is expected, which is characteristic for epithermal mineralization. Therefore, the pressure correction for these data is likely to be minimal, in agreement with the temperature of ~325 °C estimated in the invisible-gold substage using arsenopyrite geothermometry (Kretschmar and Scott, 1976).

Pyrrhotite-stage (Stage A). In quartz from Algamarca ore bodies only liquid-rich FIAs were identified. Opaque minerals were not observed; the vapor bubble occupies <20 % of the inclusion volume. They appear as secondary and pseudosecondary trails, clusters, or isolated fluid inclusions, mostly <10 μm in size. They present lower Th values than liquid-rich FIAs in quartz from Algamarca veins, from 250 to 290 °C, and higher salinities, from 13 to 16 wt% NaCl eq. (Fig. 12).

3.3.2. Raman spectroscopy of fluid inclusions

In immiscible-liquid fluid inclusions, the melting temperature point of solid CO_2 ranges from −67.7 to −65.0 °C, and the clathrate melting point reaches 12.1 °C (Tables 4 and A5), indicating that other significant components accompany the dominant CO_2 (Bodnar et al., 2014). Therefore, Raman analyses were performed on those fluid inclusions to detect such components. Carbon dioxide (CO_2) was clearly detected by its Fermi dyad bands at 1282 and 1385 cm^{-1} in the vapor phase, at 1276 and 1381 cm^{-1} in the liquid carbonic phase, and at 1279 and 1381 cm^{-1} in the aqueous liquid phase (Fig. 13; e.g., Burke, 2001; Frezzotti et al., 2012). In addition, H_2S and CH_4 were detected, respectively, by their S-H and C-H symmetric stretch vibrations respectively at 2604 and 2913 cm^{-1} in the vapor CO_2-dominated phase, and at 2597 and 2907 cm^{-1} in the liquid CO_2 phase (Fig. 13; Dubessy et al., 2012). In the aqueous
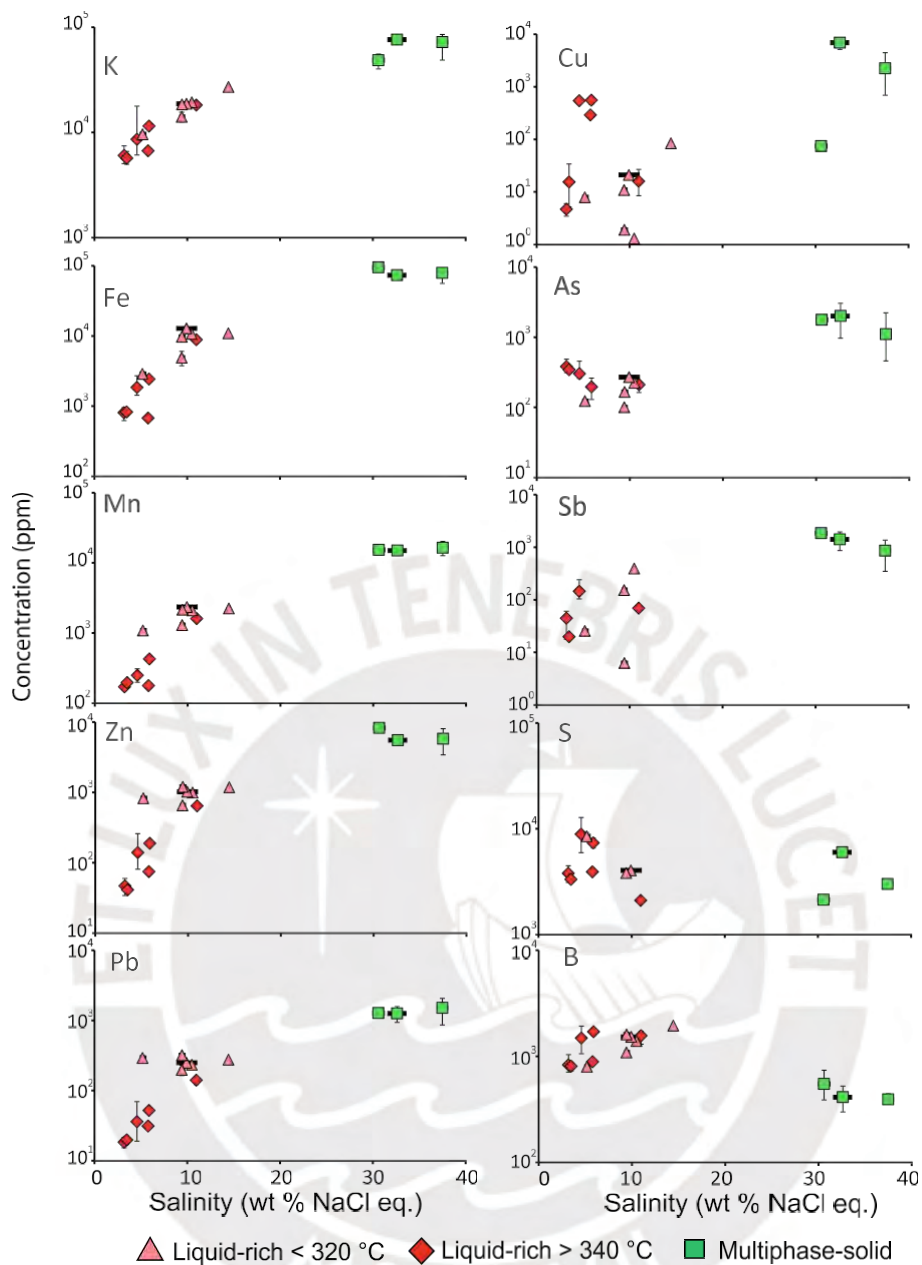
Fig. 14. Selected element concentrations vs. salinity for FIAs from the Concepció́n and San Blas veins. Each point represents an average value in a FIA; error bars correspond to the minimum and maximum value for each FIA (no error bars are shown where they are smaller than the symbol size or only one measurement is available).

liquid phase, H_2S was detected at 2585 cm^{-1} (Fig. 13). The identified H_2S peak wavenumbers are in excellent agreement with those known in the gas, liquid and aqueous phases (Pokrovski and Dubessy, 2015; references therein). Raman analyses of peak ratios in the gas phase (Burke, 2001) show the mole percentage of CO_2 in the carbonic vapor phase ranging from 60.4 to 67.2 %, H_2S from 26.4 to 31.7 %, and CH_4 from 6.4 to 10.1 % (Table 4).

No other sulfur species such as sulfate or polysulfides were detected in the aqueous liquid phase of our fluid inclusions. Sulfate may be either minor in the fluid due to relatively reduced conditions and/or taken by some of the solid phases observed in the fluid inclusions. No attempt was made in this study to specifically acquire Raman spectra on heating of fluid inclusions that might potentially reveal other sulfur species existing in aqueous solution at higher temperatures such as the trisulfur radical ion (Jacquemet et al., 2014; Pokrovski and Dubessy, 2015; Barr é et al., 2017).

Raman analyses in the vapor phase of two vapor-rich and one multiphase-solid fluid inclusions did not detect CO_2 or the other gases. Raman spectra of the small opaque mineral (with spherical shape) in one multiphase-solid fluid inclusion indicate that it is likely to be chalcopyrite.

3.3.3. LA-ICPMS analyses of fluid inclusions

Twenty-six individual liquid-rich fluid inclusions from 12 fluid inclusion assemblages (each one including 1 to 6 individual fluid inclusions) were analyzed in quartz from stage B (Qz-II) from the Concepció́n vein. The concentrations of B, Na, K, Mn, Fe, Zn, Sr, Cs, and Pb exceed the detection limit in all fluid inclusions. Other elements, such as Mg, Ca, As, Cu, Sb, Cl, and S, exceed their detection limits in >70 % of the fluid inclusion analyses. Silver was detected in 50 % of the fluid inclusions and Au was only detected in one fluid inclusion. The average element concentrations of each fluid inclusion assemblage are reported
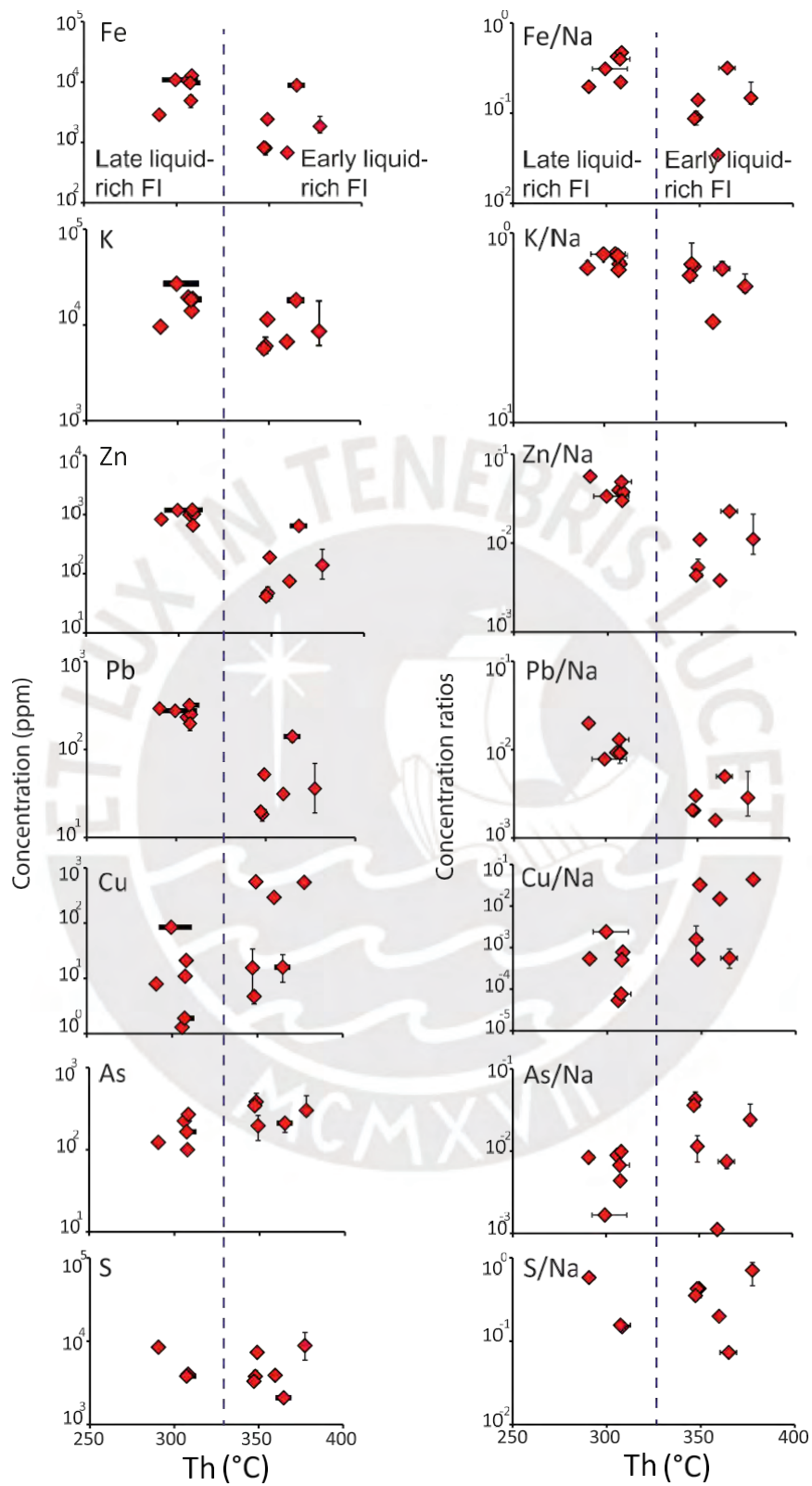
Fig. 15. Selected element concentrations and element concentration ratios (X/Na) for liquid-rich FIAs vs. Th from the Concepció́n vein (see Fig. 14 caption for more details).
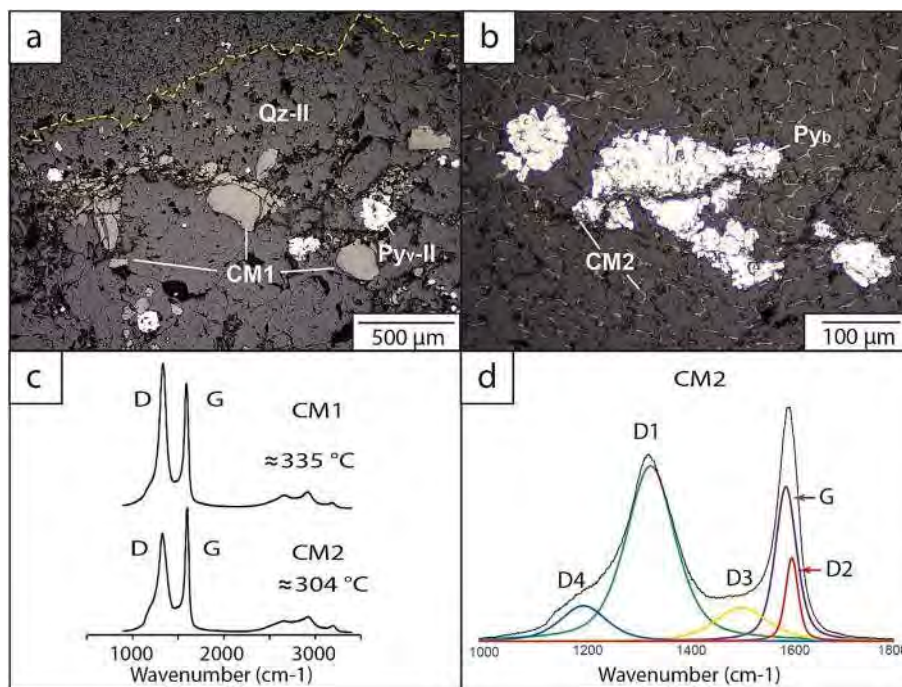
Fig. 16. Photomicrographs and Raman spectra of carbonaceous material (CM1 and CM2) from the Algamarca deposit. (a) Quartz vein hosting CM1 and pyrite. The yellow dotted line marks the contact between the sedimentary host rock and the vein. (b) Thin irregular bands of CM forming kind of a mesh, together with anhedral pyrite. (c) Raman spectra of CM1 and CM2. (d) An example of peak fitting of a Raman spectrum.
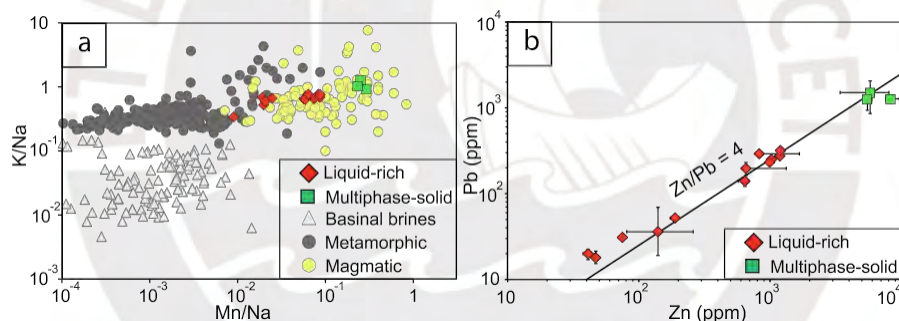
Fig. 17. LA-ICPMS data obtained from liquid-rich and multiphase-solid FIAs (red and green, respectively) and comparison with literature data. (a) K/Na vs Mn/Na ratios in FIAs from Algamarca veins, as well as from typical basinal brines (Samson et al., 2008; Zou et al., 2020; Soʹsnicka et al., 2023), metamorphic (Rauchenstein- Martinek et al., 2016) and magmatic fluids (Williams-Jones et al., 2010; Kouzmanov and Pokrovski, 2012). (b) Pb vs Zn element concentration in FIAs from Algamarca veins. The linear fit to the datapoints corresponds to a Zn/Pb ratio of 4. Error bars correspond to the minimum and maximum value within each FIA.

in Table A6 and plotted in Figs. 14 and 15. The most abundant elements in liquid-rich fluid inclusion assemblages (in the order of decreasing mean concentration) are Cl, Na, K, Fe, Ca, and S reaching up to 10,000 ppm levels, followed by moderately-abundant B, Mn, Mg, and Zn (up to 2,000 ppm), and by less abundant Cu, As, Sb, Pb, Cs, and Sr (between 100 s and 10 s ppm), and, finally, Ag ($<$5 ppm), and Au ($\leq$0.2 ppm). Positive correlations were observed between the salinity and the concentration of analyzed elements in liquid-rich fluid inclusions except for S, B, Cu, As, and Sb (Fig. 14). Late liquid-rich FIAs show higher Fe, K, Zn, and Pb concentrations and their corresponding element/Na ratios than early liquid-rich FIAs; in contrast, Cu and As concentrations and their corresponding element/Na ratios are lower (Fig. 15). Individual early liquid-rich fluid inclusions reach 650 ppm Cu and 490 ppm As, while late liquid-rich fluid inclusions show $<$80 ppm Cu and $<$270 ppm As. The concentration of S (0.1–1 wt%) is similar in both generations of liquid-rich fluid inclusions (Fig. 15).

In quartz of stage A (Qz-I) from the San Blas vein, eight multiphase-solid fluid inclusions from three FIAs were analyzed. The other types of fluid inclusions present in Qz-I (immiscible-liquid and vapor-rich,

examined by microthermometry) were not analyzed by LA-ICPMS because no suitable fluid inclusions were found, their scarcity and small size being the main impediments for quantitative measurement of trace element contents. In all multiphase-solid fluid inclusions, the concentrations of B, Na, Mg, Cl, K, Ca, Mn, Fe, Zn, As, Rb, Sr, Ag, Sb, Cs, Ba, Pb, and Bi exceed the detection limit. Other elements such as Cu, Br, S, and Mo exceed the detection limit in more than half of the analyses. Gold was not detected in any fluid inclusion. The most abundant elements in multiphase-solid FIAs are Cl, Fe, Na, K, and Mn, always showing concentrations of $>$1 wt%, followed by Zn (up to 0.8 wt%), Cu and Ca (up to 0.7 wt%), and S (up to 0.6 wt%). Minor, but omnipresent, elements are Sb, As, and Pb (reaching 1,000 ppm levels), followed by Rb, Br, B, Bi, Sr, Cs, Ba, Ag (100 s ppm), and Mo $<$ 1 ppm. No trends for these elements could be identified likely due to the too small number of FIAs analyzed and to too narrow a range in salinity and homogenization temperature. The concentrations of elements in multiphase-solid fluid inclusions are higher than in liquid-rich fluid inclusions, except for S and Mg showing similar contents and for B being slightly lower (Fig. 14; Table A6).
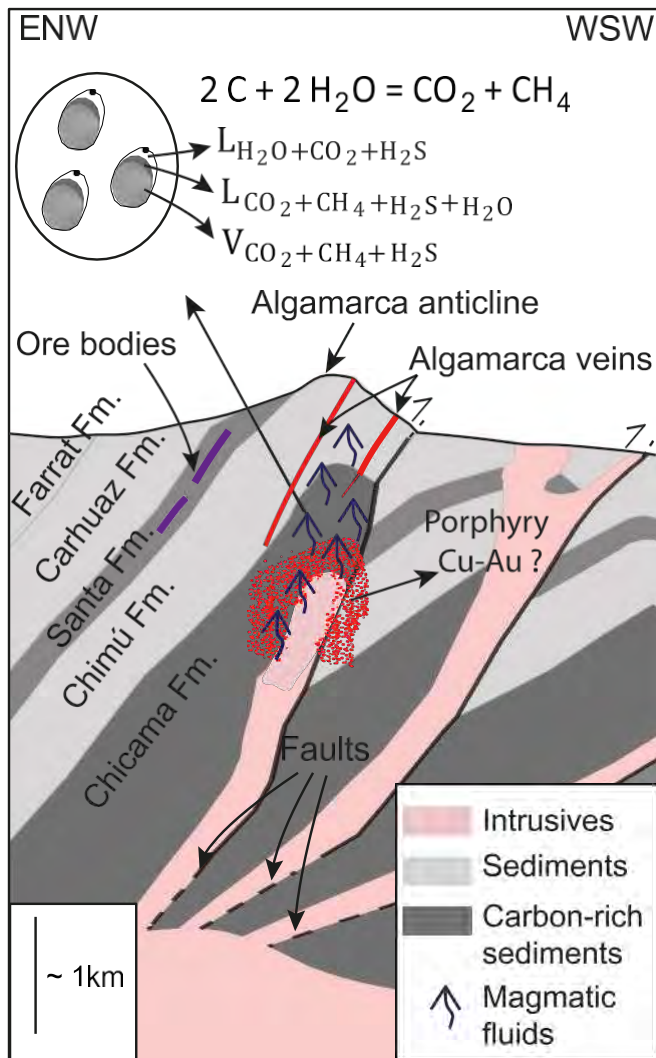
Fig. 18. Conceptual model of the Algamarca deposit formation. Immiscible-liquid fluid inclusions result from the interaction between magmatic fluids and the carbon-bearing sediments from the Chicama Formation (Fm.). These interactions, coupled with favorable tectonics (faults, anticlines), greatly favored gold transport through the sedimentary sequence and subsequent gold accumulation in arsenian pyrite.

3.4. Raman spectra of carbonaceous material (CM)

The Raman spectra of CM were collected on three representative polished sections, one from sample RRAL-07 (CM1) and two from sample RRAL-14 (CM2). The CM in sample RRAL-07 is present in narrow quartz-pyrite veins (<1 cm) with subordinate tennantite-tetrahedrite and chalcopyrite, all minerals from stage B of the Concepcio´n vein hosted by shales of the Chimú Formation (Fig. 16a). The CM in sample RRAL-14, collected in a fault zone of the Santa Formation next to the Algamarca ore bodies, is present in quartz and pyrite assemblages as disseminations and irregular interconnected bands (Fig. 16b). Potential effects on the Raman spectra of CM that might be induced by the polishing or different orientation were assumed to be negligible because the CM analyzed in this work presents a relatively low degree of graphitization at which such effects are small to negligible (Kouketsu et al., 2014, Hu et al., 2015; references therein). It can be seen in Fig. 16c that the relative intensities of the G-band versus the D-band are distinctly different in CM1 and CM2 samples, with the G-band being more intense in CM1, implying higher degree of graphitization of CM1 compared to CM2 (Lahfid et al., 2010). The graphitization peak temperature may be

quantified from these Raman peak parameters (Beyssac et al., 2002). Several geothermometers have been proposed for high and low-grade metamorphism (e.g., Beyssac et al., 2002; Rahl et al., 2005; Lahfid et al., 2010; Kouketsu et al., 2014). More recently, their application has been extended to sedimentary-hosted gold deposits (e.g., Hu et al., 2015; Wu et al., 2018). We used the geothermometers proposed by Lahfid et al. (2010) and Kouketsu et al. (2014). Fig. 16d shows an example of decomposition of a Raman spectrum of CM2 in five bands (G, D1, D2, D3, and D4); the obtained parameters and resulting temperature values are reported in Table A7.

In the Concepcio´n vein of stage B, the homogenization temperatures measured in late liquid-rich fluid inclusions (360 ± 20 °C) are similar within errors to the temperature obtained from the carbonaceous material CM1 (335 ± 40 °C). The CM-measured values directly reflect the temperature of the fluid that interacted with the carbonaceous material, and was trapped in the inclusions in quartz. The similarity of these independent temperature estimations further supports the validity of our entrapment temperature values for which pressure correction is negligible, implying that the fluid was entrapped at relatively shallow levels (<1.5 km). This conclusion is in accordance with shallow environments typical of epithermal deposits (White and Hedenquist, 1995; Hedenquist et al., 2000; Simmons et al., 2005), and is also reflected in the textures of open space deposition displayed in the veins in stages B and C (Fig. A1a-d). Same as in the Concepcio´n vein, in the ore bodies, the homogenization temperature in liquid-rich fluid inclusions (270 ± 20 °C) and Raman-measured temperatures in CM2 (305 ± 40 °C) overlap within errors, confirming shallow depths (<1.5 km) of formation.

4. Discussion

4.1. Properties, origin, and evolution of the mineralizing fluids

Algamarca and the other deposits located within the MFTB are associated with subduction-related Oligo-Miocene magmatic arc intrusions (Noble and McKee, 1999; Bissig and Tosdal, 2009). Thus, the different types of ore deposits in this belt likely reflect the large range of conditions intrinsic to porphyry systems associated with a magmatic activity (e.g., Sillitoe, 2010). Consequently, a magmatic source is commonly assumed for the mineralizing fluids (e.g., Rainbow et al., 2005; Cerpa et al., 2013; Rottier et al., 2018; Vallance et al., 2024). Our study directly supports a magmatic fluid origin for the Algamarca deposit based on fluid inclusion data, allowing to distinguish it from other potential sources such as metamorphic or basinal fluids, all of which are characterized by distinct elemental signatures (e.g., Samson et al., 2008; Nahnybida et al., 2009; Large et al., 2016).

The following lines highlight the evidence pointing to a magmatic origin of the Algamarca fluids. Firstly, the multiphase-solid fluid inclusions from Algamarca display high salt (NaCl, KCl) and metal (Fe, Cu, Zn) contents, which are diagnostic of magmatic brines from porphyry deposits (e.g., Kouzmanov and Pokrovski, 2012; Schirra et al., 2022). Secondly, the molar Br/Cl ratio obtained from the previously mentioned fluid inclusion type is 0.9 (±0.1) × 10^{-3}, which is distinctly lower than that of seawater (1.5 × 10^{-3}), and consistent with the typical range of magmatic fluids (0.5 to 1.0 × 10^{-3}; e.g., Kendrick et al., 2001; Nahnybida et al., 2009; references therein). Thirdly, the elevated Rb concentrations (500–1,000 ppm) in this fluid inclusion type are characteristic of magmatic fluids. Such fluids are enriched in Rb (>1,000 ppm Rb; Samson et al., 2008; Williams-Jones et al., 2010; Large et al., 2016; Zhao et al., 2020), and are systematically higher than values reported for basinal brines (<100 ppm; Samson et al., 2008; references therein) or metamorphic fluids (<140 ppm; Van Daele et al., 2018; references therein). Fourthly, the K/Na and Mn/Na ratios for multiphase-solid and liquid-rich fluid inclusions from Algamarca are higher than for basinal brines and metamorphic fluids (Fig. 17a; Samson et al., 2008; Williams-Jones et al., 2010). Finally, the liquid-rich and multiphase-solid fluid-inclusion types show overlapping Zn/Pb ratios of 5 ± 1 and 3 ± 1,

respectively (Fig. 17b), close to those reported for large porphyry deposits (Kouzmanov and Pokrovski, 2012; Rottier et al., 2016b). Furthermore, it is unlikely that the ratios of those pretty soluble elements that mostly stay in the fluid would have been significantly altered due to mechanisms such as boiling, sulfide precipitation and/or water- – rock interactions. As a result, their geochemical signatures clearly indicate a magmatic origin.

An uncommon feature of our fluid inclusion data set is the presence of immiscible-liquid fluid inclusions, displaying high CO_2, CH_4 and H_2S concentrations (mole percentage in the vapor phase of 60 %, 10 % and 30 %, respectively). Such high carbon volatile concentrations are quite unusual in a porphyry system. Although CO_2 was identified in several both oxidized and reduced porphyry systems (Shen et al., 2010), its concentrations estimated in fluid inclusions from typical porphyry systems are rather low (<10 mol%; Rusk et al., 2008; Catchpole et al., 2015). The scarcity of CO_2 is due to the low CO_2 solubility in magmas at shallow depths (Lowenstern, 2001), with the exsolution of most CO_2 from magmas occurring deeper in the crust in the early stages of a calc-alkaline magma evolution, in contrast to water and associated dissolved metals and salts that degas at shallower levels (Aud´etat and Simon, 2012). However, dissolution of carbonate-bearing sediments might also account for the presence of CO_2 in some hydrothermal fluids (e.g., Minissale et al., 2002), but requires the presence of carbonate rocks which are rare at Algamarca. Methane-bearing fluid inclusions are not reported in oxidized porphyry deposits (Rusk et al., 2008; Shen et al., 2010), while methane-rich inclusions are frequent in reduced porphyry deposits (Cao et al., 2014b; Zhang et al., 2019). In most cases, the origin of methane has been attributed to thermal decomposition of sedimentary organic matter. This decomposition can be generated by i) the deep burial of sediments in a typical petroleum system (Magoon and Dow, 1994), ii) contact metamorphism (e.g., Aarnes et al., 2010), or iii) magmatic assimilation (e.g., Iacono-Marziano et al., 2012; Capriolo et al., 2021). Other origins have also been invoked, including production of methane by a Fischer-Tropsch synthesis in which CO_2 is reduced to CH_4 (e.g., Cao et al., 2014a), microbial reactions (e.g., Ueno et al.,2006), or CH_4 being directly derived from the mantle (Cao et al., 2014a; references therein). Alternatively, methane as well as CO_2 may be generated by direct sedimentary organic matter interactions with hydrothermal fluids (e.g., Vallance et al., 2003; Fan et al., 2004; Zhu et al., 2012; Lang et al., 2020; Vallance et al., 2024). The latter mechanism seems to be most plausible in the context of Algamarca as discussed below.

Indeed, in the case of Algamarca—an epithermal deposit associated with an oxidized calc-alkaline magmatism—the composition of the immiscible-liquid fluid inclusions is highly unusual, with large and comparable amounts of coexisting CO_2, CH_4 and H_2S. A plausible explanation for this composition is that ascending magmatic fluids directly interacted with the carbon-bearing sediments, most likely from the Chicama Formation (Fig. 18). This would have led the production of both CO_2 and CH_4, by carbon disproportionation reaction in water such as

$$2\ Graphite + 2\ H_2O = CO_2 + CH_4 \tag{1}$$
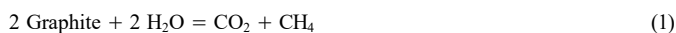
Additional dissolution of hydrocarbons, richer in H (CH_x), would result in CH_4/CO_2 ratios higher than 1 in the fluid. Mixing of the hydrothermal fluids with CH_4 produced by thermogenesis of organic matter before or during the magmatic activity could also supply some CH_4. Hydrogen sulfide may stem from original S-rich magmatic fluids and/or petroleum-related H_2S, both known to be able to carry up to several wt % of sulfur (Kouzmanov and Pokrovski, 2012; Migdisov et al., 2017). The systematically lower CH_4/CO_2 (and /CH_4/H_2S) ratios recorded in the immiscible-liquid fluid inclusions (Fig. 13) compared to those produced by reaction (1) and the other mechanisms discussed above, are fundamentally due to much lower CH_4 than CO_2 or H_2S gas solubility in aqueous solution. Indeed, $CH_{4(g)}$ is at least 10 and 30 times

less soluble in liquid water than $CO_{2(g)}$ and $H_2S_{(g)}$, respectively, according to the well-known thermodynamic Henry constants of the reactions $CH_{4(g)} = CH_{4(aq)}$, $CO_{2(g)} = CO_{2(aq)}$, and $H_2S_{(g)} = H_2S_{(aq)}$ (e.g., Naumov et al., 1971; Akinfiev and Diamond, 2003). As a result, methane produced by reaction (1) or similar would have a stronger tendency than CO_2 (and H_2S) to exsolve from the fluid into the gas phase and to leave the system before quartz growth and fluid inclusion entrapment, resulting in CH_4/CO_2 ratios less than 1, as we systematically found in fluid inclusions (Table 4). The strong interactions between the carbon-bearing sediments and the hydrothermal fluid are also reflected in the structure of the carbonaceous material, which yields a temperature value for peak metamorphism similar to those recorded for the fluid inclusions.

Interactions of magmatic fluid and carbonaceous material are likely to be common in subduction-related magmatic arc settings such as for the Miocene metallogenic belt of central and northern Peru. For example, the occurrence of low-sulfidation assemblages in epithermal deposits, like Cerro de Pasco and Shahuindo, was interpreted by interactions of the magmatic fluid with the carbonaceous material from the basement or from the sedimentary host rock (Rottier et al., 2016a, 2018; Vallance et al., 2024). Indeed, the immiscible-liquid fluid inclusions from the Algamarca deposit offer irrefutable proof of these intensive interactions. Beyond the above examples, the occurrence in the MFTB of Miocene low-sulfidation epithermal deposits, such as the Tres Cruces deposit (Montgomery, 2012) also likely reflects interactions of oxidized porphyry fluids, typical of calc-alkaline magmatism (Sillitoe and Hedenquist, 2005; Sillitoe, 2010), with the carbonaceous material of the Mesozoic sediments.

4.2. Trace elements in pyrite

The different types of pyrites found in the Algamarca deposit, i.e. in sedimentary rocks, ore bodies veins and host rocks (Py_s, Py_b, Py_v and Py_h), show differences in their textures and element concentrations (Fig. 5a-i, 7a, b, A3; Table 2). The sedimentary pyrite type is enriched in trace elements such as Co, Ni, Mo, V, Mn, Sb, and Pb (Fig. A3), which is consistent with the trace element patterns reported for sedimentary pyrite in black shales worldwide (e.g., Gregory et al., 2015). On the other hand, hydrothermal pyrite found in veins as well as disseminated in the host rock (Py_v and Py_h) is enriched in Au and As. Both elements show statistically positive correlations (Table A4), their concentrations in pyrite plot below the empirical gold solubility limit (Fig. 7b) proposed by Reich et al. (2005), and their LA-ICPMS transient signals are flat for most analyses (e.g., Fig. A5a, b). These features collectively indicate that Au is structurally bound in pyrite. The pyrite type from ore bodies was formed by replacement of pyrrhotite and marcasite, and shows the lowest Au and As concentrations, indicating that the replacement process appears to be less efficient in the incorporation of Au and As in pyrite than direct crystallization from the hydrothermal fluid.

In our paragenetic sequence, we have defined two main mineralization events, i.e., stages A (pre-gold stage) and B (gold stage), in which were found the pyrite types Py_v-I and Py_v-II, respectively. The concentration of Au and As in pyrite from stage B (Py_v-II; epithermal stage) is higher than in pyrite from stage A (Py_v-I; porphyry-like stage; Fig. 7a, b), which is also the case for many porphyry systems (e.g., Deditius et al., 2014; Franchini et al., 2015; Sykora et al., 2018). This feature thus supports a porphyry-epithermal transition for Algamarca.

4.3. Metal concentrations in the mineralizing fluid

During unmixing of a magmatic fluid to brine and vapor, Cu is partitioned preferentially into the brine, as it is shown by direct experimental measurements of vapor/liquid partition coefficients (Lerchbaumer and Aud´etat, 2012; Pokrovski et al., 2013; Kokh et al., 2016; Zajacz et al., 2017) and by the high Cu concentrations measured in brine inclusions from several porphyry deposits (0.5 wt% Cu in average;

Kouzmanov and Pokrovski, 2012; Schirra et al., 2022). Additionally, Cu concentrations in the brine-like and, more importantly, in vapor-like fluid inclusions might be modified, after fluid inclusion entrapment, by selective Cu diffusion through quartz lattice (Lerchbaumer and Aud´etat, 2012). Chalcopyrite precipitation processes from the brine phase may also contribute to variability of Cu concentrations in the fluid inclusions (e.g., Catchpole et al., 2011). At stage A of the Algamarca vein formation, quartz, pyrite, and chalcopyrite co-precipitated, and the most abundant fluid inclusions are multiphase-solid and vapor-rich types. At some places, the two types are present in the same assemblage, indicating that boiling occurred. The different FIAs show Cu concentrations varying from one FIA to another (from 70 to 7,000 ppm; Table A6), but similar Cu concentrations within a given FIAs, ruling out heterogeneous chalcopyrite entrapment during inclusion formation. Rather, the variability of Cu concentrations among the different FIAs may be due to a combination of chalcopyrite precipitation from the fluid during quartz growth and before fluid inclusion entrapment generated by cooling and fluid unmixing processes (e.g., Hezarkhani et al., 1999; Harris et al., 2005), coupled with possible post-entrapment Cu diffusion in or out the inclusion (Lerchbaumer and Aud´etat, 2012).

At stage B, the metal concentrations (Fe, K, Mn, Zn, Pb) of the liquid- rich fluid inclusions positively correlate with the salinity values (Fig. 14), as it would be expected for metals transported by chloride complexes (Kouzmanov and Pokrovski, 2012). The exception is Cu that does not show such correlations, which is likely related to the large Cu concentration variability in fluid inclusions as discussed above. Metalloids, such as As and Sb, do not show correlations with salinity values (Fig. 14), which is due to the fact that these elements are transported as hydroxide complexes (Pokrovski et al., 1996; Zotov et al., 2003). Despite the fall in temperature recorded by early to late liquid-rich FIAs (Fig. A6a), Zn and Pb are almost constant in the fluid (Fig. 15), indicating that saturation was not reached for these metals and in agreement with the absence of sphalerite and galena in the mineral assemblages (Fig. 4a), due to the relatively high solubility of ZnS and PbS over a wide range of temperature (Fontbote´ et al., 2017; references therein).

4.4. Role of arsenian pyrite in the gold concentration and deposition

The close association of Au and As in pyrite has been widely documented in several types of ore deposits (Deditius et al., 2014; references therein). It has recently been demonstrated that the coupled incorporation of Au^{II} and As^{-I} in the Fe and S pyrite crystallographic sites, respectively, is the key mechanism to explain the Au-As chemical association in arsenopyrite and arsenic-rich pyrite (Pokrovski et al., 2021). The extremely efficient partitioning into pyrite of Au and As from a fluid under-saturated with respect to metallic gold leads to large concentrations of Au and As chemically bound in pyrite at redox and pH conditions of Carlin and orogenic-type deposits (Kusebauch et al., 2018, 2019; Pokrovski et al., 2021), conditions that are similar to those determined at Algamarca.

The pyrite-fluid partition coefficients of Au and As are ~200 for both elements, as follows from the typical ratio of their concentrations in pyrite (Py$_v$-II) and in the liquid-rich type of fluid inclusions trapped in quartz (Qz-II) because both pyrite and quartz crystallized contemporaneously in the Algamarca veins. These partition coefficient values are of the same order of magnitude as those experimentally measured by Kusebauch et al. (2019) at 200 °C under redox and acidity conditions of Carlin-type deposits, and those predicted at higher temperatures, between 300 and 450 °C, by Pokrovski et al. (2021) under redox conditions for reduced porphyry and orogenic-type deposits. The enhanced Au partitioning into arsenian pyrite at our conditions allows for efficient gold scavenging even from fluids that are poor in Au (<0.1 ppm) as analyzed by LA-ICPMS in this study.

In the invisible-gold substage (B1), scavenging of Au from unsaturated fluid by arsenian pyrite is liable to be the main mechanism controlling Au deposition. In contrast, in the visible-gold substage (B2),

most gold was likely deposited as native metal. This difference may partly be related to more oxidizing conditions of sub-stage B2, manifested by the transition from low- (sub-stage B1) to intermediate-sulfidation state assemblage (sub-stage B2; Fig. 4a), conditions less favorable for both Au and As incorporation in pyrite in a chemically bound state (Pokrovski et al., 2021). Gangue minerals coeval to the native gold deposition were not found, which does not allow us to unambiguously constrain the causes for visible gold deposition. Generally, in most epithermal gold deposits, the major causes responsible for metallic gold deposition is the fluid boiling and the removal of H_2S into the vapor (Pokrovski et al., 2014; Simmons et al., 2020). Uplift and erosion are two processes that took place simultaneously during the formation of the Algamarca deposit. These events may have resulted in a pressure drop, thereby triggering fluid-phase separation during the visible-gold substage mineralization event (B2). This mechanism mainly removes H_2S from the liquid phase, destabilizing gold hydrosulfide complexes and allowing the precipitation of gold in a native state.

4.5. Role of the carbonaceous material in the gold transport and deposition

In an epithermal setting, genetically associated with a magmatic arc as for the Algamarca deposit, the mineralizing fluids are interpreted as acidic and oxidized magmatic fluids, which set high- or intermediate-sulfidation conditions (Hedenquist et al., 2000; Sillitoe and Hedenquist, 2005). The interaction between the oxidized magmatic fluid and the organic matter from the sediments produces fundamental changes in the key parameters of the fluid, i.e., a fluid pH and H_2S concentration increase, and a minor f_{O2} decrease (Vallance et al., 2024). The increase in H_2S and pH both act to enhancing the Au solubility in the form of Au^I hydrosulfide complexes, and is much stronger than the opposite affect produced by f_{O2} decrease, according to the reaction:

$$Au_{(metal)} + \tfrac{1}{4} O_2 + 2 H_2S_{(aq)} = Au(HS)_2^- + H^+ + \tfrac{1}{2} H_2O \qquad (2)$$

Other Au complexes such as those with the radical trisulfur ion, which may be important at higher temperatures and more oxidizing conditions of porphyry deposits (Au(HS)S$_3^-$ Pokrovski et al., 2015), were predicted to be minor in reduced epithermal settings such as that of our study (Vallance et al., 2024). Thus, driven by reaction (2), after the fluid-organic matter interactions, the Au-bearing fluid will continue its ascent to the surface without having lost its gold content. On its route, the fluid can reach structural and/or sedimentary traps, which can promote its accumulation. In these shallower and colder settings, the pyrite can crystallize in optimal conditions to efficiently incorporate both Au and As in its lattice. This is because the near-neutral pH and reduced conditions of the modified fluid favor the incorporation of bound Au and As in pyrite (Pokrovski et al., 2021; Vallance et al., 2024), conditions contrasting to those shown by the original acidic and oxidized magmatic fluids.

The characteristics of mineralizing fluids in sediment-hosted gold deposits of Carlin and orogenic types are similar. They are low salinity fluids, relatively reduced, with a near neutral pH, a ratio $CO_2/CH_4 > 1$ and abundant H_2S (Hofstra and Cline, 2000; Simmons et al., 2020). The fluids, recorded by immiscible-liquid fluid inclusions in the Algamarca veins, have similar characteristics to the fluids found in such sediment-hosted deposits. Indeed, our results show that the interaction of a magmatic fluid with organic matter in a basin can generate fluids like those reported in other sediment-hosted gold deposits.

4.6. Implications for exploration

The Algamarca and Shahuindo epithermal deposits are related to the same magmatic-hydrothermal center (Galdos et al., 2021), and both should be associated with a parental porphyry stock, in a similar way to other examples of porphyry-epithermal systems reported in the MFTB

(e.g., Gustafson et al., 2005; Santos et al., 2023). Our study on the origin of mineralizing fluid and ore mineralogy supports the hypothesis of a hidden porphyry-style mineralization. In the Algamarca veins, uplift and erosion synchronous to the lifespan of the deposit seem to have allowed superposition of a later epithermal stage (stage B) over an earlier porphyry-like stage (stage A). Such telescoping is a common process reported in porphyry systems worldwide (Sillitoe, 2010) and specifically in the MFTB (e. g., Catchpole et al., 2015).

In the Algamarca deposit, the mineralization event defined as stage A is composed mainly of quartz, gold-poor pyrite, and chalcopyrite. This mineral association can correspond to porphyry-type veins. As we determined in stage A, the quartz contains abundant multiphase-solid fluid inclusions. In porphyry deposits, the dense brine liquids remain at depth near the parental porphyry stock (e.g., Lerchbaumer and Aud´etat, 2012; Rottier et al., 2018). We only recognized stage A in the veins located at the northeast of the Alisos fault, providing an exploration vector toward a porphyry-style mineralization in this direction. In addition, in our study area, the intersection of NW-SE thrust faults or the anticline axis with the younger NE-SW faults that controlled the emplacement of porphyritic stocks has also been evidenced in El Galeno, Michiquillay and Shahuindo deposits within the MFTB (Davies and Williams, 2005; Vallance et al., 2024). Therefore, these intersections may be considered as potential sites for the emplacement of the parental porphyritic stock related to the Algamarca and Shahuindo epithermal mineralizations (Fig. 18).

5. Concluding remarks

We have investigated the Algamarca deposit, which is an epithermal deposit emplaced in a sedimentary basin rich in carbonaceous matter. Mineralogical and geochemical data on ore and gangue minerals were obtained by etching techniques, optical microscopy, scanning electron microscopy, X-ray diffraction, electron microprobe, and LA-ICPMS. Fluid inclusions in quartz were studied by cathodoluminescence, microthermometry, Raman spectroscopy, and LA-ICPMS.

Four stages of mineral precipitation were identified: three hypogene stages, of which the second, labelled as 'the gold stage', contains the major amounts of the metals of interest (Au, Ag, and Cu), while the first and third ('pre- and post-gold stages') events can be considered as non-economic or barren events. The hypogene events were followed by a fourth, supergene event. The main gold stage comprises an invisible-gold sub-stage, which contains mainly quartz and gold-rich arsenian pyrite, and a visible-gold sub-stage containing native gold particles associated with tetrahedrite-tennantite crystals, accompanied by minor chalcopyrite occurrences. Pyrite that occurs in the invisible-gold sub-stage is enriched in both Au and As that were likely incorporated in the pyrite structure via a coupled redox reaction.

Fluid inclusion analyses clearly point to a magmatic origin for the ore-bearing fluid. The fluid is particularly enriched in CO_2, CH_4 and H_2S, providing evidence for strong interactions between the ascending magmatic fluid and carbon-bearing sediments, mainly by reaction of graphite with water to form CO_2 and CH_4.

Interaction between an oxidized magmatic fluid and carbonaceous material from the sediments promotes the transport of gold, following the results of a companion paper (Vallance et al., 2024). Such modified hydrothermal fluids have favorable pH and high H_2S concentrations to efficiently transport dissolved gold as hydrosulfide complexes. Hence, such mineralizing fluids can follow their pathways guided by the thrust-faults system until they reach some structural and/or sedimentary traps in which arsenic-rich pyrite can precipitate due to optimal pH and redox conditions, triggering gold scavenging by the mineral from the fluid.

The differences in ore mineralogy, pyrite composition, and fluid inclusion data between the pre-gold and gold stages are interpreted as a process of telescoping of an epithermal-style overprinting a porphyry-style mineralization, which may be extended to greater depth underneath the sedimentary sequence hosting the epithermal deposit. It

follows that our investigation of the characteristics of the mineralizing fluid and ore minerals can provide a novel targeting tool for exploration of hidden porphyry-style mineralizations.

Data availability

All data are provided in the manuscript and Supplement Material.

Appendix A. Supplementary data

Supplementary data to this article can be found online at https://doi.org/10.1016/j.oregeorev.2023.105857.

References

Aarnes, I., Svensen, H., Connolly, J.A.D., Podlachikov, Y.Y., 2010. How contact metamorphism can trigger climate changes: modelling gas generation around igneous sills in sedimentary basins. Geochim. Cosmochim. Acta 74, 7179–7195.
Agangi, A., Hofmann, A., Wohlgemuth-Ueberwasser, C.C., 2013. Pyrite zoning as a record of mineralization in the Ventersdorp Contact Reef, Witwatersrand Basin, South Africa. Econ. Geol. 108, 1243–1272.
Agangi, A., Hofmann, A., Rollion-Bard, C., Marin-Carbonne, J., Cavalazzi, B., Large, R., Meffre, S., 2015. Gold accumulation in the Archaean Witwatersrand Basin, South Africa—Evidence from concentrically laminated pyrite. Earth Sci. Rev. 140, 27–53.
Akinfiev, N.N., Diamond, L.W., 2003. Thermodynamic description of aqueous nonelectrolytes over a wide range of state parameters. Geochim. Cosmochim. Acta 67, 613–627.
Arehart, G.B., 1996. Characteristics and origin of sediment-hosted disseminated gold deposits: A review. Ore Geol. Rev. 11, 383–403.
Aud´etat, A., Simon, A.C., 2012. Magmatic controls on porphyry copper genesis. Soc. Econ. Geol. Spec. Publ. 16, 553–572.
Bakker, R.J., 1997. CLATHRATES: computer programs to calculate fluid inclusion V-X properties using clathrate melting temperatures. Comput. Geosci. 23, 1–18.
Bakker, R.J., 2003. Package FLUIDS 1. Computer programs for analysis of fluid inclusion data and for modelling bulk fluid properties. Chem. Geol. 194, 3–23.
Barker, S.L., Hickey, K.A., Cline, J.S., Dipple, G.M., Kilburn, M.R., Vaughan, J.R., Longo, A.A., 2009. Uncloaking invisible gold: Use of nanoSIMS to evaluate gold, trace elements, and sulfur isotopes in pyrite from Carlin-type gold deposits. Econ. Geol. 104, 897–904.
Barr´e, G., Truche, L., Bazarkina, E.F., Michels, R., Dubessy, J., 2017. First evidence of the trisulfur radical ion S_3^- and other sulfur polymers in natural fluid inclusions. Chem. Geol. 462, 1–14.
Benavides-C´aceres, V., 1956. Cretaceous system in northern Peru. Bull. Am. Mus. Nat. Hist. 108, 352–494.
Benavides-C´aceres, V., 1999. Orogenic evolution of the Peruvian Andes: The Andean cycle. Soc. Econ. Geol. Special Publ. 7, 61–107.
Beyssac, O., Goff´e, B., Chopin, C., Rouzaud, J., 2002. Raman spectra of carbonaceous material in metasediments: a new geothermometer. J. Metamorph. Geol. 20, 859–871.
Bissig, T., Tosdal, R.M., 2009. Petrogenetic and metallogenetic relationships in the eastern Cordillera Occidental of central Peru. J. Geol. 117, 499–518.
Bodnar, R.J., 1993. Revised equation and table for determining the freezing point depression of H_2O-NaCl solutions. Geochim. Cosmochim. Acta 57, 683–684.
Bodnar, R.J., Lecumberri-Sanchez, P., Moncada, D., Steele-MacInnis, M., 2014. Fluid inclusions in hydrothermal ore deposits. In: Holland, H.D., Turekian, K.K. (Eds.), Treatise on Geochemistry, second ed.13. Elsevier, Oxford, pp. 119–142.

Chapter III

Bodnar, R.J., Vityk, M.O., 1994. Interpretation of microthermometric data for H_2O-NaCl fluid inclusions. In: De Vivo, B., Frezzotti, M.L. (Eds.), Fluid Inclusions in Minerals, Methods and Applications. Virginia Tech, Blacksburg, Virginia, pp. 117–130.

Burke, E.A.J., 2001. Raman microspectrometry of fluid inclusions. Lithos 55, 139–158.

Campbell, A.R., Robinson-Cook, S., 1987. Infrared fluid inclusion microthermometry on coexisting wolframite and quartz. Econ. Geol. 83, 1640–1645.

Cao, M.J., Qin, K.Z., Li, G.M., Evans, N.J., Jin, L.Y., 2014a. Abiogenic Fischer-Tropsch synthesis of methane at the Baogutu reduced porphyry copper deposit, western Junggar, Nwchina. Geochim. Cosmochim. Acta 141, 179–198.

Cao, M.J., Li, G.M., Qin, K.Z., Jin, L.Y., Evans, N.J., Yang, X.R., 2014b. Baogutu: an example of reduced porphyry Cu deposit in western Junggar. Ore Geol. Rev. 56, 159–180.

Capriolo, M., Marzoli, A., Aradi, L.E., Ackerson, M.R., Bartoli, O., Callegaro, S., Dal Corso, J., Ernesto, M., Gouvˆea Vasconcellos, E.M., De Min, A., Newton, R.J., Szabo´, C., 2021. Massive methane fluxing from magma-sediment interaction in the end-Triassic central Atlantic magmatic province. Nat. Commun. 12, 5534.

Catchpole, H., Kouzmanov, K., Fontbot´e, L., Guillong, M., Heinrich, C.A., 2011. Fluid evolution in zoned Cordilleran polymetallic veins—insights from microthermometry and LA-ICPMS of fluid inclusions. Chem. Geol. 281, 293–304.

Catchpole, H., Kouzmanov, K., Putlitz, B., Seo, J.H., Fontbot´e, L., 2015. Zoned base metal mineralization in a porphyry system: origin and evolution of mineralizing fluids in the Morococha District. Peru. Econ. Geol. 110, 39–71.

Cerpa, L.M., Bissig, T., Kyser, K., McEwan, C., Macassi, A., Rios, H.W., 2013. Lithologic controls on mineralization at the Lagunas Norte high-sulfidation epithermal gold deposit, northern Peru. Miner. Deposita 48, 653–673.

Chew, D., Schaltegger, U., Koˇsler, J., Whitehouse, M.J., Gutjahr, M., Spikings, R.A., Miˇskovi´c, A., 2007. U-Pb geochronologic evidence for the evolution of the Gondwanan margin of the north central Andes. Geol. Soc. Am. Bull. 119, 697–711.

Cline, J.S., Hofstra, A.H., Muntean, J.L., Tosdal, R.M., Hickey, K.A., 2005. Carlin-type gold deposits in Nevada: critical geologic characteristics and viable models. Econ. Geol. 100, 451–454.

Cooke, D.R., Hollings, P., Walshe, J.L., 2005. Giant porphyry deposits: characteristics, distribution, and tectonic controls. Econ. Geol. 100, 801–818.

Cossio, A., Jaen, H., 1967. Geología de los cuadr´angulos de Pu´emape, Chocope, Otuzo, Trujillo, Salaverry y Santa. Servicio de geología y minería del Perú, Bol. 17. 141 p.

Crede, L.-S., Liu, W., Evans, K.A., Rempel, K.U., Testemale, D., Brugger, J., 2019. Crude oil as ore fluids: An experimental in-situ XAS study of gold partitioning between brine and organic fluid from 25 to 250 °C. Geochim. Cosmochim. Acta 244, 352–365.

Davies, R.C., Williams, P.J., 2005. The El Galeno and Michiquillay porphyry Cu-Au-Mo deposits: Geological descriptions and comparison of Miocene porphyry systems in the Cajamarca district, northern Peru. Miner. Deposita 40, 598–616.

Deditius, A.P., Reich, M., Kesler, S.E., Utsunomiya, S., Chryssoulis, S.L., Walshe, J., Ewing, R.C., 2014. The coupled geochemistry of Au and As in pyrite from hydrothermal ore deposits. Geochim. Cosmochim. Acta 140, 644–670.

Defilippi, C., Muerhoff, C.V., Williams, T., 2016. In: Technical Report on the Shahuindo Mine. NI, Cajabamba, Peru, p. 307.

Ding, Z., Sun, X., Hu, S., Chen, H., Li, D., Fu, Y., Xu, L., Wu, Z., Huang, F., 2023. Role of carbonaceous material in gold precipitation for orogenic gold deposits: A case study of the Bangbu gold deposit in southern Tibet, China. Ore Geol. Rev. 152, 105231.

Dubessy, J., Caumon, M.-C., Rull, F., 2012. Raman spectroscopy applied to earth sciences and cultural heritage. EMU Notes Mineral. 12, 438 p.

Echavarria, L., Nelson, E., Humphrey, J., Chavez, J., Escobedo, L., Iriondo, A., 2006. Geologic evolution of the Caylloma epithermal vein district, southern Peru. Econ. Geol. 101, 843–863.

Emsbo, P., Groves, D.I., Hofstra, A.H., Bierlein, F.P., 2006. The giant Carlin gold province: a protracted interplay of orogenic, basinal, and hydrothermal processes above a lithospheric boundary. Miner. Deposita 41, 517–525.

Eude, A., Roddaz, M., Brichau, S., Brusset, S., Baby, P., Calderon, Y., Soula, J.C., 2015. Timing of exhumation and deformation in the northern Peruvian Eastern Andean Wedge (5–8 S) as inferred from low temperature thermochronology and balanced cross section. Tectonics 34, 715–730.

Fan, H.-R., Xie, Y.-H., Wang, K.-Y., Wilde, S.A., 2004. Methane-rich fluid inclusions in skarn near the giant REE–Nb–Fe deposit at Bayan Obo, northern China. Ore Geol. Rev. 25, 301–309.

Fontbot´e, L., Kouzmanov, K., Chiaradia, M., Pokrovski, G.S., 2017. Sulfide minerals in hydrothermal deposits. Elements 13, 97–103.

Franchini, M., McFarlane, C., Maydaga´n, L., Reich, M., Lentz, D.R., Meinert, L., Bouhier, V., 2015. Trace metals in pyrite and marcasite from the Agua Rica porphyry-high sulfidation epithermal deposit, Catamarca, Argentina: textural features and metal zoning at the porphyry to epithermal transition. Ore Geol. Rev. 66, 366–387.

Frezzotti, M.L., Tecce, F., Casagli, A., 2012. Raman spectroscopy for fluid inclusion analysis. J. Geochem. Explor. 112, 1–20.

Frimmel, H.E., Nwaila, G.T., 2020. Geologic evidence of syngenetic gold in the Witwatersrand Goldfields, South Africa. Soc. Econ. Geol. Spec. Publ. 23, 645–668.

Fuchs, S., Schumann, D., Martin, R.F., Couillard, M., 2021. The extensive hydrocarbon-mediated fixation of hydrothermal gold in the Witwatersrand Basin, South Africa. Ore Geol. Rev. 138, 104313.

Gaboury, D., MacKenzie, D., Craw, D., 2021. Fluid volatile composition associated with orogenic gold mineralization, Otago Schist, New Zealand: Implications of H_2 and C_2H_6 for fluid evolution and gold source. Ore Geol. Rev. 133, 104086.

Galdos R., Vallance J., Baby P., Pokrovski G.S., 2021. A common hydrothermal magmatic system generates different styles of gold mineralization at Algamarca and Shahuindo, northern Peru. ProEXPLO 2021, Lima, Peru. Extended Abstracts 100–104.

Gauthier A., Díaz N., Quirita V., 1999. Yacimientos la Arena-Virgen. ProEXPLO 1999, Lima, Perú. Primer volumen de monografías de yacimientos minerales peruanos. Historia, exploracio´n y geología. 73–91.

Ge, X., Shen, C., He, P., Jin, Y., Li, S., Chen, Y., 2022. The roles of hydrocarbons on the mineralization of Carlin-type gold deposits, Nanpanjiang Basin, South China. Ore Geol. Rev. 149, 105107.

Goldstein, R.H., Reynolds, T.J., 1994. Systematics of fluid inclusions in diagenetic minerals. SEPM short course Soc. for Sedimentary Geol. USA, 199 p.

Gregory, D.D., Large, R.R., Halpin, J.A., Lounejeva Baturina, E., Lyons, T.W., Wu, S., Sack, P.J., Chappaz, A., Maslennikov, V.V., Bull, S.W., Danyushevsky, L., 2015. Trace element content of sedimentary pyrite in black shales. Econ. Geol. 110, 1389–1410.

Groves, D.I., Goldfarb, R.J., Robert, F., et al., 2003. Gold deposits in metamorphic belts overview of current understanding, outstanding problems, future research, and exploration significance. Econ. Geol. 98, 1–29.

Guillong, M., Meier, D.L., Allan, M.M., Heinrich, C.A., Yardley, B.W.D., 2008. SILLS: AMATLAB-based program for the reduction of laser ablation ICP-MS data of homogeneous materials and inclusions. Miner. Ass. Can. Short Course Ser. 40, 328–333.

Gustafson, L.B., Vidal, C.E., Pinto, R., Noble, D.C., 2005. Porphyry-epithermal transition, Cajamarca region, northern Peru. Soc. Econ. Geol. Spec. Publ. 11, 279–299.

Harris, A.H., Golding, S.D., White, N.C., 2005. Bajo de la Alumbrera copper–gold deposit: stable isotope evidence for a porphyry-related hydrothermal system dominated by magmatic aqueous fluids. Econ. Geol. 100, 863–886.

Hedenquist, J.W., Arribas, A., Gonzales-Urien, E., 2000. Exploration for epithermal gold deposits. Soc. Econ. Geol. Rev. 13, 245–277.

Heinrich, C.A., Pettke, T., Halter, W.E., Aigner-Torres, M., Aud´etat, A., Gunther, D., Hattendorf, B., Bleiner, D., Guillong, M., Horn, I., 2003. Quantitative multi-element analysis of minerals, fluid and melt inclusions by LA-ICP-mass spectrometry. Geochim. Cosmochim. Acta 67, 3473–3497.

Hezarkhani, A., Williams-Jones, A.E., Gammons, C.H., 1999. Factors controlling copper solubility and chalcopyrite deposition in the Sungun porphyry copper deposit. Iran. Miner. Deposita 34, 770–783.

Hodder, R.W., Amireault, S., Arsenault, C., Huisa, F., 2010. The Shahuindo epithermal gold occurrence Cajabamba Province, Peru. Petrographic reconnaissance & interpretation of shape and size: Report Prepared for Sulliden Gold Corporation Ltd. 121 p.

Hofstra, A.H., Cline, J.S., 2000. Characteristics and models for Carlin-type gold deposits. Soc. Econ. Geol. Rev. 13, 163–220.

Hu, S., Evans, K., Craw, D., Rempel, K., Bourdet, J., Dick, J., Grice, K., 2015. Raman characterization of carbonaceous material in the Macraes orogenic gold deposit and metasedimentary host rocks, New Zealand. Ore Geol. Rev. 70, 80–95.

Iacono-Marziano, G., Gaillard, F., Scaillet, B., Polozov, A.G., Marecal, V., Pirre, M., Arndt, N., 2012. Extremely reducing conditions reached during basaltic intrusion in organic matter bearing sediments. Earth Planet. Sci. Lett. 357–358, 319–326.

INGEMMET, 2017. Mapa Geolo´gico del Perú, escala 1:100,000. https://geocatmin. ingemmet.gob.pe/geocatmin/.

Ishida, M., Romero, R., Leisen, M., Yasukawa, K., Nakamura, K., Barra, F., Reich, M., Kato, Y., 2021. Auriferous pyrite formed by episodic fluid inputs in the Akeshi and Kasuga high-sulfidation deposits, Southern Kyushu, Japan. Miner. Deposita 57, 129–145.

Jacquemet, N., Guillaume, D., Zwick, A., Pokrovski, G.S., 2014. In situ Raman spectroscopy identification of the S₃ion in S-rich hydrothermal fluids from synthetic fluid inclusions. Amer. Mineral. 99, 1109–1118.

Jaillard, E., Jacay, J., 1989. Les "Couches Chicama" du Nord du Perou: colmatage d'un bassin ne´ d'une collision oblique au tithonique. C.R. Acad. Sci. Paris 308 (II), 1459–1465.

Kendrick, M.A., Burgess, R., Pattrick, R.A.D., Turner, G., 2001. Fluid inclusion noble gas and halogen evidence on the origin of Cu-porphyry mineralizing fluids. Geochim. Cosmochim. Acta 65, 2651–2668.

Kokh, M.A., Lopez, M., Gisquet, P., Lanzanova, A., Candaudap, F., Besson, P., Pokrovski, G.S., 2016. Combined effect of carbon dioxide and sulfur on vapor-liquid partitioning of metals in hydrothermal systems. Geochim. Cosmochim. Acta 187, 311–333.

Kouketsu, Y., Mizukami, T., Mori, H., Endo, S., Aoya, M., Hara, H., Nakamura, D., Wallis, S., 2014. A new approach to develop the Raman carbonaceous material geothermometer for low-grade metamorphism using peak width. Isl. Arc 23, 33–50.

Kouzmanov, K., Pettke, T., Heinrich, C.A., 2010. Direct analysis of ore-precipitating fluids: combined IR microscopy and LA-ICPMS study of fluid inclusions in opaque ore minerals. Econ. Geol. 105, 351–373.

Kouzmanov, K., Pokrovski, G.S., 2012. Hydrothermal controls on metal distribution in porphyry Cu(-Au-Mo) systems. Soc. Econ. Geol. Spec. Publ. 16, 573–618.

Kouzmanov, K., Bailly, L., Ramboz, C., Rouer, O., Beny, J.M., 2002. Morphology, origin and infrared microthermometry of fluid inclusions in pyrite from the Radka epithermal copper deposit, Srednogorie zone, Bulgaria. Miner. Deposita 37, 599–613.

Kretschmar, U., Scott, S.D., 1976. Phase relations involving arsenopyrite in the system Fe-As-S and their application. Can. Miner. 14, 364–386.

Kusebauch, C., Oelze, M., Gleeson, S.A., 2018. Partitioning of arsenic between hydrothermal fluid and pyrite during experimental siderite replacement. Chem. Geol. 500, 136–147.

Kusebauch, C., Gleeson, S.A., Oelze, M., 2019. Coupled partitioning of Au and As into pyrite controls formation of giant Au deposits. Sci. Adv. 5, eaav5891.

Lahfid, A., Beyssac, O., Deville, E., Negro, F., Chopin, C., Goff´e, B., 2010. Evolution of the Raman spectrum of carbonaceous material in low grade metasediments of the Glarus Alps (Switzerland). Terra Nova 22, 354–360.

Lang, X., Deng, Y., Wang, X., Tang, J., Xie, F., Yang, Z., Jiang, K., 2020. Reduced fluids in porphyry copper-gold systems reflect the occurrence of the wall-rock thermogenic process: An example from the No. 1 deposit in the Xiongcun district, Tibet, China. Ore Geol. Rev. 118, 103212.

Large, R.R., Bull, S.W., Maslennikov, V.V., 2011. A carbonaceous sedimentary source-rock model for carlin-type and orogenic gold deposits. Econ. Geol. 106, 331–358.

Large, R.R., Meffre, S., Burnett, R., Guy, B., Bull, S., Gilbert, S., Goemann, K., Danyushevsky, L., 2013. Evidence for an intra basinal source and multiple concentration processes in the formation of the carbon leader reef, Witwatersrand Supergroup, South Africa. Econ. Geol. 108, 1215–1241.

Large, S.J.E., Bakker, E.Y.N., Weis, P., Wälle, M., Ressel, M., Heinrich, C.A., 2016. Trace elements in fluid inclusions of sediment-hosted gold deposits indicate a magmatic-hydrothermal origin of the Carlin ore trend. Geology 44, 1015–1018.

Lerchbaumer, L., Audétat, A., 2012. High Cu concentrations in vapor-type fluid inclusions: An artifact? Geochim. Cosmochim. Acta 88, 255–274.

Lowenstern, J.B., 2001. Carbon dioxide in magmas and implications for hydrothermal systems. Miner. Deposita 36, 490–502.

Magoon, L.B., Dow, W.G., 1994. The petroleum system. AAPG Mem. 60, 3–24.

Mégard, F., 1984. The Andean orogenic period and its major structures in central and northern Perú. J. Geol. Soc. Lond. 141, 893–900.

Migdisov, A.A., Guo, X., Williams-Jones, A.E., Sun, C.J., Vasyukova, O., Sugiyama, I., Fuchs, S., Pearce, K., Roback, R., 2017. Hydrocarbons as ore fluids: Geochem. Persp. Let. 5, 47–52.

Minissale, A., Kerrick, D.M., Magro, G., Murrell, M.T., Paladini, M., Rihs, S., Sturchio, N. C., Tassi, F., Vaselli, O., 2002. Geochemistry of Quaternary travertines in the region north of Rome (Italy): structural, hydrologic and paleoclimatic implications. Earth Planet. Sci. Lett. 203, 709–728.

Montgomery, A.T., 2012. Metallogenetic controls on Miocene high-sulphidation epithermal gold mineralization, Alto Chicama district, La Libertad, northern Perú. Queen's University, Kingston, Ontario, Canada, p. 381. Unpublished PhD thesis.

Moritz, R., 2006. Fluid salinities obtained by infrared microthermometry of opaque minerals: implications for ore deposit modeling—a note of caution. J. Geochem. Explor. 89, 284–287.

Muntean, J.L., Cline, J.S., Simon, A.C., Longo, A.A., 2011. Magmatic-hydrothermal origin of Nevada's Carlin-type gold deposits. Nature 4, 122–127.

Nahnybida, T., Gleeson, S.A., Rusk, B.G., Wassenaar, L.I., 2009. Cl/Br ratios and stable chlorine isotope analysis of magmatic–hydrothermal fluid inclusions from Butte, Montana and Bingham Canyon. Utah. Miner. Deposita 44, 837–848.

Naumov, G.B., Ryzhenko, B.N., Khodakovsky, I.L., 1971. Handbook of thermodynamic data. Atomizdat, Moscow (in Russian). English translation is available from U.S. Department of Commerce, Washington D.C., PB-226.

Navarro C.P., Rivera P.M., Monge M. R., 2010. Geología y metalogenia del Grupo Calipuy (Volcanismo Cenozoico) Segmento Santiago de Chuco, norte del Perú: Ministerio de Energía y Minas INGEMMET, Boletín N ° 28 Serie D, Estudios Regionales, 201 p.

Noble, D.C., McKee, E.H., 1999. The Miocene metallogenic belt of central and northern Peru. in: Skinner, B.J. (Ed.), Geology and Ore Deposits of the central andes. Soc. Econ. Geol. Spec. Publ. 7, 155–193.

Noble, D.C., McKee, E.H., Mégard, F., 1979. Early Tertiary "Incaic" tectonism, uplift, and volcanic activity, Andes of central Peru. Geol. Soc. Am. Bull. 90, 903–907.

Noble, D.C., McKee, E.H., Mourier, T., Mégard, F., 1990. Cenozoic stratigraphy, magmatic activity, compressive deformation and uplift in northern Peru. Geol. Soc. Am. Bull. 102, 1105–1113.

Norman, M.D., Pearson, N.J., Sharma, A., Griffin, W.L., 1996. Quantitative analysis of trace elements in geological materials by laser ablation ICP-MS: Instrumental operating conditions and calibration values of NIST glasses. Geostand. Newslett. 20, 247–261.

Ortelli, M., Kouzmanov, K., Wälle, M., Ubrig, N., Casanova, V., 2018. Fluid inclusion studies in opaque ore minerals: I. Trace element content and physical properties of ore minerals controlling textural features in transmitted near-infrared light microscopy. Econ. Geol. 113, 1845–1860.

Pinet, N., Haeri-Ardakani, O., Jautzy, J., Savard, M.M., Sack, P., Mercier-Langevin, P., 2023. Thermal history of Carlin-type gold deposits in Yukon (Canada) as revealed by organic matter geothermometry, clumped isotope data, fluid inclusion microthermometry, and apatite fission-track analyses. Miner. Deposita 58, 903–923.

Pokrovski, G.S., Gout, R., Schott, J., Zotov, A., Harrichoury, J.C., 1996. Thermodynamic properties and stoichiometry of As(III) hydroxide complexes at hydrothermal solutions. Geochim. Cosmochim. Acta 60, 737–749.

Pokrovski, G.S., Kara, S., Roux, J., 2002. Stability and solubility of arsenopyrite, FeAsS, in crustal fluids. Geochim. Cosmochim. Acta 66, 2361–2378.

Pokrovski, G.S., Borisova, A.Y., Bychkov, A.Y., 2013. Speciation and transport of metals and metalloids in geological vapors. Rev. Miner. Geochem. 76, 165–218.

Pokrovski, G.S., Akinfiev, N.N., Borisova, A.Y., Zotov, A.V., Kouzmanov, K., 2014. Gold speciation and transport in geological fluids: insights from experiments and physical-chemical modeling. In: Garofalo, P., Ripley, E. (Eds.), Gold-Transporting Fluids in the Earth's Crust, Geol. Soc. London Spec. Publ., 402, pp. 9–70.

Pokrovski, G.S., Dubessy, J., 2015. Stability and abundance of the trisulfur radical ion S^-_3 in hydrothermal fluids. Earth Planet. Sci. Lett. 411, 298–309.

Pokrovski, G.S., Kokh, M.A., Guillaume, D., Borisova, A.Y., Gisquet, P., Hazemann, J.-L., Lahera, E., Del Net, W., Proux, O., Testemale, D., Haigis, V., Jonchìere, R., Seitsonen, A.P., Ferlat, G., Vuilleumier, R., Saitta, A.M., Boiron, M.-C., Dubessy, J., 2015. Sulfur radical species form gold deposits on Earth. Proc. Nat. Acad. Sci. USA (PNAS) 112 (44), 13484–13489.

Pokrovski, G.S., Escoda, C., Blanchard, M., Testemale, D., Hazemann, J.L., Gouy, S., Kokh, M.A., Boiron, M.-C., Parseval, F., Aigouy, T., Menjot, L., de Parseval, P., Proux, O., Rovezzi, M., Béziat, D., Salvi, S., Kouzmanov, K., Bartsch, T., Pöttgen, R.,

Doert, T., 2021. An arsenic-driven pump for invisible gold in hydrothermal systems. Geochem. Persp. Let. 17, 39–44.

Potter II, W.R., Brown, D.L., 1977. The volumetric properties of aqueous sodium chloride solutions from 0° to 500 °C at pressures up to 2000 bars based on a regression of available data in the literature. U.S. Geol. Survey Bull. 1421-c, 36 p.

Prudhomme, A., Baby, P., Robert, A., Brichau, S., Cuipa, E., Eude, A., Calderon, Y., O'Sullivan, P., 2019. Western thrusting and uplift in northern central Andes (western Peruvian margin). In: Horton, B.K., Folguera, A. (Eds.), Andean Tectonics. Elsevier, Amsterdam, pp. 299–331.

Radtke, A.S., Scheiner, B.J., 1970. Studies of hydrothermal gold deposition (I). Carlin gold deposit, Nevada: The role of carbonaceous materials in gold deposition. Econ. Geol. 65, 87–102.

Rahl, J.M., Anderson, K.M., Brandon, M.T., Fassoulas, C., 2005. Raman spectroscopic carbonaceous material thermometry of low-grade metamorphic rocks: calibration and application to tectonic exhumation in Crete, Greece. Earth Planet. Sci. Lett. 240, 339–354.

Rainbow, A., Clark, A.H., Kyser, T.K., Gaboury, F., Hodgson, C.J., 2005. The Pierina epithermal Au–Ag deposit, Ancash, Peru: paragenetic relationships, alunite textures, and stable isotope geochemistry. Chem. Geol. 215, 235–252.

Rauchenstein-Martinek, K., Wagner, T., Wälle, M., Heinrich, C.A., Arlt, T., 2016. Chemical evolution of metamorphic fluids in the Central Alps, Switzerland: insight from LA-ICPMS analysis of fluid inclusions. Geofluids 16, 877–908.

Reich, M., Kesler, S.E., Utsunomiya, S., Palenik, C.S., Chryssoulis, S.L., Ewing, R., 2005. Solubility of gold in arsenian pyrite. Geochim. Cosmochim. Acta 69, 2781–2796.

Richards, J.P., Kerrich, R., 1993. Observations of zoning and fluid inclusions in pyrite using a transmitted infrared light microscope (Lambda< or= 1.9 mu m). Econ. Geol. 88, 716–723.

Rosenbaum, G., Giles, D., Saxon, M., Betts, P.G., Weinberg, R.F., Duboz, C., 2005. Subduction of the Nazca Ridge and the Inca Plateau: insights into the formation of ore deposits in Peru. Earth Planet. Sci. Lett. 239, 18–32.

Rottier, B., Kouzmanov, K., Wälle, M., Bendezú, R., Fontbote, L., 2016a. Sulfide replacement processes revealed by textural and LA-ICPMS trace element analyses: Example from the early mineralization stages at Cerro de Pasco, Peru. Econ. Geol. 111, 1347–1367.

Rottier, B., Kouzmanov, K., Bouvier, A.S., Baumgartner, L.P., Wälle, M., Rezeau, H., Bendezú, R., Fontbotè, L., 2016b. Heterogeneous melt and hypersaline liquid inclusions in shallow porphyry type mineralization as markers of the magmatic-hydrothermal transition (Cerro de Pasco district, Peru). Chem. Geol. 447, 93–116.

Rottier, B., Kouzmanov, K., Casanova, V., Wälle, M., Fontbotè, L., 2018. Cyclic dilution of magmatic metal-rich hypersaline fluids by magmatic low-salinity fluid: A major process generating the giant epithermal polymetallic deposit of Cerro de Pasco, Peru. Econ. Geol. 113, 825–856.

Rusk, B.G., Reed, M.H., Dilles, J.H., 2008. Fluid inclusion evidence formagmatic–hydrothermal fluid evolution in the porphyry copper–molybdenum deposit at Butte, Montana. Econ. Geol. 103, 307–334.

Samson, I.M., Williams-Jones, A.E., Ault, K.M., Gagnon, J.E., Fryer, B.J., 2008. Source of fluids forming distal Zn–Pb–Ag skarns: evidence from laser ablation-inductively coupled plasma-mass spectrometry analysis of fluid inclusions from El Mochito, Honduras. Geology 36, 947–950.

Santos, A., Guo, W., Chen, N., Cerpa, L., Kojima, S., 2023. Geochronologically constrained life cycles of telescoped porphyry-epithermal systems at the La Arena district, northern Peru. Ore Geol. Rev. 155, 105375.

Scherrenberg, A.F., Kohn, B.P., Holcombe, R.J., Rosenbaum, G., 2016. Thermotectonic history of the Marañon Fold-Thrust Belt, Peru: Insights into mineralisation in an evolving orogen. Tectonophysics 667, 16–36.

Schirra, M., Laurent, O., Zwyer, T., Driesner, T., Heinrich, C.A., 2022. Fluid evolution at the Batu Hijau porphyry Cu-Au deposit, Indonesia: hypogene sulfide precipitation from a single-phase aqueous magmatic fluid during chlorite–white-mica alteration. Econ. Geol. 117, 979–1012.

Seltmann, R., Goldfarb, R.J., Zu, B., Creaser, R.A., Dolgoplova, A., Shatov, V.V., 2020. Muruntau, Uzbekistan: the world's largest epigenetic gold deposit. Soc. Econ. Geol. Spe. 23, 497–521.

Shen, P., Shen, Y.C., Wang, J.B., Zhu, H.P., Wang, L.J., Meng, L., 2010. Methane-rich fluid evolution of the Baogutu porphyry Cu–Mo–Au deposit, Xinjiang, NW China. Chem. Geol. 275, 78–98.

Shepherd, T.J., Rankin, A.H., Alderton, D.H.M., 1985. A Practical Guide to Fluid Inclusion Studies. Blackie, Glasgow, p. 239.

Sillitoe, R.H., 2010. Porphyry copper systems. Econ. Geol. 105, 3–41.

Sillitoe, R.H., Bonham, H.F., 1990. Sediment-hosted gold deposits: distal products of magmatic-hydrothermal systems. Geology 18, 157–161.

Sillitoe, R.H., Hedenquist, J.W., 2005. Linkages between volcanic tectonic settings, ore fluid compositions, and epithermal precious metals deposits. Soc. Econ. Geol. Spec. Publ. 10, 315–343.

Simmons, S.F., Tutolo, B.T., Barker, S.L.L., Goldfarb, R.J., Robert, F., 2020. Hydrothermal gold deposition in epithermal, Carlin, and orogenic deposits. Soc. Econ. Geol. Spec. Publ. 23, 823–845.

Simmons, S., White, N., John, D., 2005. Geological characteristics of epithermal precious and base metal deposits. Econ. Geol. 100th anniversary, 485–522.

Sośnicka, M., Lüders, V., Duschl, F., Kraemer, D., Laurent, O., Niedermann, S., Banks, D. A., Wilke, F., Wohlgemuth-Ueberwasser, C., Wiedenbeck, M., 2023. Metal budget and origin of aqueous brines depositing deep-seated Zn-Pb mineralization linked to hydrocarbon reservoirs, north German Basin. Miner. Deposita 58, 1143–1170.

Sykora, S., Cooke, D., Meffre, S., Stephanov, A., Gardner, K., Scott, R., Selley, D., Harris, A., 2018. Evolution of pyrite trace element compositions from porphyry-style and epithermal conditions at the Lihir gold deposit: Implications for ore genesis and mineral processing. Econ. Geol. 113, 193–208.

R. Galdos et al.

Sylvester, P., Cabri, L.J., Tubrett, M., McMahon, G., Laflamme, J., Peregoedova, A., 2005. Synthesis and evaluation of a fused pyrrhotite standard reference material for platinum group elements and gold analysis by laser ablation-ICP-MS: 10th International Platinum Symposium: Oulu. Geologocal Survey of Finland, Extended Abstracts, pp. 16–20.

Tanner, D., Henley, R.W., Mavrogenes, J.A., Holden, P., 2016. Sulfur isotope and trace element systematics of zoned pyrite crystals from the El Indio Au–Cu–Ag deposit, Chile. Contrib. Mineral Petrol. 171, 1–17.

Tietz, P., Defilippi, C., 2012. Technical Report on the Shahuindo Project, Cajabamba, Peru: NI 43–101. Technical Report Sulliden Gold Corporation LTD, p. 149.

Touray, J.-C., Guilhaumou, N., 1984. Characterization of H$_2$S-bearing fluid inclusions. Bull. Min´eral. 107, 181–188.

Ueno, Y., Yamada, K., Yoshida, N., Maruyama, S., Isozaki, Y., 2006. Evidence from fluid inclusions for microbial methanogenesis in the early Archaean era. Nat. Lett. 440, 516–519.

Vallance, J., Cathelineau, M., Boiron, M., Fourcade, S., Shepherd, T., Naden, J., 2003. Fluid-rock interactions and the role of late Hercynian aplite intrusion in the genesis of the Castromil gold deposit, northern Portugal. Chem. Geol. 194, 201–224.

Vallance, J., Galdos, R., Balboa, M., Berna, B., Cabrera, O., Huisa, F., Baya, C., Van De Vyver, C., Viveen, W., B´eziat, D., Salvi, S., Brusset, S., Baby, P., Pokrovski, G.S., 2024. Combined effect of organic carbon and arsenic on the formation of sediment-hosted gold deposits: a case study of the Shahuindo epithermal deposit, Peru. Econ. Geol. (in press).

Van Daele, J., Hulsbosch, N., Dewaele, S., Boiron, M.C., Piessens, K., Boyce, A., Muchez, P., 2018. Mixing of magmatic-hydrothermal and metamorphic fluids and the origin of peribatholitic Sn vein-type deposits in Rwanda. Ore Geol. Rev. 101, 481–501.

Vaughan, J., Nelson, C.E., Polanco, J., Garcia, V., Macassi, A., Garrido, G., 2020. The Pueblo Viejo Au-Ag-Cu-(Zn) deposit, Dominican Republic. Soc. Econ. Geol. Special Publ. 23, 415–430.

Vel´asquez, G., B´eziat, D., Salvi, S., Siebenaller, L., Borisova, A.Y., Pokrovski, G.S., de Parseval, P., 2014. Formation and deformation of pyrite and implications for gold mineralization at the El Callao mining district, Venezuela. Econ. Geol. 109, 457–486.

Vikentyev, I.V., Tyukova, E.E., Vikent'Eva, O.V., Chugaev, A.V., Dubinina, E.O., Prokofiev, V.Y., Murzin, V.V., 2019. Vorontsovka Carlin-style gold deposit in the North Urals: Mineralogy, fluid inclusion and isotope data for genetic model. Chem. Geol. 508, 144–166.

Vursiy, G.L., Zibrov, I.A., Lobov, S.G., Yakubchuk, A.S., 2020. The Sukhoi Log gold deposit, Russia. Soc. Econ. Geol. Spec. Publ. 23, 523–543.

Warr, L.N., 2021. IMA–CNMNC approved mineral symbols. Mineral. Mag. 85, 291–320.

White, N.C., Hedenquist, J.W., 1995. Epithermal gold deposits: styles, characteristics and exploration. Soc. Econ. Geol. Newsletter. 23, 1–13.

Williams-Jones, A.E., Samson, I.M., Ault, K.M., Gagnon, J.E., Fryer, B.J., 2010. The genesis of distal zinc skarns: evidence from the Mochito deposit. Honduras. Econ. Geol. 105, 1411–1440.

Wilson, S.A., Ridley, W.I., Koenig, A.E., 2002. Development of sulfide calibration standards for the laser ablation inductively-coupled plasma mass spectrometry technique. J. Anal. at. Spectrom. 17, 406–409.

Wojdyr, M., 2010. Fityk: a general-purpose peak fitting program. J. Appl. Cryst. 43, 1126–1128.

Wright, P., Melnyk, P., Gomerly, L., Lupo, J., 2009. Shahuindo Gold projet Cajabamba Province, Peru, NI 43–101. Technical report on preliminary assessment prepared for Sulliden Gold Corporation Ltd, p. 196.

Wu, Y.F., Li, J.W., Evans, K., Koenig, A.E., Li, Z.K., O'Brien, H., Lahaye, Y., Rempel, K., Hu, S.Y., Zhang, Z.P., Yu, J.P., 2018. Ore-forming processes of the Daqiao epizonal orogenic gold deposit, West Qinling orogen, China: constraints from textures, trace elements, and sulfur isotopes of pyrite and marcasite, and Raman spectroscopy of carbonaceous material. Econ. Geol. 113, 1093–1132.

Wu, Y.F., Evans, K., Li, J.W., Fougerouse, D., Large, R., Guagliardo, P., 2019. Metal remobilization and ore-fluid perturbation during episodic replacement of auriferous pyrite from an epizonal orogenic gold deposit. Geochim. Cosmochim. Acta 245, 98–117.

Wu, Y.F., Evans, K., Fisher, L.A., Zhou, M.F., Hu, S.Y., Fougerouse, D., Large, R., Li, J.W., 2020. Distribution of trace elements between carbonaceous matter and sulfides in a sediment-hosted orogenic gold system. Geochim. Cosmochim Acta 276, 345–362.

Zajacz, Z., Candela, P.A., Piccoli, P.M., 2017. The partitioning of Cu, Au and Mo between liquid and vapor at magmatic temperatures and its implications for the genesis of magmatic-hydrothermal ore deposits. Geochim. Cosmochim. Acta 207, 81–101.

Zhang, D.H., Aud´etat, A., 2023. A plea for more skepticism toward fluid inclusions: Part I. Post-entrapment changes in fluid density and fluid salinity are very common. Econ. Geol. 118, 15–41.

Zhang, Y.G., Frantz, J.D., 1987. Determination of homogenization temperatures and densities of supercritical fluids in the system NaCl–KCl–CaCl$_2$–H$_2$O using synthetic fluid inclusions. Chem. Geol. 64, 335–350.

Zhang, W., Williams-Jones, A.E., Leng, C.-B., Zhang, X.-C., Chen, W.T., Su, C.-J., Qin, W.-C., Yan, J.-H., 2019. The origin of CH$_4$-rich fluids in reduced porphyry–skarn Cu–Mo–Au systems. Ore Geol. Rev. 114, 103135.

Zhao, Z.-H., Ni, P., Sheng, Z.-L., Dai, B.-Z., Wang, G.-G., Ding, J.-Y., Wang, B.-H., Zhang, H.-D., Pan, J.-Y., Li, S.-N., 2020. Thermal regime reconstruction and fluid inclusion LA–ICP–MS analysis on intermediate-sulfidation epithermal Pb–Zn veins: Implications for porphyry Cu deposits exploration in the Xianhualing District, Anhui, China. Ore Geol. Rev. 124, 103658.

Zhu, M.T., Wu, G., Xie, H.J., Liu, J., Mi, M., 2012. Geochronology and fluid inclusion studies of the Lailisigaoer and Lamasu porphyry–skarn Cu–Mo deposits in northwestern Tianshan, China. J. Asian Earth Sci. 49, 116–130.

Zotov, A.V., Shikina, N.D., Akinfiev, N.N., 2003. Thermodynamic properties of the Sb(III) hydroxide complex Sb(OH)$_{3(aq)}$ at hydrothermal conditions. Geochim. Cosmochim. Acta 67, 1821–1836.

Zou, H., Li, M., Bagas, L., Li, Y., Fang, Y., Cao, H.W., Jiang, X.W., Chen, H.F., 2020. Fluid composition and evolution of the Langxi Ba-F deposit, Yangtze Block, China: New Insight from LA-ICPMS study of individual fluid inclusion. Ore Geol. Rev. 125, 103702.

Chapter IV. CONCLUSIONS AND PERSPECTIVES

IV.1. Conclusions

The major motivation of this study was to better understand the formation and evolution of sediment-hosted gold deposits that contain the major part of minable gold on Earth. Indeed, despite the significant economic relevance of such deposits, there are still many fundamental unanswered questions about their genesis and evolution. The lack of understanding of these fundamental questions is not the result of a shortage of intense research focused on investigating this issue but, rather, of the complexity of the formation history and mechanisms for these deposits. In this work we focused on the Shahuindo and Algamarca epithermal sediment-hosted gold deposits that possess an almost complete "collection" of typical features of other similar deposits worldwide, thereby providing us with the opportunity to explore the interconnections of those features on a single natural case.

i) Both the Shahuindo and Algamarca deposits exhibit a clear spatial association between gold mineralization, carbonaceous material, and arsenian pyrite, making them truly representative of sediment-hosted gold deposits. ii) They are located in a fold and thrust belt favourable to transportation and trapping of fluids. iii) Samples of hypogene mineralization from drill cores and underground mining works are readily available. iv) The sequence of mineralization events in both deposits is relatively simple compared to other sediment-hosted gold deposits, including orogenic and Carlin types, making it easier to identify the major links. v) A greatest "advantage" of our natural case, which is rather rare in sediment-hosted gold deposits, is the availability of fluid inclusions hosted in quartz from the Algamarca veins with adequate size for a range of analyses (microthermometry, Raman spectroscopy, and LA-ICPMS), allowing us to directly explore the properties and evolution of the mineralizing fluids.

In this context, the major fundamental questions that have been the focus of our research during this project are the following: i) What is the source of gold and hydrothermal fluids? ii) What is the role of carbonaceous material in the genesis of the Shahuindo and Algamarca epithermal sediment-hosted gold deposits? iii) What is the role of arsenic in gold concentration processes? iv) How did the structural architecture of the Marañon fold and thrust belt control mineralization? Thanks to a combination of different approaches, from regional-scale basin analysis to microscale mineral and fluid inclusions characterization, coupled with modeling of fluid-rock interactions, we propose some answers to those questions.

Firstly, in order to determine the source of metals, we were needing a "geochemical view" on the amount and concentration of gold in host sedimentary rocks to figure out if there would be potentially enough metals for the deposits. Our mass-balance analysis based on detailed geochemical analyses of the sedimentary rocks surrounding the Shahuindo and Algamarca deposits and the size of the hydrothermal system indicates that the rocks did not have enough gold, arsenic, and sulfur to form those deposits. Meteoric or barren hypothetically magmatic fluids scavenging metals from sediments are insufficient to supply the required metals. This estimation indicates the need for a source of metals other than basin sediments, such as a magmatic source enriched in the metals. This conclusion is supported by our LA-ICPMS analyses in the gold-rich ore pyrite from the Shahuindo and Algamarca deposits, the ore pyrite in both deposits is enrichment in As, Se, Ge, Mo, In, Ga, and Bi. These elements are commonly present in pyrite formed in epithermal deposits hosted in volcanic rocks and genetically related to the magmatic activity. Our findings suggest a magmatic origin of the metal-rich gold-bearing fluids. In line with a magmatic origin, microthermometry and LA-ICPMS analyses of fluid inclusions in quartz from the Algamarca veins reveal the following features informing us both about the fluid origin and evolution: i) the wide range of salinity (5–35 wt % NaCl eq.) providing evidence for vapor-liquid immiscibility evidenced by the coexistence of synchronously entrapped vapor-rich and multiphase-solid fluid inclusion types, ii) the concentrations of metals show a magmatic signature (i.e. high K, Rb, Cu, As, Sb, low Sr), and iii) the element ratios are characteristic of magmatic fluids (i.e. Zn/Pb ~4, 0.1<K/Na<5; Br/Cl~0.001, mole scale). These characteristics resemble the typical features of porphyry-epithermal Cu-Au systems and, therefore, are coherent with a fluid magmatic origin and its evolution upon ascent, fluid-phase separation, and cooling.

Secondly, the state of gold itself in the deposit was an open question. Our detailed mineralogical and geochemical examination of the hypogene ore in the Shahuindo and Algamarca deposits revealed that the majority of the gold is concentrated as invisible gold in arsenian pyrite and arsenopyrite, similarly to many other sediment-hosted gold deposits of Carlin, orogenic and epithermal types. In general, the gold content in pyrite positively correlates with arsenic. LA-ICPMS signals of Au and As show flat patterns that suggest the absence of nanoparticles of Au-As-bearing minerals. These features indicate that both elements in pyrite are incorporated in the structure of pyrite, probably via a coupled substitution mechanism as proposed by Pokrovski et al. (2021).

Thirdly, the Shahuindo and Algamarca deposits are hosted in a fold and thrust belt (MFTB), and by an over-mature petroleum system with high amounts of organic carbon in some stratigraphic levels. To understand the thrust-belt structure, a balanced

regional cross-section was constructed and modelled using the MOVE software (Petroleum Experts, 2022). It shows that the Shahuindo and Algamarca deposits are located in a system of four thrust-related anticlines. The deposits have been trapped in three reservoir sandstones of these anticlines, and along thrust faults and transverse strike-slip faults. The source rocks of the petroleum system correspond to two regional levels of black shale through which hydrothermal fluids have passed. The most important is the Chicama 1000-meter thick black shale level, which controlled the Algamarca-Shahuindo thrust system propagation and the pathways for fluid migration.

Hydrothermal fluids must have therefore interacted with the organic carbon of the black shales. However, to understand the detailed physical chemistry of fluid-rock interactions, we had to go to a smaller mineralogical scale. This interaction is evidenced by high volatile contents, including CO_2, CH_4 and H_2S, that we found in one of the major types of inclusions in Algamarca (immiscible-liquid fluid inclusions). Another independent evidence was provided by the coherence of the temperature values we have determined using Raman spectroscopy for the graphite metamorphism peak of carbonaceous material and, independently, by fluid-inclusion microthermometry in quartz veins at the Algamarca deposit.

However, our detailed natural sample characterization does not provide insight into the hydrothermal fluid behavior and the effectiveness of concentration mechanisms that may have occurred at the Shahuindo and Algamarca deposits, such as the effect on gold solubility by simultaneous changes in fluid parameters, produced by fluid-organic matter interactions. Thus other, independent, approaches were necessary. One of them is thermodynamic modeling of fluid-rock interactions. The application of this method benefited from our actual good knowledge of gold and sulfur aqueous species nature and stability, allowing us to predict mineral solubilities and thus the potential capacity of the fluid to transport gold. Our thermodynamic predictions of gold solubility demonstrate that interactions between an oxidized (sulfate-dominated, likely acidic, and enriched in Au, As and probably Fe) magmatic fluid and the organic matter from the sediments enhances gold solubility. This is because the fluid-organic carbon reaction produces large changes in the key parameters of the fluid, i.e., an increase in both fluid pH and H_2S concentration, and a minor decrease in f_{O2}. The combined effect of these changes enhances Au solubility in the form of Au^I hydrosulfide complexes. Upon the fluid contact with organic carbon, the hydrothermal fluid therefore acquired properties favorable for gold transport across the organic-matter rich sediments rather than to deposit gold in contact with organic matter. On its route towards the surface, the fluid reached favorable structures (e.g., faults, breccias) and sedimentary reservoirs within the anticlines, which

could promote its accumulation. In these shallower and colder settings, pyrite could crystallize at optimal conditions to efficiently incorporate Au and As in its lattice. This is because both the near-neutral pH and reduced conditions of the modified fluid favor the incorporation of bound Au and As in pyrite (Pokrovski et al., 2021), conditions contrasting to those showed by the original acidic and oxidized magmatic fluid (Fig.1).
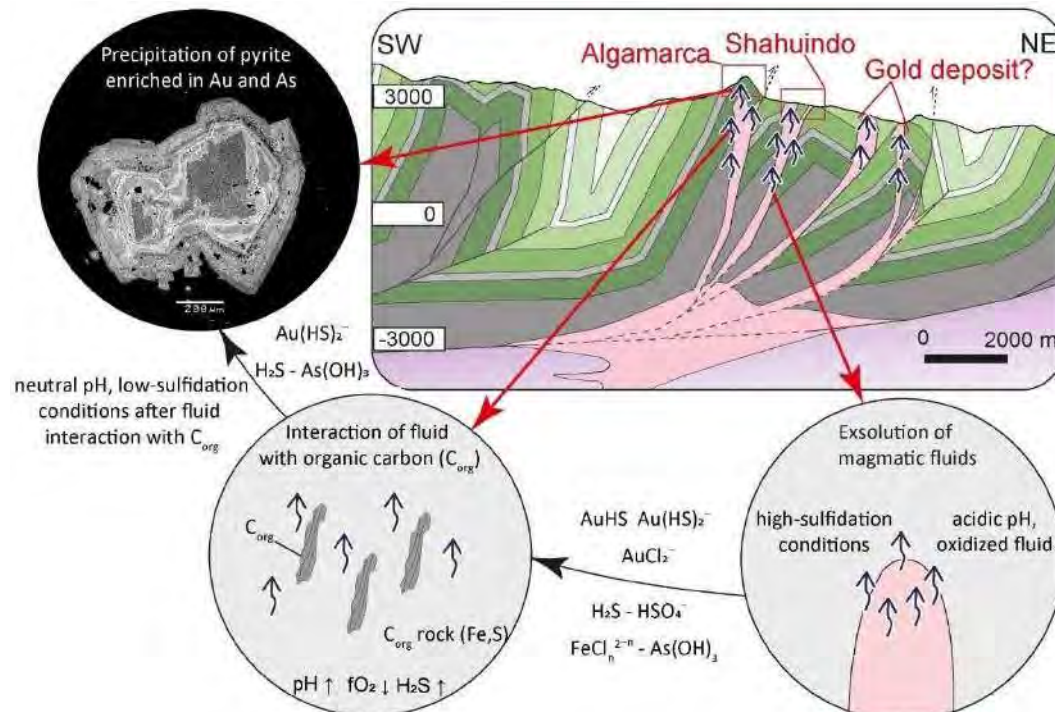
Fig. 1. A cartoon summarizing the novel genetic model proposed in this study for the formation of the Shahuindo and Algamarca sediment-hosted gold deposit.

IV.2. Implications for Exploration

Our work opens some new implications for exploration. An interesting point regarding the Shahuindo and Algamarca deposits is that they are hosted in sedimentary sandstones reservoirs of the San Jose and Algamarca anticlines. The fluid pathways for magmatic intrusions, hydrothermal fluids, and hydrocarbons generated in the basin are controlled by thrust structures of the Marañón fold and thrust belt. In this way, our structural section (Fig. 1) shows that there are potential exploration targets to the east of the Shahuindo deposit. Therefore, the concepts and tools utilized in the petroleum industry for oil exploration such as the balanced section method and petroleum system concept (e.g., McQuillin et al., 1984; Baby et al., 2023), can serve to improve the

exploration of sediment-hosted gold deposits at the MFTB. These techniques should be combined with traditional tools such as geochemical sampling and electrical, gravimetric and magnetotelluric geophysical methods widely used in the exploration of mineral deposits. (e.g., Leary et al., 2016).

Additionally, in our research, we have found evidence of a potential concealed porphyry style mineralization beneath the sediments hosting the Shahuindo and Algamarca epithermal deposits (Galdos et al., 2023). Such presumable porphyry mineralization has to be genetically associated with the Shahuindo and Algamarca epithermal deposits, similar to other porphyry-epithermal systems reported at the MFTB and worldwide (e.g., Gustafson et al., 2005; Sillitoe et al., 2010; Catchpole et al., 2015; Santos et al., 2023). The possible porphyry style mineralization is indicated by the presence of multiphase-solid fluid inclusions with high metallic content, which have only been reported in magmatic-derived brines from porphyry systems (Kouzmanov and Pokrovski, 2012), and by the composition of the pyrite from stage A showing low contents of gold and arsenic, typical of high-temperature porphyry stages (e.g., Deditius et al., 2014; Franchini et al., 2015; Sykora et al., 2018). This potential target should be better refined using complementary methods such as the electrical, gravimetric, magnetotelluric and seismic reflection geophysical tools mentioned above.

IV.3. Perspectives

The results obtained in this PhD work emphasize the necessity for further research to answer many remaining questions about those specific deposits. Our results also open several more general perspectives to explore in future research.

Our study has clarified the paragenetic sequence for the Shahuindo and Algamarca deposits; however, their ages of formation lack precise constraints. Consequently, further geochronological studies are required. The mineralization of Shahuindo and Algamarca is hosted in part by igneous intrusions, providing the opportunity to collect zircon ($ZrSiO_4$), which is a ubiquitous accessory mineral in such magmatic rocks, for robust U-Pb analyses (Harley and Kelly, 2007). Additionally, hypogene alunite ($KAl_3(SO_4)_2(OH)_6$), a mineral that can accurately be dated by the $^{40}Ar/^{39}Ar$ method (e.g., Bendezú et al., 2008; Baumgartner et al., 2009), was identified in the last paragenetic event of each deposit. The obtention of the radiometric age of the igneous intrusions and the alteration minerals would thus bracket the age of magmatic-

hydrothermal activity in both deposits. Furthermore, these data could provide additional independent confirmation that the two deposits are part of the same magmatic-hydrothermal system and directly related to magmatic activity in the Marañon fold and thrust belt.

The immiscible-liquid type of fluid inclusions in quartz of the Algamarca veins arise from the interaction between magmatic fluids and the carbonaceous material in the basin. The composition of these fluid inclusions, obtained by LA-ICPMS analyses, could better clarify the result of these interactions. For instance, a high gold content in the immiscible-liquid fluid inclusions would serve as independent confirmation that interactions between the magmatic fluid and the organic matter enhance the gold solubility in the fluid. Previous to the LA-ICPMS analyses, it is necessary to estimate the salinity of the fluid inclusions using Raman spectroscopy analysis (Mernagh and Wilde, 1989; Burke, 2001; Dubessy et al., 2002) due to the high H_2S and CH_4 contents in this type of fluid inclusions that prevent salinity determination using traditional microthermometry analyses. Salinity values are indispensable in estimating the Na concentration in the fluid inclusions that is used as an internal standard for the LA-ICPMS analyses (Heinrich et al., 2003).

Minerals other than quartz may also hold precious fluid inclusions. Their study may help to clarify the actual fundamental question whether gangue and ore mineral are really co-genetic (e.g., Wilkinson et al., 2009). Indeed, sphalerite from stage III of the Algamarca deposit does contain fluid inclusions that could be analyzed by microthermometry and infrared spectroscopy coupled with LA-ICPMS (e.g., Kouzmanov et al., 2010; Rottier et al., 2018). The results could provide valuable information on the nature of the mineralizing fluids that deposited this mineral and others coexisting sulfides. This method could further be complemented with Raman spectroscopy analyses of carbonaceous material (as it was done at Algamarca deposit in our work) to better constrain the temperature of ore deposition and the organic matter graphitization stages (e.g., Hu et al., 2015).

Recent studies have reported the use of in-situ sulfur isotope analysis on individual pyrite crystals to determine sulfur provenance and trace the mechanism of gold concentration and deposition (e.g., Barker et al., 2009; Holley et al., 2022). The use of this technique in pyrite from Shahuindo and Algamarca deposits could provide more insights into the origin of this key element, i.e. sulfur is essentially derived from the magmatic fluids or from dissolution of carbonaceous material (petroleum) that usually contains several wt% sulfur. In-situ micro-analyses, such as SIMS, are needed due to the fine zoning of pyrite grains in both deposits, for which conventional bulk analyses are

unable to properly characterize pyrite in such cases. Additionally, detailed analyses of other stable light isotopes (e.g., H, O, C) performed on gangue minerals (e.g., quartz, alunite, calcite) can provide additional confirmations of the magmatic origin of the fluids, and better assess the contribution of meteoric or basinal fluids (e.g., Hedenquist and Lowenstern, 1994; Emsbo et al., 2003; John et al., 2003; Zhai et al., 2009; Corral et al., 2017).

In conclusion, this thesis work has shown that the genetic models for sediment-hosted gold deposits are not fully resolved. Integrated approaches including geological, geochemical and thermodynamic modeling studies, along with fine microanalyses of trace elements and fluid inclusions, are needed to provide a better overall understanding of the genesis and evolution of these deposits (e.g., Fig. 2). This combination will enable the improvement of exploration strategies for sediment-hosted gold deposits in Northern Peru and worldwide.
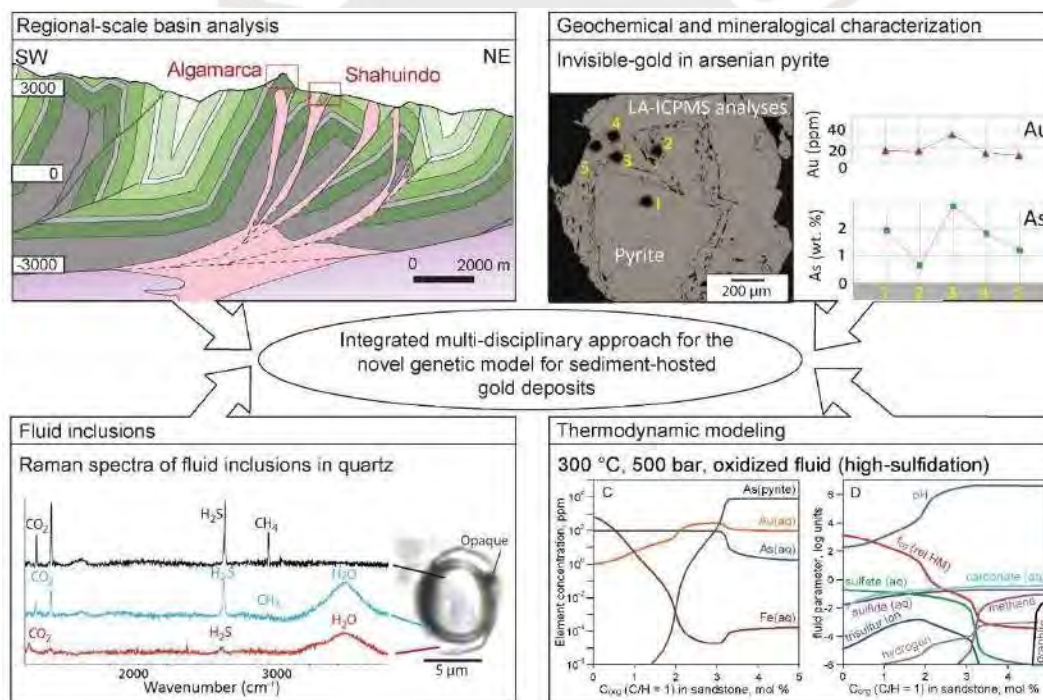
Fig. 2. Different approaches combined in this this thesis work to study the Shahuindo and Algamarca deposits.

IV.3. Conclusions in French

La principale motivation de cette étude était de mieux comprendre la formation et l'évolution des gisements d'or hébergés dans des sédiments. Dans ce travail, nous nous sommes concentrés sur les gisements d'or épithermaux de Shahuindo et d'Algamarca qui possèdent une "collection" presque complète de caractéristiques typiques d'autres gisements similaires dans le monde, ce qui nous a permis d'explorer les interconnexions de ces caractéristiques sur un seul cas naturel.

Tout d'abord, afin de déterminer la source des métaux, nous avions besoin d'une "vision géochimique" de la quantité et de la concentration d'or dans les roches sédimentaires hôtes pour déterminer si ces dernières contenaient potentiellement assez de métaux pour former les gisements. Notre analyse de bilan de masse, basée sur des analyses géochimiques détaillées des roches sédimentaires entourant les gisements de Shahuindo et d'Algamarca, et sur la taille du système hydrothermal, indique que les roches ne contenaient pas suffisamment d'or, d'arsenic et de soufre pour former ces gisements. Des fluides météoriques ou hypothétiquement magmatiques stériles, lixiviant les métaux des sédiments, n'ont donc pas pu fournir les métaux nécessaires. Cette estimation indique la nécessité d'une source de métaux autre que les sédiments du bassin, telle qu'une source magmatique enrichie en métaux. Cette conclusion est étayée par nos analyses LA-ICPMS de la pyrite riche en or des gisements de Shahuindo et d'Algamarca, la pyrite des deux gisements étant en outre enrichie en As, Se, Ge, Mo, In, Ga et Bi. Ces éléments sont généralement présents dans la pyrite formée dans les gisements épithermaux situés dans des roches volcaniques et sont génétiquement liés à l'activité magmatique. Nos résultats suggèrent ainsi une origine magmatique des fluides aurifères riches en métaux. En accord avec une origine magmatique, les analyses microthermométriques et LA-ICPMS des inclusions fluides dans le quartz des veines d'Algamarca révèlent les caractéristiques suivantes, qui nous informent à la fois sur l'origine et l'évolution des fluides : i) la large gamme de salinité (5-35 % en poids de NaCl eq.), ce qui prouve l'immiscibilité vapeur-liquide attestée par la coexistence de d'inclusions fluides riches en vapeur et d'inclusions fluides multiphasiques piégées de manière synchrone, ii) les concentrations de métaux qui montrent une signature magmatique (c'est-à-dire une teneur élevée en K, Rb, Cu, As, Sb, une faible teneur en Sr) et iii) les rapports entre les éléments, caractéristiques des fluides magmatiques (c'est-à-dire Zn/Pb ˜4, 0,1<K/Na<5 ; Br/Cl˜0,001, à l'échelle de la mole). Ces caractéristiques correspondent aux attributs typiques des systèmes porphyriques-épithermaux à cuivre-or et, par conséquent, sont cohérentes avec une origine

magmatique du fluide et de son évolution lors de l'ascension, de la séparation de phase (démixtion liquide-vapeur) et du refroidissement.

Deuxièmement, la question de l'état de l'or lui-même dans le gisement restait ouverte. Nos analyses minéralogiques et géochimiques détaillées du minerai hypogène des gisements de Shahuindo et d'Algamarca ont révélé que la majorité de l'or était concentrée sous forme d'or invisible dans la pyrite arséniée et l'arsénopyrite, à l'instar de nombreux autres gisements d'or sédimentaires de type Carlin, orogénique et épithermal. En général, la teneur en or de la pyrite montre une corrélation positive avec l'arsenic. Les signaux LA-ICPMS de l'Au et de l'As présentent des profils plats qui suggèrent l'absence de nanoparticules de minéraux propres d'or ou d'arsenic. Ces caractéristiques indiquent que les deux éléments présents dans la pyrite sont incorporés dans la structure du minéral, probablement par le biais d'un mécanisme de substitution couplée tel que proposé par Pokrovski et al. (2021).

Troisièmement, les gisements de Shahuindo et d'Algamarca sont situés dans une ceinture de plis et de chevauchement (MFTB) et dans un système pétrolier surmature présentant de grandes quantités de carbone organique dans certains niveaux stratigraphiques. Pour comprendre la structure de la ceinture de plis et chevauchements, une coupe régionale équilibrée a été construite et modélisée à l'aide du logiciel MOVE (Petroleum Experts, 2022). Elle montre que les gisements de Shahuindo et d'Algamarca sont situés dans un système de quatre anticlinaux associés à des chevauchements. Les métaux ont été piégées dans trois réservoirs grèseux de ces anticlinaux et le long de failles de chevauchement et de failles décrochantes transversales. Les roches mères du système pétrolier correspondent à deux niveaux régionaux de lutites noires traversés par des fluides hydrothermaux. Le plus important est le niveau de lutites noires de Chicama, d'une épaisseur de 1000 mètres, qui forme un excellent niveau de décollement où se connecte le système de chevauchement Algamarca-Shahuindo controlant les voies de migration des fluides.

Les fluides hydrothermaux ont donc dû interagir avec le carbone organique des lutites noires. Cependant, pour comprendre la physico-chimie détaillée des interactions fluide-roche, nous avons dû passer à l'échelle minéralogique. Ces interactions sont attestées par des teneurs élevées en composés volatils, notamment en CO_2, CH_4 et H_2S, que nous avons trouvés dans l'un des principaux types d'inclusions d'Algamarca (inclusions fluides type « liquides immiscibles- »). Une autre preuve indépendante a été fournie par la cohérence des valeurs de température que nous avons déterminées à l'aide de la spectroscopie Raman pour le pic de métamorphisme du graphite du matériau

carboné et, indépendamment, par la microthermométrie des inclusions fluides dans les veines de quartz du gisement d'Algamarca.

Cependant, notre caractérisation détaillée des échantillons naturels n´a pas permis de comprendre le comportement des fluides hydrothermaux et l'efficacité des mécanismes de concentration qui ont pu se produire dans les gisements de Shahuindo et d'Algamarca, tels que l'effet sur la solubilité de l'or des changements simultanés des paramètres des fluides, produits par les réactions entre les fluides et la matière organique. D'autres approches complémentaires ont donc été nécessaires. L'une d'entre elles est la modélisation thermodynamique des interactions fluide-roche. L'application de cette méthode a bénéficié de notre bonne connaissance actuelle de la nature et de la stabilité des espèces aqueuses d'or et de soufre. Cette connaissance nous a permis de prédire les solubilités minérales et donc la capacité potentielle du fluide à transporter l'or. Nos prédictions thermodynamiques de la solubilité de l'or démontrent que les interactions entre un fluide magmatique oxydé (dominé par les sulfates, probablement acide, et enrichi en Au, As et probablement Fe) et la matière organique des sédiments augmentent la solubilité de l'or. Ceci est dû au fait que la réaction fluide-carbone organique produit des changements importants dans les paramètres clés du fluide, c'est- à-dire une augmentation du pH du fluide et de la concentration en H_2S, ainsi qu'une diminution mineure de fO_2. L'effet combiné de ces changements augmente la solubilité de l'Au sous la forme de complexes Au^I hydrosulfure. Au contact du carbone organique, le fluide hydrothermal a donc acquis des propriétés favorables au transport de l'or à travers les sédiments riches en matière organique plutôt qu'au dépôt de l'or au contact de la matière organique. Sur son trajet vers la surface, le fluide a été piégé et s'est accumulé dans des brèches associées aux failles et dans les réservoirs gréseux présents dans les anticlinaux. Dans ces environnements moins profonds et de plus basse température, la pyrite a pu cristalliser dans des conditions optimales pour incorporer efficacement l'Au et l'As dans son réseau. En effet, le pH du fluide proche de la neutralité, couplé aux conditions réduites du fluide après sa réaction avec le carbone organique ont favorisé l'incorporation de l'Au et de l'As dans la pyrite (Pokrovski et al., 2021), conditions qui contrastent avec celles du fluide magmatique d'origine, acide et plus oxydé (Fig.1).

References

Baby P., Van De Vyver C., Galdos R., Quinteros A., Medina, J., Salvi, S., Brusset S., J. Ramirez J., Torró L., Vallance, J., Pokrovski G.S., 2023. Petroleum system concepts for assessing mineral resources in Andean fold and thrust belts of Peru. ProEXPLO 2023, Lima, Peru. Extended Abstracts 46-50.

Barker, S.L., Hickey, K.A., Cline, J.S., Dipple, G.M., Kilburn, M.R., Vaughan, J.R., Longo, A.A., 2009. Uncloaking invisible gold: Use of nanoSIMS to evaluate gold, trace elements, and sulfur isotopes in pyrite from Carlin-type gold deposits. Econ. Geol.104, 897-904.

Baumgartner, R., Fontboté, L., Spikings, R., Ovtcharova, M., Schaltegger, U., Schneider, J., Page, L., Gutjahr, M., 2009. Bracketing the age of magmatic- hydrothermal activity at the Cerro de Pasco epithermal polymetallic deposit, Central Peru: a U-Pb and $^{40}Ar/^{39}Ar$ study. Econ. Geol. 104, 479-504.

Bendezú, R., Page, L., Spikings, R.A., Pecskay, Z., Fontboté, L., 2008. New 40Ar/39Ar alunite ages from the Colquijirca district, Peru: evidence of a long period of magmatic SO2 degassing during formation of epithermal Au-Ag and Cordilleran polymetallic ores. Miner. Deposita 43, 777-789.

Burke, E.A.J., 2001. Raman microspectrometry of fluid inclusions. Lithos 55, 139-158.

Catchpole, H., Kouzmanov, K., Putlitz, B., Seo, J.H., Fontboté, L., 2015. Zoned base metal mineralization in a porphyry system: origin and evolution of mineralizing fluids in the Morococha District, Peru. Econ. Geol. 110, 39-71.

Corral, I., Cardellach, E., Corbella, M., Canals, A., Griera, A., Gomez-Gras, D., Johnson, C. A., 2017. Origin and evolution of mineralizing fluids and exploration of the Cerro Quema Au-Cu deposit (Azuero Peninsula, Panama) from a fluid inclusion and stable isotope perspective. Ore Geol. Rev. 80, 947-960.

Deditius, A.P., Reich, M., Kesler, S.E., Utsunomiya, S., Chryssoulis, S.L., Walshe, J., Ewing, R.C., 2014. The coupled geochemistry of Au and As in pyrite from hydrothermal ore deposits. Geochim. Cosmochim. Acta 140, 644-670.

Dubessy, J., Lhomme, T., Boiron, M., Rull, F., 2002. Determination of chlorinity in aqueous fluids using Raman spectroscopy of the stretching band of water at room temperature: application to fluid inclusions. Appl. Spectrosc. 56, 99-106.

Emsbo, P., Hofstra, A.H., Lauha, E.A., Griffin, G.L., Hutchinson, R.W., John, D.A., Theodore, T.G., 2003. Origin of high- grade gold ore, source of ore fluid components, and genesis of the Meikle and neighboring Carlin-type deposits, northern Carlin Trend, Nevada. Econ. Geol. 98, 1069-1105.

Franchini, M., McFarlane, C., Maydagán, L., Reich, M., Lentz, D.R., Meinert, L., Bouhier V., 2015. Trace metals in pyrite and marcasite from the Agua Rica porphyry-high sulfidation epithermal deposit, Catamarca, Argentina: textural features and metal zoning at the porphyry to epithermal transition. Ore Geol. Rev. 66, 366-387.

Galdos, R., Vallance, J., Baby, P., Salvi, S., Schirra, M., Velazquez, G., Pokrovski, G.S., 2023. Origin and evolution of gold-bearing fluids in a carbon-rich sedimentary basin: a case study of the Algamarca epithermal gold-silver-copper deposit, Northern Peru. Ore Geol. Rev. https://doi.org/10.1016/j.oregeorev.2023.105857.

Gustafson, L.B., Vidal, C.E., Pinto, R., Noble, D.C., 2005. Porphyry-epithermal transition, Cajamarca region, Northern Peru. Soc. Econ. Geol. Spec. Publ. 11, 279-299.

Harley, S.L., Kelly, N.M., 2007. Zircon tiny but timely. Elements 3, 13-18.

Hedenquist, J.W., Lowenstern, J.B., 1994. The role of magmas in the formation of hydrothermal

ore deposits. Nature 370, 519-527.

Heinrich, C.A., Pettke, T., Halter, W. E., Aigner-Torres, M., Audetat, A., Gunther, D., Hattendorf, B., Bleiner, D., Guillong, M., Horn, I., 2003. Quantitative multi-element analysis of minerals, fluid and melt inclusions by LA-ICP-mass spectrometry. Geochim. Cosmochim. Acta 67, 3473-3497.

Holley, E.A., Fulton, A., Jilly-Rehak, C., Johnson, C., Pribil, M., 2022. Nanoscale isotopic evidence resolves origins of giant Carlin-type ore deposits. Geology 50, 660-664.

Hu, S., Evans, K., Craw, D., Rempel, K., Bourdet, J., Dick, J., Grice, K., 2015. Raman characterization of carbonaceous material in the Macraes orogenic gold deposit and metasedimentary host rocks, New Zealand. Ore Geol. Rev. 70, 80-95.

John, D.A., Hofstra, A.H., Fleck, R.J., Brummer, J.E., Saderholm, E.C., 2003. Geologic setting and genesis of the Mule Canyon low-sulfidation epithermal gold-silver deposit, north-central Nevada. Econ. Geol. 98, 425-463.

Kouzmanov, K., Pettke, T., Heinrich, C.A., 2010. Direct analysis of ore-precipitating fluids: combined IR microscopy and LA-ICP-MS study of fluid inclusions in opaque ore minerals. Econ. Geol. 105, 351-373.

Kouzmanov, K., Pokrovski, G.S., 2012. Hydrothermal controls on metal distribution in Cu(-Au-Mo) porphyry systems. Soc. Econ. Geol. Spec. Publ. 16, 573-618.

Leary, S., Sillitoe, R.H., Stewart, P.W., Roa, K.J., Nicolson, B.E., 2016. Discovery, geology, and origin of the fruta del Norte epithermal gold-silver deposit, southeastern Ecuador. Econ. Geol. 111, 1043-1072.

McQuillin, R.M., Bacon, M., Barclay, W., 1984. An Introduction to Seismic Interpretation, 2nd Edition, Graham and Trotman, London. 624 pp.

Mernagh, T.P., Wilde, A.R., 1989. The use of the laser Raman microprobe for the determination of salinity in fluid inclusions. Geochim. Cosmochim. Acta 53, 765-771.

Petroleum Experts, 2022. Petroleum engineering and structural geology software (https://www.petex.com/products/move-suite/).

Pokrovski, G. S., Escoda, C., Blanchard, M., Testemale, D., Hazemann, J.L., Gouy, S., Kokh, M. A., Boiron, M. C., Parseval F., Aigouy, T., Menjot, L., de Parseval, P., Proux, O., Rovezzi, M., Béziat, D., Salvi, S., Kouzmanov, K., Bartsch, T., Pöttgen, R., Doert, T., 2021. An arsenic-driven pump for invisible gold in hydrothermal systems. Geochem. Persp. Lett. 17, 39-44.

Rottier, B., Kouzmanov, K., Casanova, V., Wälle, M., Fontboté, L., 2018. Cyclic dilution of magmatic metal-rich hypersaline fluids by magmatic low-salinity fluid: A major process generating the giant epithermal polymetallic deposit of Cerro de Pasco, Peru. Econ. Geol. 113, 825-856.

Santos, A., Guo, W., Chen, N., Cerpa, L., Kojima, S., 2023. Geochronologically constrained life cycles of telescoped porphyry-epithermal systems at the La Arena district, Northern Peru. Ore Geol. Rev. 155, 105375.

Sillitoe, R.H., 2010. Porphyry copper systems. Econ. Geol. 105, 3-41.

Sykora, S., Cooke, D., Meffre S., Stephanov, A., Gardner, K., Scott, R., Selley, D., Harris, A., 2018. Evolution of pyrite trace element compositions from porphyry-style and epithermal conditions at the Lihir gold deposit: Implications for ore genesis and mineral processing. Econ. Geol. 113, 193-208.

Wilkinson, J.J., Stoffell, B., Wilkinson, C.C., Jeffries, T.E., Appold, M.S., 2009. Anomalously metal-rich fluids form hydrothermal ore deposits. Science 323, 764-767.

Zhai, W., Sun, X., Sun, W., Su, L., He, X., Wu, Y., 2009. Geology, geochemistry, and genesis of Axi: A Paleozoic low-sulfidation type epithermal gold deposit in Xinjiang, China. Ore Geol. Rev. 36, 265-281.

Annexes

Annex I.

List of Figures

inclusion water in quartz; Zhai et al., 2009), and Comstock Lode ($\delta^{18}O$ values calculated based on data from quartz, and δD measured in fluid inclusion in quartz;

Hedenquist and Lowenstern, 1994). Fields for magmatic and metamorphic fluids, seawater, and connate brines are from Huston et al. (2023). Field for water that precipitate barren quartz in low sulfidation deposits (area delimited by dotted lines; Hedenquist and Lowenstern, 1994). The arrows are pointing to the corresponding indicated isotope reservoir. Abbreviations: SMOW (Standard mean oceanic water), J (Julcani deposit, Peru), LN (Lagunas Norte deposit, Peru), CQ (Cerro Quema deposit, Panama), MC (Mule Canyon deposit, United States), A (Axi deposit, China), CL (Comstock Lode, United States).

Figures from the article published in Economic Geology, Chapter II

(C) by pyrite II (pyII), locally infilling plant cells (center of the picture). Reflected light.

Fig. 8.   Scanning electron microscope (SEM) photomicrographs (in backscattered electron   60
              mode) of ore samples from the Shahuindo deposit. A. Replacement zone of pyrite II
              (pyII) by pyrite III (pyIII) and tetrahedrite-tennantite (tt). C = graphite, po =
              pyrrhotite inclusion in pyrite II. B. Pyrite II (pyII) rimmed by oscillatory-zoned pyrite
              III (pyIII) and arsenopyrite (apyIII). C. Same view as in B, with different contrast
              enhancing the arsenopyrite zoning and the later tetrahedrite-tennantite (tt) and galena
              (gn). D. Details of the oscillatory zoning in pyrite III (pyIII); tetrahedrite-tennantite
              (tt) and chalcopyrite (cpy) inclusions are preferentially located at the limit between
              bands; later enargite (eng) partially replacing tetrahedrite-tennantite. E. Arsenopyrite
              (apyIII) precipitated at the contact between coarse pyrite II (pyII) and finer pyrite III
              (pyIII) grains with local replacement of the latter; chalcopyrite (cpy) filling spaces
              between arsenopyrite euhedral terminations. F. Late subhedral oscillatory-zoned and
              inclusion-free pyrite IV (pyIV) occurring as overgrowth on oscillatory-zoned
              inclusion-bearing pyrite III (pyIII).

Fig. 9.   Electron probe microanalyses (in at %) of pyrite from the Shahuindo deposit. A. As   61
              versus S for the indicated pyrite generations. Dashed lines represent 1:1 correlation;
              r is the Pearson correlation coefficient. B. As versus S for the pyIII generation from
              different host-rock types or tectonic position.

Fig. 10.   Box plots showing the contents of 17 trace elements (in log10 units of ppm) analyzed   62
              by laser ablation-inductively coupled plasma-mass spectrometry in the four pyrite
              generations (pyI to pyIV) and in arsenopyrite (apyIII, belonging to pyIII generation).

Fig. 11.   Results of laser ablation-inductively coupled plasma-mass spectrometry (LA-ICP-   64
              MS) analyses of gold and arsenic concentrations in representative pyrite (py I to
              pyIV) and arsenopyrite samples from the Shahuindo deposit. A. Logarithmic plot of
              As versus Au for all pyrite generations. B. Logarithmic plot of As versus Au for pyIII
              from different host rocks. C. Scanning electron microscope photomicrograph of an
              Au-poor pyII grain with later Au- and As-bearing pyIII and coexisting arsenopyrite
              (apyIII); green circles show the position of LA-ICP-MS laser spots. D. As and Au
              concentrations obtained in the laser ablation spots indicated in C.

Fig. 12.   Diagrams showing the results of thermodynamic modeling of fluid-rock interactions   66
              in the context of the Shahuindo deposit. Two contrasting cases of the initial S-Au-
              As-Fe bearing epithermal fluid are monitored: (A,B) reduced (H_2S-dominated) and
              (C,D) oxidized (sulfate-dominated). The low-salinity acidic (7 wt % NaCl
              equivalent; 1 m NaCl+0.1 m KCl+0.05 HCl,pH = 2.5) magmatic-derived fluid
              containing 100 ppm As and saturated with pyrite and metallic gold was allowed to
              react at 300 °C and 500 bar with a hydrocarbon-bearing shale at a mass fluid:rock
              ratio of 1:1 as a function of organic carbon content in the rock (C_{org}, with C/H atomic
              ratio of 1). A and C. Concentrations of dissolved Au, Fe and As in the fluid (aq) and
              of As in pyrite as a function of CH content for a reduced (f_{O2} is close to the
              conventional pyrite-pyrrhotite-magnetite redox buffer, PPM≈HM–3) and an
              oxidized (f_{O2} is above that of the hematite-magnetite buffer, HM+3) initial fluid. B
              and D. Corresponding evolution of the fluid-phase concentrations (in log10 units of
              molality) of sulfide, sulfate, the S_3– ion, dissolved hydrogen, and carbon-bearing
              species, pH and oxygen fugacity (relative to the HM buffer). It can be seen that
              organic carbon may exert a contrasting effect on the transport of different metals,

depending on the initial fluid properties and the organic carbon content. In particular, organic matter may promote, rather than limit, gold fluid transport in C_{org}-bearing sedimentary/metamorphic rocks.

Figures from the article published in Ore Geology Reviews, Chapter III

rounded porous core with silicate inclusions rimmed by a massive euhedral rim. (i) Anhedral to subhedral synsedimentary to diagenetic disseminated pyrite (Py$_s$) forming a mosaic of spongy crystals. (j) Association of Bi-Te minerals and tetrahedrite surrounded by chalcopyrite. (k) Small inclusion of tellurides in tetrahedrite. (l) Hübnerite embedded in chalcopyrite.

Figures in the manuscript text of the Chapter IV

List of Tables

Annex II.

Electronic Supplementary Material of Chapter II

This file contains:

Figures A1 to A3

Tables A1 to A4

Fig. A1. A. Comparison of element concentrations (in ppm) from barren (MSHA-01, MSHA-22, MSHA-23) and mineralized gold-rich (MSHA-02, MSHA-03, MSHA-05, MSHA-11, MSHA-04, MSHA-08, MSHA-14) samples from the Shahuindo area with those reported for a selection of black shales from the Sukhoi Log, Carlin, and Bendigo Districts (Large et al., 2011), and for the barren black shales (Johnson et al., 2017). B. Logarithm of Fe/S molar ratio versus S concentration (in wt%). C. Logarithm of Fe/S molar ratio versus Au concentration (in ppm).
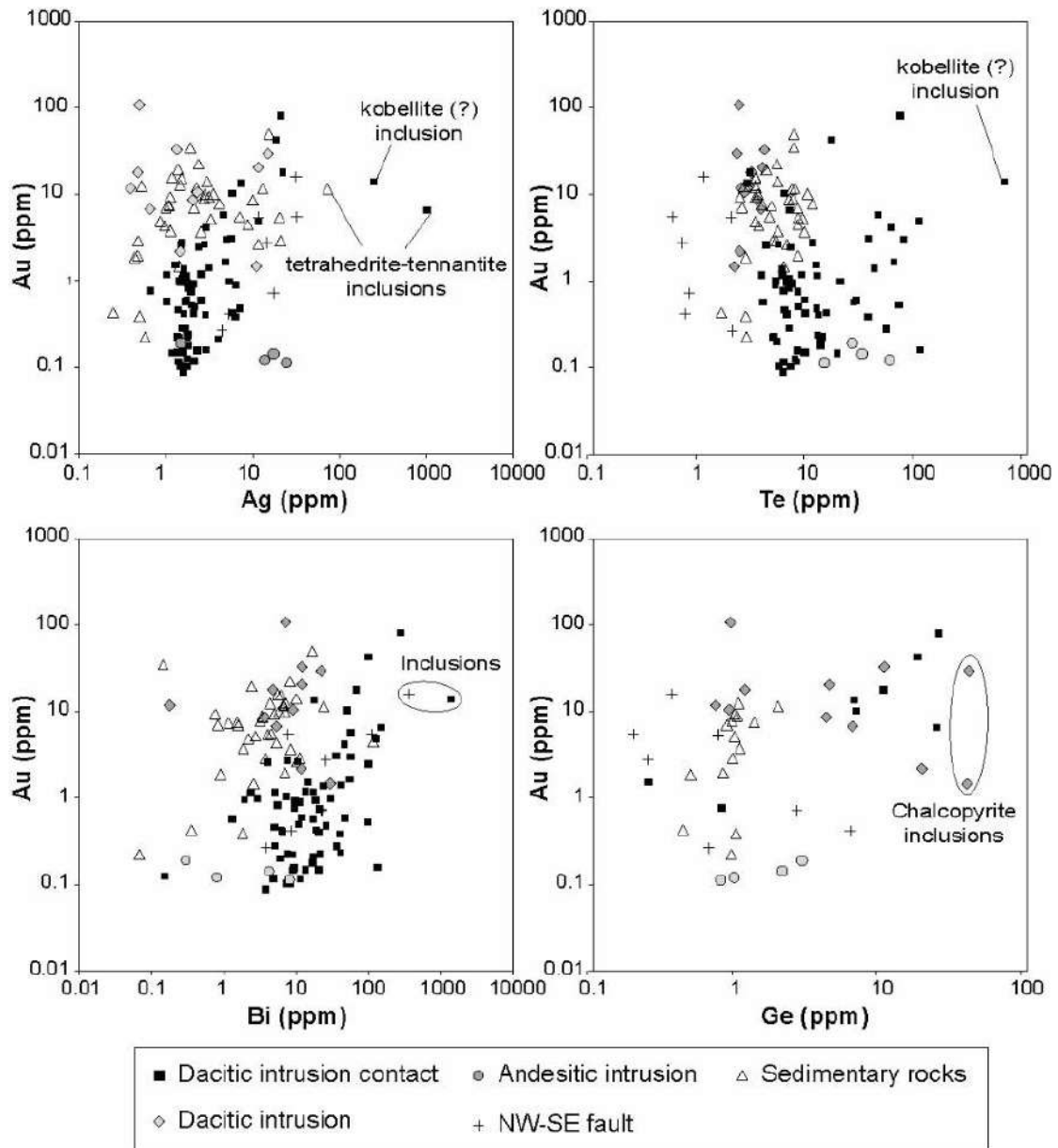
Fig. A2. Logarithmic plots of Au vs. Ag, Te, Bi, and Ge concentrations analyzed by LA-ICPMS in pyIII from the indicated settings within the Shahuindo deposit.
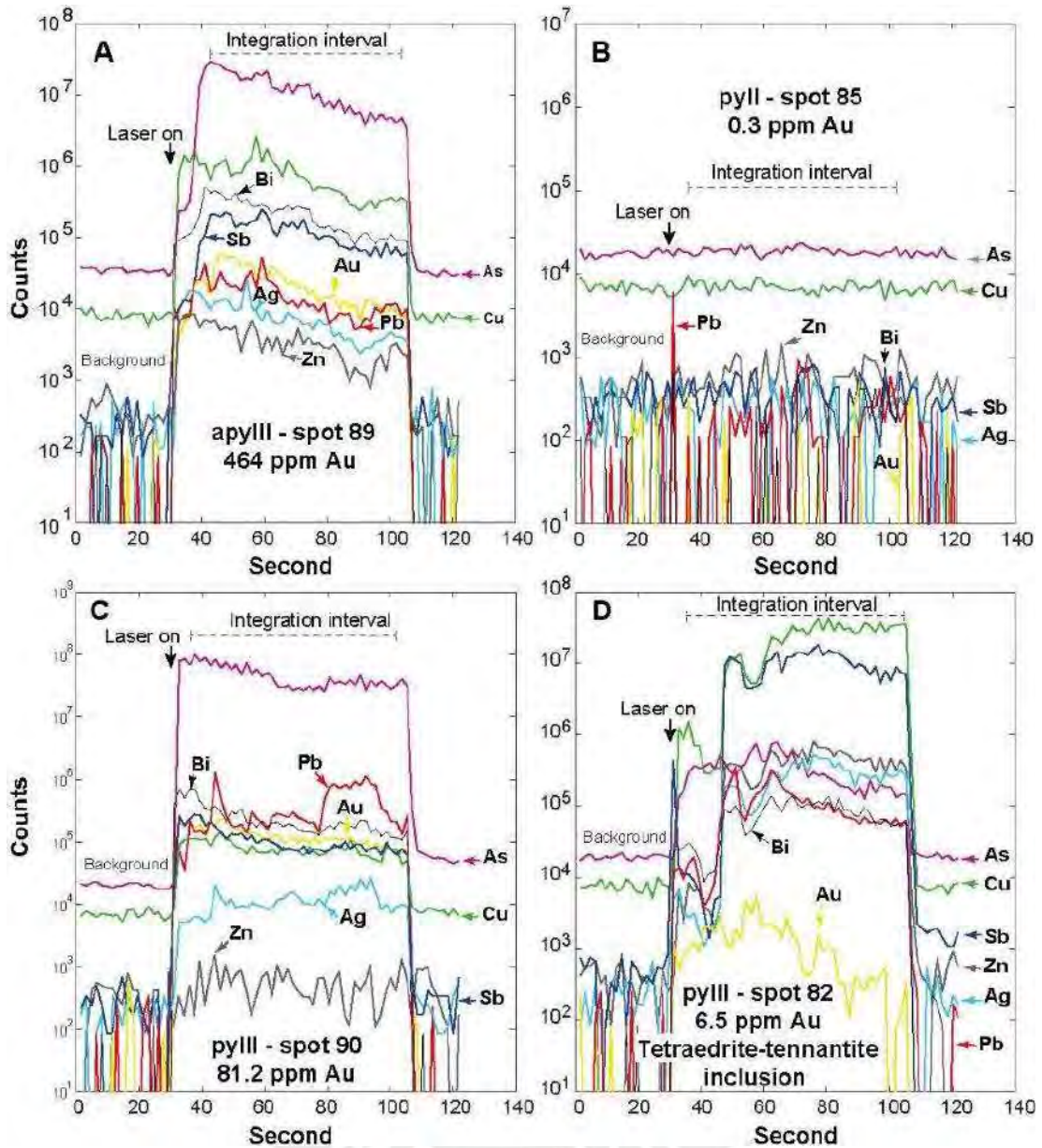
Fig. A3. Example of transient LA-ICP-MS signals and analyzed element concentration for pyII, pyIII and arsenopyrite from a single representative sample. A. Gold-rich arsenopyrite; B. Gold-poor pyrite II; C. Gold-rich pyrite III; D. Pyrite III showing a tetraedrite-tennantite inclusion.

Annex II

Table A1. Analyses of representative bulk-rock samples from the Shahuindo deposit including major and trace elements, total carbon and sulfur.

Element		Au	As	Ag	Cu	Zn	Sb	C	S	SiO₂
Unit		ppm	ppm	ppm	ppm	ppm	ppm	wt.%	wt.%	wt.%
Analytical procedure		Au-ICP22	ME-ICP41	ME-ICP41	ME-ICP41	ME-ICP41	ME-MS42	C-IR07	S-IR08	ME-ICP06
Reference material		LEA-16	MRGeo08	MRGeo08	MRGeo08	MRGeo08	MRGeo08	GGC-03	CCU-1d	AMIS0304
Detection limit		0.01	2	0.2	1	2	0.2	0.01	0.01	0.01
Sample	MSHA-01	0.002	12	<0.2	30	46	2.0	0.43	0.22	63.20
	MSHA-02	0.017	16	<0.2	130	31	0.7	0.94	0.44	59.60
	MSHA-03	0.017	21	0.2	124	26	1.0	0.93	0.53	59.50
	MSHA-04	0.180	743	0.7	31	2	1.6	0.13	7.15	44.00
	MSHA-05	0.032	41	0.6	37	250	8.8	0.65	0.75	68.20
	MSHA-08	0.950	1000	3.4	8250	394	11.1	0.03	19.30	58.90
	MSHA-11	0.030	237	3.9	64	257	18.6	1.43	5.09	44.60
	MSHA-14	0.250	2460	0.6	57	12	7.6	0.20	21.90	42.10
	MSHA-22	0.001	12	<0.2	21	85	0.1	1.91	0.44	66.80
	MSHA-23	<0.001	23	<0.2	26	102	0.1	2.27	0.37	60.80

Element		Pb	Ba	Ce	Cr	Cs	Dy	Er	Eu	Ga
Unit		ppm	ppm	ppm	ppm	ppm	ppm	ppm	ppm	ppm
Analytical procedure		ME-ICP41	ME-MS81	ME-MS81	ME-MS81	ME-MS81	ME-MS81	ME-MS81	ME-MS81	ME-MS81
Reference material		MRGeo08	GRE-3	GRE-3	GRE-3	GRE-3	GRE-3	GRE-3	GRE-3	GRE-3
Detection limit		2	0.5	0.1	10	0.01	0.05	0.03	0.03	0.1
Sample	MSHA-01	10	229	106	80	9.07	6.95	4.2	1.41	23.1
	MSHA-02	13	374	80.3	70	10.45	5.53	3.58	0.95	22.5
	MSHA-03	15	386	79	80	10.15	5.38	3.39	0.91	24.1
	MSHA-04	6	280	142	100	7.63	8.01	4.8	2.06	30.8
	MSHA-05	20	324	95.7	80	15.20	7.12	4.19	1.43	18.0
	MSHA-08	70	18.6	20.1	10	1.06	4.33	2.19	0.65	20.1
	MSHA-11	262	252	82.9	100	32.20	5.02	3.39	1.38	27.0
	MSHA-14	60	94.8	71.9	50	2.12	6.30	3.59	1.93	12.8
	MSHA-22	20	358	91.6	70	6.61	6.28	3.84	1.65	17.5
	MSHA-23	25	281	112	80	10.60	7.28	4.43	1.81	21.0

Element		Th	Tm	U	V	W	Y	Yb	Zr	Bi
Unit		ppm	ppm	ppm	ppm	ppm	ppm	ppm	ppm	ppm
Analytical procedure		ME-MS81	ME-MS81	ME-MS81	ME-MS81	ME-MS81	ME-MS81	ME-MS81	ME-MS81	ME-MS42
Reference material		GRE-3	GRE-3	GRE-3	GRE-3	GRE-3	GRE-3	GRE-3	GRE-3	MRGeo08
Detection limit		0.05	0.01	0.05	5	1	0.1	0.03	2	0.01
Sample	MSHA-01	14.60	0.62	3.51	123	1	38.6	4.26	252	0.39
	MSHA-02	15.85	0.52	2.40	113	1	27.0	3.28	211	0.67
	MSHA-03	14.35	0.54	2.52	115	<1	26.3	3.23	206	0.84
	MSHA-04	20.20	0.70	4.01	156	1	41.1	4.18	208	1.60
	MSHA-05	13.55	0.63	4.08	114	2	40.4	4.05	349	1.66
	MSHA-08	2.07	0.26	0.72	9	3	22.0	1.46	205	1.38
	MSHA-11	16.00	0.51	2.80	132	11	29.9	3.41	209	0.30
	MSHA-14	12.60	0.49	3.80	70	69	31.2	3.39	188	10.35
	MSHA-22	12.80	0.60	3.89	106	1	35.4	3.69	444	0.24
	MSHA-23	16.00	0.64	3.34	128	2	39.8	4.45	317	0.34

* calculated on the basis of the oxide analysis.

** Fe excess compared to FeS_2 assuming that all S is in pyrite = $[Fe_2O_3]/2*M_{Fe_2O_3} - [S]/M_S$

Analytical procedures:

Au-AA25: Fire assay with atomic absorption spectrophotometry finish

ME-ICP06: Lithium borate fusion prior to acid dissolution and ICP-AES analysis

OA-GRA05: Loss on Ignition at 1000°C, furnace

C-IR07: Total carbon by induction furnace (Leco)

S-IR08: Total sulfur by induction furnace (Leco)

ME-MS81: Lithium borate fusion prior to acid dissolution and ICP-MS analysis

ME-MS42: aqua regia digestion and ICP-MS analysis

ME-ICP41: aqua regia digestion and ICP-AES analysis

Al$_2$O$_3$	Fe$_2$O$_3$	Fe*	CaO	MgO	Na$_2$O	K$_2$O	TiO$_2$	MnO	P$_2$O$_5$	LOI
wt.%	wt.%	%	wt.%	wt.%	wt.%	wt.%	wt.%	wt.%	wt.%	wt.%
ME-ICP06	ME-ICP06		ME-ICP06	ME-ICP06	ME-ICP06	ME-ICP06	ME-ICP06	ME-ICP06	ME-ICP06	OA-GRA05
AMIS0304	AMIS0304		AMIS0304	AMIS0304	AMIS0304	AMIS0304	AMIS0304	AMIS0304	AMIS0304	AMIS0250
0.01	0.01		0.01	0.01	0.01	0.01	0.01	0.01	0.01	0.01
17.10	7.34	5.31	0.08	1.06	0.60	2.50	1.07	0.02	0.14	7.09
19.10	5.31	3.84	0.04	1.05	0.46	3.39	1.03	0.02	0.06	9.34
18.80	5.74	4.15	0.04	0.88	0.49	3.62	1.05	0.02	0.06	9.25
25.90	9.41	6.81	0.01	0.25	1.38	4.57	1.30	<0.01	0.04	12.20
14.65	5.17	3.74	0.30	1.55	0.12	3.61	1.07	0.13	0.12	6.47
2.44	23.10	16.71	0.15	0.10	0.09	0.54	0.20	0.01	0.07	12.40
16.95	6.50	4.70	2.90	2.61	0.12	4.98	0.86	0.69	0.15	17.65
10.10	26.00	18.81	0.03	0.10	0.09	2.67	0.93	0.01	0.02	16.00
15.10	3.84	2.78	0.30	0.76	0.64	2.05	1.09	0.05	0.12	9.64
18.05	4.63	3.35	0.35	0.50	0.67	1.83	1.22	0.04	0.12	10.70

Gd	Hf	Ho	La	Lu	Nb	Nd	Pr	Rb	Sm	Sn
ppm	ppm	ppm	ppm	ppm	ppm	ppm	ppm	ppm	ppm	ppm
ME-MS81	ME-MS81	ME-MS81	ME-MS81	ME-MS81	ME-MS81	ME-MS81	ME-MS81	ME-MS81	ME-MS81	ME-MS81
GRE-3	GRE-3	GRE-3	GRE-3	GRE-3	GRE-3	GRE-3	GRE-3	GRE-3	GRE-3	GRE-3
0.05	0.2	0.01	0.1	0.01	0.2	0.1	0.03	0.2	0.03	1
7.89	7.4	1.29	51.7	0.57	21.2	48.7	13.05	117.5	8.52	2
4.56	5.6	1.27	39.6	0.49	24.6	31	8.97	168	4.6	4
4.07	5.6	1.11	40	0.48	24.5	30.9	8.91	172.5	4.56	4
8.27	5.9	1.61	71.2	0.63	26.6	59.9	16.55	163.5	10.2	5
7.14	9.4	1.39	46.2	0.63	22.8	43.4	10.90	170.5	7.78	3
3.16	5.1	0.74	9.4	0.21	3.3	9.5	2.31	16.1	2.92	2
5.30	5.3	1.08	44.3	0.55	27.9	38.2	10.70	300	6.63	14
5.40	5.4	1.17	33.5	0.50	19.5	29.5	7.79	67.1	6.03	1
6.77	11.9	1.27	42.8	0.59	19.4	40.8	10.65	79.3	7.65	2
7.64	8.9	1.37	50.7	0.73	24.2	49.5	12.80	90.1	8.91	4

Hg	In	Re	Se	Te	Tl	Cd	Co	Mo	Ni	Sc
ppm	ppm	ppm	ppm	ppm	ppm	ppm	ppm	ppm	ppm	ppm
ME-MS42	ME-MS42	ME-MS42	ME-MS42	ME-MS42	ME-MS42	ME-ICP41	ME-ICP41	ME-ICP41	ME-ICP41	ME-ICP41
MRGeo08	MRGeo08	MRGeo08	MRGeo08	MRGeo08	MRGeo08	MRGeo08	MRGeo08	MRGeo08	MRGeo08	MRGeo08
0.005	0.005	0.001	0.2	0.01	0.02	0.5	1	1	1	1
0.018	0.053	0.001	<0.2	0.07	0.11	<0.5	5	2	19	5
0.072	0.162	0.002	0.5	0.08	0.12	<0.5	2	1	7	2
0.061	0.192	0.002	0.6	0.10	0.13	<0.5	2	1	7	2
0.017	0.008	<0.001	0.6	1.27	0.09	<0.5	7	1	30	1
0.045	0.06	0.001	<0.2	0.75	0.13	<0.5	21	1	32	3
0.026	0.271	<0.001	0.3	0.08	0.76	2.6	4	<1	3	<1
0.072	0.081	0.002	1.0	0.20	0.21	1.1	18	1	35	4
0.046	0.017	<0.001	8.6	6.64	0.17	0.5	81	<1	53	1
0.067	0.049	<0.001	<0.2	0.04	0.03	<0.5	14	1	11	4
0.056	0.075	<0.001	0.3	0.05	0.06	<0.5	14	1	17	6

Total	Fe	S	** Fe excess
wt.%	mol/kg	mol/kg	mol/kg
TOT-ICP06			
0.01			
100.20	0.09	0.01	0.09
99.40	0.07	0.01	0.06
99.45	0.07	0.02	0.06
99.06	0.12	0.22	0.01
101.39	0.06	0.02	0.05
98.00	0.29	0.60	-0.01
98.01	0.08	0.16	0.00
98.05	0.33	0.68	-0.02
100.39	0.05	0.01	0.04
98.91	0.06	0.01	0.05

Sr	Ta	Tb
ppm	ppm	ppm
ME-MS81	ME-MS81	ME-MS81
GRE-3	GRE-3	GRE-3
0.1	0.1	0.01
51.3	1.4	1.17
70.9	1.6	0.80
68.5	1.5	0.77
78.9	1.5	1.21
23.6	1.4	1.03
4.0	0.1	0.70
33.6	1.1	0.80
26.2	1.0	0.95
72.0	1.3	0.98
113.5	1.6	1.11
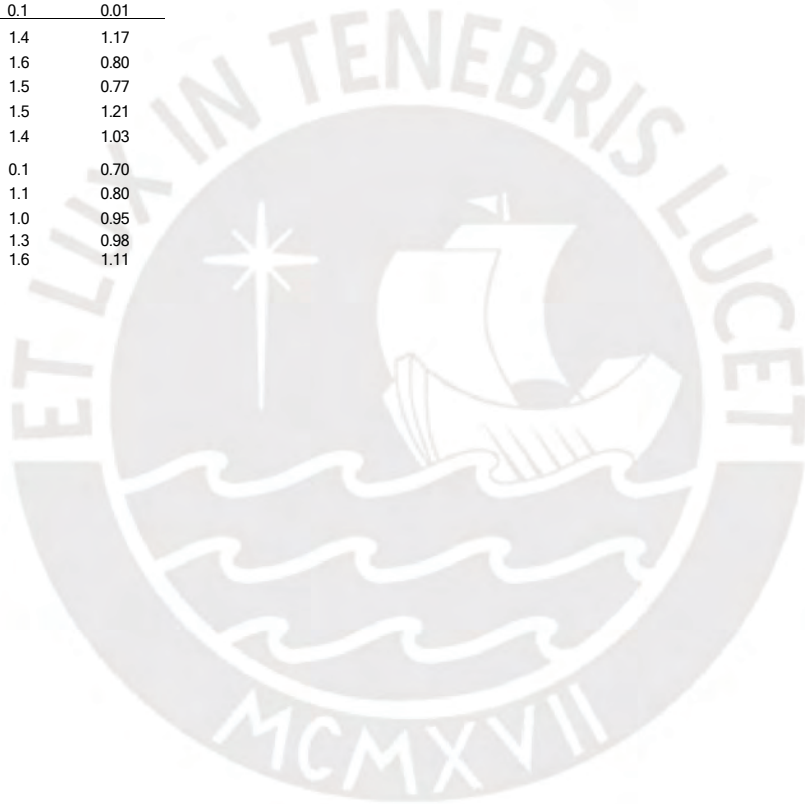
Table A2. Electron probe microanalyses (in wt %) of selected arsenopyrite and pyrite grains from the Shahuindo mine.

Mineral	Analysis no.	As	Sb	Cu	Fe	S	Total
Detection limits		0.20	0.07	0.06	0.14	0.06	
apyIII	BSHA7-c1-5	44.41	bdl	bdl	34.59	21.14	100.16
	BSHA7-c1-6	45.80	0.07	0.15	34.41	20.17	100.59
	BSHA7-c2-1	45.44	0.21	0.13	34.16	20.59	100.54
	BSHA7-c2-2	46.78	bdl	0.67	34.11	20.03	101.60
	BSHA7-c2-3	45.92	bdl	0.66	34.83	20.20	101.70
	BSHA7-c2-4	46.28	bdl	0.18	34.85	19.89	101.23
	BSHA7-c2-7	43.81	0.31	bdl	35.24	21.13	100.49
	BSHA7-c3-2	43.93	bdl	bdl	35.10	21.57	100.75
	BSHA7-c3-3	41.39	0.11	bdl	35.74	23.07	100.32
	BSHA7-c3-8	43.29	0.18	bdl	35.41	22.16	101.06
	BSHA13-c3-1	44.36	bdl	bdl	35.13	21.59	101.14
	BSHA19-c2-4	44.05	bdl	bdl	35.10	21.01	100.18
	BSHA18-c1-3	43.11	0.82	bdl	34.78	21.51	100.23
	BSHA18-c2-1	43.78	0.07	bdl	34.94	21.02	99.84
	BSHA18-c2-6	44.55	bdl	bdl	35.13	20.82	100.54
	BSHA18-c3-1	45.62	0.49	bdl	34.75	19.95	100.85
	BSHA18-c3-2	43.83	0.11	bdl	35.34	21.61	100.91
	BSHA18-c3-3	40.95	1.27	bdl	36.06	23.11	101.40
	BSHA18-c3-4	44.62	bdl	0.07	34.77	20.98	100.52
	BSHA18-c3-5	44.57	0.34	bdl	35.43	20.89	101.24
	BSHA18-c3-6	44.48	0.17	bdl	35.23	21.11	101.04
	BSHA18-c3-7	42.84	0.33	bdl	35.97	22.05	101.22
	BSHA18-c3-8	41.70	1.21	bdl	35.94	22.56	101.41
pyI	BSHA09b-c2-1	bdl	bdl	bdl	46.73	53.78	100.68
	BSHA09b-c2-2	bdl	bdl	bdl	46.49	53.96	100.45
	BSHA09b-c2-3	bdl	bdl	bdl	47.07	54.34	101.41
	MSHA11-34	bdl	bdl	bdl	46.50	51.77	98.28
	MSHA11-35	bdl	bdl	bdl	46.62	52.22	98.96
	MSHA11-36	bdl	bdl	bdl	46.69	52.35	99.07
	MSHA11-37	bdl	bdl	bdl	46.94	53.67	100.63
	MSHA11-8	bdl	bdl	bdl	45.47	51.41	96.96
	MSHA11-9	bdl	bdl	bdl	45.14	51.28	96.50
	MSHA11-10	bdl	bdl	bdl	44.69	51.78	96.51
	MSHA11-11	bdl	bdl	bdl	46.85	53.02	99.89
pyII	MSHA11-39	bdl	bdl	bdl	47.11	53.53	100.65
	BSHA9-c6-1	0.23	bdl	bdl	47.29	53.42	100.94
	BSHA9-c6-2	bdl	bdl	bdl	47.35	53.79	101.21
	BSHA9-c6-5	0.53	bdl	bdl	47.16	53.24	100.98
	BSHA9-c7-3	bdl	bdl	bdl	46.69	53.80	100.49
	BSHA9-c7-4	bdl	bdl	bdl	47.01	53.93	100.95
	BSHA7-c3-1	bdl	bdl	bdl	47.07	54.12	101.20
	BSHA9-c1-2	bdl	bdl	bdl	47.05	53.67	100.74
	BSHA9-c1-3	bdl	bdl	bdl	46.94	53.60	100.54
	BSHA9-c2-4	bdl	bdl	bdl	46.59	53.68	100.27
	BSHA9-c2-5	bdl	bdl	bdl	46.54	53.62	100.16
	BSHA9-c2-6	bdl	bdl	bdl	46.50	53.92	100.43
	BSHA9-C3-1	bdl	bdl	bdl	46.73	53.54	100.36
	BSHA9-C3-2	bdl	bdl	bdl	47.29	53.95	101.26
	BSHA9-c4-1	bdl	bdl	bdl	46.75	53.48	100.38
	BSHA9-c4-2	bdl	bdl	bdl	46.79	53.74	100.59
	BSHA9-c4-3	0.23	bdl	bdl	46.91	53.78	100.95
	BSHA9-c5-1	bdl	bdl	bdl	46.62	53.58	100.23
	BSHA9-c5-2	bdl	bdl	bdl	47.21	53.72	100.97
	BSHA3-c1-1	bdl	bdl	bdl	46.48	53.48	100.03
	BSHA3-c2-1	bdl	bdl	bdl	47.24	53.73	101.12
	BSHA3-c2-6	0.28	bdl	bdl	47.43	53.48	101.19
	BSHA3-c3-1	0.52	bdl	bdl	46.90	53.37	100.84
	BSHA4-c1-1	0.23	bdl	bdl	47.19	53.47	100.91
	BSHA4-c1-2	bdl	bdl	bdl	47.08	53.80	100.93
	BSHA13-c1-1	bdl	bdl	bdl	47.03	53.38	100.46
	BSHA13-c1-2	2.35	bdl	bdl	46.44	52.00	100.81
	BSHA13-c2-1	bdl	bdl	bdl	47.43	53.45	100.95
	BSHA13-c2-2	bdl	bdl	bdl	47.14	53.00	100.18
	BSHA13-c3-3	bdl	bdl	bdl	46.96	53.22	100.32
	BSHA09b-c1-3	bdl	bdl	bdl	46.95	54.10	101.31
	BSHA09b-c1-4	bdl	bdl	bdl	47.14	53.95	101.16
	BSHA09b-c1-8	0.47	bdl	bdl	46.50	53.63	100.65
	BSHA09b-c1-9	bdl	bdl	bdl	46.79	53.71	100.69

bdl = below detection limit

Mineral	Analysis no.	As	Sb	Cu	Fe	S	Total
Detection limits		0.20	0.07	0.06	0.14	0.06	
pyII	BSHA09b-c1-10	bdl	bdl	bdl	46.51	53.72	100.35
	BSHA09b-c1-11	0.31	bdl	bdl	46.67	53.93	100.91
	BSHA09b-c1-12	bdl	bdl	bdl	46.57	53.68	100.44
	BSHA09b-c2-4	0.32	bdl	bdl	46.78	53.87	100.99
	BSHA09b-c2-5	0.22	bdl	bdl	46.47	53.86	100.54
	BSHA09b-c2-6	0.73	bdl	bdl	47.10	53.78	101.62
	BSHA18-c1-1	0.30	bdl	bdl	46.87	53.06	100.25
	BSHA18-c1-2	bdl	bdl	bdl	47.34	53.94	101.46
	BSHA18-c1-4	0.32	bdl	bdl	47.12	53.56	101.01
	BSHA18-c1-5	0.77	bdl	bdl	47.34	53.50	101.62
	BSHA18-c1-6	0.35	bdl	bdl	47.43	53.39	101.29
	BSHA18-c1-7	0.89	bdl	bdl	47.15	53.22	101.31
	BSHA18-c1-8	0.25	bdl	bdl	47.26	53.45	100.98
	BSHA18-c1-9	bdl	bdl	bdl	47.26	53.70	100.99
	BSHA18-c1-10	0.22	bdl	bdl	47.40	53.66	101.28
	BSHA18-c2-4	0.31	bdl	bdl	46.79	53.66	100.88
	BSHA18-c2-5	bdl	bdl	bdl	47.58	53.97	101.64
pyIII	BSHA4-c1-3	2.80	bdl	0.06	46.13	51.73	100.72
	BSHA13-c3-2	1.62	bdl	bdl	47.05	52.32	101.00
	BSHA19-c1-1	2.43	bdl	bdl	46.74	52.01	101.21
	BSHA19-c1-2	2.26	bdl	bdl	46.65	52.03	100.98
	BSHA19-c1-3	bdl	bdl	bdl	47.16	53.83	101.07
	BSHA19-c1-4	1.98	bdl	bdl	46.55	51.90	100.45
	BSHA19-c1-5	2.29	bdl	bdl	46.19	51.79	100.35
	BSHA19-c1-6	bdl	bdl	bdl	46.53	53.80	100.47
	BSHA19-c2-1	bdl	bdl	0.23	47.22	53.10	100.62
	BSHA19-c2-2	bdl	bdl	0.11	46.58	53.58	100.27
	BSHA19-c2-3	2.34	bdl	bdl	46.19	51.83	100.40
	BSHA19-c2-5	2.05	bdl	bdl	46.26	51.93	100.27
	BSHA19-c2-6	0.43	bdl	bdl	47.23	53.47	101.15
	BSHA19-c2-7	bdl	bdl	bdl	47.10	53.75	100.97
	BSHA19-c3-1	1.56	bdl	bdl	46.67	52.79	101.11
	BSHA19-c3-2	bdl	bdl	0.24	47.07	53.20	100.59
	BSHA19-c3-3	bdl	bdl	0.14	46.95	53.83	100.92
	BSHA19-c3-4	bdl	bdl	0.12	47.04	53.43	100.60
	BSHA19-c3-5	1.58	bdl	bdl	46.78	52.49	100.85
	BSHA19-c3-6	1.95	bdl	bdl	47.04	52.03	101.13
	BSHA7-c1-1	bdl	bdl	bdl	46.56	53.37	100.13
	BSHA7-c1-2	bdl	bdl	0.66	45.86	52.78	99.44
	BSHA7-c1-3	bdl	bdl	bdl	46.69	53.38	100.09
	BSHA7-c1-4	1.97	bdl	bdl	46.46	52.32	100.78
	BSHA7-c1-7	0.33	bdl	bdl	46.58	53.85	100.76
	BSHA7-c1-8	1.61	bdl	bdl	46.45	52.68	100.78
	BSHA7-c1-9	bdl	bdl	0.09	46.40	53.47	99.95
	BSHA7-c1-10	2.07	bdl	bdl	45.93	52.12	100.14
	BSHA7-c2-5	bdl	bdl	bdl	47.28	53.73	101.27
	BSHA7-c2-6	1.57	bdl	bdl	46.42	52.55	100.60
	BSHA7-c3-4	bdl	bdl	0.92	45.84	53.52	100.38
	BSHA7-c3-5	bdl	bdl	0.37	45.79	53.50	99.72
	BSHA7-c3-6	0.78	bdl	bdl	46.43	53.73	100.95
	BSHA7-c3-7	bdl	bdl	0.13	46.61	53.53	100.37
	BSHA7-c3-10	bdl	bdl	bdl	46.71	53.94	100.65
	BSHA9-c1-1	4.61	bdl	0.15	45.56	50.04	100.36
	BSHA9-c2-1	3.92	bdl	0.20	45.61	50.72	100.51
	BSHA9-c2-2	4.21	bdl	0.18	45.72	50.77	100.88
	BSHA9-c2-3	3.90	bdl	0.19	45.44	50.28	99.82
	BSHA9-c4-4	0.52	bdl	bdl	46.11	52.86	99.51
	BSHA9-c4-5	0.51	bdl	bdl	45.95	52.98	99.47
	BSHA9-c5-3	0.32	bdl	bdl	46.79	53.33	100.46
	BSHA9-c5-4	0.20	bdl	bdl	46.69	53.09	100.00
	BSHA9-c6-3	4.33	bdl	0.16	45.86	50.48	100.83
	BSHA9-c6-4	4.61	bdl	0.13	45.45	50.15	100.34
	BSHA9-c6-6	2.49	bdl	0.11	46.75	51.66	101.01
	BSHA9-c7-1	5.62	bdl	0.20	45.01	49.57	100.40
	BSHA9-c7-2	5.22	bdl	0.24	44.75	49.71	99.93
	BSHA16-c2-1	2.05	bdl	bdl	46.45	52.29	100.79
	BSHA16-c2-2	2.95	bdl	bdl	45.83	51.40	100.22
	BSHA16-c2-6	1.44	bdl	bdl	46.09	52.72	100.27

bdl = below detection limit

Mineral	Analysis no.	As	Sb	Cu	Fe	S	Total
Detection limits		0.20	0.07	0.06	0.14	0.06	
pyIII	BSHA16-c2-7	1.05	bdl	bdl	46.54	52.63	100.27
	BSHA16-c3-3	1.86	bdl	bdl	46.80	52.60	101.26
	BSHA16-c3-4	bdl	bdl	bdl	47.29	53.83	101.12
	BSHA3-c1-2	0.40	bdl	bdl	46.62	53.31	100.35
	BSHA3-c1-3	0.72	bdl	bdl	46.30	52.83	99.87
	BSHA3-c2-2	bdl	bdl	bdl	47.16	53.59	100.95
	BSHA3-c2-3	0.38	bdl	bdl	46.93	53.30	100.61
	BSHA3-c2-4	1.36	bdl	bdl	46.62	52.21	100.30
	BSHA3-c2-5	0.37	bdl	bdl	47.35	53.32	101.15
	BSHA3-c3-2	0.46	bdl	bdl	46.79	53.34	100.62
	BSHA3-c3-3	0.30	bdl	bdl	46.84	52.85	100.01
	BSHA09b-c1-1	5.00	bdl	0.11	45.53	50.21	100.84
	BSHA09b-c1-2	1.30	bdl	bdl	46.52	52.91	100.78
	BSHA09b-c1-5	1.48	bdl	bdl	46.44	53.33	101.27
	BSHA09b-c1-6	4.22	bdl	0.10	45.72	51.06	101.11
	BSHA09b-c1-7	1.85	bdl	bdl	46.19	52.57	100.65
	BSHA09b-c1-13	3.73	bdl	0.06	45.60	52.16	101.55
	BSHA09b-c2-7	4.46	bdl	0.13	45.35	50.99	100.93
	BSHA09b-c2-8	1.56	bdl	bdl	46.25	53.10	100.94
	BSHA18-c2-2	0.46	bdl	bdl	46.86	53.58	100.96
	BSHA18-c2-3	0.62	bdl	bdl	47.06	53.15	100.84
	BSHA18-c2-7	bdl	bdl	bdl	46.90	53.85	100.91
	BSHA18-c2-8	0.66	bdl	bdl	47.03	53.27	101.01
	BSHA18-c2-9	bdl	bdl	bdl	46.99	53.69	100.87
	BSHA18-c2-10	0.25	bdl	bdl	47.48	53.37	101.11
	BSHA09b-c1-2	1.22	bdl	bdl	46.28	52.79	100.31
	MSHA-14(a)-4	bdl	bdl	bdl	46.74	53.29	100.17
	MSHA-14(a)-5	1.78	bdl	bdl	46.80	52.28	100.89
	MSHA-14(a)-6	bdl	bdl	bdl	46.94	53.35	100.38
	MSHA-14(a)-7	bdl	bdl	bdl	47.10	53.28	100.48
	MSHA-14(a)-8	bdl	bdl	bdl	47.01	53.50	100.57
	MSHA-14(a)-9	bdl	bdl	bdl	47.01	52.97	100.09
	MSHA-14(a)-10	bdl	bdl	bdl	46.89	53.07	100.18
	MSHA-14(a)-11	0.20	bdl	bdl	46.89	52.25	99.36
	MSHA-14(a)-12	0.24	bdl	bdl	47.45	53.13	100.87
	MSHA-14(a)-13	0.38	bdl	bdl	46.77	53.48	100.75
	MSHA-14(a)-14	bdl	bdl	bdl	46.97	52.76	99.92
	MSHA-14(a)-15	2.23	bdl	bdl	46.20	50.14	98.65
	MSHA-14(a)-16	2.60	bdl	bdl	38.88	43.70	85.23
	MSHA-14(a)-17	0.14	bdl	bdl	46.96	52.99	100.20
	MSHA-14(a)-18	bdl	bdl	bdl	46.68	52.01	98.89
	MSHA-14(a)-19	1.31	bdl	bdl	46.88	52.69	100.97
	MSHA-14(a)-20	0.74	bdl	bdl	46.08	51.66	98.52
	MSHA-14(b)-21	bdl	bdl	bdl	47.17	53.31	100.64
	MSHA-14(b)-22	0.15	bdl	bdl	46.93	53.20	100.31
	MSHA-14(b)-23	2.81	bdl	bdl	46.37	51.63	100.91
	MSHA-14(b)-28	bdl	bdl	bdl	47.19	53.18	100.48
	MSHA-14(b)-24	0.99	bdl	bdl	46.92	52.64	100.64
	MSHA-14(b)-25	0.64	bdl	bdl	46.97	52.73	100.39
	MSHA-14(b)-26	bdl	bdl	bdl	47.26	52.97	100.31
	MSHA-14(b)-27	bdl	bdl	bdl	47.21	52.82	100.12
	MSHA-14(b)-29	bdl	bdl	bdl	46.94	53.25	100.33
	MSHA-14(b)-30	1.39	bdl	bdl	46.11	52.09	100.25
	MSHA-14(b)-31	0.43	bdl	bdl	46.62	52.45	99.58
	MSHA-14(b)-32	0.17	bdl	bdl	47.29	53.38	100.87
	MSHA-14(b)-33	bdl	bdl	bdl	46.28	52.47	98.88
pyIV	BSHA16-c1-1	2.08	bdl	bdl	46.36	52.19	100.69
	BSHA16-c1-2	1.39	bdl	bdl	46.41	52.83	100.64
	BSHA16-c1-3	2.87	bdl	bdl	46.18	51.64	100.78
	BSHA16-c1-4	bdl	bdl	bdl	47.12	53.69	100.82
	BSHA16-c1-5	1.83	bdl	bdl	46.31	52.39	100.53
	BSHA16-c1-6	0.78	bdl	bdl	47.13	53.29	101.20
	BSHA16-c1-7	bdl	bdl	bdl	47.00	53.79	100.94
	BSHA16-c2-3	bdl	bdl	bdl	46.54	54.29	100.84
	BSHA16-c2-4	bdl	bdl	bdl	46.91	53.52	100.58
	BSHA16-c2-5	0.89	bdl	bdl	46.58	53.28	100.78
	BSHA16-c3-1	2.85	bdl	bdl	46.04	51.31	100.21
	BSHA16-c3-2	bdl	bdl	bdl	47.01	53.83	100.86

bdl = below detection limit

Table A3. Laser Ablation ICPMS analyses (in ppm) of selected representative arsenopyrite and pyrite grains from the Shahuindo mine.

Mineral	Sample	Host rock/structure	^{51}V	^{59}Co	^{60}Ni	^{63}Cu	^{66}Zn	^{71}Ga
apyIII	BSHA-13-3-59	Sandstone	29	2.9	21	190.00	14	6.8
	BSHA-18-2-29	NE-SW Fault	8.5	8.5	17	210.00	37	2.8
	BSHA-18-3-34	NE-SW Fault	1.0	22	23	100.00	15	1.3
	BSHA-18-3-35	NE-SW Fault	0.8	13	25	230.00	8.4	0.8
	BSHA-18-3-40	NE-SW Fault	0.6	17	34	160.00	3.1	0.7
	BSHA-18-5-44	NE-SW Fault	0.2	6.1	9.5	280.00	3.9	0.1
	BSHA-07-2-78	Dacitic intrusion contact	0.4	0.5	12.0	26710.00	940.00	5.8
	BSHA-07-2-80	Dacitic intrusion contact	0.3	2.1	11.8	40320.00	110.00	6.5
	BSHA-07-3-87	Dacitic intrusion contact	0.2	0.7	9.9	680.00	10.4	12
	BSHA-07-3-89	Dacitic intrusion contact	0.2	4.5	13	300.00	3.6	0.4
	BSHA-19-2-34	Dacitic intrusion	5.5	2.8	12	84	9.1	3.2
		MIN	0.2	0.5	9.5	84	3.1	0.1
		MAX	29	22	34	40320	940	12
		MEAN	1.0	4.2	16	520	17	1.7
Mineral	Sample	Host rock/structure	^{51}V	^{59}Co	^{60}Ni	^{63}Cu	^{66}Zn	^{71}Ga
pyI	BSHA-09b-1-8	Sandstone	0.5	580	97.9	2.5	2.4	0.6
	BSHA-09b-1-14	Sandstone	2.6	60	650	1670	16	3.3
	BSHA-09b-2-15	Sandstone	2.0	460	260	4970	39	2.6
	64-MSHA11b	Sandstone	NA	120	160	270	190	NA
	31-MSHA11a	Sandstone	NA	64	140	270	190	NA
	62-MSHA11b	Sandstone	NA	63	200	460	200	NA
	67-MSHA11a	Sandstone	NA	44	31	82	110	NA
	36-MSHA11b	Sandstone	NA	50	180	190	280	NA
	35-MSHA11b	Sandstone	NA	66	330	560	380	NA
	67-MSHA11b	Sandstone	NA	9.5	200	44	100	NA
	55-MSHA11a	Sandstone	NA	66	120	190	120	NA
	66-MSHA11a	Sandstone	NA	43	150	290	140	NA
	68-MSHA11a	Sandstone	NA	100	340	630	530	NA
	30-MSHA11a	Sandstone	NA	22	84	330	210	NA
	53-MSHA11a	Sandstone	NA	340	278	200	54	NA
	60-MSHA11b	Sandstone	NA	7.5	60	580	100	NA
	04-MSHA11b	Sandstone	NA	10	41	720	750	NA
	03-MSHA11b	Sandstone	NA	150	300	480	360	NA
	49-MSHA11a	Sandstone	NA	9.2	40	110	4160	NA
	32-MSHA11a	Sandstone	NA	89	160	260	110	NA
	65-MSHA11b	Sandstone	NA	1.5	25	450	220	NA
	01-MSHA11b	Sandstone	NA	8.4	110	740	130	NA
	02-MSHA11b	Sandstone	NA	29	200	360	260	NA
	60-MSHA11a	Sandstone	NA	130	1000	1150	600	NA
	06-MSHA23a	Fine-grained Sandstone	NA	7.5	<43	120	100	NA
	37-MSHA23b	Fine-grained Sandstone	NA	6.8	<44	64	220	NA
	71-MSHA23b	Fine-grained Sandstone	NA	78	<44	70	850	NA
	61-MSHA23a	Fine-grained Sandstone	NA	10	<64	110	310	NA
	26-MSHA23b	Fine-grained Sandstone	NA	260	420	290	2240	NA
	31-MSHA23b	Fine-grained Sandstone	NA	23	41	120	300	NA
	29-MSHA23b	Fine-grained Sandstone	NA	200	85	520	9390	NA
	17-MSHA23a	Fine-grained Sandstone	NA	7.3	83	19	73	NA
	23-MSHA23b	Fine-grained Sandstone	NA	13	100	46	260	NA
	68-MSHA23b	Fine-grained Sandstone	NA	22	<49	100	330	NA
	33-MSHA23b	Fine-grained Sandstone	NA	66	46	73	750	NA
	63-MSHA23a	Fine-grained Sandstone	NA	7.5	<46	57	200	NA
	32-MSHA23b	Fine-grained Sandstone	NA	40	96	140	580	NA
	24-MSHA23b	Fine-grained Sandstone	NA	180	210	560	5090	NA
	09-MSHA23a	Fine-grained Sandstone	NA	260	380	550	3120	NA
	66-MSHA23b	Fine-grained Sandstone	NA	710	590.00	920	12290	NA
	29-MSHA23	Fine-grained Sandstone	NA	740	590.00	660	8730	NA
	15-MSHA23a	Fine-grained Sandstone	NA	94	130.00	160	340	NA
	36-MSHA23b	Fine-grained Sandstone	NA	88	38	100	730	NA
	60-MSHA23a	Fine-grained Sandstone	NA	6.5	<51	94	350	NA
	30-MSHA23b	Fine-grained Sandstone	NA	260	220.00	1040	19180	NA
	12-MSHA23a	Fine-grained Sandstone	NA	24	110.00	310	560	NA
	25-MSHA23b	Fine-grained Sandstone	NA	8.9	100.00	49	110	NA
	69-MSHA23b	Fine-grained Sandstone	NA	12	<85	85	300	NA
	67-MSHA23b	Fine-grained Sandstone	NA	250	270.00	1210	5640	NA
	19-MSHA23a	Fine-grained Sandstone	NA	45	190.00	1190	2010	NA
	65-MSHA23b	Fine-grained Sandstone	NA	25	140.00	71	280	NA
	26-MSHA23	Fine-grained Sandstone	NA	210.00	650.00	1190	2360	NA
	08-MSHA23a	Fine-grained Sandstone	NA	790.00	430.00	910	8850	NA
	28-MSHA23	Fine-grained Sandstone	NA	430.00	2250.00	1100	10960	NA
	16-MSHA23a	Fine-grained Sandstone	NA	150.00	520.00	1860	77860	NA
	07-MSHA23a	Fine-grained Sandstone	NA	45	<400	1690	2530	NA
		MIN	0.5	1.5	25	2.5	2.4	0.6
		MAX	2.6	79.00	2250.00	4970	77860	3.3
		MEAN	1.4	53	140.00	260	500	1.7

^{74}Ge	^{75}As	^{77}Se	^{95}Mo	^{107}Ag	^{115}In	^{121}Sb	^{130}Te	^{197}Au	^{208}Pb	^{209}Bi
1.9	337250	25	1.9	11	1.7	390	250	130	40	49
0.6	255190	11	0.5	12	2.5	2610	14	100	180	790
1.5	233070	6.2	0.2	13	2.4	7280	1.2	1.8	210	22
0.6	208410	4.4	0.1	18	2.1	2480	0.8	24	380	220
0.7	163150	3.5	0.04	16	1.7	3540	0.8	18	450	140
0.6	231870	4.3	0.09	43	2.4	2340	2.2	87	340	600
7.0	347300	45	0.6	790.00	3.6	4540	19	73	1780	730
8.2	293150	48	0.6	1260.00	4.3	560	17	170	29	220
2.6	206660	45	0.4	9.3	2.9	960	24	37	140	450
1.0	377170	40	0.4	38	1.0	440	120	460	920	310
0.9	332800	71	0.4	0.6	0.9	70	160	68	6.0	4.7
0.6	163150	3.5	0.04	0.6	0.9	70	0.8	1.8	6.0	4.7
8.2	377170	71	1.9	1260.00	4.3	7280	250	460	1780	790
1.4	*263070*	*17*	*0.3*	*27*	*2.1*	*1250*	*12*	*55*	*170*	*160*
^{74}Ge	^{75}As	^{77}Se	^{95}Mo	^{107}Ag	^{115}In	^{121}Sb	^{130}Te	^{197}Au	^{208}Pb	^{209}Bi
0.6	2570	17	0.04	0.3	0.02	4.0	1.6	1.7	2.8	7.2
0.4	2890	8.8	0.09	1.5	0.2	8.0	2.7	1.1	11	15.3
0.3	2850	7.7	0.03	4.7	0.6	10	1.0	1.1	8.2	18.6
NA	550	NA	NA	14	NA	41	5.7	0.1	220	1.9
NA	780	NA	NA	30	NA	26	3.6	0.1	390	1.6
NA	910	NA	NA	49	NA	69	11	0.2	680	2.3
NA	180	NA	NA	14	NA	8.6	5.0	0.2	240	1.0
NA	1980	NA	NA	13	NA	34.8	10	0.2	270	1.4
NA	1610	NA	NA	29	NA	76.3	3.0	0.2	590	3.5
NA	77	NA	NA	16	NA	6.0	56	0.2	10	1.0
NA	1140	NA	NA	17	NA	23.3	10	0.2	500	1.7
NA	280	NA	NA	32	NA	45.3	4.9	0.2	240	0.8
NA	2260	NA	NA	41	NA	130	10	0.2	630	2.7
NA	460	NA	NA	41	NA	20	3.1	0.3	460	2.4
NA	2160	NA	NA	8.6	NA	26	18	0.3	190	0.8
NA	1850	NA	NA	3.7	NA	11	7.6	0.6	81	0.4
NA	13670	NA	NA	5.0	NA	37	8.9	0.1	230	0.6
NA	1150	NA	NA	39	NA	120	13	0.2	490	4.3
NA	11160	NA	NA	5.7	NA	16.9	9.0	0.2	160	0.2
NA	1940	NA	NA	42	NA	23	8.5	0.2	510	3.0
NA	13470	NA	NA	3.5	NA	21	6.0	0.2	140	0.4
NA	5000	NA	NA	8.4	NA	34	11	0.6	200	0.4
NA	3850	NA	NA	17.8	NA	44	11	1.1	210	0.8
NA	4670	NA	NA	78.1	NA	58	270	4.5	670	6.2
NA	17	NA	NA	NA	NA	1.8	NA	0.2	50	<0.6
NA	92	NA	NA	NA	NA	27	NA	0.7	100	0.8
NA	52	NA	NA	NA	NA	13	NA	0.8	88	1.0
NA	49	NA	NA	NA	NA	19	NA	1.2	1050	8.0
NA	100	NA	NA	NA	NA	1.9	NA	<0.03	200	1.6
NA	35	NA	NA	NA	NA	0.9	NA	<0.1	34	0.8
NA	520	NA	NA	NA	NA	6.7	NA	<0.2	72	0.9
NA	25	NA	NA	NA	NA	<1.3	NA	<0.2	21	<0.4
NA	30	NA	NA	NA	NA	1.1	NA	<0.2	36	2.7
NA	100	NA	NA	NA	NA	46	NA	<0.3	140	6.1
NA	50	NA	NA	NA	NA	1.0	NA	<0.3	35	0.6
NA	24	NA	NA	NA	NA	4.5	NA	<0.4	74	1.0
NA	87	NA	NA	NA	NA	64	NA	<0.4	220	2.2
NA	570	NA	NA	NA	NA	8.7	NA	<0.4	95	4.8
NA	360	NA	NA	NA	NA	2.8	NA	<0.4	170	5.2
NA	770	NA	NA	NA	NA	9.1	NA	<0.5	200	15
NA	680	NA	NA	NA	NA	8.6	NA	<0.5	150	14
NA	960	NA	NA	NA	NA	4.1	NA	<0.5	1990	8.6
NA	350	NA	NA	NA	NA	410	NA	<0.5	580	3.1
NA	36	NA	NA	NA	NA	26	NA	<0.6	190	1.7
NA	440	NA	NA	NA	NA	9.5	NA	<0.6	160	5.0
NA	57	NA	NA	NA	NA	<3.7	NA	<0.6	130	1.5
NA	32	NA	NA	NA	NA	<2.3	NA	<0.7	20	1.1
NA	37	NA	NA	NA	NA	11	NA	<0.7	210	<1.0
NA	1150	NA	NA	NA	NA	17	NA	<0.8	320	78
NA	680	NA	NA	NA	NA	21	NA	<0.9	270	5.7
NA	70	NA	NA	NA	NA	<3.7	NA	<0.9	34	3.7
NA	340	NA	NA	NA	NA	<7.4	NA	<1.7	270	6.1
NA	490	NA	NA	NA	NA	<17	NA	<2.1	160	<4.5
NA	1310	NA	NA	NA	NA	31	NA	<2.6	730	54
NA	690	NA	NA	NA	NA	530	NA	<3.6	48520	99
NA	1170	NA	NA	NA	NA	310	NA	<4.1	10340	7.6
0.3	*17*	*7.7*	*0.03*	*0.3*	*0.02*	*0.9*	*1.0*	*0.03*	*2.8*	*0.2*
0.6	*13670*	*17*	*0.09*	*78*	*0.6*	*530.00*	*270*	*4.5*	*48520*	*99*
0.4	*430*	*10*	*0.05*	*12*	*0.1*	*15*	*7.8*	*0.4*	*180*	*2.5*

137

Mineral	Sample	Host rock/structure	^{51}V	^{59}Co	^{60}Ni	^{63}Cu	^{66}Zn	^{71}Ga
pyII	BSHA-03-1-16	Siltstone	3.4	33	23	6.0	<2.3	0.3
	BSHA-03-2-22	Siltstone	<0.2	0.6	<10	19	<2.7	<0.3
	BSHA-03-2-27	Siltstone	<0.2	34	83	<1.7	<2.7	0.3
	BSHA-09-1-64	Sandstone	<0.3	<0.4	46	<3.2	<3.0	<0.3
	BSHA-09-1-65	Sandstone	<0.3	<0.5	63	<3.4	3.7	<0.3
	BSHA-09-2-68	Sandstone	4.4	64	450.00	55	<3.3	0.8
	BSHA-09-2-69	Sandstone	0.6	<0.4	92	<3.0	<2.8	<0.3
	BSHA-09-4-71	Sandstone	<0.3	9.7	27	29	<3.6	<0.4
	BSHA-09b-1-5	Sandstone	3.9	9.0	13	1.4	7.1	5.5
	BSHA-09b-1-6	Sandstone	0.3	3.4	5.1	<0.4	3.0	<0.08
	BSHA-09b-1-10	Sandstone	2.3	2.1	4.0	2.6	3.3	1.2
	BSHA-09b-1-11	Sandstone	0.4	7.2	17	12	2.0	0.3
	BSHA-09b-1-12	Sandstone	1.6	12	17	2.9	3.1	1.5
	BSHA-09b-1-13	Sandstone	0.2	11	13	17	1.5	0.2
	BSHA-09b-2-17	Sandstone	0.2	5.7	13	0.6	2.1	0.1
	BSHA-13-1-52	Sandstone	<0.5	14	<19	42	<6.4	<0.5
	BSHA-13-1-53	Sandstone	<0.4	21	<19	21	<6.3	<0.8
	BSHA-13-2-57	Sandstone	<0.3	17	130	35	<4.3	0.7
	BSHA-13-2-58	Sandstone	1.8	12	27	78	<5.7	3.9
	BSHA-13-3-61	Sandstone	4.6	5.0	<11	40	<3.3	2.2
	19-MSHA8b	Sandstone	NA	2.5	3.9	6.4	4.7	NA
	16-MSHA8a	Sandstone	NA	0.2	17	3.1	5.4	NA
	51-MSHA8a	Sandstone	NA	0.3	7.1	2.1	6.5	NA
	47-MSHA8a	Sandstone	NA	0.3	15	6.0	5.3	NA
	48-MSHA8a	Sandstone	NA	0.5	6.2	45	13	NA
	53-MSHA8a	Sandstone	NA	0.6	7.3	5.5	6.5	NA
	36-MSHA8b	Sandstone	NA	1070	52	4.6	8.6	NA
	53-MSHA8a	Sandstone	NA	0.6	19	4.2	8.0	NA
	20-MSHA8a	Sandstone	NA	1.1	21	20	12	NA
	48-MSHA8b	Sandstone	NA	5.6	28	53660	11	NA
	39-MSHA8b	Sandstone	NA	2.0	17	1370	8.0	NA
	44-MSHA8b	Sandstone	NA	4.3	24	19940	10	NA
	45-MSHA8b	Sandstone	NA	7.1	25	9780	34	NA
	BSHA-18-1-26	NE-SW Fault	1.0	4.0	11	63	2.4	1.1
	BSHA-18-1-27	NE-SW Fault	0.2	4.2	11	17	2.4	0.4
	BSHA-18-1-28	NE-SW Fault	0.5	9.5	8.6	160	4.7	0.4
	BSHA-18-2-31	NE-SW Fault	1.4	5.2	12	7.3	1.2	0.8
	BSHA-18-2-32	NE-SW Fault	0.5	17	12	47	6.4	0.6
	BSHA-18-2-33	NE-SW Fault	0.9	8.3	3.9	91	6.4	1.0
	BSHA-18-5-47	NE-SW Fault	0.1	1.6	4.4	17	1.8	0.1
	BSHA-04-1-21	Dacitic intrusion contact	<0.06	59	13	1.5	14	<0.05
	BSHA-04-1-23	Dacitic intrusion contact	<0.06	13	230	1.6	65	<0.05
	BSHA-04-1-25	Dacitic intrusion contact	<0.05	12	140	3.7	9.4	0.02
	BSHA-07-3-84	Dacitic intrusion contact	<0.2	<0.3	<10	<2.7	2.8	<0.2
	BSHA-07-3-85	Dacitic intrusion contact	<0.2	<0.3	<10	<2.8	3.0	<0.3
		MIN	*0.1*	*0.2*	*3.9*	*0.4*	*1.2*	*0.02*
		MAX	*4.6*	*1070*	*450*	*53660*	*65*	*5.5*
		MEAN	*0.5*	*4.0*	*19*	*16*	*4.9*	*0.4*

⁷⁴Ge	⁷⁵As	⁷⁷Se	⁹⁵Mo	¹⁰⁷Ag	¹¹⁵In	¹²¹Sb	¹³⁰Te	¹⁹⁷Au	²⁰⁸Pb	²⁰⁹Bi
<0.8	1820	7.2	0.2	<0.4	<0.09	3.7	6.4	0.5	2.1	5.7
<1	1730	8.1	<0.2	<0.5	<0.08	1.8	<2.3	0.3	3.7	0.7
<1	1650	<5.3	<0.5	<0.5	<0.08	<0.3	<2.4	0.1	<0.2	0.9
<0.9	46	4.6	<0.4	<0.4	<0.1	<0.6	<2.8	0.2	<0.08	<0.1
<0.9	19	<3.4	<0.3	<0.5	<0.09	<0.5	<2.8	0.09	<0.1	<0.04
<1	1810	<3.4	0.3	0.9	<0.09	77	4.3	1.4	10	0.3
<0.8	55	3.2	<0.4	<0.5	<0.1	<0.5	<2.5	0.2	1.1	0.1
<0.9	3240	<3.7	<0.5	0.6	<0.1	12	<2.9	0.9	4.8	3.8
<0.5	340	<17	0.05	<0.2	<0.02	1.8	<1.5	0.06	1.0	1.9
<0.5	320	<14	0.04	<0.2	<0.02	0.9	<1.3	<0.06	0.5	0.8
<0.5	800	<13	0.06	<0.2	<0.02	4.1	<1.3	<0.03	3.3	5.6
<0.4	1390	<11	<0.02	<0.2	<0.02	1.8	<1.1	0.08	0.8	1.2
<0.4	4220	<10	0.2	<0.2	0.03	2.8	1.2	3.1	3.2	6.2
0.3	730	<9.7	0.04	0.6	<0.02	3.2	1.8	0.8	21	6.8
<0.3	3290	<6.9	<0.06	<0.1	0.03	0.6	<0.8	0.05	0.4	0.7
<1.7	10610	<8.9	<1.2	1.6	0.4	26	<5.3	9.9	68	4.3
<1.7	3970	<6.6	<1.1	2.1	0.3	34	<5.5	4.4	96	1.0
1.2	1770	<4.6	<0.4	18	<0.2	200	<3.8	1.1	810	2.7
<1.5	5850	<6.6	<0.9	3.4	0.2	43	<5.5	5.7	78	20
<1.0	1100	<4.7	<0.5	15	0.2	200	<3.3	0.4	790	3.1
NA	6300	NA	NA	0.8	NA	20	2.8	0.04	100	0.1
NA	6	NA	NA	12	NA	30	3.3	0.04	400	0.05
NA	17	NA	NA	1.0	NA	0.3	3.5	0.05	2.6	0.06
NA	43	NA	NA	37	NA	95	3.0	0.05	1010	0.4
NA	38	NA	NA	23	NA	67	3.2	0.06	670	1.3
NA	2580	NA	NA	5.5	NA	15	3.6	0.06	180	0.2
NA	1900	NA	NA	1.3	NA	0.4	5.3	0.1	0.5	0.7
NA	6	NA	NA	6.4	NA	25.9	4.9	0.1	150	0.1
NA	6530	NA	NA	5.6	NA	15.4	6.9	1.3	160	0.2
NA	860	NA	NA	8.5	NA	23.5	7.1	1.4	27	1.0
NA	6140	NA	NA	1.4	NA	2.4	4.5	1.6	3.5	1.2
NA	5260	NA	NA	8.1	NA	15	6.2	1.8	12	5.2
NA	4430	NA	NA	4.9	NA	17	6.4	5.0	62	3.3
<0.4	2650	<6.3	<0.09	15	0.05	290	<1.0	0.9	140	5.3
<0.6	2240	<11	0.07	2.9	<0.04	41	<1.7	0.4	37	3.8
0.7	2720	<9.2	<0.1	38	0.08	480	<1.6	0.5	280	10
<0.2	2750	<3.6	<0.05	1.3	0.02	24	<0.6	0.2	14	3.6
<0.3	2730	<3.7	<0.09	10	0.09	95	<0.7	0.8	220	23
<0.3	7260	<3.9	0.09	24	0.1	250	<0.7	2.7	180	16
<0.2	920	<3.3	<0.07	1.3	<0.02	32	<0.7	0.1	68	0.9
<0.3	400	8.7	<0.07	<0.1	<0.02	72	1.3	0.05	3.7	2.3
<0.2	1340	<5.5	<0.05	0.2	<0.02	120	1.5	0.06	10	3.6
<0.3	810	<5.1	<0.1	0.9	<0.02	46	1.9	0.06	5.2	2.4
<0.7	8	<2.9	0.2	0.4	<0.1	6.2	<2.4	0.1	14	0.2
<0.8	11	<2.6	<0.55	<0.4	<0.09	<0.6	<2.4	0.3	0.3	0.1
0.20	*6*	*2.60*	*0.02*	*0.2*	*0.02*	*0.3*	*0.7*	*0.03*	*0.08*	*0.04*
1.70	*10610*	*17*	*1.2*	*38*	*0.4*	*480*	*7.1*	*9.9*	*1010*	*23*
0.6	*730*	*6.0*	*0.2*	*1.6*	*0.06*	*11*	*2.5*	*0.3*	*14*	*1.1*

Mineral	Sample	Host rock/structure	^{51}V	^{59}Co	^{60}Ni	^{63}Cu	^{66}Zn	^{71}Ga
pyIII	BSHA-03-1-17	Siltstone	2.9	18	<8.8	270	2.5	<0.3
	BSHA-03-1-21	Siltstone	0.9	0.4	<10.7	140	<3.2	<0.2
	BSHA-03-2-23	Siltstone	0.9	13	<10.2	85	<3.0	<0.4
	BSHA-03-2-24	Siltstone	1.7	3.8	<10.1	49	<2.6	<0.3
	BSHA-03-2-25	Siltstone	<0.2	18.3	23	2.1	<2.8	<0.3
	BSHA-03-2-26	Siltstone	<0.3	12.6	43	7.4	<2.8	<0.3
	BSHA-09-1-62	Sandstone	<0.2	1.9	86	790	3.4	<0.2
	BSHA-09-1-63	Sandstone	<0.3	1.1	76	410	<3.8	<0.3
	BSHA-09-2-66	Sandstone	<0.2	6.3	110	1380	<3.0	<0.2
	BSHA-09-2-67	Sandstone	0.4	3.7	<10	1840	<3.0	<0.3
	BSHA-09-4-70	Sandstone	2.3	<0.5	<12	160	<3.6	3
	BSHA-09b-1-4	Sandstone	<0.1	0.3	<1.2	290	2.9	0.09
	BSHA-09b-1-7	Sandstone	0.5	0.3	<2.0	260	3.5	1.7
	BSHA-09b-1-9	Sandstone	<0.09	1.0	2.8	14	2.3	<0.06
	BSHA-13-3-60	Sandstone	2.9	11	<22	850	170	<0.9
	50-MSHA8b	Sandstone	NA	4.0	22	240	9.2	NA
	38-MSHA8b	Sandstone	NA	7.8	23	9540	10	NA
	18-MSHA8b	Sandstone	NA	7.5	18	69940	7.7	NA
	25-MSHA8a	Sandstone	NA	3.6	29	1020	16	NA
	28-MSHA8a	Sandstone	NA	5.1	6.7	27	5.7	NA
	29-MSHA8a	Sandstone	NA	8.2	26	43470	52	NA
	14-MSHA8a	Sandstone	NA	2.4	4.0	30	4.9	NA
	47-MSHA8b	Sandstone	NA	6.4	30	54220	13	NA
	52-MSHA8a	Sandstone	NA	11	8.4	6470	7.7	NA
	27-MSHA8a	Sandstone	NA	2.0	25	1180	14	NA
	51-MSHA8a	Sandstone	NA	1.9	17	35	29	NA
	54-MSHA8a	Sandstone	NA	4.0	25.24	26550	10	NA
	20-MSHA8b	Sandstone	NA	2.2	4	2020	5.1	NA
	17-MSHA8a	Sandstone	NA	2.3	4.6	680	5.5	NA
	55-MSHA8a	Sandstone	NA	3.7	35	11880	15	NA
	49-MSHA8a	Sandstone	NA	9.7	14	8550	13	NA
	55-MSHA8a	Sandstone	NA	3.9	6.6	650	5.9	NA
	50-MSHA8a	Sandstone	NA	0.7	6.3	43	5.8	NA
	30-MSHA8a	Sandstone	NA	7.6	17	810	9.6	NA
	27-MSHA8a	Sandstone	NA	4.7	5.4	60	5.4	NA
	46-MSHA8a	Sandstone	NA	0.4	6.3	54	5.7	NA
	15-MSHA8a	Sandstone	NA	2.0	5.6	34	6.2	NA
	54-MSHA8a	Sandstone	NA	2.6	10	480	8.9	NA
	43-MSHA8b	Sandstone	NA	6.0	27	10	12	NA
	26-MSHA8a	Sandstone	NA	5.0	23	23870	13	NA
	BSHA-18-2-30	NE-SW Fault	1.1	3.3	<3.2	120	19	2.3
	BSHA-18-3-41	NE-SW Fault	0.1	11.8	8.6	42	1.1	0.2
	BSHA-18-3-42	NE-SW Fault	0.4	31.7	68	27	1.5	0.1
	BSHA-18-3-43	NE-SW Fault	0.5	12.1	12	53	6.5	0.3
	BSHA-18-5-45	NE-SW Fault	0.1	4.6	12	34	2.1	56
	BSHA-18-5-46	NE-SW Fault	1.6	6.8	4.6	11	8.5	24
	BSHA-18-5-48	NE-SW Fault	0.2	10	5.3	70	<1.6	0.2
	BSHA-19-1-28	Dacitic intrusion	<0.3	<0.5	<12	19	<2.8	<0.3
	BSHA-19-1-29	Dacitic intrusion	<0.2	<0.4	<9.3	150	4.5	<0.4
	BSHA-19-1-30	Dacitic intrusion	<0.2	<0.3	<8.5	410	21	4.6
	BSHA-19-1-31	Dacitic intrusion	<0.2	<0.4	<9.1	650	17	7.5
	BSHA-19-1-32	Dacitic intrusion	<0.2	<0.3	<8.3	1290	43	23
	BSHA-19-2-33	Dacitic intrusion	<0.2	<0.3	<8.2	1840	110	40
	BSHA-19-2-35	Dacitic intrusion	<0.2	<0.3	<8.3	2250	200	66
	BSHA-19-2-40	Dacitic intrusion	<0.2	<0.3	<8.8	31	<2.7	<0.2
	BSHA-19-3-41	Dacitic intrusion	<0.2	<0.3	<8.0	19	<2.3	<0.2
	BSHA-19-3-42	Dacitic intrusion	<0.3	<0.5	<12	21490	25	7.6
	BSHA-19-3-45	Dacitic intrusion	<0.3	<0.5	<12	2000	11	8.5
	BSHA-04-1-22	Dacitic intrusion contact	12	0.9	<1.9	180	300	3.8
	BSHA-04-1-24	Dacitic intrusion contact	0.9	8.6	22	52	11	0.2
	BSHA-07-2-82	Dacitic intrusion contact	<0.4	3.7	<17	125500	8270	52
	BSHA-07-2-83	Dacitic intrusion contact	<0.2	<0.4	<11	1650	36	7.5
	BSHA-07-3-86	Dacitic intrusion contact	<0.2	2.7	13	1810	39	30
	BSHA-07-3-88	Dacitic intrusion contact	<0.2	7.9	<12	2020	45	41
	BSHA-07-3-90	Dacitic intrusion contact	<0.3	5.8	<13	2780	44	50
	BSHA-07-3-91	Dacitic intrusion contact	<0.3	6.4	<13	400	12	18
	19-MSHA14b	Dacitic intrusion contact	NA	700	17	3.4	10	NA
	09-MSHA14b	Dacitic intrusion contact	NA	440	18	3.6	11	NA
	40-MSHA14a	Dacitic intrusion contact	NA	170	28	6.6	13	NA
	10-MSHA14b	Dacitic intrusion contact	NA	370	21	10	12	NA
	08-MSHA14b	Dacitic intrusion contact	NA	120	17	8.8	9.9	NA
	43-MSHA14a	Dacitic intrusion contact	NA	130	19	6.9	9.4	NA
	35-MSHA14a	Dacitic intrusion contact	NA	370	17	11	8.3	NA
	21-MSHA14a	Dacitic intrusion contact	NA	6.6	20	150	9.7	NA
	34-MSHA14b	Dacitic intrusion contact	NA	340	1130	11	10	NA

^{74}Ge	^{75}As	^{77}Se	^{95}Mo	^{107}Ag	^{115}In	^{121}Sb	^{130}Te	^{197}Au	^{208}Pb	^{209}Bi
<0.8	8710	<3.7	0.3	<0.5	<0.1	8.7	7.7	2.0	14	6.9
<1.0	9450	15	<0.3	0.5	<0.09	11	<2.5	12	3.6	4.3
<0.9	4580	7.0	<0.5	0.5	<0.1	9.2	4.5	2.9	13	3.7
<0.9	5720	19	<0.3	1.1	<0.1	16	<2.2	9.3	26	0.8
<0.9	9330	<5.1	<0.5	<0.6	<0.1	0.4	<2.6	0.2	1.1	0.07
<1.0	7500	<4.1	<0.4	<0.5	0.1	45	<2.5	0.4	24	1.8
<1.0	15770	3.5	<0.3	1.1	<0.1	33	5.0	3.8	45	1.8
<1.0	9920	<5.4	<0.4	2.7	<0.1	43	7.0	8.8	33	3.3
<0.9	28720	7.2	<0.5	3.3	<0.1	76	8.6	5.1	120	2.7
<0.9	38990	13	<0.5	4.1	0.1	120	11	7.7	180	3.2
<1.3	7360	7.1	<0.4	1.1	<0.1	25	3.7	7.4	9.4	1.5
<0.5	12940	<16	<0.03	0.4	0.1	6.8	2.5	1.9	3.0	0.9
<0.8	14840	<23	<0.05	1.0	0.1	19	2.4	7.0	7.2	0.8
<0.4	3510	<11	<0.02	0.2	0.03	3.3	1.5	0.4	1.2	0.4
<1.9	34990	13	<1.2	73	0.4	530	6.8	11	110	24
NA	3650	NA	NA	1.4	NA	4.8	5.7	1.5	7.4	2.6
NA	8320	NA	NA	12	NA	37	6.1	2.6	59	10
NA	8120	NA	NA	21	NA	31	4.8	2.9	51	11
NA	5820	NA	NA	2.5	NA	24	8.8	3.7	44	8.4
NA	7980	NA	NA	1.0	NA	7.4	3.3	4.3	22	5.3
NA	4030	NA	NA	8.8	NA	100	7.7	4.4	16210	120
NA	12030	NA	NA	0.9	NA	5.2	3.1	4.8	6.7	2.2
NA	2410	NA	NA	20	NA	41	7.8	5.4	140	4.1
NA	7710	NA	NA	7.0	NA	26	4.2	5.5	78	4.5
NA	11280	NA	NA	2.1	NA	3.6	7.7	6.9	5.8	1.6
NA	7150	NA	NA	1.1	NA	2.6	4.4	7.3	8.7	1.2
NA	3810	NA	NA	10	NA	14	6.4	8.6	7.9	3.5
NA	5680	NA	NA	3.1	NA	10	3.1	9.3	25	4.9
NA	7150	NA	NA	2.8	NA	29	3.3	10.0	53	5.7
NA	7440	NA	NA	3.5	NA	13	9.5	10	45	7.0
NA	7620	NA	NA	13	NA	40	7.2	12	22	6.7
NA	6870	NA	NA	2.2	NA	20	3.2	12	36	6.7
NA	10050	NA	NA	1.4	NA	12	3.1	13	14	7.1
NA	10210	NA	NA	3.0	NA	28	5.0	14	78	9.9
NA	11440	NA	NA	1.5	NA	14	3.1	15	19	6.1
NA	10720	NA	NA	1.2	NA	14	3.2	16	15	5.5
NA	10010	NA	NA	1.4	NA	22	3.9	19	56	2.4
NA	8340	NA	NA	2.4	NA	16	4.9	22	21	8.2
NA	3	NA	NA	1.9	NA	0.6	7.1	34	0.7	0.1
NA	13820	NA	NA	15	NA	57	7.1	49	190	17
<0.7	10780	<10	<0.2	12	0.3	200	<1.9	5.4	150	7.7
<0.2	39570	<2.3	0.09	32	0.4	630	<0.5	5.5	1060	110
<0.2	20790	<2.9	<0.06	15	0.2	560	<0.7	2.8	800	26
<0.3	75280	<4.5	0.07	31	0.8	320	<1.0	16	1400	360
6.0	2530	18	<0.1	5.3	0.0	30	<0.7	0.4	120	8.5
2.6	3120	8.1	<0.1	17	0.2	180	<0.8	0.7	200	22
<0.6	2300	<7.6	<0.2	4.4	<0.06	46	<1.9	0.3	30	3.8
<1.1	19560	19	<0.3	<0.5	<0.1	1.1	<2.9	18	0.5	4.8
<0.9	24630	27	<0.4	<0.5	<0.09	1.6	2.2	110	1.1	7.1
6.2	3810	13	<0.3	0.7	1.0	1.9	3.5	6.8	2.2	5.3
10	16530	13	<0.6	1.3	1.6	6.2	3.8	33	6.2	12
19	990	13	<0.5	1.5	4.5	4.4	2.2	2.2	4.1	12
38	480	13	<0.3	11	9.2	25	<2.0	1.5	12	29
40	17390	4.1	<0.4	15	15	36	<2.1	30	30	22
<0.9	11790	4.6	<0.6	2.3	<0.09	2.6	<2.5	11	5.8	9.0
<0.7	14700	17	<0.4	<0.4	<0.09	<0.2	<2.3	12	<0.1	0.2
4.3	14300	12	<0.6	12	2.8	6.1	3.6	20	3.2	12
4.1	9380	12	<0.7	2.0	1.4	3.0	<3.3	8.6	0.8	3.7
0.8	9950	<10	<0.09	0.7	0.10	110	5.7	0.8	60	9.4
<0.2	3010	10	0.3	1.3	0.04	53	11	1.5	11	15
24	3580	7.0	<0.7	1030	13	48740	6.4	6.5	330	150
6.4	18390	<4.6	<0.4	7.3	1.5	11	<2.6	14	88	18
18	27140	15	<0.6	18	7.1	51	16	43	120	99
10	4350	12	0.3	22	10.0	31	<2.8	18	120	67
25	94270	23	<0.5	21	8.2	480	67	81	33	280
6.6	23410	4.2	<0.6	5.8	1.7	126	5.8	10	51	50
NA	650	NA	NA	1.6	NA	1.0	5.7	0.09	0.7	3.8
NA	1370	NA	NA	1.8	NA	3.4	6.6	0.1	1.9	8.3
NA	1070	NA	NA	2.3	NA	3.5	7.7	0.2	1.9	9.3
NA	900	NA	NA	2.8	NA	3.5	100	0.2	39	130
NA	1130	NA	NA	1.8	NA	5.8	13	0.2	3.9	17
NA	1920	NA	NA	1.4	NA	2.7	4.9	0.2	1.3	6.0
NA	2380	NA	NA	1.3	NA	3.0	4.6	0.2	52	7.6
NA	11420	NA	NA	1.5	NA	3.2	6.4	0.3	21	5.1
NA	3050	NA	NA	2.8	NA	6.5	12	0.4	410	20

Mineral	Sample	Host rock/structure	^{51}V	^{59}Co	^{60}Ni	^{63}Cu	^{66}Zn	^{71}Ga
	08-MSHA14a	Dacitic intrusion contact	NA	370	20	22	10	NA
	09-MSHA14a	Dacitic intrusion contact	NA	15	9.2	130.00	12	NA
	13-MSHA14b	Dacitic intrusion contact	NA	43	8.0	48	5.6	NA
	18-MSHA14a	Dacitic intrusion contact	NA	15	22	250	11	NA
	15-MSHA14a	Dacitic intrusion contact	NA	0.8	26	120	13	NA
	28-MSHA14b	Dacitic intrusion contact	NA	74	29	64	11	NA
	41-MSHA14a	Dacitic intrusion contact	NA	0.6	18	950	270	NA
	39-MSHA14a	Dacitic intrusion contact	NA	0.9	26	105	12	NA
	10-MSHA14a	Dacitic intrusion contact	NA	32	20	61	9.9	NA
	45-MSHA14a	Dacitic intrusion contact	NA	12	18	43	9.0	NA
	70-MSHA14a	Dacitic intrusion contact	NA	0.81	27	130	10.3	NA
	47-MSHA14a	Dacitic intrusion contact	NA	14	21	48	10.4	NA
	43-MSHA14b	Dacitic intrusion contact	NA	160	6.9	50	6.7	NA
	37-MSHA14a	Dacitic intrusion contact	NA	7.6	31	93	15.1	NA
	45-MSHA14b	Dacitic intrusion contact	NA	220	11	86	10.2	NA
	30-MSHA14b	Dacitic intrusion contact	NA	33	38	130	11.1	NA
	10-MSHA14b	Dacitic intrusion contact	NA	15.54	6.2	180	4.8	NA
	11-MSHA14b	Dacitic intrusion contact	NA	7.0	4.0	190	4.8	NA
	05-MSHA14b	Dacitic intrusion contact	NA	390	3480	980	9.8	NA
	06-MSHA14b	Dacitic intrusion contact	NA	130	3520	2390	37	NA
	07-MSHA14b	Dacitic intrusion contact	NA	11	120	11	10	NA
	11-MSHA14b	Dacitic intrusion contact	NA	240	7020	7.8	12	NA
	15-MSHA14b	Dacitic intrusion contact	NA	180	130	710	11	NA
	16-MSHA14b	Dacitic intrusion contact	NA	550	610	10	10	NA
	17-MSHA14b	Dacitic intrusion contact	NA	2070	3190	2880	45	NA
	18-MSHA14b	Dacitic intrusion contact	NA	28	860	5.4	9.0	NA
	36-MSHA14a	Dacitic intrusion contact	NA	280	92	5.6	7.4	NA
	38-MSHA14a	Dacitic intrusion contact	NA	430	490	170	12	NA
	42-MSHA14a	Dacitic intrusion contact	NA	2.9	69	120	33	NA
	44-MSHA14a	Dacitic intrusion contact	NA	330	460	27	10	NA
	46-MSHA14a	Dacitic intrusion contact	NA	500	3490	1470	16	NA
	09-MSHA14a	Dacitic intrusion contact	NA	140	320	310	10	NA
	11-MSHA14a	Dacitic intrusion contact	NA	60	62	1400	10	NA
	12-MSHA14a	Dacitic intrusion contact	NA	26	120	118	9.3	NA
	13-MSHA14a	Dacitic intrusion contact	NA	1570	1360	14	9.0	NA
	14-MSHA14a	Dacitic intrusion contact	NA	59	39	49	9.7	NA
	16-MSHA14a	Dacitic intrusion contact	NA	1.7	24	6.3	12	NA
	17-MSHA14a	Dacitic intrusion contact	NA	360	670	220	10	NA
	19-MSHA14a	Dacitic intrusion contact	NA	43	1590	300	11	NA
	20-MSHA14a	Dacitic intrusion contact	NA	64	1180	140	12	NA
	25-MSHA14b	Dacitic intrusion contact	NA	19	1390	8.2	13	NA
	26-MSHA14b	Dacitic intrusion contact	NA	150	1150	30	11	NA
	27-MSHA14b	Dacitic intrusion contact	NA	110	37	14	11	NA
	29-MSHA14b	Dacitic intrusion contact	NA	700	1480	7.6	9.5	NA
	31-MSHA14b	Dacitic intrusion contact	NA	120	22	61	9.5	NA
	32-MSHA14b	Dacitic intrusion contact	NA	740	1190	6.0	9.8	NA
	33-MSHA14b	Dacitic intrusion contact	NA	44	1780	810	16	NA
	35-MSHA14b	Dacitic intrusion contact	NA	200	17	15	7.5	NA
	71-MSHA14a	Dacitic intrusion contact	NA	820	21	9605	8.2	NA
	44-MSHA14b	Dacitic intrusion contact	NA	890	660	630	12	NA
	BSHA-16-2-8	Andesitic intrusion	0.3	<0.2	<4.4	1130	440	3.2
	BSHA-16-2-11	Andesitic intrusion	<0.2	<0.3	<7.0	25	<2.2	<0.3
	BSHA-16-3-14	Andesitic intrusion	0.3	<0.3	<6.3	18	<2.1	<0.2
	BSHA-16-3-15	Andesitic intrusion	0.5	<0.3	<6.0	88	4.7	<0.2
	MIN		0.09	0.2	1.2	2.1	1.1	0.06
	MAX		12	2070	7020	125500	8270	66
	MEAN		0.4	11	30	170	10	1.4
Mineral	Sample	Host rock/structure	^{51}V	^{59}Co	^{60}Ni	^{63}Cu	^{66}Zn	^{71}Ga
pyIV	BSHA-16-1-4	Andesitic intrusion	0.1	<0.1	<3.6	21	1.6	<0.1
	BSHA-16-1-5	Andesitic intrusion	<0.1	<0.2	<4.1	21	<1.5	<0.2
	BSHA-16-1-6	Andesitic intrusion	<0.1	<0.2	<4.5	5.1	<1.6	<0.2
	BSHA-16-1-7	Andesitic intrusion	<0.1	<0.2	<4.6	8.1	<1.6	<0.2
	BSHA-16-2-9	Andesitic intrusion	0.2	<0.2	<4.3	4.0	1.5	<0.2
	BSHA-16-2-10	Andesitic intrusion	6.4	<0.2	<5.8	8.1	12	2.8
	BSHA-16-3-12	Andesitic intrusion	5.2	<0.3	<7.2	11	11	2.3
	BSHA-16-3-13	Andesitic intrusion	0.7	<0.2	<6.0	11	4.3	<0.3
	MIN		0.1	0.1	3.6	4.0	1.5	0.2
	MAX		6.4	0.3	7.2	21	12	2.8
	MEAN		0.4	0.2	4.9	9.5	2.9	0.4

^{74}Ge	^{75}As	^{77}Se	^{95}Mo	^{107}Ag	^{115}In	^{121}Sb	^{130}Te	^{197}Au	^{208}Pb	^{209}Bi
NA	3890	NA	NA	1.4	NA	1.4	5.8	0.5	7.8	4.9
NA	24240	NA	NA	2.1	NA	6.9	7.8	0.5	36	11
NA	13680	NA	NA	1.0	NA	0.3	3.7	0.6	2.2	1.3
NA	15120	NA	NA	1.7	NA	30	8.9	0.6	260	12
NA	22320	NA	NA	1.9	NA	5.7	7.7	0.8	22	21
NA	9470	NA	NA	1.8	NA	2.3	6.3	0.8	18	5.4
NA	7660	NA	NA	6.3	NA	15	4.8	0.9	110	11
NA	27740	NA	NA	2.0	NA	6.7	7.0	0.9	41	9.7
NA	12140	NA	NA	1.5	NA	0.9	6.0	1.0	8.6	1.9
NA	8310	NA	NA	1.4	NA	3.2	4.8	1.0	22	2.9
NA	17330	NA	NA	1.5	NA	5.1	6.4	1.0	9.4	7.2
NA	6710	NA	NA	1.6	NA	3.4	5.6	1.2	6.8	5.1
NA	10810	NA	NA	1.0	NA	3.2	3.6	1.2	56	17
NA	20960	NA	NA	2.5	NA	4.3	8.3	1.2	42	13
NA	13770	NA	NA	1.6	NA	2.2	5.5	1.4	130	24
NA	16250	NA	NA	2.4	NA	170	6.6	2.5	2080	100
NA	24760	NA	NA	1.5	NA	4.1	3.9	2.6	39	4.0
NA	26070	NA	NA	2.8	NA	18	5.1	2.7	220	10
NA	7120	NA	NA	1.7	NA	12	50	0.3	5.9	36
NA	7910	NA	NA	6.3	NA	47	34	0.4	24	40
NA	2840	NA	NA	1.8	NA	17	13	0.2	6.3	21
NA	12660	NA	NA	2.1	NA	4.2	7.5	0.1	2.5	4.8
NA	9860	NA	NA	3.1	NA	25	39	1.4	12	42
NA	3330	NA	NA	1.6	NA	5.3	25	0.6	2.1	17
NA	7880	NA	NA	7.0	NA	34	11	0.5	19	26
NA	3730	NA	NA	1.5	NA	7.1	5.1	0.1	3.1	7.1
NA	590	NA	NA	1.2	NA	2.8	18	0.1	1.2	9.0
NA	8010	NA	NA	2.9	NA	16	56	4.2	35	46
NA	21870	NA	NA	5.3	NA	5.1	19	1.0	65	30
NA	5820	NA	NA	5.9	NA	23	14	0.4	64	19
NA	6780	NA	NA	4.0	NA	21	13	0.2	59	17
NA	8870	NA	NA	4.8	NA	32	59	1.7	19	55
NA	12010	NA	NA	5.7	NA	11	34	3.1	20	36
NA	21190	NA	NA	4.6	NA	16	42	5.8	14	56
NA	4550	NA	NA	1.4	NA	29	8.7	0.1	13	20
NA	14220	NA	NA	1.5	NA	13	10	2.7	9.2	7.6
NA	180	NA	NA	1.8	NA	0.7	7.2	0.1	0.7	0.2
NA	15080	NA	NA	12	NA	40	100	4.9	240	120
NA	4790	NA	NA	2.5	NA	25	27	0.6	21	47
NA	4900	NA	NA	2.0	NA	24	66	0.5	43	98
NA	16940	NA	NA	2.1	NA	7.2	9.0	0.4	4.5	6.3
NA	2920	NA	NA	1.8	NA	32	12	0.2	16	41
NA	8600	NA	NA	1.7	NA	4.0	12	1.1	2.5	2.4
NA	3590	NA	NA	1.4	NA	9.4	6	0.1	400	11
NA	7030	NA	NA	1.6	NA	3.5	6	0.4	16	6.5
NA	4040	NA	NA	1.6	NA	15	9	0.1	6.4	13
NA	5040	NA	NA	1.7	NA	21	7	0.9	18	18
NA	2440	NA	NA	1.4	NA	4.3	5	0.2	13	8.8
NA	1090	NA	NA	250	NA	580	620	14	150	1380
NA	7830	NA	NA	5.0	NA	27	72	3.0	28	57
0.9	22220	97	<0.1	14	1.1	53	54	0.1	570	0.8
2.8	16610	290.00	<0.3	1.5	<0.07	15	24	0.2	73	0.3
2.0	8870	180.00	<0.3	17	<0.07	10	30	0.1	200	4.2
<0.8	200	27	<0.4	24	<0.06	8.4	13	0.1	460	8.1
0.2	3	2.3	0.02	0.2	0.03	0.2	0.5	0.09	0.10	0.07
40	94270	290.00	1.3	1030	15	48740	620	110.00	16210	1380
1.9	6950	11	0.3	2.9	0.3	14	6.8	1.9	23	8.92

^{74}Ge	^{75}As	^{77}Se	^{95}Mo	^{107}Ag	^{115}In	^{121}Sb	^{130}Te	^{197}Au	^{208}Pb	^{209}Bi
1.4	18870	200	<0.1	3.2	0.05	18	7.5	0.1	100	<0.03
1.2	10180	170	<0.1	1.8	0.04	0.6	9.6	0.2	8.1	0.02
1.3	4230	130	<0.2	0.6	<0.04	3.4	18	0.2	39	0.03
0.7	13700	44	<0.2	0.6	<0.04	0.7	<1.7	1.2	0.6	0.05
1.8	2970	170	<0.1	1.1	<0.04	9.7	17	0.1	39	0.08
<0.7	6930	17	<0.3	<0.4	<0.07	0.4	<2.0	0.3	8.4	0.04
<0.8	14560	32	<0.2	0.5	<0.06	1.0	<2.3	2.6	4.3	0.4
0.8	5810	100	<0.3	0.9	<0.06	26	13	0.5	19	2.6
0.7	2970	17	0.1	0.4	0.04	0.4	1.7	0.1	0.6	0.02
1.8	18870	200	0.3	3.2	0.07	26	18	2.6	100	2.6
1.0	8140	80	0.2	0.9	0.05	2.7	6.2	0.4	12	0.09

Table A4. Pearson correlation coefficients among all elements of interest analyzed in pyrite and arsenopyrite samples arranged according to their host lithology.

pyI (sedimentary rocks)

	V	Co	Ni	Cu	Zn	Ga	Ge	As	Se	Mo	Ag	In	Sb	Te	Au	Pb	Bi
V																	
Co	-0.86																
Ni	0.89	0.45															
Cu	0.54	0.36	0.35														
Zn	0.58	0.22	0.25	0.29													
Ga	1.00	-0.85	0.88	0.56	0.60												
Ge	-0.83	0.43	-0.49	-0.92	-0.93	-0.85											
As	0.98	-0.10	-0.03	0.12	-0.06	0.99	-0.92										
Se	-0.92	0.59	-0.64	-0.83	-0.85	-0.93	0.98	-0.98									
Mo	0.66	-0.95	0.93	-0.27	-0.22	0.64	-0.14	0.52	-0.32								
Ag	0.49	-0.17	0.54	-0.11	-0.07	0.52	-0.89	-0.31	-0.80	-0.32							
In	0.52	-0.01	0.08	1.00	1.00	0.54	-0.91	0.67	-0.81	-0.29	1.00						
Sb	0.79	-0.07	0.09	0.21	0.63	0.81	-1.00	-0.03	-0.97	0.07	0.56	0.93					
Te	0.44	0.00	0.76	0.06	0.05	0.41	0.13	0.05	-0.36	0.96	0.61	-0.54	0.12				
Au	-0.92	0.22	0.56	0.43	0.43	-0.93	0.98	0.00	1.00	-0.33	0.40	-0.81	0.47	0.86			
Pb	1.00	-0.01	0.13	0.27	0.92	0.99	-0.79	-0.05	-0.89	0.72	0.85	0.46	0.76	0.33	0.51		
Bi	0.84	0.26	0.47	0.42	0.75	0.86	-1.00	-0.07	-0.99	0.16	-0.08	0.90	0.47	0.08	0.47	0.69	

Upper half: all pyII - Lower half : pyII from dacitic intrusion contact

	V	Co	Ni	Cu	Zn	Ga	Ge	As	Se	Mo	Ag	In	Sb	Te	Au	Pb	Bi
V		0.30	0.28	0.11	-0.14	0.62	0.13	-0.01	0.18	0.03	0.04	0.09	0.07	0.31	0.03	0.24	0.07
Co	-0.60		0.07	-0.04	0.03	-0.06	0.12	-0.02	-0.04	0.08	-0.09	0.05	-0.08	0.19	-0.07	-0.09	-0.07
Ni	-0.64	-0.14		-0.04	0.30	-0.11	0.09	-0.11	-0.29	0.01	-0.14	-0.04	0.06	0.08	-0.03	-0.07	-0.13
Cu	0.22	-0.59	-0.08		0.14	0.15	0.18	0.01	-0.09	0.13	0.06	0.28	-0.08	0.45	0.10	-0.09	-0.05
Zn	-0.53	0.07	0.86	-0.56		-0.07	-0.18	0.05	-0.04	-0.09	-0.02	-0.10	0.06	0.15	0.10	-0.04	0.00
Ga	0.95	-0.54	-0.60	0.17	-0.47		0.17	0.14	0.39	0.16	0.06	0.09	0.03	0.12	0.22	0.15	0.29
Ge	1.00	-0.60	-0.66	0.27	-0.57	0.95		0.37	-0.13	0.91	0.00	0.84	-0.05	0.86	0.62	0.23	-0.08
As	-0.81	0.13	0.96	-0.23	0.87	-0.75	-0.82		0.00	0.51	0.02	0.64	0.10	0.31	0.75		0.37
Se	-0.80	0.95	0.14	-0.56	0.28	-0.75	-0.81	0.40		-0.22	-0.10	-0.24	-0.10	-0.16	0.04	-0.19	-0.02
Mo	0.75	-0.47	-0.48	0.30	-0.47	0.90	0.77	-0.61	-0.65		-0.06	0.90	-0.10	0.76	0.75	0.18	0.01
Ag	-0.04	-0.46	0.10	0.96	-0.42	-0.10	0.00	-0.01	-0.36	0.09		0.17	0.77	-0.03	-0.03	0.78	0.28
In	0.98	-0.61	-0.63	0.26	-0.55	0.87	0.97	-0.80	-0.80	0.61	0.01		0.10	0.71	0.79	0.36	0.12
Sb	-0.83	0.47	0.77	-0.60	0.89	-0.77	-0.86	0.90	0.68	-0.70	-0.39	-0.83		-0.22	0.00	0.45	0.40
Te	0.87	-0.82	-0.44	0.66	-0.60	0.79	0.89	-0.66	-0.93	0.68	0.44	0.88	-0.89		0.43	0.05	-0.16
Au	0.81	-0.52	-0.47	0.25	-0.42	0.95	0.83	-0.62	-0.71	0.99	0.02	0.68	-0.69	0.72		-0.07	0.34
Pb	0.04	-0.28	0.28	-0.11	0.32	-0.23	0.00	0.20	-0.17	-0.58	-0.09	0.21	0.18	0.07	-0.48		0.03
Bi	-0.93	0.43	0.83	-0.37	0.80	-0.87	-0.95	0.95	0.67	-0.72	-0.12	-0.93	0.96	-0.86	-0.75	0.10	

Upper half: pyII from sedimentary rocks - Lower Half: pyII from NW-SE fault

	V	Co	Ni	Cu	Zn	Ga	Ge	As	Se	Mo	Ag	In	Sb	Te	Au	Pb	Bi
V		0.43	0.35	0.28	0.19	0.58	-0.04	-0.11	0.13	-0.11	0.20	-0.02	0.37	0.23	-0.07	0.24	0.16
Co	0.02		0.08	-0.05	0.06	-0.05	0.25	-0.03	-0.26	0.14	-0.09	0.11	-0.09	0.18	-0.08	-0.10	-0.07
Ni	0.30	0.27		-0.05	-0.12	-0.11	0.14	-0.09	-0.43	0.00	-0.07	-0.01	0.25	0.08	-0.01	-0.04	-0.12
Cu	-0.05	0.35	-0.23		0.34	0.29	0.63	0.00	-0.34	0.60	0.10	0.55	-0.04	0.46	0.08	-0.11	-0.01
Zn	-0.12	0.82	-0.22	0.57		0.63	0.64	0.24	0.19	0.64	0.18	0.60	-0.03	0.56	0.33	0.04	-0.02
Ga	0.81	0.10	0.20	0.10	0.16		0.06	0.07	0.41	0.08	0.14	0.00	0.15	0.04	0.15	0.13	0.46
Ge	-0.39	-0.03	0.21	0.55	0.02	-0.32		0.58	-0.46	0.94	0.31	0.90	0.34	0.82	0.69	0.28	0.20
As	0.40	0.27	-0.39	0.37	0.63	0.59	-0.18		-0.03	0.71	-0.22	0.71	-0.08	0.41	0.75	-0.21	0.34
Se	-0.35	-0.15	0.32	0.34	-0.10	-0.23	0.96	-0.19		-0.39	-0.29	-0.37	-0.34	-0.43	-0.01	-0.27	0.11
Mo	-0.24	0.49	-0.14	0.89	0.68	0.10	0.45	0.23	0.27		0.24	0.94	0.27	0.73	0.80	0.22	0.28
Ag	0.02	0.35	-0.24	0.99	0.60	0.20	0.51	0.46	0.31	0.88		0.36	0.66	0.13	-0.11	0.93	-0.09
In	0.07	0.63	-0.32	0.59	0.94	0.39	-0.01	0.85	-0.10	0.62	0.65		0.39	0.73	0.78	0.36	0.13
Sb	0.06	0.20	-0.14	0.96	0.42	0.25	0.56	0.31	0.38	0.87	0.96	0.48		0.10	0.45	0.83	0.06
Te	-0.45	-0.16	0.25	0.35	-0.11	-0.36	0.97	-0.25	0.99	0.28	0.31	-0.13	0.37		0.45	0.01	0.15
Au	0.25	0.26	-0.47	0.34	0.68	0.58	-0.23	0.96	-0.23	0.32	0.44	0.88	0.31	-0.28		-0.12	0.49
Pb	-0.14	0.69	-0.12	0.87	0.81	0.11	0.31	0.32	0.10	0.95	0.86	0.71	0.80	0.11	0.37		-0.09
Bi	0.04	0.94	0.03	0.39	0.94	0.26	-0.14	0.54	-0.23	0.54	0.42	0.84	0.25	-0.26	0.57	0.72	

Upper half: all pyIII - Lower half : pyIII for Andesitic intrusion

	V	Co	Ni	Cu	Zn	Ga	Ge	As	Se	Mo	Ag	In	Sb	Te	Au	Pb	Bi
V		0.01	-0.13	-0.04	0.00	-0.12	-0.15	-0.07	-0.08	-0.07	-0.03	-0.14	-0.03	-0.05	-0.13	-0.07	-0.08
Co	-0.32		0.42	-0.08	-0.04	-0.13	-0.21	-0.19	-0.23	-0.06	0.01	-0.13	-0.04	0.28	-0.16	-0.04	0.21
Ni	-0.30	1.00		-0.06	-0.03	-0.15	-0.14	-0.09	-0.16	0.10	-0.04	-0.12	-0.03	0.03	-0.15	-0.04	-0.02
Cu	0.02	-0.93	-0.95		0.76	0.37	0.31	-0.09	-0.06	0.28	0.75	0.49	0.76	-0.04	0.04	0.25	0.06
Zn	-0.03	-0.92	-0.94	1.00		0.37	0.31	-0.05	-0.04	0.24	0.97	0.48	1.00	-0.02	0.00	0.01	0.08
Ga	-0.05	-0.91	-0.93	1.00	1.00		0.84	0.08	-0.12	0.13	0.37	0.85	0.36	0.15	0.25	-0.09	0.33
Ge	-0.86	0.75	0.74	-0.53	-0.49	-0.46		0.09	-0.08	0.23	0.30	0.91	0.29	0.15	0.27	-0.14	0.28
As	-0.72	-0.40	-0.42	0.68	0.71	0.73	0.27		-0.01	0.12	-0.03	0.10	-0.04	-0.03	0.46	0.01	0.16
Se	-0.94	0.62	0.61	-0.36	-0.31	-0.29	0.98	0.44		-0.10	-0.05	-0.11	-0.05	0.46	-0.08	0.01	-0.11
Mo	0.21	0.72	0.69	-0.68	-0.71	-0.71	0.19	-0.57	0.08		0.27	0.25	0.25	0.05	0.24	-0.30	0.01
Ag	0.93	-0.36	-0.32	0.00	-0.03	-0.06	-0.80	-0.70	-0.89	-0.06		0.48	0.97	0.20	0.02	0.01	0.30
In	-0.04	-0.92	-0.93	1.00	1.00	1.00	-0.47	0.72	-0.30	-0.72	-0.04		0.47	0.15	0.28	-0.04	0.37
Sb	-0.14	-0.86	-0.88	0.99	0.99	1.00	-0.38	0.79	-0.20	-0.70	-0.16	0.99		-0.01	0.00	0.01	0.09
Te	-0.34	-0.78	-0.79	0.89	0.91	0.92	-0.17	0.84	0.00	-0.88	-0.22	0.92	0.93		0.04	-0.01	0.93
Au	-0.86	0.72	0.70	-0.44	-0.40	-0.38	0.96	0.35	0.97	0.31	-0.90	-0.39	-0.29	-0.17		-0.02	0.14
Pb	0.69	-0.89	-0.89	0.74	0.71	0.69	-0.96	0.01	-0.89	-0.36	0.63	0.70	0.62	0.42	-0.90		0.09
Bi	0.88	0.10	0.13	-0.43	-0.47	-0.49	-0.54	-0.95	-0.69	0.40	0.88	-0.48	-0.57	-0.66	-0.61	0.29	

Upper half: pyIII from sedimentary rocks - Lower Half: pyIII from NW-SE fault

	V	Co	Ni	Cu	Zn	Ga	Ge	As	Se	Mo	Ag	In	Sb	Te	Au	Pb	Bi
V		0.31	-0.32	-0.09	0.54	0.43	0.60	0.07	0.00	0.48	0.53	0.53	0.47	0.19	0.38	0.01	0.64
Co	-0.30		0.07	0.14	0.21	-0.22	0.17	0.01	-0.51	0.41	0.26	0.23	0.22	0.19	-0.20	0.11	0.16
Ni	-0.25	0.94		0.06	0.02	-0.23	0.18	0.25	-0.52	0.17	0.04	-0.01	0.12	0.44	-0.09	0.04	0.02
Cu	0.85	-0.59	-0.57		0.08	-0.12	0.23	-0.19	0.00	0.38	0.33	0.24	0.05	0.29	0.00	0.39	0.43
Zn	0.71	-0.48	-0.37	0.83		0.13	0.78	0.42	0.11	0.81	0.90	0.94	0.93	0.23	0.06	0.23	0.39
Ga	0.01	-0.42	-0.19	-0.10	-0.13		0.43	-0.03	0.14	0.15	0.12	0.28	0.10	-0.12	0.28	-0.11	0.06
Ge	-0.01	-0.45	-0.22	-0.08	-0.11	1.00		0.45	-0.09	0.89	0.78	0.86	0.79	0.30	0.61	0.37	0.77
As	-0.24	0.23	0.07	-0.33	-0.08	-0.45	-0.48		0.15	0.58	0.43	0.56	0.65	0.31	0.02	-0.12	-0.04
Se	0.03	-0.62	-0.36	0.15	0.19	0.86	0.89	-0.56		-0.21	0.11	0.10	0.09	-0.30	0.46	0.01	0.00
Mo	0.19	-0.59	-0.58	0.65	0.53	-0.12	-0.06	-0.50	0.35		0.83	0.85	0.86	0.47	0.40	0.56	0.82
Ag	0.01	0.16	-0.03	-0.16	-0.05	-0.43	-0.49	0.85	-0.68	-0.54		0.95	0.91	0.27	0.11	0.05	0.24
In	0.01	0.08	-0.05	-0.05	0.23	-0.52	-0.54	0.95	-0.53	-0.32	0.84		0.93	0.27	0.46	0.37	0.90
Sb	-0.20	0.67	0.54	-0.42	-0.25	-0.55	-0.60	0.53	-0.80	-0.59	0.71	0.46		0.28	0.05	0.13	0.29
Te	0.13	-0.36	-0.39	0.56	0.52	-0.35	-0.28	-0.24	0.15	0.90	-0.46	-0.07	-0.53		0.13	0.19	0.25
Au	-0.07	0.05	-0.06	-0.10	0.21	-0.43	-0.44	0.95	-0.41	-0.29	0.74	0.98	0.34	-0.01		-0.08	0.01
Pb	-0.29	0.46	0.30	-0.49	-0.25	-0.46	-0.50	0.94	-0.69	-0.69	0.89	0.85	0.75	-0.46	0.81		0.97
Bi	-0.15	0.07	-0.08	-0.24	-0.05	-0.31	-0.33	0.96	-0.41	-0.45	0.77	0.92	0.30	-0.17	0.95	0.84	

Upper half: pyIII from Dacitic intrusion contact - Lower Half: pyIII from Dacitic intrusion

	V	Co	Ni	Cu	Zn	Ga	Ge	As	Se	Mo	Ag	In	Sb	Te	Au	Pb	Bi
V		-0.45	-0.72	-0.15	-0.10	-0.43	-0.46	-0.19	-0.02	-0.67	-0.15	-0.43	-0.14	-0.17	-0.33	-0.18	-0.35
Co	0.87		0.35	-0.07	-0.08	0.19	-0.02	-0.26	0.19	0.10	-0.03	0.15	-0.07	0.23	-0.12	-0.05	0.18
Ni	0.86	0.96		-0.05	-0.06	0.16	0.19	-0.11	-0.02	0.42	-0.07	0.21	-0.06	-0.03	-0.13	-0.07	-0.07
Cu	0.49	0.37	0.46		1.00	0.53	0.54	-0.05	-0.24	0.58	0.97	0.64	1.00	-0.03	0.06	0.11	0.08
Zn	-0.32	-0.43	-0.37	0.02		0.51	0.51	-0.07	-0.25	0.55	0.97	0.62	1.00	-0.04	0.03	0.12	0.07
Ga	-0.30	-0.42	-0.36	0.00	0.99		0.92	0.42	0.47	0.68	0.53	0.95	0.52	0.46	0.57	0.59	0.84
Ge	-0.34	-0.54	-0.45	-0.05	0.93	0.96		0.56	0.51	0.77	0.54	0.86	0.52	0.58	0.69	0.55	0.90
As	0.09	0.37	0.30	0.04	-0.14	-0.23	-0.38		0.76	0.25	-0.07	0.16	-0.06	-0.04	0.78	0.05	0.06
Se	0.02	0.20	0.26	0.10	-0.51	-0.52	-0.46	0.39		-0.02	-0.23	0.33	-0.24	0.86	0.86	-0.26	0.73
Mo	0.55	0.54	0.40	0.28	-0.36	-0.29	-0.35	-0.03	-0.22		0.58	0.63	0.57	0.20	0.33	0.58	0.57
Ag	0.04	-0.16	-0.04	0.53	0.82	0.80	0.74	-0.39	-0.16			0.64	0.97	0.19	0.08	0.12	0.30
In	-0.28	-0.41	-0.34	0.08	0.99	1.00	0.95	-0.21	-0.50	-0.30	0.84		0.63	0.24	0.38	0.74	0.67
Sb	-0.25	-0.41	-0.33	0.05	0.98	0.96	0.94	-0.12	-0.49	-0.34	0.86	0.98		-0.02	0.04	0.12	0.08
Te	0.59	0.53	0.52	0.40	-0.44	-0.46	-0.46	0.05	0.06	0.43	-0.20	-0.43	-0.41		0.18	0.01	0.97
Au	-0.28	0.03	0.02	-0.06	-0.10	-0.15	-0.21	0.74	0.61	-0.07	-0.13	-0.15	-0.09	-0.13		0.02	0.30
Pb	-0.33	-0.41	-0.38	-0.02	0.96	0.93	0.85	0.00	-0.61	-0.26	0.78	0.93	0.95	-0.38	-0.04		0.09
Bi	-0.23	-0.48	-0.34	0.14	0.79	0.82	0.91	-0.32	-0.36	-0.25	0.79	0.83	0.87	-0.36	-0.11	0.74	

Upper half: arsenopyrite from NW-SE fault - Lower half: arsenopyrite from dacitic intrusion contact

	V	Co	Ni	Cu	Zn	Ga	Ge	As	Se	Mo	Ag	In	Sb	Te	Au	Pb	Bi
V		-0.36	-0.23	0.02	0.96	0.93	-0.27	0.59	0.97	0.98	-0.45	0.51	-0.22	0.99	0.63	-0.66	0.69
Co	0.22		0.74	-0.93	-0.19	-0.02	0.80	-0.42	-0.27	-0.33	-0.61	-0.39	0.84	-0.49	-0.92	0.03	-0.91
Ni	0.04	0.73		-0.64	-0.24	-0.01	0.19	-0.32	-0.33	-0.67	-0.82	0.27	-0.37	-0.75	0.47	-0.72	
Cu	-0.39	-0.37	0.08		-0.14	-0.30	-0.80	0.20	-0.08	-0.01	0.74	0.18	-0.87	0.15	0.70	0.25	0.68
Zn	-0.26	-0.58	0.11	0.49		0.97	-0.01	0.71	0.99	0.99	-0.53	0.64	0.02	0.92	0.49	-0.83	0.55
Ga	-0.32	-0.81	-0.95	0.13	0.04		0.04	0.54	0.95	0.94	-0.70	0.47	0.10	0.86	0.32	-0.74	0.40
Ge	-0.48	-0.56	-0.07	0.97	0.59	0.30		0.11	-0.06	-0.14	-0.32	0.18	0.99	-0.34	-0.65	-0.41	-0.66
As	0.19	0.59	0.96	0.03	0.29	-0.94	-0.10		0.74	0.73	0.09	0.99	0.05	0.64	0.59	-0.89	0.61
Se	0.97	0.06	-0.10	-0.22	-0.23	-0.15	-0.30	0.05		1.00	-0.44	0.68	-0.02	0.95	0.57	-0.83	0.63
Mo	-0.31	-0.68	-0.14	0.91	0.72	0.32	0.96	-0.08	-0.13		-0.42	0.66	-0.10	0.96	0.61	-0.79	0.67
Ag	-0.39	-0.34	0.10	1.00	0.46	0.11	0.97	0.05	-0.23	0.90		0.15	-0.40	-0.29	0.40	0.29	0.32
In	-0.59	-0.70	-0.37	0.86	0.47	0.59	0.94	-0.41	-0.39	0.89	0.85		0.12	0.57	0.57	-0.89	0.57
Sb	-0.36	-0.64	0.00	0.40	0.98	0.16	0.53	0.17	-0.34	0.66	0.37	0.47		-0.29	-0.65	-0.40	-0.66
Te	0.75	0.75	0.48	-0.67	-0.46	-0.71	-0.80	0.52	0.59	-0.75	-0.66	-0.94	-0.53		0.75	-0.65	0.80
Au	-0.31	0.85	0.78	-0.15	-0.30	-0.70	-0.28	0.59	-0.47	-0.47	-0.12	-0.40	-0.31	0.36		-0.33	1.00
Pb	-0.39	-0.18	0.42	0.17	0.84	-0.26	0.25	0.54	-0.48	0.31	0.15	0.12	0.86	-0.22	0.18		-0.36
Bi	-0.69	-0.61	-0.13	0.27	0.79	0.34	0.44	-0.06	-0.68	0.48	0.24	0.50	0.89	-0.68	-0.13	0.81	

pyIV (andesitic intrusion)

	V	Co	Ni	Cu	Zn	Ga	Ge	As	Se	Mo	Ag	In	Sb	Te	Au	Pb	Bi
V																	
Co	0.70																
Ni	0.75	0.98															
Cu	-0.18	-0.33	-0.32														
Zn	0.98	0.80	0.85	-0.17													
Ga	1.00	0.69	0.75	-0.18	0.98												
Ge	-0.53	-0.60	-0.62	0.03	-0.57	-0.53											
As	0.05	-0.09	-0.07	0.66	0.06	0.06	-0.25										
Se	-0.75	-0.76	-0.77	0.45	-0.76	-0.75	0.85	0.00									
Mo	0.54	0.69	0.70	-0.50	0.59	0.52	-0.70	-0.41	-0.75								
Ag	-0.46	-0.66	-0.66	0.79	-0.48	-0.47	0.50	0.52	0.79	-0.71							
In	0.85	0.72	0.75	-0.01	0.89	0.83	-0.59	0.02	-0.61	0.71	-0.28						
Sb	-0.38	-0.03	-0.08	0.17	-0.27	-0.40	0.21	-0.04	0.43	0.09	0.44	0.11					
Te	-0.61	-0.40	-0.39	-0.23	-0.59	-0.62	0.72	-0.66	0.67	-0.20	0.12	-0.48	0.40				
Au	0.48	0.72	0.73	-0.12	0.56	0.49	-0.52	0.42	-0.64	0.17	-0.44	0.27	-0.33	-0.58			
Pb	-0.40	-0.63	-0.59	0.34	-0.42	-0.40	0.62	0.29	0.72	-0.54	0.81	-0.27	0.51	0.35	-0.48		
Bi	-0.06	0.50	0.45	-0.04	0.10	-0.09	-0.29	-0.23	-0.10	0.57	-0.14	0.40	0.75	0.20	0.06	-0.15	

Annex III.

Electronic Supplementary Material of Chapter III

This file contains:

Figures A1 to A6

Tables A1 to A7
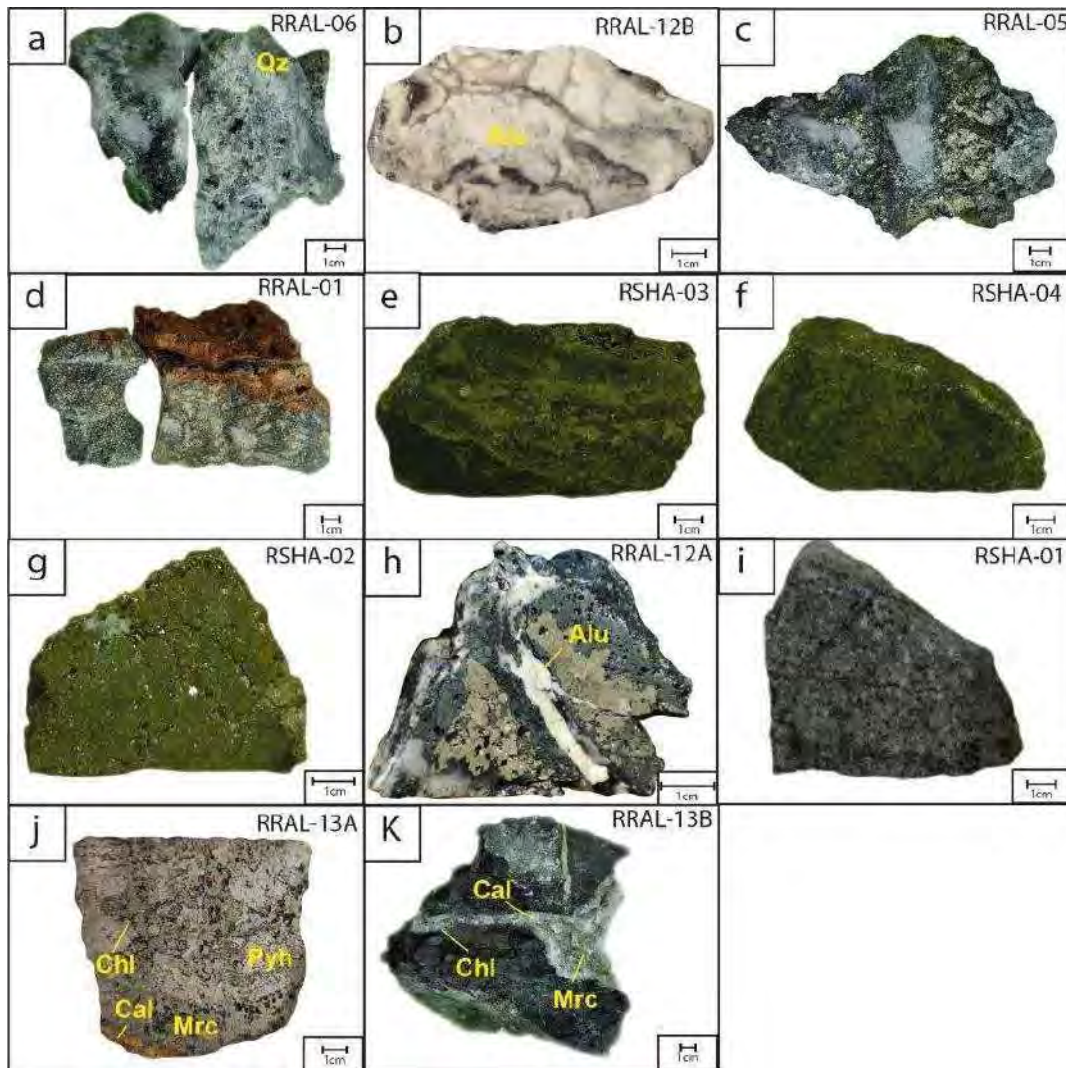
Fig. A1. Representative hand specimens, labeled by their sample numbers (displayed in the upper right corner). (a) Centimetric hydrothermal quartz crystals from the Concepción vein showing a crustiform texture. (b) Colloform alunite from Lucy vein. (c) Typical mineral assembles of the Lucy vein matrix formed by pyrite-quartz-tennantite-tetrahedrite accompanied by clasts of quartzite from the Chimú formation. (d) Hydrothermal breccia from the Choloque vein with clasts of quartzite and matrix of quartz and pyrite, partially oxidized. (e) Typical ore mineral assemblage of tennantite-pyrite-chalcopyrite from the Alisos vein. (f) Typical ore mineral assemblage of chalcopyrite-quartz-tetrahedrite-pyrite from the San Blas vein. (g) Massive pyrite, with minor barite (white) from the San Blas vein. (h) Pyrite and tennantite-tetrahedrite from stage B, both crosscut by an alunite vein from stage C, Lucy vein. (i) Pre-ore diorite intrusive rock with abundant disseminated pyrite. (j) Massive pyrrhotite was replaced by marcasite. Chlorite and calcite are mainly in the contact between pyrrhotite and marcasite. (k) Veins of calcite-marcasite with narrow chlorite halo. Mineral abbreviations follow Warr (2021).
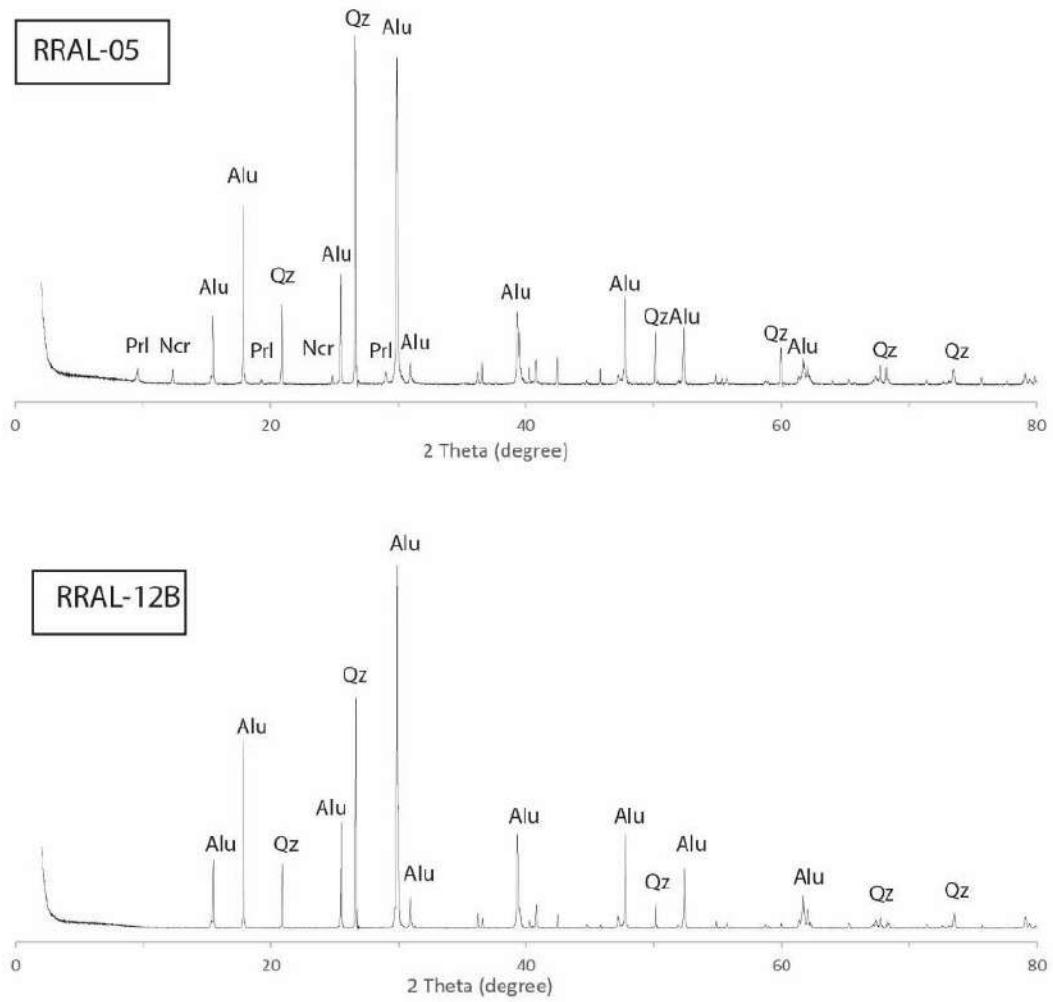
Fig. A2. XRD patterns of gangue mineral from Stage C labeled with the sample code. Mineral abbreviations follow Warr (2021).
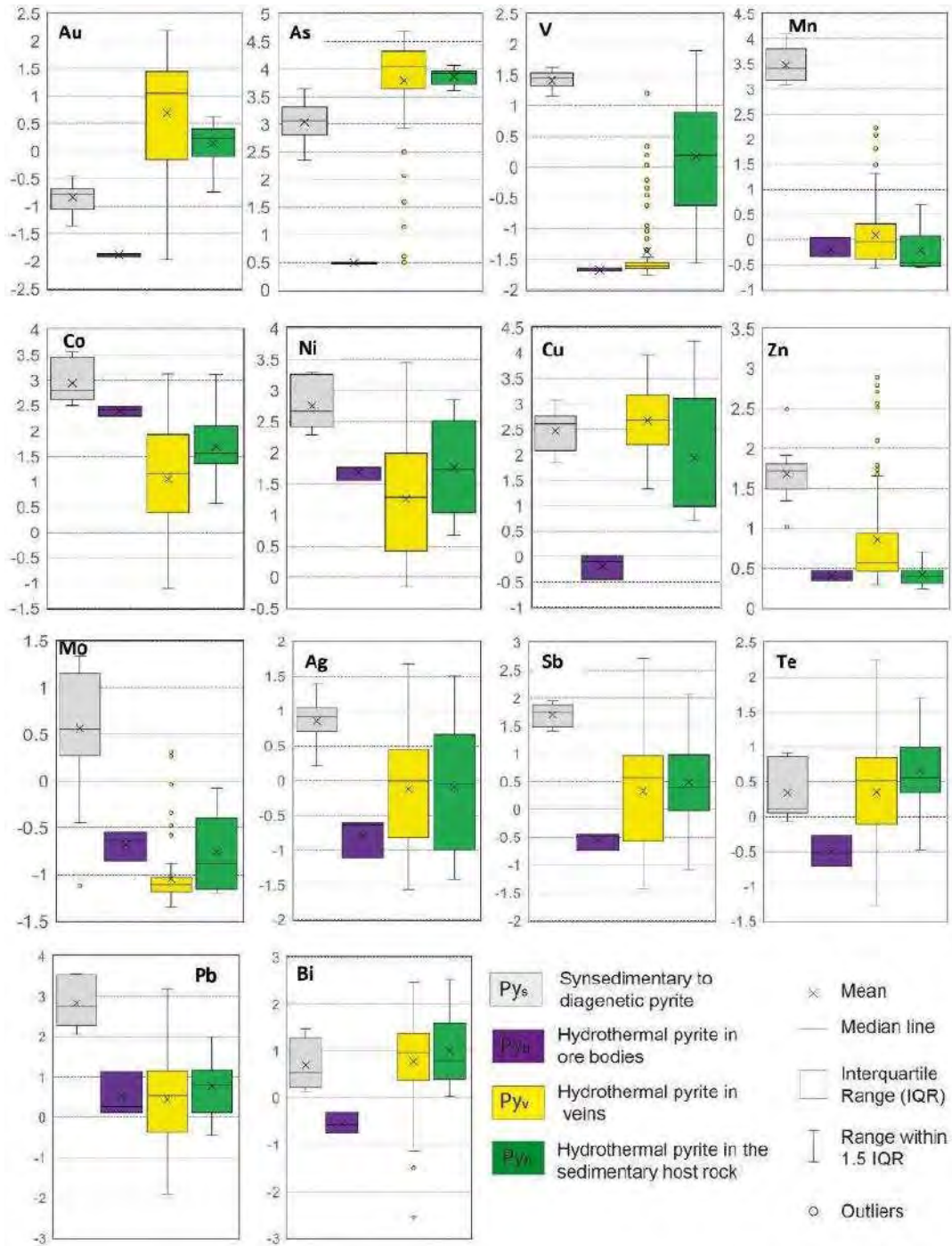
Fig. A3. Box plot comparison of the content in log$_{10}$ (ppm) of elements analyzed by LA-ICP-MS in the different pyrite types from the Algamarca deposit.
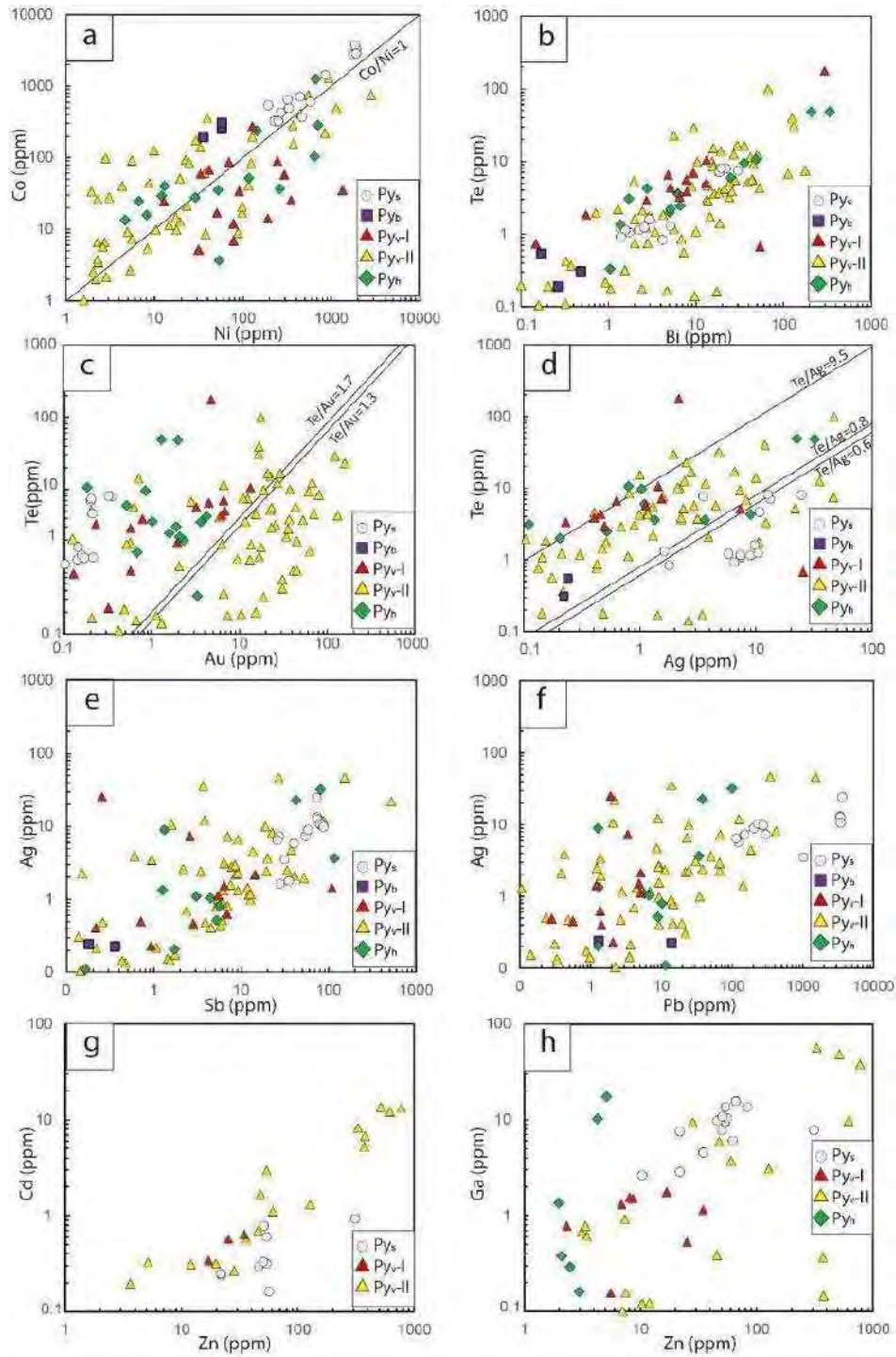
Fig. A4. Scatter diagrams of traces elements in all the types of pyrite from the Algamarca deposit. Abbreviations for pyrites types are the same as in Table 2. (a) Co vs. Ni. (b) Te vs. Bi. (c) Te vs. Au. (d) Te vs. Ag. (e) Ag vs. Sb. (f) Ag vs. Pb. (g) Cd vs. Zn. (h) Ga vs. Zn. The lines in Fig. A4c, d represents the ratios of common Au-Ag tellurides: calaverite (Te/Au= 1.3), petzite (Te/Au= 1.3 and Te/Ag= 0.8), sylvanite (Te/Au= 1.7 and Te/Ag= 9.5), and hessite (Te/Ag= 0.6).
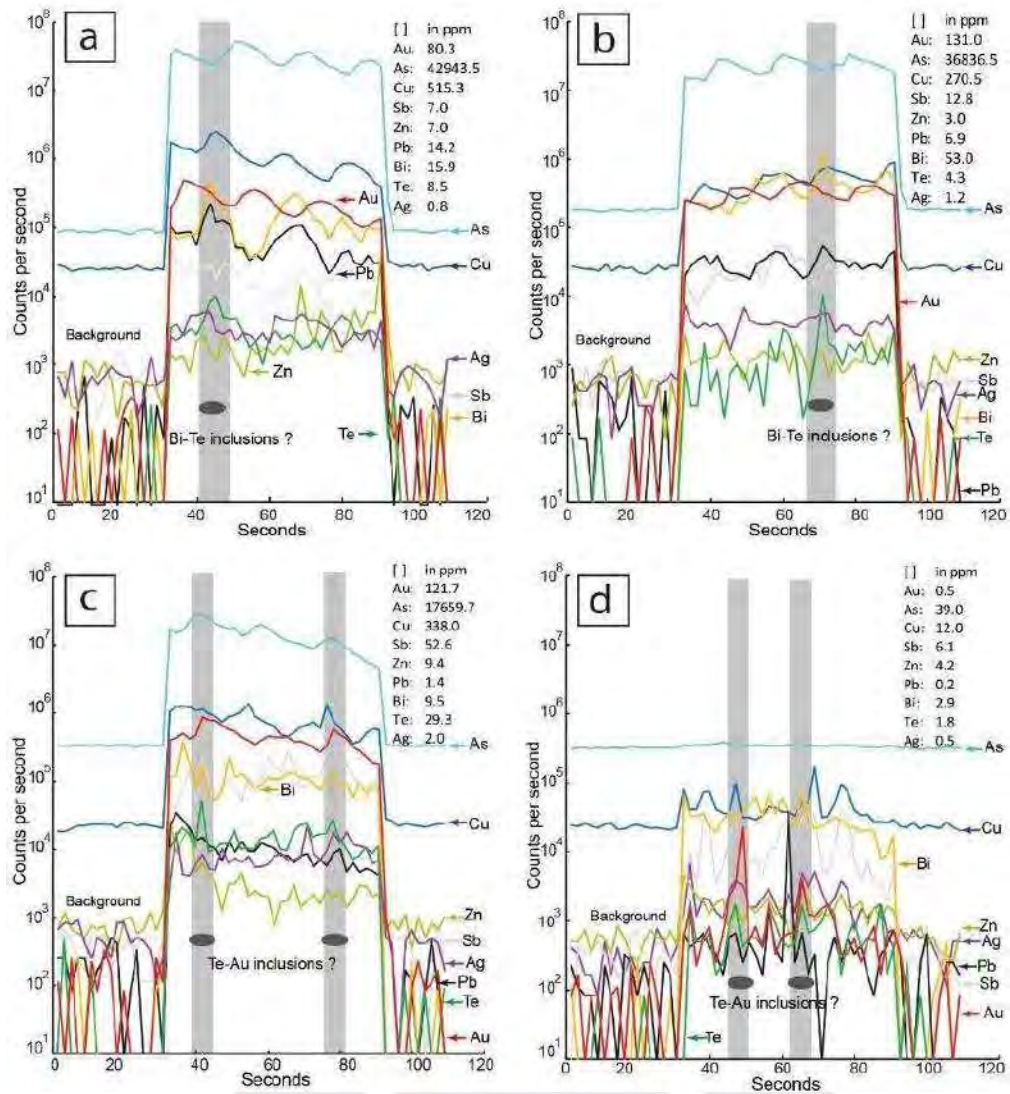
Fig. A5. LA-ICP-MS signals for selected elements obtained from spot analyses of hydrothermal pyrites in veins. The spiky peaks highlighted in gray indicate the presence of inclusions. (a) Pyv-II$_b$ from the Concepción vein, (b) Pyv-II$_e$ from the Lucy vein, (c) Pyv-II$_b$ from the San Blas vein, and (d) Pyv-II$_c$ from the San Blas vein.
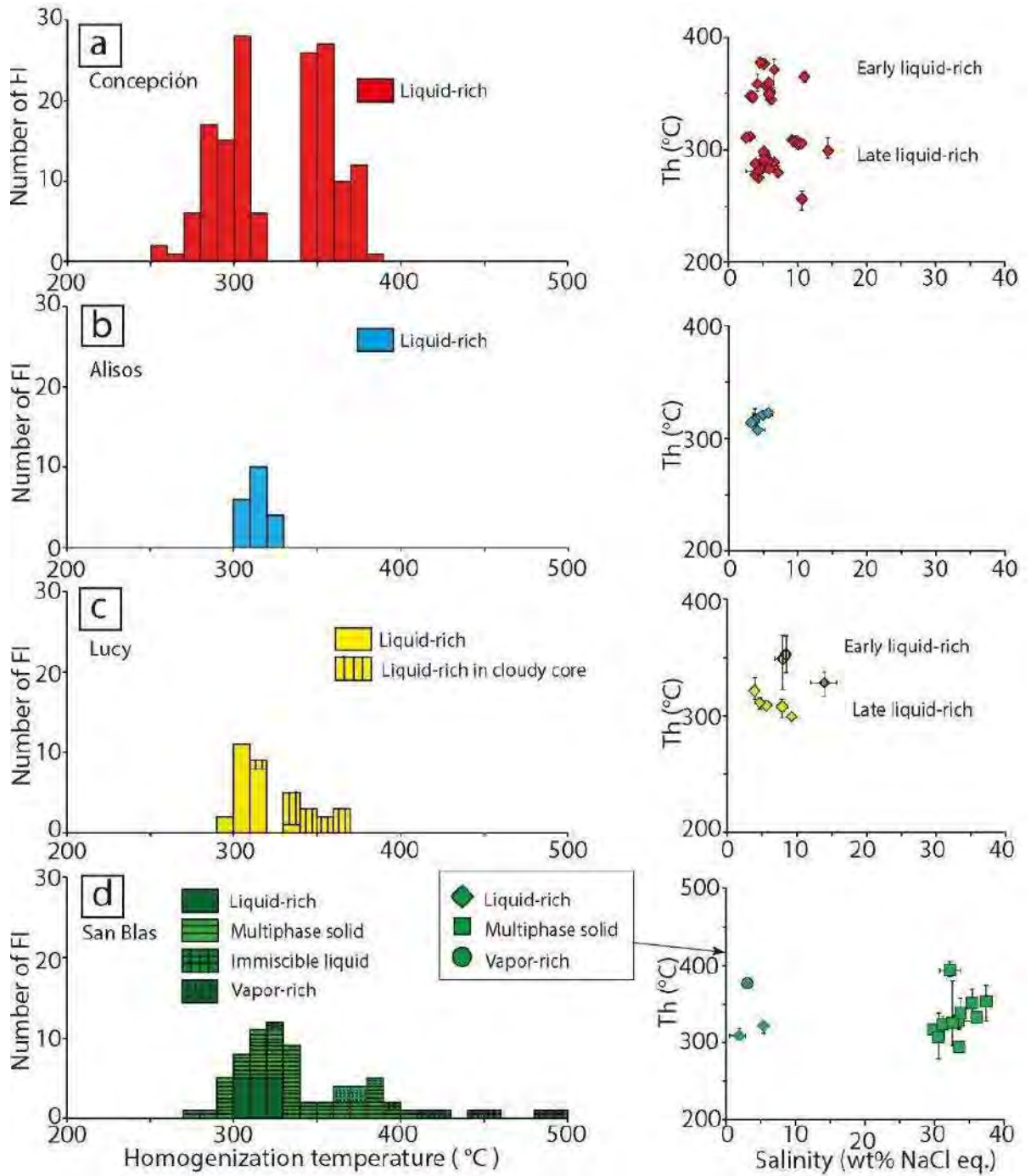
Fig. A6. Frequency vs. temperature of homogenization and temperature of homogenization vs. salinity for the Algamarca veins. The error bars correspond to the minimum and maximum value for each fluid inclusion assemblage.

Annex III

Table A1. Representative EPMA analyses of different hydrothermal pyrites types. Including the chemical composition and structural formulas.

Stage	Stage A		Stage B										Pyrite in the host rock		d.l.
Mineral	Pyrite in veins		Pyrite in veins										Pyh		
	Pyv-I						Pyv-II								
	Pyv-I		Pyv-IIa		Pyv-IIb		Pyv-IIc		Pyv-IId		Pyv-IIe		core	rim	
Sample	RSHA-04	RSHA-04	RRAL-06	RRAL-06	RRAL-06	RSHA-02	RRAL-06	RRAL-05	RRAL-05	RRAL-06	RSHA-01	RRAL-06	RRAL-01A	RRAL-01A	
#	47		3		8		27		25		74		5	10	
As (wt%)	0.22	1.15	0.15	0.15	3.77	2.58	2.02	b.d.l.	0.53	2.77	0.12	2.56	0.16	1.12	0.06
S	53.54	52.46	53.17	53.17	50.68	51.63	52.11	53.79	53.99	51.67	53.14	51.78	53.88	52.63	0.06
Fe	47.67	47.52	47.13	47.13	46.65	46.46	46.69	47.13	47.88	46.83	47.59	46.68	47.34	47.19	0.07
Sb	b.d.l.	b.d.l.	b.d.l.	b.d.l.	b.d.l.	b.d.l.	b.d.l.	b.d.l.	b.d.l.	b.d.l.	b.d.l.	b.d.l.	b.d.l.	b.d.l.	0.03
Cu	n.m.	n.m.	n.m.	n.m.	n.m.	b.d.l.	n.m.	n.m.	n.m.	n.m.	n.m.	n.m.	n.m.	n.m.	
Total	101.45	101.14	100.46	100.46	101.11	100.67	100.82	100.93	102.4	101.28	100.85	101.02	101.40	100.94	
As (apfu)	0.00	0.02	0.00	0.00	0.06	0.04	0.03	0.00	0.01	0.04	0.00	0.04	0.00	0.02	
S	1.98	1.96	1.99	1.99	1.92	1.95	1.96	2.00	1.98	1.94	1.98	1.95	1.99	1.97	
Fe	1.02	1.02	1.01	1.01	1.02	1.01	1.01	1.00	1.01	1.01	1.02	1.01	1.00	1.01	
Total	3.00	3.00	3.00	3.00	3.00	3.00	3.00	3.00	3.00	3.00	3.00	3.00	3.00	3.00	

= number of electron microprobe analysis, d.l. = detection limit in wt %, b.d.l.= below detection limit, n.m. = not measured. Abbreviations for pyrites types are the same as in Table 2.

Table A2. Representative EPMA analyses of sedimentary pyrite and sulfides from veins and ore bodies. Including the chemical composition and structural formulas.

	Synsedimentary to diagenetic pyrite		Sulfides in ore bodies						Sulfide in veins from Stage B						d.l.
Mineral	Py$_s$		Py$_b$		Po		Mrc		Ttr		Tnt		Ccp		
Sample	RRAL-03	RRAL-03	RRAL-13A	RRAL-13A	RRAL-13A	RRAL-13A	RRAL-13A	RRAL-13A	RSHA-04	RSHA-04	RSHA-03	RSHA-02	RSHA-04	RSHA-04	
#		12		10		4		10		23		6		12	
As (wt%)	0.08	0.22	b.d.l.	b.d.l.	b.d.l.	b.d.l.	b.d.l.	b.d.l.	1.73	2.91	18.67	20.40	b.d.l.	b.d.l.	0.06
S	53.34	51.94	52.6	53.03	39.05	39.18	53.05	52.5	25.21	26.04	28.16	28.43	34.65	34.85	0.06
Fe	47.48	46.81	47.72	47.62	61.72	61.12	47.7	47.25	5.12	5.45	6.19	8.29	30.27	30.48	0.07
Sb	b.d.l.	b.d.l.	b.d.l.	b.d.l.	b.d.l.	b.d.l.	b.d.l.	b.d.l.	26.22	24.74	2.35	0.79	b.d.l.	b.d.l.	0.03
Cu	n.m.	n.m.	n.m.	n.m.	n.m.	n.m.	n.m.	n.m.	38.12	37.93	43.75	42.42	34.80	34.70	0.05
Ag	n.m.	n.m.	n.m.	n.m.	n.m.	n.m.	n.m.	n.m.	1.35	1.58	b.d.l.	b.d.l.	b.d.l.	b.d.l.	0.2
Zn	n.m.	n.m.	n.m.	n.m.	n.m.	n.m.	n.m.	n.m.	1.73	1.65	1.05	0.32	b.d.l.	b.d.l.	0.2
Bi	n.m.	n.m.	n.m.	n.m.	n.m.	n.m.	n.m.	n.m.	0.3	b.d.l.	b.d.l.	b.d.l.	b.d.l.	b.d.l.	0.3
Total	100.9	98.98	100.35	100.66	100.77	100.3	100.75	99.75	99.80	100.30	100.17	100.65	99.72	100.03	
As (apfu)	0.00	0.00	0.00	0.00	0.00	0.00	0.00	0.00	0.38	0.64	3.67	3.98	0.00	0.00	
S	1.98	1.98	1.97	1.98	1.10	1.12	1.94	1.94	12.89	13.27	12.93	12.96	1.98	1.99	
Fe	1.02	1.02	1.03	1.02	1.00	1.00	1.00	1.00	1.50	1.59	1.63	2.17	0.99	1.00	
Sb									3.53	3.32	0.28	0.09	1.01	1.00	
Cu									9.83	9.75	10.13	9.76	0.00	0.00	
Ag									0.21	0.24	0.00	0.00	0.00	0.00	
Zn									0.43	0.41	0.24	0.07	0.00	0.00	
Bi									0.03	0.00	0.00	0.00	0.00	0.00	
Total	3.00	3.00	3.00	3.00	2.10	2.12	2.94	2.94	28.80	29.23	28.88	29.04	3.98	3.99	

= number of electron microprobe analysis, d.l. = detection limit in wt %, b.d.l.= below detection limit, n.m. = not measured. Abbreviations for minerals follow Warr (2021) and for pyrite types are the same as in Table 2

Table A3. Representative LA-ICP-MS analyses (in ppm) of minerals from the Algamarca deposit.

Mineral	Type	Structure	Sample	Au	As	V	Mn	Co	Ni	Cu	Zn	Ga	Se	Mo	Ag	Cd	In	Sn	Sb	Te	W	Pb	Bi
Pyrite	Py$_s$		RRAL-03	0.3	1,100	30	1300	3300	1900	1,100	66	16	98	11	25	b.d.l.	0.03	2	73	8	0.08	3,600	22
	Py$_s$		RSHA-13	0.06	2,200	43	1700	550	190	70	54	14	4	3	6	0.3	0.02	0.6	40	1	0.1	120	1
	Py$_s$		RSHA-13	0.2	2,500	30	6600	500	330	120	51	11	6	22	9	0.8	0.03	0.4	58	1	0.1	200	2
Pyrite	Py$_s$	Ore bodies	RRAL-13	b.d.l.	b.d.l.	b.d.l.	1	260	58	1	2	b.d.l.	b.d.l.	0.3	0.1	b.d.l.	b.d.l.	b.d.l.	0.3	0.2	0.01	2	0.3
	Py$_s$	Ore bodies	RRAL-13	b.d.l.	b.d.l.	b.d.l.	b.d.l.	200	35	1	2	b.d.l.	2	0.2	0.2	b.d.l.	b.d.l.	b.d.l.	0.2	0.5	b.d.l.	1	0.2
	Py$_s$	Ore bodies	RRAL-13	b.d.l.	b.d.l.	b.d.l.	b.d.l.	310	58	b.d.l.	3	b.d.l.	2	0.1	0.2	b.d.l.	b.d.l.	b.d.l.	0.4	0.3	b.d.l.	14	0.5
Pyrrhotite	Po	Ore bodies	RRAL-13	b.d.l.	17	b.d.l.	b.d.l.	230	54	b.d.l.	2	b.d.l.	2	b.d.l.	0.3	b.d.l.	b.d.l.	b.d.l.	0.3	1	b.d.l.	4	0.8
	Po	Ore bodies	RRAL-13	0.04	b.d.l.	0.2	14	240	40	1	2	0.2	3	b.d.l.	0.6	b.d.l.	0.03	0.5	1	b.d.l.	b.d.l.	6	1
Marcasite	Mrc	Ore bodies	RRAL-13	1	b.d.l.	b.d.l.	2	300	65	1	3	b.d.l.	2	0.2	0.1	b.d.l.	b.d.l.	b.d.l.	0.4	0.8	0.02	3	0.5
	Mrc	Ore bodies	RRAL-13	b.d.l.	b.d.l.	0.05	1	300	68	1	b.d.l.	2	0.2	0.2	0.1	b.d.l.	b.d.l.	b.d.l.	0.5	0.2	0.05	3	0.2
Pyrite	Py$_v$-I	San Blas vein	RSHA-04	4	15,700	b.d.l.	65	7	78	270	b.d.l.	0.2	44	b.d.l.	0.6	b.d.l.	0.02	b.d.l.	7	7	b.d.l.	1	5
	Py$_v$-I	San Blas vein	RSHA-04	5	17,100	b.d.l.	9	17	51	1,840	35	1	52	b.d.l.	2	0.6	0.3	19	14	180	0.03	5	290
Pyrite	Py$_v$-II$_a$	Concepción vein	RRAL-06	19	6,700	b.d.l.	b.d.l.	b.d.l.	32	1,800	520	48	9	b.d.l.	2	14	18	490	9	10	0.03	22	15
	Py$_v$-II$_a$	Concepción vein	RRAL-06	7	2,800	b.d.l.	2	b.d.l.	15	2,000	330	56	10	b.d.l.	4	8	20	390	20	12	b.d.l.	50	42
Pyrite	Py$_v$-II$_b$	Concepción vein	RRAL-06	41	27,800	b.d.l.	b.d.l.	280	370	21	3	b.d.l.	14	b.d.l.	0.4	b.d.l.	0.03	b.d.l.	3	0.8	b.d.l.	15	3
	Py$_v$-II$_b$	Concepción vein	RRAL-06	67	34,300	b.d.l.	1	5	32	950	50	6	23	b.d.l.	2	2	2	74	20	13	0.04	38	50
	Py$_v$-II$_b$	San Blas vein	RSHA-02	122	17,700	0.2	b.d.l.	13	19	340	9	0.1	22	b.d.l.	2	b.d.l.	0.03	b.d.l.	53	29	0.05	1	9
Pyrite	Py$_v$-II$_c$	Concepción vein	RRAL-06	23	20,200	0.3	2	750	550	470	3	0.1	21	b.d.l.	1	b.d.l.	0.03	b.d.l.	5	15	0.03	35	16
	Py$_v$-II$_c$	Concepción vein	RRAL-06	45	21,600	b.d.l.	b.d.l.	120	10	120	3	b.d.l.	21	b.d.l.	b.d.l.	b.d.l.	b.d.l.	b.d.l.	2	b.d.l.	2	2	0.7
	Py$_v$-II$_c$	San Blas vein	RSHA-02	0.5	40	b.d.l.	2	10	10	12	4	b.d.l.	11	b.d.l.	0.5	b.d.l.	b.d.l.	b.d.l.	6	2	b.d.l.	0.2	3
Pyrite	Py$_v$-II$_d$	Concepción vein	RRAL-06	23	20,600	2	b.d.l.	7	3	65	3	b.d.l.	11	b.d.l.	0.9	b.d.l.	0.04	b.d.l.	6	3	600	14	13
	Py$_v$-II$_d$	Lucy vein	RRAL-05	62	27,200	b.d.l.	6	b.d.l.	b.d.l.	180	36	b.d.l.	16	b.d.l.	7	0.6	0.1	0.9	7	9	0.01	68	45
	Py$_v$-II$_d$	Concepción vein	RRAL-06	29	17,350	b.d.l.	21	176	29	136	9	0.06	22	b.d.l.	2.8	b.d.l.	0.03	b.d.l.	8	17	b.d.l.	9	35
Pyrite	Py$_v$-II$_e$	Lucy vein	RRAL-05	64	21,900	b.d.l.	b.d.l.	0.4	b.d.l.	150	4	b.d.l.	10	b.d.l.	0.5	0.2	0.03	b.d.l.	4	1	0.01	3	19
	Py$_v$-II$_e$	Concepción vein	RRAL-06	31	28,400	b.d.l.	b.d.l.	197	52	3	b.d.l.	16	b.d.l.	0.05	b.d.l.	b.d.l.	0.4	b.d.l.	0.5	0.3			
	Py$_v$-II$_e$	Alisos vein	RSHA-03	0.7	800	b.d.l.	165	15	17	3,700	28	9	72	b.d.l.	10	0.3	4	67	19	14	0.08	24	19
Pyrite	Py$_h$ core	Choloque vein	RRAL-01A	0.2	6,100	3	b.d.l.	100	650	11	2	1	35	b.d.l.	0.8	b.d.l.	b.d.l.	b.d.l.	6	11	0.8	10	49
	Py$_h$ core	Choloque vein	RRAL-01A	0.5	4,700	3	4	4	54	400	2	0.3	39	b.d.l.	1	b.d.l.	b.d.l.	b.d.l.	3	6	5	6	25
	Py$_h$ core	Choloque vein	RRAL-01A	2	11,900	78	5	1300	670	17,100	5	17	67	0.7	32	b.d.l.	0.05	1	82	49	76	100	340
Pyrite	Py$_h$ rim	Choloque vein	RRAL-01A	3	11,600	b.d.l.	b.d.l.	25	7	13	2	b.d.l.	8	b.d.l.	b.d.l.	b.d.l.	b.d.l.	b.d.l.	0.4	0.3	0.05	0.4	1
	Py$_h$ rim	Choloque vein	RRAL-01A	1	7,100	6	1	36	52	62	3	b.d.l.	11	0.7	4	b.d.l.	b.d.l.	b.d.l.	120	4	9	34	6
	Py$_h$ rim	Choloque vein	RRAL-01A	2	8,400	6	b.d.l.	13	5	10	2	0.1	9	0.3	0.2	b.d.l.	0.03	0.4	2	2	23	1	5
Arsenopyrite	Apy	San Blas vein	RSHA-01	5	424,100	6	b.d.l.	b.d.l.	3	870	11	0.1	21	0.9	0.9	0.4	1	1	200	3	83	3	5
	Apy	San Blas vein	RSHA-01	0.6	450,000	110	1	0.3	56	1	2	0.1	16	b.d.l.	0.3	b.d.l.	0.3	0.3	230	3	77	2	10
	Apy	San Blas vein	RSHA-04	320	417,400	b.d.l.	b.d.l.	120	350	55	b.d.l.	b.d.l.	160	b.d.l.	0.1	b.d.l.	0.6	b.d.l.	26	1200	b.d.l.	0.1	13
Tennantite	Tnt	Alisos vein	RSHA-03	0.04	84,400	b.d.l.	23	9	b.d.l.	106,700	5,400	5	30	3,300	530	180	5	17,500	8,200	28	0.05	110	310
	Tnt	Alisos vein	RSHA-03	0.04	87,200	b.d.l.	24	9	b.d.l.	133,200	6,500	4	35	3,100	600	210	5	17,100	8,900	39	0.07	0.5	450
Tetrahedrite	Ttr	San Blas vein	RSHA-04	0.06	30,400	b.d.l.	770	2	b.d.l.	298,900	29,100	10	89	b.d.l.	10,200	745	8	0.6	200,200	60	b.d.l.	0.2	2,360
	Ttr	San Blas vein	RSHA-04	0.05	31,700	b.d.l.	700	2	b.d.l.	305,300	29,200	12	83	b.d.l.	9,800	760	9	0.9	205,700	59	b.d.l.	0.4	2,500
Chalcopyrite	Ccp	San Blas vein	RSHA-04	b.d.l.	b.d.l.	b.d.l.	b.d.l.	b.d.l.	b.d.l.	317,400	32	91	33	b.d.l.	3	b.d.l.	15	1,100	2	5	b.d.l.	0.9	1
	Ccp	San Blas vein	RSHA-04	0.1	b.d.l.	0.04	2	b.d.l.	b.d.l.	317,600	14	14	36	b.d.l.	2	b.d.l.	11	320	3	4	0.04	1	0.7

b.d.l.= below detection limit.

Table A4. Pearson correlation coefficients for all bivariate trace element combinations in hydrothermal pyrite from the Algamarca veins (Py$_v$). Weak (light gray), moderate (medium gray) and high correlation (dark gray).

	Au	As	V	Mn	Co	Ni	Cu	Zn	Ga	Se	Mo	Ag	Cd	In	Sn	Sb	Te	Pb	Bi
Au	1																		
As	0.6	1																	
V	-0.1	0.0	1																
Mn	-0.1	-0.1	0.0	1															
Co	0.0	0.1	0.0	-0.1	1														
Ni	-0.1	-0.1	0.0	0.0	0.6	1													
Cu	-0.1	-0.2	0.0	0.1	0.2	0.2	1												
Zn	-0.1	-0.1	0.0	0.0	-0.1	-0.1	0.2	1											
Ga	-0.1	-0.1	0.0	0.0	-0.1	-0.1	0.1	0.7	1										
Se	0.0	-0.2	-0.2	0.3	0.0	0.0	0.2	0.0	0.0	1									
Mo	-0.1	-0.1	0.6	-0.1	0.2	0.2	0.4	0.0	0.0	-0.2	1								
Ag	-0.1	-0.1	-0.1	0.1	0.0	0.0	0.4	0.3	0.0	0.3	0.0	1							
Cd	-0.1	-0.1	0.0	0.0	-0.1	-0.1	0.2	1.0	0.8	0.0	0.0	0.3	1						
In	-0.1	-0.1	0.0	0.1	-0.1	0.0	0.1	0.8	0.9	-0.1	0.0	0.0	0.8	1					
Sn	-0.1	-0.1	0.0	0.0	-0.1	0.0	0.1	0.8	0.8	0.0	0.0	0.0	0.9	1.0	1				
Sb	0.0	-0.1	0.0	0.1	-0.1	-0.1	0.5	0.4	0.0	0.2	-0.1	0.4	0.3	0.0	0.0	1			
Te	0.1	0.0	-0.1	0.1	0.0	-0.1	0.2	0.1	0.1	0.5	-0.1	0.3	0.1	0.0	0.1	0.2	1		
Pb	-0.1	-0.1	0.0	0.0	-0.1	-0.1	0.0	0.3	0.0	0.1	0.0	0.6	0.2	0.0	0.0	0.1	0.1	1	
Bi	0.0	0.0	-0.1	0.2	-0.1	-0.1	0.1	0.3	0.1	0.2	-0.1	0.4	0.2	0.1	0.1	0.1	0.7	0.5	1

Table A5. Microthermometric results of immiscible-liquid fluid inclusion assemblages (FIAs) in quartz of stage A from the San Blas vein. For each microthermometric parameter, the average values are given, while the number of analyzed fluid inclusions are in brackets.

Sample	Type	Th (°C)		$Tm_{(CO2)}$ (°C)		$Tm_{(clath)}$ (°C)		$Th_{(CO2)}$ (°C)	
RSHA-04	C	>370	(5)	−66.8 ± 1.3	(3)	10.6 ± 2.1	(3)	29.2 ± 0.3	(3)
RSHA-04	I	498	(1)	−66.2	(1)	10.1	(1)	29.5	(1)
RSHA-04	I	327	(1)	−65.8	(1)	10.3	(1)	30.0	(1)
RSHA-04	C	404 ± 17	(2)	−65.9 ± 1.1	(3)	9.1 ± 4.3	(2)	30.9 ± 0.4	(3)
RSHA-04	C	444 ± 25	(3)	−66.5 ± 0.5	(3)	9.8 ± 1.7	(3)	31.0 ± 0.1	(4)

Th = homogenization temperature, $Tm_{(CO2)}$ = melting temperature of solid CO_2, $Tm_{(clath)}$ = melting temperature of clathrate, $Th_{(CO2)}$ = homogenization temperature of CO_2, C = cluster, I = isolated.

Table A6. Element concentration obtained by LA-ICP-MS for 15 fluid inclusion assemblages from the Algamarca veins.

FIA	Type	S		Cl		B		Na		Mg		K		Ca		Mn	
RRAL-06_3_1	Liquid-rich	8,900 ± 2,300	(6)	12,400 ± 9,000	(3)	1,500 ± 300	(6)	12,600 ± 1,200	(6)	40 ± 30	(5)	8,600 ± 700	(6)	2,700 ± 600	(4)	250 ± 40	(6)
RRAL-06_2_1	Liquid-rich	7,400 ± 1,100	(2)	11,300 ± 900	(2)	1,700 ± 200	(2)	17,200 ± 400	(2)	140 ± 140	(2)	11,500 ± 5,000	(2)	1,000 ± 200	(2)	430 ± 70	(2)
RRAL-06_1_1	Liquid-rich	3,800 ± 1,000	(2)	10,000 ± 3,400	(3)	800 ± 200	(3)	9,000 ± 500	(3)	150 ± 110	(2)	6,000 ± 1,200	(3)	1,600 ± 700	(3)	170 ± 20	(3)
RRAL-06_10_1	Liquid-rich	4,000	(1)	13,400	(1)	900	(1)	19,600	(1)	1,600	(1)	6,700	(1)	3,100	(1)	180	(1)
RRAL-06_10_2	Liquid-rich	2,100	(1)	37,200 ± 10,000	(3)	1,600 ± 200	(3)	28,100 ± 1,400	(3)	90 ± 40	(3)	18,000 ± 600	(3)	6,400 ± 2,000	(3)	1,600 ± 10	(3)
RRAL-06_6_1	Liquid-rich	8,500 ± 1,000	(2)	17,100 ± 2,700	(2)	800 ± 20	(2)	14,600 ± 200	(2)	290 ± 20	(2)	9,600 ± 500	(2)	1,400	(1)	1,100 ± 100	(2)
RRAL-06_13_1	Liquid-rich			39,000	(1)	1,400	(1)	25,100	(1)	420	(1)	19,000	(1)	5,000	(1)	2,100	(1)
RRAL-06_11_1	Liquid-rich	4,000	(1)	15,000	(1)	1,500	(1)	27,200	(1)	450	(1)	19,000	(1)	4,100	(1)	2,300	(1)
RRAL-06_11_2	Liquid-rich			70,000 ± 400	(2)	1,100 ± 50	(2)	21,900 ± 2,000	(2)	250 ± 90	(2)	14,000 ± 2,000	(2)	9,700	(1)	1,300 ± 140	(2)
RRAL-06_11_4	Liquid-rich	3,800	(1)	50,000	(1)	1,600	(1)	24,500	(1)	410	(1)	18,400	(1)	2,900	(1)	2,100	(1)
RRAL-06_11_6	Liquid-rich			31,000	(1)	1,900	(1)	35,000	(1)	570	(1)	27,000	(1)	9,800	(1)	2,200	(1)
RRAL-06_12_1	Liquid-rich	3,300 ± 300	(3)	21,800 ± 14,500	(2)	800 ± 80	(3)	9,500 ± 700	(3)	80 ± 10	(3)	5,700 ± 800	(3)	2,700 ± 1,300	(3)	200 ± 10	(3)
RRAL-04_2_1	multiphase solid	2,100	(1)	247,000 ± 14,000	(3)	550 ± 200	(3)	53,000 ± 5,000	(3)	130 ± 50	(3)	48,500 ± 7,800	(3)	7,000 ± 800	(3)	15,300 ± 1,000	(3)
RRAL-04_2_2	multiphase solid	6,000 ± 600	(2)	262,500 ± 10,000	(2)	400 ± 160	(2)	60,000 ± 6,000	(2)	460 ± 60	(2)	76,000 ± 5,000	(2)	6,000 ± 700	(2)	15,000 ± 3,200	(2)
RRAL-04_3_1	multiphase solid	3,000	(1)	270,000 ± 75,000	(3)	400 ± 50	(3)	75,000 ± 17,000	(3)	300 ± 90	(3)	72,000 ± 20,000	(3)	5,000 ± 1,400	(3)	16,400 ± 3,800	(3)

FIA	Type	Fe		Cu		Zn		As		Br		Rb		Sr		Mo	
RRAL-06_3_1	Liquid-rich	1,900 ± 400	(6)	540 ± 60	(6)	140 ± 70	(6)	300 ± 80	(6)	n.m.		n.m.		5 ± 1	(6)	n.m.	
RRAL-06_2_1	Liquid-rich	2,400 ± 400	(2)	560 ± 130	(2)	190 ± 20	(2)	200 ± 90	(2)	n.m.		n.m.		12 ± 1	(2)	n.m.	
RRAL-06_1_1	Liquid-rich	800 ± 170	(3)	10 ± 1	(3)	50 ± 20	(3)	380 ± 90	(3)	n.m.		n.m.		11 ± 1	(3)	n.m.	
RRAL-06_10_1	Liquid-rich	700	(1)	290	(1)	80	(1)			n.m.		n.m.		42	(1)	n.m.	
RRAL-06_10_2	Liquid-rich	8,900 ± 600	(3)	20 ± 10	(3)	640 ± 60	(3)	200 ± 42	(3)	n.m.		n.m.		48 ± 4	(3)	n.m.	
RRAL-06_6_1	Liquid-rich	2,900 ± 300	(2)	10	(2)	830 ± 30	(2)	120 ± 10	(2)	n.m.		n.m.		24 ± 1	(2)	n.m.	
RRAL-06_13_1	Liquid-rich	10,700	(1)			1,000	(1)	220	(1)	n.m.		n.m.		44	(1)	n.m.	
RRAL-06_11_1	Liquid-rich	12,800	(1)	20	(1)	1,000	(1)	270	(1)	n.m.		n.m.		52	(1)	n.m.	
RRAL-06_11_2	Liquid-rich	4,900 ± 1,600	(2)			660 ± 30	(2)	100	(1)	n.m.		n.m.		31 ± 1	(2)	n.m.	
RRAL-06_11_4	Liquid-rich	9,700	(1)			1,200	(1)	170	(1)	n.m.		n.m.		41	(1)	n.m.	
RRAL-06_11_6	Liquid-rich	10,900	(1)	80	(1)	1,200	(1)			n.m.		n.m.		41	(1)	n.m.	
RRAL-06_12_1	Liquid-rich	830 ± 70	(3)	20 ± 20	(3)	40 ± 5	(3)	340 ± 40	(3)	n.m.		n.m.		11 ± 1	(3)	n.m.	
RRAL-04_2_1	multiphase solid	95,000 ± 10,000	(3)	70	(1)	8,200 ± 1,200	(3)	1,800 ± 200	(3)	550 ± 200	(1)	600 ± 100	(3)	74 ± 7	(3)	0.5	(1)
RRAL-04_2_2	multiphase solid	73,500 ± 4,400	(2)	6,900 ± 2,500	(2)	5,500 ± 600	(2)	2,000 ± 1,500	(2)	570 ± 130	(2)	800 ± 100	(2)	310 ± 2	(2)	0.3	(1)
RRAL-04_3_1	multiphase solid	79,000 ± 20,000	(3)	2,000 ± 2,000	(3)	5,800 ± 2,300	(3)	1,100 ± 1,000	(3)	500 ± 80	(2)	800 ± 200	(3)	270 ± 80	(3)	0.8	(1)

FIA	Type	Ag		Sb		Cs		Ba		Au		Pb		Bi	
RRAL-06_3_1	Liquid-rich	4 ± 3	(4)	145 ± 80	(5)	31 ± 4	(6)	n.m.				40 ± 20	(6)	n.m.	
RRAL-06_2_1	Liquid-rich	1 ± 1	(2)			46 ± 7	(2)	n.m.		0.2	(1)	52 ± 2	(2)	n.m.	
RRAL-06_1_1	Liquid-rich	0.2	(1)	45 ± 20	(3)	14 ± 3	(3)	n.m.				18 ± 3	(3)	n.m.	
RRAL-06_10_1	Liquid-rich	1	(1)			22	(1)	n.m.				30	(1)	n.m.	
RRAL-06_10_2	Liquid-rich	2.0 ± 0.3	(3)	70 ± 10	(3)	64 ± 4	(3)	n.m.				140 ± 20	(3)	n.m.	
RRAL-06_6_1	Liquid-rich	1	(1)	26 ± 3	(2)	11 ± 1	(2)	n.m.				290 ± 40	(2)	n.m.	
RRAL-06_13_1	Liquid-rich			390	(1)	18	(1)	n.m.				230	(1)	n.m.	
RRAL-06_11_1	Liquid-rich	1	(1)			17	(1)	n.m.				250	(1)	n.m.	
RRAL-06_11_2	Liquid-rich			150	(1)	12 ± 3	(2)	n.m.				200 ± 50	(2)	n.m.	
RRAL-06_11_4	Liquid-rich	2	(1)	6	(1)	18	(1)	n.m.				320	(1)	n.m.	
RRAL-06_11_6	Liquid-rich					20	(1)	n.m.				280	(1)	n.m.	
RRAL-06_12_1	Liquid-rich			20	(1)	16 ± 3	(3)	n.m.				20 ± 3	(3)	n.m.	
RRAL-04_2_1	multiphase solid	50 ± 20	(3)	1,900 ± 400	(3)	200 ± 30	(3)	100 ± 30	(3)			1,300 ± 100	(3)	110 ± 60	(3)
RRAL-04_2_2	multiphase solid	100 ± 10	(2)	1,400 ± 770	(2)	225 ± 30	(2)	210 ± 5	(2)			1,300 ± 500	(2)	490 ± 20	(2)
RRAL-04_3_1	multiphase solid	110 ± 60	(3)	900 ± 500	(3)	200 ± 70	(3)	200 ± 30	(3)			1,500 ± 600	(3)	370 ± 180	(3)

Notes: The number of corresponding single measurements are in brackets. Data are reported as the assemblage average, with a standard deviation, n.m. = not measured.

Table A.7. Relevant parameters and estimated temperatures from Raman spectra of carbonaceous material at the Algamarca deposit.

Sample	Analysis	Position (cm⁻¹)					Area					FWHM	Area ratio	Estimated temperature (°C)	
		D4	D1	D3	G	D2	D4	D1	D3	G	D2	D1	RA1	Tw	Ta
RRAL-07	1	1215	1338	1521	1593	1610	58118	323058	51090	110599	40040	83	0.65	300	348
	2	1230	1338	1516	1593	1611	257913	810020	230738	363517	22683	86	0.63	293	323
RRAL-14A	1	1207	1333	1506	1593	1603	141804	718590	177509	273185	102037	109	0.61	243	291
	2	1205	1332	1507	1593	1603	275069	1058620	259769	456584	75651	114	0.63	233	315
	3	1202	1331	1508	1593	1603	233581	1072050	261730	452602	78045	114	0.62	232	308
	4	1207	1333	1506	1593	1604	105506	411466	94436	133517	87863	109	0.62	245	306
RRAL-14B	1	1204	1330	1511	1593	1603	251648	1225450	364442	537825	56424	113	0.61	234	288
	2	1205	1331	1511	1593	1603	296607	1040610	293744	458089	44465	114	0.63	232	314

Notes: FWHM = half width at half maximum, RA1 = (D1 + D4) Ủ (D1 + D2 + D3 + D4 + G) area ratio, Tw = temperature estimated using the D1 width (FWHM) after Kouketsu et al. (2014), Ta = temperature estimated with area ratio RA1 after Lahflid et al. (2010).

Annex IV

Galdos R., Vallance J., Baby P., Pokrovski G.S., 2021. A common hydrothermal magmatic system generates different styles of gold mineralization at Algamarca and Shahuindo, Northern Peru. ProEXPLO 2021, Lima, Peru. Extended Abstracts 100-104.

Galdos, R., Vallance, J., Baby, P., Salvi, S., Schirra, M., Velazquez, G., Viveen, W., Soto, R., Pokrovski, G.S., 2023b. Decoding hydrothermal fluids in organic carbon-rich basins: The case of the Algamarca Au-Ag-Cu deposit, Northern Peru. Implications for targeting hidden porphyry deposits. ProEXPLO 2023, Lima, Peru. Extended Abstracts 20-23.

A common hydrothermal magmatic system generates different styles of gold mineralization at Algamarca and Shahuindo, Northern Peru

Renzo Galdos[1],   **Jean Vallance[1],**   **Patrice Baby[2],**   **Gleb S. Pokrovski[2]**

[1] Facultad de ciencias e ingeniería, Especialidad Ingeniería Geológica, Pontificia Universidad Católica del Perú Av. Universitaria 1801, San Miguel, Lima 15088, Perú. E-mail: rgaldosp@pucp.edu.pe

[2] Groupe Métallogénie Expérimentale, Géosciences Environnement Toulouse (GET), UMR 5563, Observatoire Midi-Pyrénées, Université de Toulouse, Centre National de la Recherche Scientifique (CNRS), Institut de Recherche pour le Développement (IRD), 14, Avenue Edouard Belin, F-31400 Toulouse, France

1 Abstract

Algamarca and Shahuindo are two neighboring intermediate-sulfidation Au-Ag epithermal deposits of Miocene age located in the Marañon fold and thrust belt in the north of Peru, hosted in sedimentary sequences rich in carbonaceous matter of the Goyllarisquizga Group. These two deposits show strongly different styles of mineralization. At Algamarca, mineralization is expressed by up to 2 m-thick veins of quartz and sulfide minerals, with native gold content, traces of gold telluride minerals and possibly invisible gold in arsenical pyrite. In contrast, at Shahuindo, disseminated and replacement sulfide mineralization dominates, with gold exclusively present as invisible gold in arsenical pyrite and arsenopyrite. Algamarca and Shahuindo deposits show, however, similarities in age and paragenetic sequences that strongly suggest they were formed at the same time and were part of the same magmatic-hydrothermal system.
KEYWORDS: Arsenical pyrite; Invisible gold; Native gold; Intermediate-sulfidation deposit.

2 Resumen

Un mismo sistema magmático hidrotermal generó distintos estilos de mineralización aurífera en Algamarca y Shahuindo, Norte de Perú
Algamarca y Shahuindo son depósitos contiguos de oro y plata, de sulfuración intermedia, del Mioceno, están ubicados en la faja corrida y plegada del Marañón al norte de Perú y están hospedados en las secuencias sedimentarias, ricas en materia orgánica, del grupo Goyllarisquizga. Estos dos depósitos muestran diferentes estilos de mineralización, Algamarca consiste en vetas de cuarzo y sulfuros de hasta 2m de potencia, donde el oro se presenta bajo la forma de oro nativo, teluros de oro a nivel de trazas y además se infiere la presencia de oro en pirita arsenical; mientras que en Shahuindo, la mineralización se encuentra como sulfuros diseminados o de remplazamiento y el oro se presenta únicamente como oro invisible en pirita arsenical y arsenopirita. Sin embargo, Algamarca y Shahuindo muestran similitud en edad y en sus características mineralógicas y paragenéticas, indicando que se formaron coetáneamente y son probablemente parte de un mismo sistema magmático hidrotermal.

3 Introduction

The Marañon fold and thrust belt of Northern Peru hosts various porphyry-to epithermal-style gold deposits of Miocene age. Some of these deposits (e.g., La Arena, Lagunas Norte, Fig. 1), hosted by sedimentary sequences rich in organic matter of the Goyllarisquizga Group, are known as the metallogenic belt XXIA (Acosta et al., 2009). Algamarca and Shahuindo are two intermediate-sulfidation epithermal deposits that are part of this belt and are just ~2 km one from another (Fig. 1).

At Algamarca, mining has started since the colonial period (Defilippi et al, 2012) and continued more recently, between 1940 and 1989, with 1.5 million tons of ore grading 2.0% Cu and 680 g Ag/t with "some gold" extracted (Saucier and Poulin, 2004). Mineralization consists of veins of 0.1 to 2 m filling NE-SW to E-W strike faults, cutting the Chimu bedded quartzite of the NW-SE Algamarca

anticline. The veins are filled mainly by quartz, chalcopyrite, tetrahedrite-tennantite, and pyrite (Tumialan, 2003). Sphalerite, galena, bornite, and enargite were also reported (Reyes, 1980; Sánchez, 2012; Defilippi et al., 2016). The underground mine is currently worked by small-scale miners. The main mineralized structure is known as the Descubridora vein where punctual values of 8.4 g/t Au, 2058 g/t Ag, and 13.3% Cu were reported (Defilippi et al., 2016). A K-Ar age of 15.5±0.4 Ma was reported by Noble and McKee (1999) from hydrothermal muscovite bordering a polymetallic vein.

At Shahuindo, exploration started in the 1980s and the gold production started in 2016. Proven plus probable reserves are of ~55 t Au (1,763 koz Au) at 0.46 g/t (Cesar Alvarez, 2019 pers. comm.). The mineralization is expressed as disseminations and replacements in the Carhuaz and Farrat sandstone to siltstone Formations and, to a lesser extent, within andesitic to dacitic intrusives and as massive pyrite bodies at the intrusive contacts. Pyrite is the most abundant sulfide mineral and occurs together with lesser amounts of chalcopyrite, arsenopyrite, pyrrhotite, sphalerite, galena, tetrahedrite-tennantite and enargite, white mica is the main gangue mineral with scarce carbonate and quartz. Pre-ore andesitic to dacitic intrusives were dated to 26 and 16 Ma, respectively, using the U-Pb method on zircon (although no error margins reported; Bussey and Nelson, 2011). These similar ages suggest that the two deposits formed at ca. 15.5 Ma similarly to other intermediate-sulfidation deposits of the same belt like Quiruvilca from 15.18± 0.08 to 15.41± 0.13 Ma or Las Princesas 15.69 ± 0.07 Ma, estimated using $^{39}Ar/^{40}Ar$ data from hydrothermal minerals (Montgomery, 2012).

4 Sampling and methods

Twenty polished sections were studied: 7 samples from Algamarca, from dumps and ore load of underground mining works in Alisos and San Blas veins, and 13 samples from Shahuindo, from drill cores. A detailed mineralogical study has been performed using optical microscopy combined with Scanning Electron Microscope (SEM) at PUCP University, Lima. Quantitative analyses, Electron Probe Microanalyses (EPMA) of pyrite, arsenopyrite, marcasite, sphalerite, chalcopyrite, tennantite-tetrahedrite and enargite were performed by CAMECA SXFive instrument at the Centre of Microcaractérisation R. Castaing (Toulouse, France).

5 Results

Petrography

At Algamarca, veins show crustiform banding and breccias, textures of open space precipitation, with abundant, up
to 4-mm-size, euhedral quartz intergrown with pyrite (Py-C) of the same size; grains of native gold up to 20 µm across were identified in 3 polished sections. They mainly fill micro fractures in tetrahedrite, or at the contact between chalcopyrite and tetrahedrite grains. At Shahuindo, ore is mainly present as sulfides with replacement textures or as disseminations, the host rock permeability controls the gold mineralization, presents scarce quartz up to 250 µm in size. Native gold or electrum have not been observed. Based on the analytical data obtained, the paragenetic sequences of Algamarca and Shahuindo have been established (Fig. 1). Both show several generations of pyrite, 3 at Algamarca (Py-A, Py-B, and Py-C) and 4 at Shahuindo (Py-I, Py-II, Py-III, and Py-IV) where the most recent generations overgrowed or replaced earlier ones. Diagenetic pyrite was only observed at Shahuindo (Py-I). Both sequences exhibit an As-rich pyrite stage, Py-B at Algamarca and Py-III at Shahuindo, the main gold carrier mineral in this deposit (Vallance et al., 2019). Followed by a Cu-Ag stage dominated by chalcopyrite and tetrahedrite. Late minerals like sphalerite and enargite previously reported at Algamarca (Reyes 1980, Sanchez 2012 and Defilippi et al 2016) and identified at Shahuindo were not found in our Algamarca's samples.

Compositional data

Native gold at Algamarca contains 13.9 wt% Ag (on average). The generations of pyrite with highest As concentrations are Py-B at Algamarca with a mean value of 2.3 wt%, and Py-III at Shahuindo with a mean value of 1.8 wt%. At Algamarca and Shahuindo, all tetrahedrite is systematically Fe-rich with values from 1.1 to 2.2 apfu, with tetrahedrite at Shahuindo being more enriched in Zn and Ag than at Algamarca. Ag was not detected in enargite and tennantite (detection limit 0.2 wt%), while in tetrahedrite the values reached 1.6 and 5.9 wt% at Algamarca and Shahuindo, respectively.

6 Discussion and conclusions

The spatial proximity, age and paragenetic sequence similarities, all indicate that both Algamarca and Shahuindo are related to the same magmatic-hydrothermal center. However, although

they were generated from a common source, they do show strongly different mineralization styles. At Algamarca, ore occurs as veins with typical textures of open space precipitation, gold is present as native gold and as gold-telluride minerals. Arsenical pyrite occurs in a similar position as at Shahuindo and it is expected to host bound gold (LA-ICP-MS analysis are in progress to evaluate its gold content). The main and most common Au ore-bearing minerals in epithermal deposits are known to be electrum, native gold, and Au tellurides (White and Hedenquist, 1995; Simmons et al., 2005), but arsenical pyrite has also been recognized as an important gold carrier in many cases (e.g., Reich et al., 2005; Deditius et al., 2014; Morishita et al. 2018; Sykora et al., 2018; references therein). Efficient gold scavenging by pyrite and arsenopyrite may occur from low-concentrated fluids undersaturated with respect to metallic gold, whereas native gold precipitation requires much more Au-concentrated fluids. Thermodynamic modeling of fluid-rock interactions at Shahuindo indicates that carbonaceous matter favor gold transport in chemically reactive few competent carbonaceous-bearing rocks (Vallance et al., 2019). By contrast, we infer that in Algamarca in highly competent and less reactive rocks other gold transport and mechanisms (e.g. uptake of reduced sulfur from the fluid related to sulfide precipitation) lead to native gold precipitation. Our findings highlight the importance of further studies such as fluid inclusions, stable isotopes, geochronology and, most importantly, the true state of this bound gold in the mineral that can only be assessed by direct in situ techniques (synchrotron), coupled with the full range of more traditional microanalytical methods, to understand the respective gold transport, deposition, at Shahuindo and Algamarca. Our results show an example of different styles of gold epithermal mineralization present in a same hydrothermal-magmatic system; they thus offer important perspectives for improving exploration models for gold mineralization in Northern Peru.

Acknowledgements

References

Acosta, J., Rivera, R., Valencia, M., Chirif, H., Huanacuni, D., Rodríguez, I., Villareal, E., Paico, D., Santisteban, A., Santisteban, A., 2009, Memoria mapa metalogenético del Perú 2009. Instituto geológico minero y metalúrgico (INGEMMET), Perú, 17 p.

Bussey, S., Nelson, E., 2011, Geological analysis of the Shahuindo district, Cajabamba Province, Peru. Prepared by Western Mining Services LLC for Sulliden Gold Corporation.

Defilippi, C., Dyer, T., Tietz, P., 2012, Technical Report on the Shahuindo Heap Leach Project Cajabamba, Peru. NI 43-101 Technical Prepared for Sulliden Gold Corporation, Ltd, 420 p.

Defilippi, C., Muerhoff, C., Williams, T., 2016, Technical Report on the Shahuindo Mine, Cajabamba, Peru. NI 43-101 Technical Report for Tahoe Resources, 307 p.

Deditius, A., Reich, M., Kesler, S., Utsunomiya, S., Chryssoulis, S., Walshe, J., Ewing, R., 2014, The coupled geochemistry of Au and As in pyrite from hydrothermal ore deposits. Geochimica et Cosmochimica Acta, v. 140, p. 644-670.

Eude A., 2014, La croissance des Andes centrales du nord du Pérou (5-9°S): Propagation d'un prisme orogénique dans un contexte d'héritage tectonique et de subduction plane. Unpublished Ph.D. thesis, Toulouse, France, Paul Sabatier University, 323 p. https://tel.archives-ouvertes.fr/tel-01080498.

Montgomery, A., 2012, Metallogenetic controls on Miocene high sulphidation epithermal gold mineralization, Alto Chicama district, La Libertad, Northern Peru. Unpublished PhD dissertation Department of Geological Sciences and Geological Engineering. Kingston, Queen's University. 382 p.

Morishita, Y., Shimada, N., Shimada, K., 2018, Invisible gold in arsenian pyrite from the high-grade Hishikari gold deposit, Japan: Significance of variation and distribution of Au/As ratios in pyrite.Ore geology reviews, v. 95, p. 79-93.

Noble, D., McKee, E., 1999, The Miocene metallogenic belt of central and northern Peru. Soc. Economic Geology Special Publication 7, p. 155-193.

Reich, M., Kesler, S., Utsunomiya, S., Palenik, C., Chryssoulis, S., Ewing, R., 2005, Solubility of gold in arsenian pyrite. Geochimica et Cosmochimica Acta, v. 69, p. 2781-2796.

Reyes, L., 1980, Geología de los cuadrángulos de Cajamarca, San Marcos y Cajabamba. Instituto geológico minero y metalúrgico (INGEMMET), Perú, 75 p.

Sánchez Rodas Ramón. (2012), Determinación de los vectores de mineralización y zonamiento de alteraciones hidrotermales del proyecto Shahuindo-Perú, Facultad De Ingeniería. Universidad nacional de Cajamarca, p 48.

Saucier, G., and Poulin, L., 2004, Resources Estimation, Shahuindo Project, Peru, prepared for Sulliden Exploration by Met-Chem Canada Inc.

INSTITUTO
DE INGENIEROS
DE MINAS
DEL PERÚ

Annex IV

proEXPLO2021

Simmons, S., White, N., John D., 2005, Geological characteristics of epithermal precious and base metal deposits. v. 100th anniversary, p. 485-522.

Sillitoe, R., 2010, Porphyry copper systems. Economic geology, v. 105, p. 3-41.

Sykora, S., Cooke D., Meffre, S., Stephanov A., Gardner, K., Scott R., Selley D., Harris, A., 2018, Evolution of pyrite trace element compositions from porphyry-style and epithermal conditions at the Lihir gold deposit: Implications for ore genesis and mineral processing. Economic Geology, v. 113, p. 193-208.

Tumilan, P., 2003, Compendio de yacimientos minerales del Perú – Boletín 10. Instituto geológico minero y metalúrgico, Perú, 619 p.

Vallance, J., Balboa, M., Berna, B., Baya, C., Baby P., Pokrovski, G., 2019, Links between organic matter and gold-bearing arsenian pyrite at Shahuindo (Cajamarca, Peru): an integrated analytical and modeling study. XI congreso internacional de prospectores y exploradores, Extended Abstracts, Peru, 5 p.

White, N., Hedenquist J, 1995, Epithermal gold deposits: styles, characteristics, and exploration. SEG newsletter, v. 23 p. 9-13.
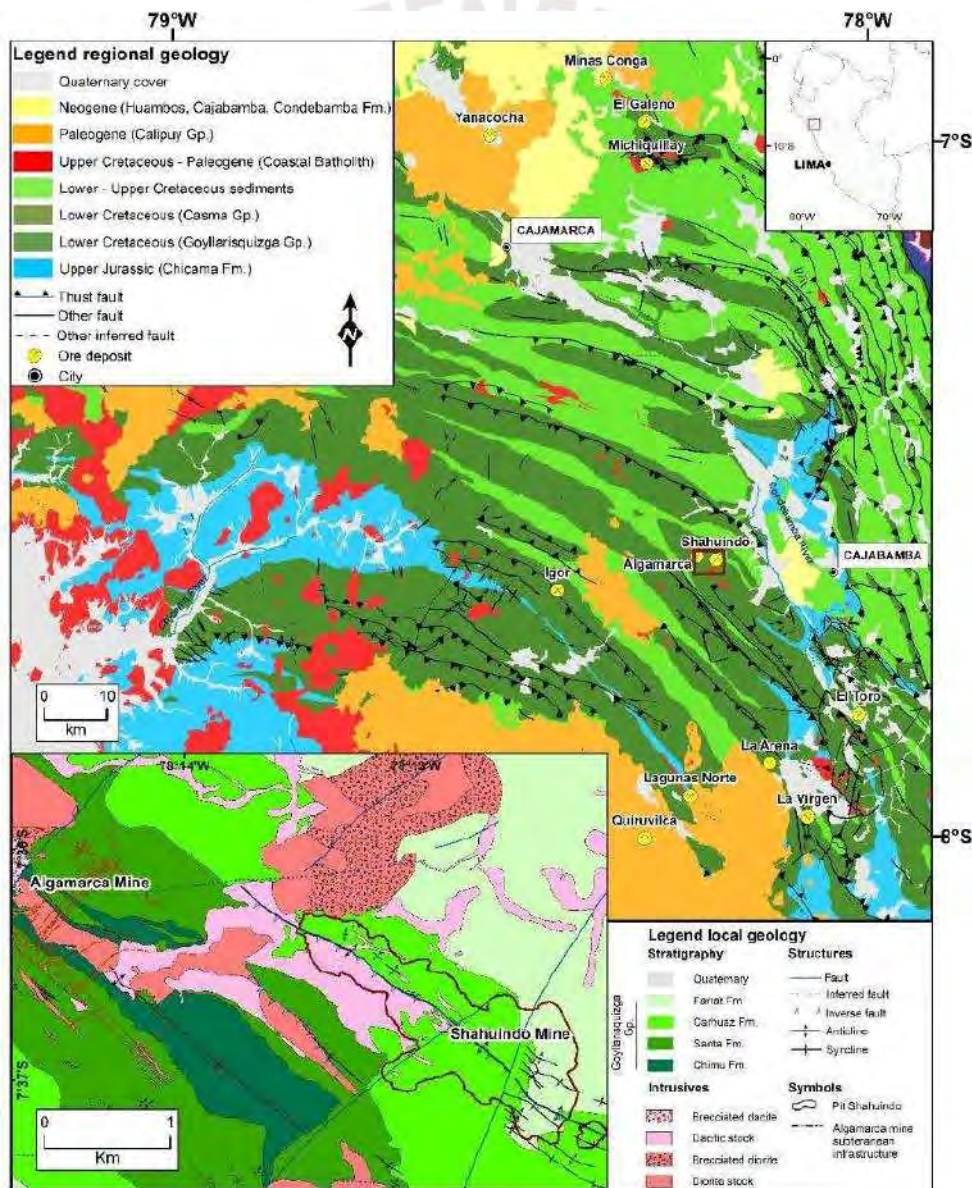
Fig.1. Geological map of the Marañon Fold and Thrust Belt in northern Peru with location of major deposit and projects, modified from Eude (2014). Inset: Geological map of the study area with location of the

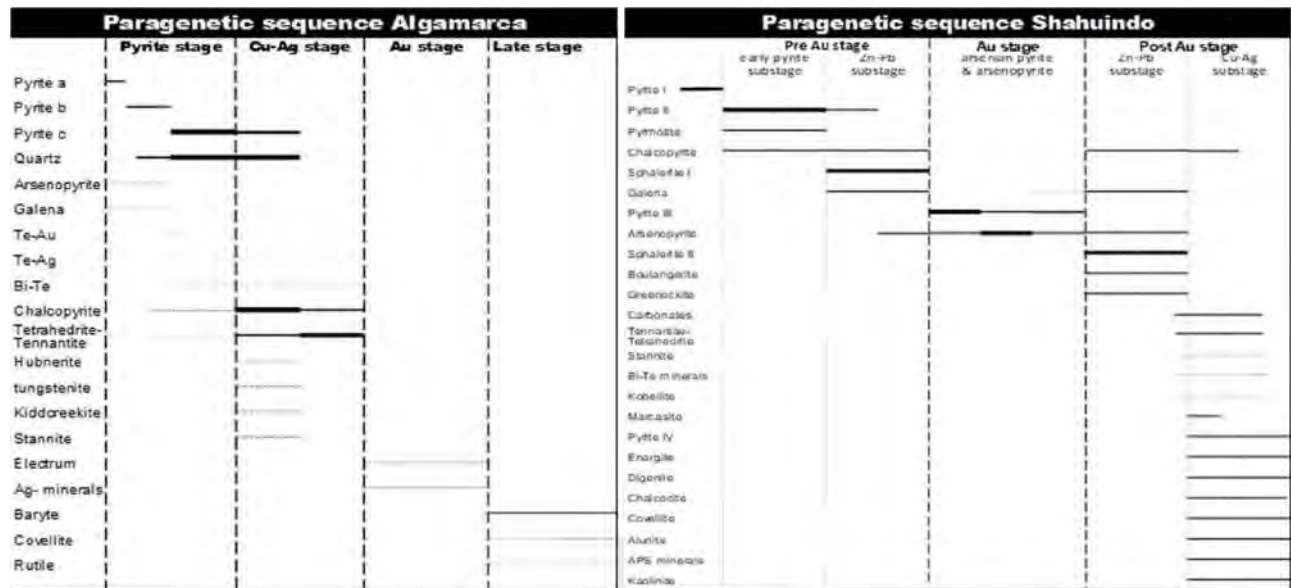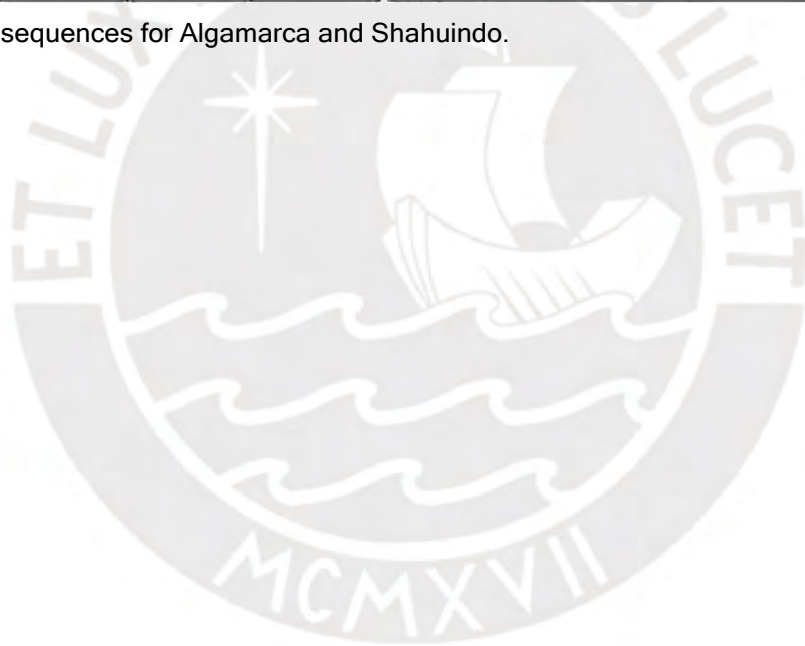Shahuindo open pit and the former Algamarca mine (Pan American Silver, 2019).

Fig. 2. Paragenetic sequences for Algamarca and Shahuindo.

Decoding hydrothermal fluids in organic carbon-rich basins: The case of the Algamarca Au-Ag-Cu deposit, Northern Peru. Implications for targeting hidden porphyry deposits

Renzo Galdos[1,2], Jean Vallance[1,3], Patrice Baby[1,2], Stefano Salvi[2], Michael Schirra[4], German Velasquez[2,5] and Gleb S. Pokrovski[2]

[1] Grupo de investigación en Geología de Yacimientos, Especialidad de Ingeniería Geológica, Pontificia Universidad Católica del Perú, Av. Universitaria 1801, San Miguel, Lima 15088, Perú. E-mail : rgaldosp@pucp.edu.pe

[2] Géosciences Environnement Toulouse, Université Toulouse III - Paul Sabatier, CNRS, IRD, CNES, OMP, 14 avenue Edouard Belin, F-31400 Toulouse, France.

[3] Thin Section Lab, 1223 rue du Bois la Ville, F-54200 Toul, France.

[4] Department of Earth Sciences, University of Geneva, rue des Maraîchers 13, CH-1205 Geneva, Switzerland.

[5] Instituto de Geología Económica Aplicada, Universidad de Concepción, casilla 160-C, Concepción, Chile.

1. Abstract

The nature of the gold-bearing fluid and the source of gold in sedimentary-hosted gold deposits of Carlin, orogenic or epithermal types is still matter of debate. Most authors point to magmatic/metamorphic origin for the fluids, however, the properties of such fluids and their interactions with organic carbon – a common component in this type of deposits – are not sufficiently well known. Here we present a large set of novel geochemical, mineralogical and fluid-inclusion data obtained from the Algamarca Au-Ag-Cu epithermal veins, corresponding to lateral manifestation of the neighbouring sedimentary-hosted epithermal-gold deposit at Shahuindo. Our data reveal that strong interactions of a metal-bearing magmatic fluid with the organic carbon in the sedimentary basin exerted a primary control on gold transport, precipitation and distribution.

Keywords: Fluid inclusions; Pyrite; Epithermal; Gold.

Resumen

La naturaleza del fluido aurífero y el origen del oro en los yacimientos de oro hospedados en sedimentos del tipo Carlin, orogénico y epitermal continúan siendo tema de debate. Los modelos más recientes apuntan a un origen magmático; sin embargo, las propiedades de dichos fluidos y sus interacciones con el carbón orgánico (un componente común en este tipo de depósitos) no han sido suficientemente estudiadas. Aquí presentamos datos de las vetas epitermales de Au-Ag-Cu del depósito de Algamarca, que son un equivalente lateral del deposito epitermal de oro hospedado en sedimentos de Shahuindo. Nuestros datos revelan directamente fuertes interacciones de un fluido de origen magmático con el carbón orgánico de la cuenca sedimentaria. Estas interacciones ejercieron un control primordial sobre el transporte, la precipitación y la distribución del oro en el yacimiento.

2. Introduction

Recent models inferred a magmatic source for gold-bearing fluids in sedimentary-hosted gold deposits. However, most of these inferences come from indirect data of sulfur isotopes or trace elements in arsenian pyrite (e.g., Barker et al., 2009; Vallance et al., 2023) - the main gold ore in this kind of deposits. Recent thermodynamic modeling suggests that interactions between hydrothermal fluids and organic carbon may favor gold transport rather than its precipitation (Vallance et al., 2023), as commonly assumed. However, the source of gold-bearing fluids is poorly understood and the consequences of their interaction with the organic carbon remain elusive.

The aim of this work is to assess the origin, properties and evolution of the gold-bearing fluids responsible for Au-Ag-Cu mineralization in the Algamarca deposit, which is hosted in sedimentary sequences rich in carbonaceous material. We studied a large set of samples of ore veins from the Algamarca deposit. The samples were analyzed by

a series of analytical techniques: etching, scanning electron microscopy (SEM), X-ray powder diffraction (XRD), Raman spectroscopy (RS), electron microprobe analyses (EPMA), and laser ablation inductively coupled plasma mass spectrometry (LA-ICPMS). Fluid inclusions trapped in vein quartz were also investigated.

3. Geological setting

The Algamaca Au-Ag-Cu deposit is located 22 km west of the town of Cajabamba (Cajamarca region) of northern Peru, within the Marañon fold and thrust belt (MFTB). The MFTB hosts a suite of epithermal, porphyry and skarn deposits associated with intrusions from the Oligo-Miocene subduction-related magmatic arc (Noble and McKee, 1999; Scherrenberg et al., 2016). The Algamarca deposit consists of veins trending perpendicularly or obliquely to the Algamarca Anticline axis. This anticline corresponds to a partially eroded structure of the MFTB, which is an east-verging thin-skinned thrust system developed during late Cretaceous and the middle Eocene (early period of the Andean orogeny; Noble et al., 1979; Mégard, 1984). The close proximity (<1 km) between Algamarca and Shahuindo, and their similar age and ore mineralogy, suggest that both deposits correspond to the same magmatic/hydrothermal system (Galdos et al., 2021). The Mezosoic sediments that form the MFTB and host the Algamarca and Shahuindo deposits are enriched in carbon (mostly graphite, up to 2 wt%) that likely represents an overmature petroleum system.

4. Results

4.1. Sulfide ore minerals

4.1.1. Paragenetic sequence
Three mineralization stages have been identified: i) a pre-gold stage (stage A), characterized by quartz (Qz-I), pyrite (Py-I) and chalcopyrite; ii) a main gold stage (stage B), which presents an invisible-gold substage characterized by quartz (Qz-II) and arsenian pyrite hosting invisible gold (Py-II), and a visible-gold substage characterized by tetrahedrite-tennantite and chalcopyrite, where native gold occurs within microfractures in tetrahedrite-tennantite or along the contacts between the latter and chalcopyrite grains; iii) a barren post-gold stage (stage C), characterized by alunite, pyrophyllite, covellite and chalcocite. The

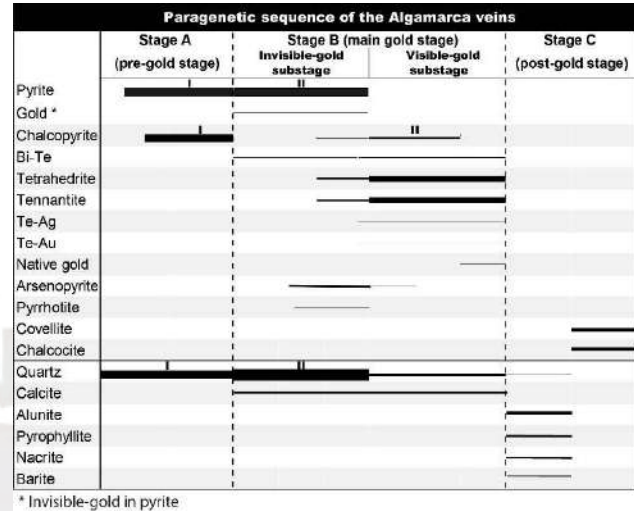paragenetic sequence for the Algamarca deposits is shown in Figure 1.

Fig. 1. Paragenetic sequence of the Algamarca veins. The line thickness is roughly proportional to the mineral abundance.

4.1.2. Sulfide mineral composition
Pyrite, chalcopyrite, tetrahedrite and tennantite, the most abundat ore minerals, and native gold from the veins were analyzed by EPMA and LA-ICPMS. Pyrite is the most important host of invisible gold (up to 160 ppm Au), whereas the other sulfides show much lower Au contents (<1 ppm Au). The pre-gold-stage pyrite (Py-I) presents lower invisible gold contents than the main-gold-stage pyrite (Py-II). The invisible gold contents in the latter significantly correlate with As contents and both show smooth patterns in the LA-ICPMS ablation signals, thus suggesting the absence of micro-particles of Au-bearing minerals. The main Ag host is tetrahedrite, with up to 1.6 wt% Ag, whereas tennantite and pyrite present much lower concentrations (<600 and <50 ppm, respectively). Native gold grains contain 14 wt% Ag, on average. Copper is mainly concentrated in chalcopyrite (in the pre-gold and main gold stages), tetrahedrite and tennantite (in the main gold stage). In the post-gold stage copper contents are lower, limited to scarse covellite and chalcocite.

4.2. Fluid inclusions

4.2.1. Fluid inclusions petrography
Four different types of fluid inclusions (FI), recognizable by their different phases present at room temperature, were identified in quartz from the

Algamarca veins (Fig. 2). These types of inclusions are distributed in two quartz generations, Qz-I (from the pre-gold stage) and Qz-II (from the invisible-gold substage). In chronological order these are: i) Immiscible-liquid FI (IL; Fig. 2a), containing a CO_2-H_2S-CH_4 gas bubble, a CO_2-H_2S-CH_4-H_2O liquid, an aqueous liquid, plus an opaque daughter mineral. ii) Multiphase-solid-bearing FI (MS), containing a brine, a vapour bubble, a halite crystal plus two additional solid phases consisting of an opaque mineral and a rounded transparent mineral (Fig. 2b). The number and proportion of phases is consistent in each FI assemblage; however, either of the latter two solids may be absent from a MS-type FI population. iii) Vapor-rich FI (VR) containing a dominant vapor phase and a liquid phase (Fig. 2c); these FI are found to coexist with the MS FI type. iv) Liquid-rich FI (LR) contain a dominat liquid phase and a vapor phase (Fig. 2d). The IL type occurs in Qz-I as clusters, pseudosecondary trails, or isolated FI. The MS and VR types occur in Qz-I as pseudosecondary and secondary trails, also crosscutting the IL type, and in clusters. The MS and VR types commonly form the same FI assemblage, suggesting boiling of the fluid. The LR type is hosted by Qz-II, which is clearly discernable by a darker cathodoluminescence than Qz-I. The LR type comprises primary FI parallel to growth bands, pseudosecondary and secondary FI trails, and FI in clusters and isolated individuals.
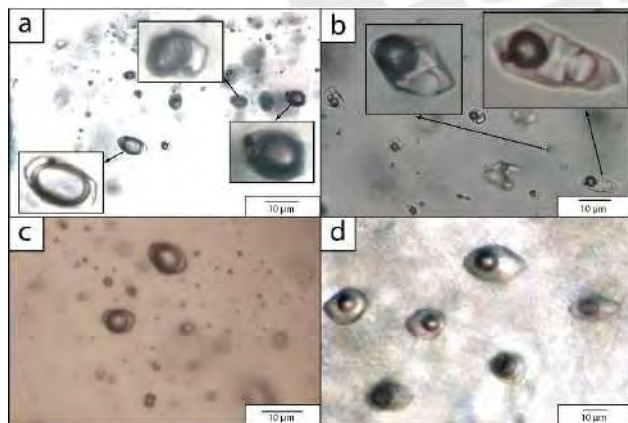

Fig. 2. (a) Immiscible-liquid fluid inclusions. (b) Multiphase-solid-bearing fluid inclusions. (c) Cluster of vapor-rich fluid inclusions. (d) Cluster of liquid-rich fluid inclusions.

4.1.2. Composition of fluid inclusions

The different types of FI show a wide salinity range. IL type vary from 1 to 3 wt% NaCl eq.; MS type vary from 30 to 38 wt% NaCl eq.; VR type vary from 2 to 3 wt% NaCl eq.; and LR type vary from 3 to 15 wt% NaCl eq. Raman analysis of the gas phase of the IL type shows presence of CO_2, CH_4 and H_2S, with average molar percentages of 63, 28 and 9 %, respectively. LA-ICPMS analyses on the FI show that LR assemblages contain (in order of decreasing mean concentration) Cl, Na, K, Fe, Ca and S, each one reaching up to 10,000 ppm levels, followed by moderately-abundant B, Mn, Mg, Zn (each one up to 2000 ppm), and by less abundant Cu, As, Sb, Pb, Cs, Sr (each one between 100s and 10s ppm), and, finally, Ag (< 5 ppm) and Au (≤0.2 ppm). The MS assemblages contain Cl, Fe, Na, K, and Mn always showing concentrations >1 wt %, followed by Zn (up to 0.8 wt %), Cu and Ca (both up to 0.7 wt %), and S (up to 0.6 wt %). Other minor, though omnipresent elements are Sb, As and Pb (each one up to 1,000 ppm levels), as well as Rb, Br, B, Bi, Sr, Cs, Ba, Ag (each one up to100s ppm) and Mo (<1 ppm). Gold was not detected in any of the inclusions.

5. Origin and evolution of the ore fluid

The structural and sedimentary architecture of the MFTB has controlled the emplacement of the intrusive bodies and dictated the pathways of the hydrothermal fluids and their interaction with the host, during and after thrust fault propagation. In the Miocene (period of Au-Ag-Cu deposition; Noble and Mckee, 1999), the Algamarca anticline was buried and formed a structural trap large enough to focus an important fluid flow, sufficient to produce the Algamarca deposit. However, this deposit is currently at the surface, as a result of modern Andean tectonic uplift and unroofing.

The IL type FI are strongly enriched in CO_2, CH_4 and H_2S, which is quite unusual for an epithermal or, for that matter, porphyry-style mineralization. This finding provides direct evidence suggesting that the hydrothermal fluid interacted with organic carbon, most likely in the sedimentary rocks. This led to massive production of CO_2 and CH_4 (and H_2S), according to carbon dissolution reactions such as: $2\,C + 2\,H_2O = CO_2 + CH_4$.

The mineralogy and FI data for the pre-gold stage (Qz-I) point to a porphyry-style mineralization, as suggested by high salt (NaCl, KCl) and ore metal (Fe, Cu, Zn) contents of the MS type FI. Such high contents are diagnostic of magmatic-derived brines in porphyry systems (e.g., Kouzmanov and Pokrovski, 2012). Conversely, the homogenization

169

temperature and salinity of the LR type FI (320 °C and 7 wt% NaCl eq., on average) in the main gold stage (Qz-II) are more consistent with epithermal conditions.

It thus appears that the Algamarca veins recorded an epithermal-type fluid flow, resulting in mineralization, superimposed onto previous porphyry-type fluid circulation. Similar Zn/Pb ratios measured in the MS type FI (Zn/Pb = 5±1) and LR type FI (Zn/Pb = 4±1; Fig. 3) attest for a common magmatic origin of the fluids evolving from porphyry-stage to epithermal-stage. Such Zn/Pb ratios are also consistent with those reported in giant porphyry deposits (from 1 to 6; Kouzmanov and Pokrovski, 2012). It follows that our investigation on the origin of mineralizing fluids at Algamarca has revealed the presence of a porphyry system at depth, providing a potential targeting tool for exploration.
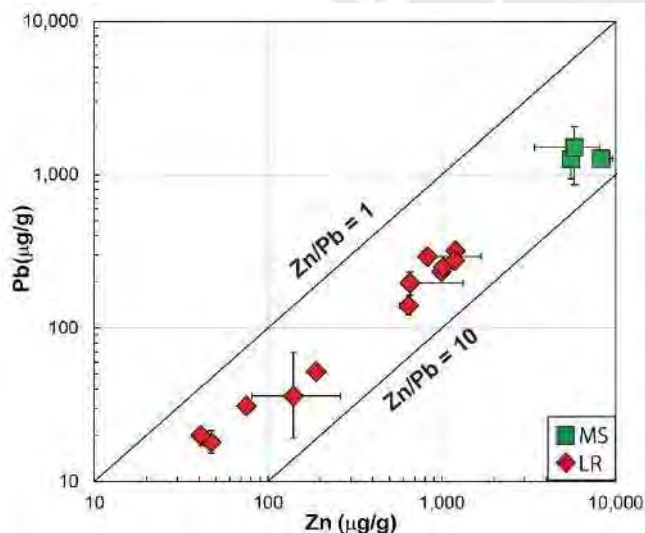

Fig. 3. Pb vs. Zn concentration analysed in the indicated types of fluid inclusion assemblages (FIAs). Each point represents an average concentration value, the error bars (shown when bigger than the symbol size) correspond to the minimun and maximun value within each FIA. MS = Multiphase-solid-bearing fluid inclusions, LR = liquid-rich fluid inclusions.

References

Barker, S.L., Hickey, K.A., Cline, J.S., Dipple, G.M., Kilburn, M.R., Vaughan, J.R., Longo, A.A., 2009. Uncloaking invisible gold: Use of nanoSIMS to evaluate gold, trace elements, and sulfur isotopes in pyrite from Carlin-type gold deposits. Economic Geology, v. 104, p. 897-904.

Galdos R., Vallance J., Baby P., Pokrovski G.S., 2021. A common hydrothermal magmatic system generates different styles of gold mineralization at Algamarca and Shahuindo, Northern Peru. ProEXPLO 2021, Lima, Peru. Extended Abstracts, p. 100-104.

Kouzmanov, K., Pokrovski, G.S., 2012. Hydrothermal controls on metal distribution in porphyry Cu (-Mo-Au) systems. SEG Special Publication, v. 16, p. 573-618.

Mégard, F., 1984. The Andean orogenic period and its major structures in central and northern Perú. Journal of the Geological Society, v. 141, p. 893-900.

Noble, D.C., McKee, E.H., Mégard, F., 1979. Early Tertiary "Incaic" tectonism, uplift, and volcanic activity, Andes of central Peru. Geological Society of America Bulletin, v. 90, p. 903-907.

Noble, D.C., McKee, E.H., 1999. The Miocene Metallogenic Belt of Central and Northern Peru. In: Skinner, B.J. (Ed.), Geology and ore deposits of the Central Andes. SEG Special Publication, v. 7, p.155-193.

Scherrenberg, A.F., Kohn, B.P., Holcombe, R.J., Rosenbaum, G., 2016. Thermotectonic history of the Marañón Fold-Thrust Belt, Peru: Insights into mineralisation in an evolving orogen. Tectonophysics, v. 667, p. 16-36.